AD-A173 639 PROCEEDINGS OF THE ARMY SCIENCE CONFERENCE (1986) HELD 1/4
AT WEST POINT NEW..(U) DEPUTY CHIEF OF STAFF FOR
RESEARCH DEVELOPMENT AND ACQUISITIO.. 20 JUN 86

UNCLASSIFIED F/G 5/2 NL

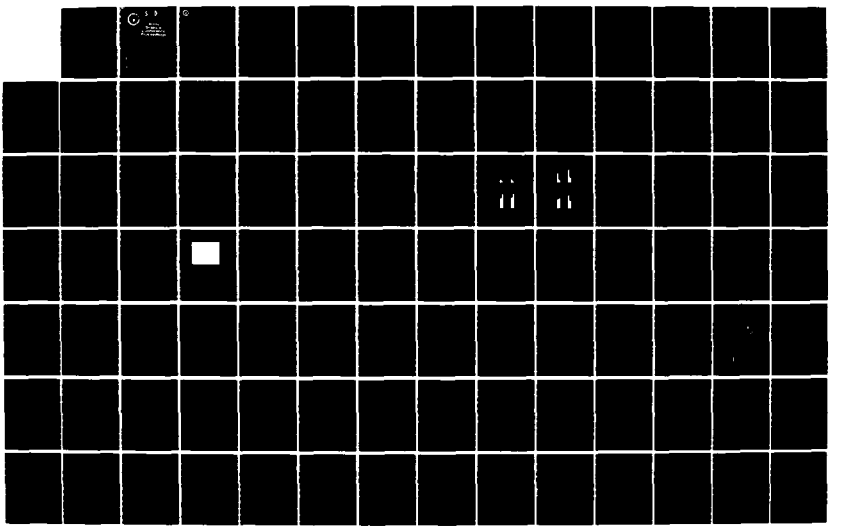

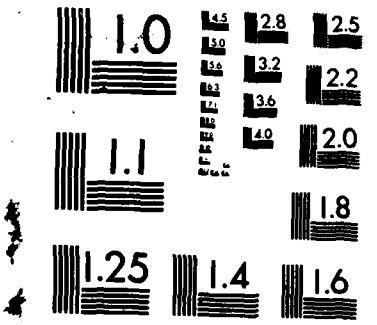

MICROCOPY RESOLUTION TEST CHART
NATIONAL BUREAU OF STANDARDS-1963-A

DTIC
ELECTE
OCT 2 8 1986
S D
D

(13)

AD-A173 639

Army Science Conference Proceedings

17-19 June 1986
Volume II
Principal Authors H through L

This document has been approved for public release and sale; its distribution is unlimited.

DTIC FILE COPY

Deputy Chief of Staff for Research,
Development & Acquisition
Department of the Army

86 10 28 009

DEPARTMENT OF THE ARMY
OFFICE OF THE DEPUTY CHIEF OF STAFF
FOR RESEARCH, DEVELOPMENT, AND ACQUISITION
WASHINGTON, DC 20310-0600

REPLY TO
ATTENTION OF

DAMA-ARR

20 June 1986

SUBJECT: Proceedings of the 1986 Army Science Conference

SEE DISTRIBUTION

1. The 15th in a series of Army Science Conferences was held at the United States Military Academy, 17-19 June 1986. The conference presented a cross section of the many significant scientific and engineering programs carried out by the Department of the Army. Additionally, it provided an opportunity for Department of the Army civilian and military scientists and engineers to present the results of their research and development efforts before a distinguished and critical audience.

2. These Proceedings of the 1986 Army Science Conference are a compilation of all papers presented at the conference and the supplemental papers that were submitted. The Proceedings consist of five volumes, four of which are unclassified (Volumes I through IV). Volume V contains limited distribution and classified papers.

3. Our purpose for soliciting these papers was to:

a. Stimulate the involvement of scientific and engineering talent within the Department of the Army.

b. Demonstrate Army competence in research and development.

c. Provide a forum wherein Army personnel can demonstrate the full scope and depth of their current projects.

d. Promote the interchange of ideas among members of the Army scientific and engineering community.

4. The information contained in these volumes will be of benefit to those who attended the conference and to others interested in Army research and development. It is requested that these Proceedings be placed in technical libraries where they will be available for reference.

LOUIS C. WAGNER, JR.
Lieutenant General, GS
Deputy Chief of Staff for
Research, Development
and Acquisition

QUALITY INSPECTED 4

odes
or
Special
A-1

DISTRIBUTION:
Office of the Secretary of Defense, Strategic Defense Initiative Orgn, ATTN: IST, Wash, DC 20301-7100
Office of the Under Secretary of Defense for Research and Engineering, Wash, DC 20301-3010
Office of the Under Secretary of Defense for Research and Advanced Technology, Wash, DC 20301-3080
Office of the Assistant Secretary of the Army (RD&A), Wash, DC 20310-0103
HQDA, Assistant Chief of Staff for Intelligence, ATTN: DAMI-ZS, Wash, DC 20310-1001
U.S. Army Foreign Science and Technology Center, ATTN: AMXST-OC, Charlottesville, VA 22901-5396
HQDA, Deputy Chief of Staff for Logistics, ATTN: DALO-ZD, Wash, DC 20310-0500
HQDA, Deputy Chief of Staff for Operations & Plans, ATTN: DAMO-ZD, Wash, DC 20310-3200
HQDA, Deputy Chief of Staff for Personnel, ATTN: DAPE-PSR, Wash, DC 20310-0300
HQDA, Deputy Chief of Staff for Research, Development and Acquisition, ATTN: DAMA-ARR, Wash, DC 20310-0632
Combat Support Systems Directorate, ATTN: DAMA-CSZ, Wash, DC 20310-0601
Materiel Plans & Programs Directorate, ATTN: DAMA-PPF, Wash, DC 20310-0600
Weapons Systems Directorate, ATTN: DAMA-WSZ, Wash, DC 20310-0600
Office of the Chief of Engineers, ATTN: DAEN-RDZ, Wash, DC 20314-1000
Office of the Surgeon General, ATTN: DASG-RDZ, Wash, DC 20310-2300
COMMANDERS/DIRECTORS:
US Army Strategic Defense Command, P. O. Box 1500, Huntsville, AL 35807-3801
US Army Information Systems Engineering Command, Ft. Belvoir, VA 22060-5456
US Army Concepts Analysis Agency, 8120 Woodmont Avenue, Bethesda, MD 20814-2797
US Army Forces Command, Ft. McPherson, GA 30330-6000
US Army Logistics Center, ATTN: ATCL-M, Ft. Lee, VA 23801-6000
US Army Missile Command, ATTN: AMSMI-RD, Redstone Arsenal, AL 35898-5248
US Army Materiel Command, ATTN: AMCLD, 5001 Eisenhower Avenue, Alexandria, VA 22333-0001
US Army Materiel Systems Analysis Activity, ATTN: AMXSY-D, APG, MD 21005-5071
US Army Armament, Munitions & Chemical Cmd, ATTN: AMSMC-CG, Rock Island, IL 61299-6000
US Army Armament R&D Center, ATTN: SMCAR-TD, Dover, NJ 07801-5001
Fire Support Armaments Center, ATTN: SMCAR-FS, Dover, NJ 07801-5001
Armament Engineering Directorate, ATTN: SMCAR-AE, Dover, NJ 07801-5001
Close Combat Armaments Center, ATTN: SMCAR-CC, Dover, NJ 07801-5001
Chief, Benet Weapons Lab, Watervliet Arsenal, Watervliet, NY 12189-4050
Chemical R&D Center, ATTN: SMCCR-TD, APG, MD 21010-5423
US Army Aviation Systems Cmd, ATTN: AMSAV-GTD, 4300 Goodfellow Blvd., St. Louis, MO 63120-1798
USARTA, Ames Research Center, ATTN: SAVRT-D, Moffett Field, CA 94035-1099
USARTA, Aeroflightdynamics Dir., ATTN: SAVRT-AF, Moffett Field, CA 94035-1099
USARTA, Aviation Applied Technology Dir., ATTN: SAVRT-TY, Ft. Eustis, VA 23604-5577
USARTA, Propulsion Dir., ATTN: SAVRT-PN, 21000 Brook Park Rd., Cleveland, OH 44135-3127

USARTA, Aerostructures Dir., ATTN: SAVRT-SD, Hampton, VA 23665-5225
Aviation Engineering Flight Activity, ATTN: SAVTE-C, Edwards AFB, CA 93523-5000
Avionics R&D Activity, ATTN: SAVAA-G, Ft. Monmouth, NJ 07703-5401
US Army Communications-Electronics Cmd, ATTN: AMSEL-TDD, Ft. Monmouth, NJ 07703-5001
Night Vision and Electro-Optics Lab, ATTN: AMSEL-NV-D, Ft. Belvoir, VA 22060-5166
Signals Warfare Lab, ATTN: AMSEL-SW-D, Vint Hill Farms Station, Warrenton, VA 22186-5100
Electronics Warfare TSTA Ctr, ATTN: AMSEL-EW-D, Ft. Monmouth, NJ 07703-5303
US Army Laboratory Command, ATTN: AMSLC-CG, 2800 Powder Mill Road, Adelphi, MD 20783-1145
US Army Ballistic Research Lab, ATTN: SLCBR-OD, APG, MD 21005-5006
Atmospheric Sciences Laboratory, ATTN: SLCAS-DD, WSMR, NM 88002-5501
Electronics Technology & Devices Lab, ATTN: SLCET-D, Ft. Monmouth, NJ 07703-5302
Vulnerability Assessment Lab, ATTN: SLCEW-M-D, WSMR, NM 88002-5513
Harry Diamond Laboratories, ATTN: SLCHD-D, Adelphi, MD 20783-1197
Human Engineering Lab, ATTN: SLCHE-D, Aberdeen Proving Ground, MD 21005-5001
Materials and Technology Lab, ATTN: SLCMT-D, Watertown, MA 02172-0001
US Army Research Office, ATTN: SLCRO-D, Rsch Triangle Park, NC 27709-2211
US Army Research, Development & Standardization Group (Europe), Box 65, FPO New York 09510
US Army Tank-Automotive Command, ATTN: AMSTA-CR, Warren, MI 48397-5000
Tank-Automotive Systems Lab, ATTN: AMSTA-R, Warren, MI 48397-5000
Tank-Automotive Concepts Lab, ATTN: AMSTA-Z, Warren, MI 48397-5000
US Army Test & Evaluation Command, ATTN: AMSTE-TD, APG, MD 21005-5055
Aberdeen Proving Ground, ATTN: STEAP-OC, APG, MD 21005-5001
Dugway Proving Ground, ATTN: STEDP-CO, Dugway, UT 84022-5000
Electronic Proving Ground, ATTN: STEEP-DO, Ft. Huachuca, AZ 85613-7110
Aviation Development Test Activity, ATTN: STEBG-CO, Ft. Rucker, AL 36362-5276
Combat Systems Test Activity, ATTN: STECS-CO, APG, MD 21005-5059
White Sands Missile Range, ATTN: STEWS-CG, WSMR, NM 88002-5000
US Army Troop Support Cmd, ATTN: AMSTR-G, 4300 Goodfellow Blvd., St. Louis, MO 63120-1798
Belvoir R&D Center, ATTN: STRBE-ZT, Ft. Belvoir, VA 22060-5606
Natick R&D Center, ATTN: STRNC-T, Natick, MA 01760-5000
US Army Corps of Engineers
Cold Regions Rsch & Engineering Lab, ATTN: CRREL-TD, Hanover, NH 03755-1290
Construction Engineering Rsch Lab, ATTN: CERL-ZT, Champaign, IL 61820-1305
Engineer Topographic Laboratories, ATTN: ETL-TD, Ft. Belvoir, VA 22060-5546
Waterways Experiment Station, ATTN: WESTV, P.O. Box 631, Vicksburg, MS 39180-0631
US Army Medical R&D Command, ATTN: SGRD-ZA, Ft. Detrick, Frederick, MD 21701-5012
Aeromedical Research Lab, ATTN: SGRD-UAC, Ft. Rucker, AL 36362-5000
Institute of Dental Research, WRAMC, ATTN: SGRD-UDZ, Wash, DC 20307-5300
Inst of Surgical Research, ATTN: SGRD-USZ, Ft. Sam Houston, TX 78234-6200

Letterman Army Inst of Rsch, ATTN: SGRD-ULZ, Presidio of San Francisco, CA 94129-6800
Medical Bioengineering R&D Lab, ATTN: SGRD-UBZ, Frederick, MD 21701-5010
Medical Rsch Inst of Chemical Defense, ATTN: SGRD-UV-ZA, APG, MD 21010-5425
Medical Rsch Inst of Environmental Medicine, ATTN: SGRD-UEZ, Natick, MA 01760-5007
Medical Rsch Inst of Infectious Diseases, ATTN: SGRD-UIZ-A, Frederick, MD 21701-5011
Walter Reed Army Inst of Research, ATTN: SGRD-UWZ, Washington, DC 20307-5100
US Army Health Services Command, Ft. Sam Houston, TX 78234-6000
US Army Environmental Hygiene Agency, ATTN: HSHB-Z, APG, MD 21010-5422
US Army Research Institute for the Behavioral and Social Sciences, ATTN: PERI-BR, 5001 Eisenhower Avenue, Alexandria, VA 22333-5600
ARI Field Unit, ATTN: PERI-IJ, PO Box 2086, Ft. Benning, GA 31905-0686
ARI Field Unit, ATTN: PERI-SB, PO Box 6057, Ft. Bliss, TX 79906-0057
ARI Field Unit, ATTN: PERI-SH, HQ TCATA, Ft. Hood, TX 76544-5065
ARI Field Unit, ATTN: PERI-IK, Steele Hall, Ft. Knox, KY 40121-5620
ARI Field Unit, ATTN: PERI-SL, PO Box 290, Ft. Leavenworth, KS 66048-0290
ARI Field Unit, ATTN: PERI-IR, Ft. Rucker, AL 36362-5000
ARI Field Unit, ATTN: PERI-IO, PO Box 5787, Presidio of Monterey, CA 93944-5011
US Army Training and Doctrine Command, ATTN: ATCG, Fort Monroe, VA 23651-5000
TRADOC Research Analysis Center, WSMR, NM 88002-5502
Training Technology Agency, ATTN: ATTG-D, Ft. Monroe, VA 23651-5000

COMMANDANTS:
US Army Air Defense School, ATTN: ATSA-CG, Ft. Bliss, TX 79916-5000
US Army Armor School, ATTN: ATSB-CG, Ft. Knox, KY 40121-5000
US Army Transportation and Aviation Logistics School, ATTN: ATSG-CG, Ft. Eustis, VA 23604-5361
US Army Chemical School, ATTN: ATZN-CG, Ft. McClellan, AL 36205-5020
US Army Engineer School, ATTN: ATZA-CG, Ft. Belvoir, VA 22060-5331
US Army Field Artillery School, ATTN: ATSF-CG, Ft. Sill, OK 73503-5600
US Army Infantry School, ATTN: ATSH-CG, Ft. Benning, GA 31905-5007
US Army Intelligence Center and School, ATTN: ATSI-CG, Ft. Huachuca, AZ 85613-7000
US Army Logistics Center, ATTN: ATCL-CG, Ft. Lee, VA 23801-6000
US Army Ordnance Center and School, ATTN: ATSL-CG, APG, MD 21005-5201
US Army Signal Center, ATTN: ATZH-CG, Ft. Gordon, GA 30905-5000
US Army Soldier Support Center, ATTN: ATZI-CG, Ft. Harrison, IN 46216-5000

SUPERINTENDENT:
US Military Academy, ATTN: Technical Library, West Point, NY 10996-1799

COPIES FURNISHED:
DOD
Defense Advanced Research Projects Agency, 1400 Wilson Blvd., Arlington, VA 22209-2308
Defense Technical Information Center, Cameron Station, Alexandria, VA 22304-6145
US Army
US Army Information Systems Engineering Support Activity, Ft. Huachuca, AZ 85613-5300
US Army Field Office, HQ AFSC/SDOA, Andrews AFB, MD 20331
US Army Inst for Research in Management Information & Computer Sciences, 115 O'Keefe Bldg., Georgia Inst of Technology, Atlanta, GA 30332-0800

US Navy
Naval Air Systems Command, Code AIR-93-D, 1411 Jefferson Davis Hwy., Wash, DC 20361-3000
Naval Research Lab, ATTN: Director of Research, Wash, DC 20375-5000
Office of Naval Research, Code 10, 800 North Quincy Street, Arlington, VA 22217-5000
HQ US Marine Corps, Code RD-1, Washington, DC 20380-0001

US Air Force
Air Force Systems Command, ATTN: Deputy Chief of Staff for Science and Tech, Andrews AFB, MD 20334-5000
Air Force Office of Scientific Research, ATTN: Tech Director, Bolling AFB, Wash, DC 20332-6448

Lawrence Livermore National Lab, ATTN: L-191, P.O. Box 808, Univ of California, Livermore, CA 94550

Los Alamos National Lab, ATTN: Dir for Energy, Res & Tech, Los Alamos, NM 87545

NASA HQS, ATTN: Suite 7237, 400 Maryland Avenue, SW, Wash, DC 20546

National Science Foundation, 1800 G Street, NW, Wash, DC 20550

United Nations Library, ATTN: Acquisiton Section, Room L-138A, NY, NY 10017

PROCEEDINGS

OF THE

1986 ARMY SCIENCE CONFERENCE

UNITED STATES MILITARY ACADEMY

WEST POINT, NEW YORK

17-19 JUNE 1986

VOLUME II

Principal Authors H through L

TABLE OF CONTENTS

PROCEEDINGS OF THE 1986 ARMY SCIENCE CONFERENCE

Author	Title	Vol	Page
Abele, Gunars	The Effects of Cold Environment on Rapid Runway Repairs	I	1
Adams, George F. Page, Michael J.	Thermochemistry of Boron Compounds	I	11
Alexander, Millard H.	See Melius, Carl F.	III	25
Alster, Jack	See Sollott, Gilbert P.	IV	173
Alving, Carl R.	See Owens, Roberta R.	III	163
Anderson, Jeffrey W.	The Army's Warrior Spirit	I	31
Andre, Richard G.	See Golenda, Claudia F.	I	327
Ashley, Paul R. Davis, Jack H.	Amorphous Silicon Liquid Crystal Spatial Light Modulator	I	45
Askew, Eldon W.	See Cucinell, Samuel A.	I	235
AuCoin, Thomas R.	See Ross, Raymond L.	III	311
AuCoin, Thomas R.	See Shappirio, Joel R.	IV	95
Avara, Elton P.	Comparison of Estimates of Average Transmission	V	1
Bacastow, Todd S.	See Guth, Peter L.	I	371
Bagwell, Thomas H. Jr.	Use of Streaming Current as a Method for Automatic Polyelectrolyte Dosage Control	I	53
Ballou, W. Ripley	See Hockmeyer, Wayne T.	II	27
Banderet, Louis E.	See Munro, Ilse	III	85
Bandy, John T. Smith, Edgar D.	A Practical Field Laundry Wastewater Recycling System	I	63
Barber, Teddy L.	See Measure, Edward M.	V	87
Barrett, Ann	See Briggs, Jack	I	81
Beatrice, Edwin S.	See Penetar, David M.	III	183

Author	Title	Vol	Page
Beaudoin, Richard	See Hockmeyer, Wayne T.	II	27
Behar, Isaac	See Simmons, Ronald	IV	127
Behncke, Robert	See Coe, Mark W.	I	217
Beichler, Glenn P. Lawler, Charles R.	Decoys, A Tool for Survival	V	15
Bergman, Werner	See Fedele, Paul D.	I	279
Bissett, Frank H.	See Cornell, John H.	I	225
Boobar, Lewis R.	See Sardelis, Michael R.	IV	33
Bosco, Charles D. Reitmeyer, Randolph Ferraglio, Robert	The "Science of Design" Opens the Door to Rapdid and Affordable Electronic Systems Development and Life Cycle Management	I	71
Boucher, Lisa J.	See Little, James S.	II	271
Boucher, Lisa J.	See Ray, Radharaman	III	221
Bovino, Lawrence J.	See Weiner, Maurice	IV	291
Boy, J. H.	See Stephenson, L. D.	IV	189
Briggs, Jack Dunne, C. Patrick Graham, Maryann Risvik, Einar Cardello, Armand Barrett, Ann Taub, Irwin	A Calorically Dense Ration for the 21st Century	I	81
Britan, Ronnie G.	See White, James L.	IV	335
Brooks, Larry W.	Effects of Summarized and Expanded Test on Readers' Content and Structural Knowledge	I	97
Broomfield, Clarence A.	See Little, James S.	II	271
Broomfield, Clarence A.	See Ray, Radharaman	III	221
Bryant, George Hynes, Thomas Swab, Jeffrey J.	Continuous Intrusive Temperature Sensor for Molten Metals Process Control	I	111
Bryk, Darryl C.	See Rose, Douglas N.	III	283

Author	Title	Vol	Page
Burden, Henry S.	See Jamison, Keith A.	II	95
Burke, Terence	See Weiner, Maurice	IV	291
Butler, Chalmers M.	See Schwering, Felix K.	IV	81
Canonico, Peter G. Gibbs, Paul H. Huggins, John W. Linden, Carol D. MacDonald, Carolyn McKee, Kelly T. Meegan, James Morrill, John Oland, Dwayne D. Peters, C. J. Reed, Lauren V.	Ribavirin Prophylaxis of Sandfly Fever - Sicilian Infection in Human Volunteers	I	127
Cardello, Armand	See Briggs, Jack	I	81
Carlson, Dawn	See Schnakenberg, David D.	IV	69
Celmins, Aivars K.	A New Crater Size Model Derived by Fuzzy Data Analysis	I	141
Cespedes, Ernesto R. Cress, Daniel H.	Analysis of Passive Imaging Concepts for Remote Minefield Detection Application	V	31
Chang, Lang-Mann	Diagnostic Ignition Studies in Support of the Development of Advanced 105-mm and 120-mm Tank Ammunition	I	155
Chen, P.C.T.	A New Method of Predicting Residual Stresses in Autofrettaged Gun Barrels	I	171
Chin, T. N.	Self-Induced Nonlinear Optical Effects and Device Concepts for Ocular Protection	I	185
Choi, Chang Sun	See Prask, Henry J.	III	207
Chu, Shih-Chi	Nonlinear Behavior of Weapon Structural Materials	I	201
Claybaugh, John R.	See Cucinell, Samuel A.	I	235
Clay, Wallace H.	See Kayser, Lyle D.	II	141

Author	Title	Vol	Page
Coe, Mark W. Riggins, Robert E. Behncke, Robert	Innovative Systems Concepts for Integrated Training Management	I	217
Collett, Marc S.	See Dalrymple, Joel M.	I	249
Conrad, Raymond W.	See Patterson, Stanley P.	III	173
Cornell, John H. Cullen, John Richard, Gretchen C. Stapler, John T. Bissett, Frank H.	Synthesis and Evaluation of Reactive Polymers for Chemical Protection	I	225
Cress, Daniel H.	See Cespedes, Ernesto R.	V	31
Cucinell, Samuel A. Askew, Eldon W. Claybaugh, John R.	Influence of Rations on the Physical Performance of Troops at High Altitude	I	235
Cullen, John	See Cornell, John H.	I	225
Curtis, John O.	See Scoggins, Randy K.	V	157
Dagdigian, Paul J.	See Melius, Carl F.	III	25
Dalrymple, Joel M. Morrill, John C. Smith, Jonathan F. Collett, Marc S.	Evaluation of a Recombinant Vaccinia Virus Vaccine Candidate for Rift Valley Fever	I	249
D'Amico, William P.Jr.	See Kayser, Lyle D.	II	141
D'Amico, William P.Jr.	See Nusca, Michael J.	III	111
Davio, Stephen R.	See Martin, Dale G.	III	1
Davis, Edward G. Mioduszewski, Robert J.	Chemical Computer Man: Chemical Agent Response Simulation	I	263
Davis, Jack H.	See Ashley, Paul R.	I	45
Dekanski, Deborah A.	See Ross, Raymond L.	III	299
Dekanski, Deborah A.	See Ross, Raymond L.	III	311
Deponai, John M., III	See Snellen, James E.	IV	143
Diggs, Carter L.	See Hockmeyer, Wayne T.	II	27
Ditillo, John T.	See Kroutil, Robert T.	V	71

Author	Title	Vol	Page
Dixon, Samuel	See Ross, Raymond L.	III	311
Duncan, Louis D.	Transmittance Models for Broadband Systems	V	47
Dunne, C. Patrick	See Briggs, Jack	I	81
Durst, H. Dupont	See Landis, Wayne G.	II	217
Eckart, Donald W.	See Gualtieri, John G.	I	357
Escarsega, Dawn	See Rodriguez, Gumersindo	III	251
Fallesen, Jon J.	See Kurtz, Gary L.	II	183
Fedele, Paul D. Bergman, Werner McCallen, Rose Sutton, Steven	Hydrodynamically Induced Aerosol Transport Through Clothing	I	279
Ferraglio, Robert	See Bosco, Charles D.	I	71
Feuer, Henry	See Rodriguez, Gumersindo	III	251
Finnegan, John J.	See Shappirio, Joel R.	IV	95
Flanigan, Dennis F.	See Kroutil, Robert T.	V	71
Fox, Donald C.	See Shappirio, Joel R.	IV	95
Fox-Talbot, Mary K.	See Little, James S.	II	271
Francesconi, Ralph	See Schnakenberg, David D.	IV	69
Friar, Glenn S.	See Jones, Donald E.	II	125
Gallo, Benedict J.	See Walker, John E.	V	251
Gatza, Paul	See Rodriguez, Gumersindo	III	251
Gerhart, Grant R. Thomas, David J. Martin, Gary L. Gonda, Terry G.	Concept Vehicle Thermal Image Simulation	I	295
Gibbs, Paul H.	See Canonico, Peter G.	I	127
Gilbert, Everett E.	See Sollott, Gilbert P.	IV	173
Goehring, Dwight J. Hart, Roland J.	The Simulated Annealing Algorithm Applied to Scheduling of Army Unit Training	I	311

Author	Title	Vol	Page
Golenda, Claudia F. Wirtz, Robert A. Andre, Richard G.	An In Vivo Bioassay as a Primary Screen for Nerve Agent Antidotes	I	327
Gonda, Terry G.	See Gerhart, Grant R.	I	295
Graham, Maryann	See Briggs, Jack	I	81
Gray, Wayne D. Mutter, Sharon A. Swartz, Merryanna L. Psotka, Joseph	Novice to Expert: Implications for Artificial Intelligence Systems	I	341
Gregory, Don A.	See Johnson, John L.	II	111
Gualtieri, John G. Eckart, Donald W.	Electrode Diffusion and its Suppression in Alpha-Quartz	I	357
Gupta, Raj K.	See Rutledge, Louis C.	III	343
Guth, Peter L. Ressler, Eugene K. Bacastow, Todd S.	Computerized Terrain Analysis for the Field: Technology and Software Deployable Today	I	371
Hagman, Joseph D. Hayes, John F.	Learning Cooperatively Can Be More Effective Than Learning Alone	II	1
Harper, Bruce G. Midgley, Leonora P. Resnick, I. Gary Landis, Wayne G.	Scale-Up Production and Purification of Diisopropylfluorophosphatase from Tetrahymena Thermophila	II	17
Harper, Bruce G.	See Landis, Wayne G.	II	217
Hart, Roland J.	See Goehring, Dwight J.	I	311
Hawkins, George S.	See Reifenrath, William G.	III	235
Hayes, John F.	See Hagman, Joseph D.	II	1
Heath, Linda S.	See Shappirio, Joel R.	IV	95
Hockmeyer, Wayne T. Young, James F. Ballou, W. Ripley Wirtz, Robert A. Schneider, Imogene Miller, Louis H. Beaudoin, Richard Diggs, Carter L.	Development of a Genetically Engineered Malaria Vaccine for Man	II	27
Hockmeyer, Wayne T.	See Owens, Roberta R.	III	163

Author	Title	Vol	Page
Hock, V. F.	See Stephenson, L. D.	IV	189
Hoenig, Stuart A.	See Yalamanchili, Rao	IV	361
Hollinger, Jeffrey O. Schmitz, John P.	A Synthetic Bone Repair Material	II	39
Holter, John J.	See Seiders, Barbara A. B.	V	189
Homan, Clarke G. Scholz, W.	Superconducting Augmented Rail Gun (SARG)	II	55
Hsu, Chen C. Pistritto, Joseph V.	Catalytic Air Purification for Collective Protection	II	67
Hubbard, Roger W.	See Schnakenberg, David D.	IV	69
Huggins, John W.	See Canonico, Peter G.	I	127
Hynes, Thomas	See Bryant, George	I	111
Iafrate, Gerald J.	See Ross, Raymond L.	III	299
Iyer, Sury	Radiation Casting of Energetic Material Formulations with Binders	II	81
Jamison, Keith A. Powell, John D. Marquez-Reines, Miguel Burden, Henry S.	Results from Railgun Plasma - Armature Investigations	II	95
Johnson, Bruce D.	See Weisman, Idelle M.	IV	303
Johnson, John L. Gregory, Don A.	Adaptive Phased Array Radar, Artificial Neural Networks, and Optics	II	111
Johnson, Richard	See Schnakenberg, David D.	IV	69
Jones, Donald E. Friar, Glenn S.	Development of an Experimental Manipulator Arm for Applications in the Close Combat Mission Area	II	125
Jourdan, Mark R. Sullivan, Garrett J.	Hydrologic Forecasting in the Tactical Environment	V	57
Kayser, Lyle D. Clay, Wallace H. D'Amico, William P.Jr.	Surface Pressure Measurements on a 155mm Projectile in Free-Flight at Transonic Speeds	II	141
Klein, Joel M.	Modeling the Spread of Liquid Droplets on Non-Ideal Surfaces	II	155

Author	Title	Vol	Page
Knox, Francis S.	See Simmons, Ronald	IV	127
Koza, Walter	See Ward, Janet E.	IV	265
Krishnamurthy, Thaiya Szafraniec, Linda Sarver, Emory W.	Structural Investigations and Analysis of Fresh Water Blue-Green Algal (Microcystis Aeruginosa and Anabena-Flos-Aquae) Hepatotoxic Peptides by Tandem Mass Spectrometric Techniques	II	169
Kroutil, Robert T. Ditillo, John T. Flanigan, Dennis F.	An Autonomous Background Compensation Algorithm for Stand-Off Chemical Agent Detection	V	71
Kurtz, Gary L. Fallesen, Jon J.	Display and Control Research to Enhance Performance of Short-Range Air Defense (SHORAD) Fire Unit Personnel	II	183
Kwiatkowski, Joseph H.	See Shappirio, Joel R.	IV	95
Lakhani, Hyder	Enlisted Manpower Costs of the Bradley Fighting Vehicle and the M113: An Application of a Prototype Army Manpower Cost (AMCOS) Model	II	199
Landis, Wayne G. Durst, H. Dupont Savage, Russell E.Jr. Harper, Bruce G.	The Tetrahymena-DFPases: Elucidation, Characteristics, Therapeutic Potential, and Utility as Non-Corrosive Decontaminants	II	217
Landis, Wayne G.	See Harper, Bruce G.	II	17
Lane, Gerald R.	See Leighty, Robert D.	II	243
Langley, William H.	See Lorton, Lewis	II	285
Lawler, Charles R.	See Beichler, Glenn P.	V	15
Lee, Claire H.	See Silverman, Gerald J.	V	205
Leibrecht, Bruce C. Patterson, James H.Jr.	Controlling Impulse Noise Hazards: Programmatic Model for Developing Validated Exposure Standards	II	233
Leighty, Robert D. Lane, Gerald R.	Developing Technologies for Army Autonomous Land Vehicles	II	243
Leipertz, Donald F.	See White, James L.	IV	335
Lengsfield, Byron H.III	Application of Theoretically Computed Vibrational Spectra to the Remote Sensing of Chemical Agents and the Study of Energetic Compounds	II	259

Author	Title	Vol	Page
Leonard, Joseph M.	See Seiders, Barbara A. B.	V	189
Linden, Carol D.	See Canonico, Peter G.	I	127
Little, James S. Broomfield, Clarence A. Fox-Talbot, Mary K. Boucher, Lisa J.	A Potential Nerve Agent Decontaminant from Mammalian Liver	II	271
Lorton, Lewis Langley, William H.	Computer Assisted Postmortem Identification	II	285
Lovelace, Donald E. Sims, S. Richard F.	The Analysis of Shaped Charge Jet Flash Radiographs Using Image Processing Techniques	II	301
Lowell, George H. Smith, Lynette F. Seid, Robert C. Zollinger, Wendell D.	A Small Synthetic Peptide Bound via its Hydrophobic Foot to Meningococcal Outer Membrane Proteins Becomes a Highly Immunogenic Vaccine	II	313
Lukes, George E.	Automated Screening of Reconnaissance Imagery	II	329
Lussier, Adrien R.	See Munro, Ilse	III	85
Luteran, Thomas	See Seiders, Barbara A. B.	V	189
Lux, Robert A.	See Ross, Raymond L.	III	299
Lux, Robert A.	See Ross, Raymond L.	III	311
Lux, Robert A.	See Shappirio, Joel R.	IV	95
MacDonald, Carolyn	See Canonico, Peter G.	I	127
Manavalli, Shekhar	See Willingham, Reginald A.	IV	349
Marquez-Reines, Miguel	See Jamison, Keith A.	II	95
Martin, Dale G. Parker, Gerald W. Davio, Stephen R.	Medical Defense Against Saxitoxin	III	1
Martin, Gary L.	See Gerhart, Grant R.	I	295
McCallen, Rose	See Fedele, Paul D.	I	279
McDonald, Joseph K.	Wide Spectral Range Laser Research	III	15
McKee, Kelly T.	See Canonico, Peter G.	I	127

Author	Title	Vol	Page
McLachlan, Anthony D.	See Meyer, Fred P.	V	101
Measure Edward M. Yee, Young P. Barber, Teddy L.	Artillery Meteorology Without the Balloon	V	87
Meegan, James	See Canonico, Peter G.	I	127
Melius, Carl F. Thorne, Larry R. Dagdigian, Paul J. Alexander, Millard H. Miziolek, Andrzej W.	Gas Phase Combustion Chemistry of Nitramine Propellants	III	25
Mescall, John F. Tracy, Carl	Improved Modeling of Fracture in Ceramic Armors	III	41
Meyer, Fred P. Walck, James C. McLachlan, Anthony D.	Hardening of High Silica Content Optical Glasses to Infra-Red Laser Radiation	V	101
Midgley, Leonora P.	See Harper, Bruce G.	II	17
Milham, Merrill E.	CW Agent Detection by Lidar Returns from Ensembles of Optically Large Particles	III	55
Miller, Lewis D.	Nonlinear Mechanics of Granular Media: A Practical Application of Soliton Dynamics?	III	71
Miller, Louis H.	See Hockmeyer, Wayne T.	II	27
Mioduszewski, Robert J.	See Davis, Edward G.	I	263
Mitchell, Glen W.	See Simmons, Ronald	IV	127
Miziolek, Andrzej W.	See Melius, Carl F.	III	25
Moerkirk, Robert P.	See Ross, Raymond L.	III	299
Morrill, John C.	See Canonico, Peter G.	I	127
Morrill, John C.	See Dalrymple, Joel M.	I	249
Munro, Ilse Rauch, Terry M. Tharion, William Banderet, Louis E. Lussier, Adrien R. Shukitt, Barbara	Factors Limiting Endurance of Armor, Artillery and Infantry Units Under Simulated NBC Conditions	III	85

Author	Title	Vol	Page
Mutter, Sharon A.	See Gray, Wayne D.	I	341
Nauman, Robert K.	See Olenick, John G.	III	127
Nunes, John	Predicting Tensile Failure Stresses in Metal Matrix Composites	III	97
Nusca, Michael J. D'Amico, William P.Jr.	Parametric Study of Low Reynolds Number Precessing/Spinning Incompressible Flows	III	111
Oland, Dwayne D.	See Canonico, Peter G.	I	127
Olenick, John G. Wolff, Ruth Nauman, Robert K.	Nonvariant Nature, Cellular Localization and Protective Potential of a Membrane Fraction from Trypanosoma rhodesiense	III	127
O'Neill, Timothy R. Scott, Brad D.	"Dazzle" Camouflage and Tracking Performance	III	139
Owens, Frank J.	Computer Molecular Synthesis of Energetic Molecules	III	151
Owens, Roberta R. Wirtz, Robert A. Hockmeyer, Wayne T. Alving, Carl R.	Liposomes as Carriers for a Malaria Peptide Vaccine: Developmental Aspects	III	163
Page, Michael J.	See Adams, George F.	I	11
Parker, Gerald W.	See Martin, Dale G.	III	1
Patil, Ashok S.	Multispectral Camouflage Materials	V	119
Patterson, James H.Jr.	See Leibrecht, Bruce C.	II	233
Patterson, Stanley P. Conrad, Raymond W. Russell, Stephen D.	Scintillation Smoothing of Pulsed and CW, Visible Laser Beams	III	173
Penetar, David M. Beatrice, Edwin S.	Effects of Atropine and 2-PAM Cl on Human Pursuit Tracking Performance	III	183
Peters, C. J.	See Canonico, Peter G.	I	127
Pistritto, Joseph V.	See Hsu, Chen C.	II	67
Powanda, Michael C.	See Reifenrath, William G.	III	235
Powell, John D.	See Jamison, Keith A.	II	95

Author	Title	Vol	Page
Prakash, Anand	Rebatron: A Compact Accelerator for Producing High Energy, Ultra-High Current Electron Beams	III	193
Prask, Henry J. Choi, Chang S.	The Nondestructive Determination of Residual Stresses in Armament-System Components	III	207
Previte, Joseph J.	See Silverman, Gerald J.	V	205
Psotka, Joseph	See Gray, Wayne D.	I	341
Puri, Narindra N.	See Schwering, Feliz K.	IV	81
Rauch, Terry M.	See Munro, Ilse	III	85
Ray, Radharaman Boucher, Lisa J. Broomfield, Clarence A.	Specific Soman Hydrolyzing Enzyme in a Clonal Neuronal Cell Culture: Possible Application in Soman Detection, Decontamination, Prophylaxis and Therapy	III	221
Reed, Lauren V.	See Canonico, Peter G.	I	127
Reifenrath, William G. Waring, Paul P. Hawkins, George S. Powanda, Michael C.	Semi-Automated System for Testing the Efficacy of Nerve Agent Protection/Decontamination Formulations	III	235
Reifenrath, William G.	See Rutledge, Louis C.	III	343
Reitmeyer, Randolph	See Bosco, Charles D.	I	71
Resnick, I. Gary	See Harper, Bruce G.	II	17
Ressler, Eugene K.	See Guth, Peter L.	I	371
Richard, Gretchen C.	See Cornell, John H.	I	225
Richmond, Paul	Land Mine Use in Winter	V	133
Riggins, Robert E.	See Coe, Mark W.	I	217
Rigsbee, J. M.	See Stephenson, L. D.	IV	189
Rinker, Jack N.	See Satterwhite, Melvin B.	IV	41
Risvik, Einar	See Briggs, Jack	I	81
Roach, Lisa K.	See Schall, James E.	IV	57
Robbins, Frederick M.	See Walker, John E.	V	251

Author	Title	Vol	Page
Robertson, Donald H.	Rapid Monitoring of Materials Penetration by Toxins and Chemical Surrogates	V	149
Rodriguez, Gumersindo Touchet, Paul Gatza, Paul Teets, Alan Escarsega, Dawn Feuer, Henry	Development of Elastomeric Tank Pad Compounds with Improved Service Life	III	251
Rohde, Frederick W. Jr.	Radar Descriptors for the Classification of Terrain Features	III	267
Rose, Douglas N. Bryk, Darryl C.	Photoacoustic Microscopy - Thermal Wave Probing	III	283
Ross, Raymond L. Lux, Robert A. Dekanski, Deborah A. Iafrate, Gerald J. Moerkirk, Robert P.	Ballistic-Launched Advanced Millimetric Oscillators	III	299
Ross, Raymond L. Winter, John J. Lux, Robert A. Dixon, Samuel Dekanski, Deborah A. AuCoin, Thomas R.	The Zero-Bias Depletion Diode: A Promising New Subhármonic Mixer	III	311
Roy, Gerald G.	See Silverman, Gerald J.	V	205
Rumsey, Michael G.	Work Sample and Job Knowledge Measures: Interchangeable or Complementary?	III	327
Russell, Stephen D.	See Patterson, Stanley P.	III	173
Rutledge, Louis C. Reifenrath, William G. Gupta, Raj K.	Sustained-Release Formulations of the U.S. Army Insect Repellent	III	343
Sahu, Jubaraj	Computational Investigation of Base Flow in the Presence of a Centered Propulsive Jet	IV	1
Sandmeyer, Richard S.	Optimum Aiming of Artillery Indirect Fire	IV	17
Sandus, Oscar	See Sollott, Gilbert P.	IV	173
Sardelis, Michael R. Boobar, Lewis R.	Pesticide Dispersal Unit (PUD), Multicapability, Helicopter Slung	IV	33

Author	Title	Vol	Page
Sarver, Emory W.	See Krishnamurthy, Thaiya	II	169
Satterwhite, Melvin B. Rinker, Jack N.	Effect of Shadows on the Reflectance Spectra of Vegetation and their Digital Classification	IV	41
Savage, Robert O.	See Shappirio, Joel R.	IV	95
Savage, Russell E. Jr.	See Landis, Wayne G.	II	217
Sawyers, Michael	See Schnakenberg, David D.	IV	69
Schall, James E., Jr. Roach, Lisa K.	Chemical Munition Effects Analysis in Support of Targeting Manual Development	IV	57
Schick, Milton J.	See Yalamanchili, Rao	IV	361
Schnakenberg, David D. Carlson, Dawn Sawyers, Michael Vogel, James A. Johnson, Richard Szlyk, Patricia C. Francesconi, Ralph Hubbard, Roger W.	Nutritional Evaluation of a New Combat Field Feeding System for the Army	IV	69
Schmitz, John P.	See Hollinger, Jeffrey O.	II	39
Schneider, Imogene	See Hockmeyer, Wayne T.	II	27
Scholz, Wilfred	See Homan, C. G.	II	55
Schwering, Felix K. Puri, Narindra N. Butler, Chalmers M.	Modified Diakoptic Theory of Antennas	IV	81
Scoggins, Randy K. Curtis, John O.	Thermal Camouflage for Fixed Installations	V	157
Scott, Brad D.	See O'Neill, Timothy R.	III	139
:ott, P. A.	See Stephenson, L. D.	IV	189
Seagraves, Mary Ann	Target Acquisition Intelligence Techniques	V	173
Seiders, Barbara A.B. Holter, John J. Leonard, Joseph M. Luteran, Thomas	Technology for the Soldier: Visualizing Penetrants	V	189

Author	Title	Vol	Page
Seid, Robert C.	See Lowell, George H.	II	313
Shappirio, Joel R. Finnegan, John J. Lux, Robert A. Kwiatkowski, Joseph H. Fox, Donald C. Heath, Linda S. Wade, Melvin J. Savage, Robert O. AuCoin, Thomas R.	New Metallization Technologies for Advanced Military Microelectronics	IV	95
Shukitt, Barbara	See Munro, Ilse	III	85
Siering, George D.	See Simmons, Ronald	IV	127
Silber, Leo Tauber, Arthur Wilber, William	Hexagonal Ferrites for Millimeter-Wave Control Devices	IV	111
Silverman, Gerald J. Roy, Gerald G., Jr. Woodbury, Charles T. Lee, Claire H. Previte, Joseph J.	Environmental Stability and Detoxification of Staphylococcal Enterotoxin A and Botulinum Neurotoxin A	V	205
Simmons, Ronald R. Knox, Francis Siering, George Behar, Isaac Mitchell, Glenn	Effects of Chemical Defense Antidotes on Aviator Performance	IV	127
Sims, S. Richard F.	See Lovelace, Donald E.	II	301
Singler, Robert E.	See Willingham, Reginald A.	IV	349
Skudera, William J. Jr.	Real Time Transition Detection Method for BPSK Signals in the Presence of Narrow Band Interference	V	215
Slagg, Norman	See Sollott, Gilbert P.	IV	173
Smith, Edgar D.	See Bandy, John T.	I	63
Smith, Jonathan F.	See Dalrymple, Joel M.	I	249
Smith, Lynette F.	See Lowell, George H.	II	313
Smith, William J.	See Walker, John E.	V	251
Snellen, James E. Deponai, John M. III	The MALOS Combat Engineer Simulation Environment	IV	143

Author	Title	Vol	Page
Soicher, Haim	Variability of Transionospheric Signal Time Delay at High Latitudes	IV	159
Sollott, Gilbert P. Alster, Jack Gilbert, Everett E. Sandus, Oscar Slagg, Norman	Synthesis of More Powerful Explosives	IV	173
Stapler, John T.	See Cornell, John H.	I	225
Stephenson, L. D. Hock, V. F. Boy, J. H. Scott, P. A . Rigsbee, J. M.	Ion-Plated Conductive Ceramic and Metal/Ceramic Composite Coatings	IV	189
Sturek, Walter B.	See Weinacht, Paul	IV	275
Sullivan, Garrett J.	See Jourdan, Mark R.	V	57
Sutton, Steven	See Fedele, Paul D.	I	279
Swab, Jeffrey J.	See Bryant, George	I	111
Swartz, Merryanna L.	See Gray, Wayne D.	I	341
Szafraniec, Linda	See Krishnamurthy, Thaiya	II	169
Szlyk, Patricia C.	See Schnakenberg, David D.	IV	69
Tauber, Arthur	See Silber, Leo	IV	111
Taub, Irwin A.	See Briggs, Jack	I	81
Teets, Alan	See Rodriguez, Gumersindo	III	251
Tharion, William J.	See Munro, Ilse	III	85
Thomas, David J.	See Gerhart, Grant R.	I	295
Thompson, Edward F.	Sea State Prediction for Military and Civil Works Applications	IV	205
Thorne, Larry R.	See Melius, Carl F.	III	25
Touchet, Paul	See Rodriguez, Gumersindo	III	251
Tracy, Carl	See Mescall, John F.	III	41
Trevino, S. F. Tsai, D. H.	The Simulation of Condensed Matter Chemistry and Detonation	IV	219

Author	Title	Vol	Page
Tsai, D. H.	See Trevino, S. F.	IV	219
Turetsky, Abraham L.	Novel Infrared Chaff	V	229
Viechnicki, Dennis J.	Factors Controlling the Ballistic Behavior of Armor Ceramics	IV	233
Vogel, James A.	See Schnakenberg, David D.	IV	69
Wade, Melvin J.	See Shappirio, Joel R.	IV	95
Wade, Melvin J.	See Weiner, Maurice	IV	291
Walck, James C.	See Meyer, Fred P.	V	101
Walker, John E.	Use of Spin Labeled Organophosphonates in the Measurement, Binding and Detoxifying Properties of CBW Protecting Substances Attached to Fabrics	V	241
Walker, John E. Robbins, Frederick M. Smith, William J. Gallo, Benedict J.	Enzymes from Microbial Sources with Activities Against G-Agents	V	251
Walton, W. Scott	Dynamic Response of Armor Plate to Non-Penetrating Projectile Impact	IV	249
Ward, Janet E. Koza, Walter	Hi-Tech Fibers for Improved Ballistic Protection	IV	265
Waring, Paul P.	See Reifenrath, William G.	III	235
Weinacht, Paul Sturek, Walter B.	Simulation of the Supersonic Flow About Finned Projectiles	IV	275
Weiner, Maurice Bovino, Lawrence J. Burke, Terence Youmans, Robert J. Wade, Melvin J.	Optically Activated Switch Technology	IV	291
Weisman, Idelle M. Zeballos, R. Jorge Johnson, Bruce D.	Acute Strenuous Exercise at a Simulated Altitude of 2300M (7500 ft.) Compared to Sea Level in Individuals with Sickle Cell Trait (SCT): A Controlled Study in Basic Trainees	IV	303
Wells, Francine S.	Acoustic Birefringence Measurements in Rolled 5083 Aluminum Plate	IV	319

Author	Title	Vol	Page
White, James L. Leipertz, Donald F. Britan, Ronnie G.	The Army's Key Operational Capabilities Analysis of C3 Contribution	IV	335
Wilber, William	See Silber, Leo	IV	111
Willingham, Reginald A. Singler, Robert E. Manavalli, Shekhar	Liquid Crystalline Side Chain Polymers as Potential Detection Agents for Chemical Defense	IV	349
Winter, John J.	See Ross, Raymond L.	III	311
Wirtz, Robert A.	See Golenda, Claudia F.	I	327
Wirtz, Robert A.	See Hockmeyer, Wayne T.	II	27
Wirtz, Robert A.	See Owens, Roberta R.	III	163
Wolff, Ruth	See Olenick, John G.	III	127
Woodbury, Charles T.	See Silverman, Gerald J.	V	205
Yalamanchili, Rao Hoenig, Stuart A. Schick, Milton J.	Cooling of Weapons by Electrostatic Phenomena	IV	361
Yee, Young P.	See Measure, Edward M.	V	87
Youmans, Robert J.	See Weiner, Maurice	IV	291
Young, James F.	See Hockmeyer, Wayne T.	II	27
Zeballos, R. Jorge	See Weisman, Idelle M.	IV	303
Zollinger, Wendell D.	See Lowell, George H.	II	313

LEARNING COOPERATIVELY CAN BE MORE EFFECTIVE THAN LEARNING ALONE (U)

*JOSEPH D. HAGMAN, DR.
JOHN F. HAYES, MR.
U.S. ARMY RESEARCH INSTITUTE
ALEXANDRIA, VIRGINIA 22333-5600

The last 15 years have seen a growing interest in the potential use of cooperative learning methods for improving training effectiveness (13,16). Under cooperative learning, trainees spend some of their class time working in small groups where they are expected to help one another learn. This is in contrast to individualistic learning where trainees are supposed to learn on their own with help from an instructor rather than from one another.

Evidence indicates that working cooperatively is more effective than working individualistically on a wide variety of tasks (7,11,20). Group productivity, however, does not necessarily result in enhanced individual achievement. Sometimes individuals perform better after having learned in a group (17); other times they perform better after having learned on their own (3). For both theoretical and practical reasons, it is important to determine whether cooperative learning can be used to promote individual achievement and, if so, identify training conditions that produce consistent achievement gains.

EXPERIMENT 1

Slavin (16) suggests group members must be rewarded (e.g., recognized, praised) as a group for cooperative learning to be effective. For Slavin, group reward must be contingent upon demonstration of successful performance by each group member. This differs from independent reward where group members are rewarded individually on the basis of their own performance regardless of that of others.

Experiment 1 examined whether or not group reward is a prerequisite for obtaining individual achievement gains through cooperative learning. The general approach was to compare the test performance of individual trainees following cooperative learning under either an independent or group reward contingency.

The effect of group size on individual achievement was also examined under each reward contingency. According to Steiner's (18) complementary

task model, performance should vary directly with group size because each group member possesses knowledge not possessed by others. The probability of a correct response, therefore, should increase as this knowledge pool expands provided that group members are willing to share information with one another.

Generally speaking, overall group performance does improve as group size increases (1,9). The question of interest, however, is whether gains in individual achievement track these overall group gains. To date, the answer has been no (e.g., 12). Past studies, however, have not used a group reward contingency. Group reward should encourage effective within-group communication, and thereby promote individual achievement gains paralleling those found for overall group performance.

The present experiment examined whether effects of group size on individual achievement are influenced by the kind of reward provided. If group reward promotes within-group communication, then individual achievement should vary directly with group size. Conversely, individual achievement should not improve, and perhaps even decline, as group size increases under independent reward because there is no incentive for group members to communicate.

Method

Subjects. Two hundred and eighty male soldiers receiving advanced individual training for the 76C (Equipment Records and Parts Specialist) military occupational specialty participated in the Experiment.

Design. Trainees were assigned randomly to one of seven classes. Each class was then assigned randomly to one of six treatment conditions formed by the between-subjects, factorial combination of two kinds of reward (independent vs. group) and three group sizes (1, 2, and 4 members). Hereafter, group size is referred to by number, and reward is abbreviated "I" for independent and "G" for group.

To obtain at least 20 groups per condition, two classes were assigned to Conditions 4I and 4G, whereas for Conditions 1I and 1G a single class was divided in two with one half assigned to each condition. This division was possible because there is no difference between group and indepedent reward when group size equals one. Scores for two quads from Condition 4G and one pair from Condition 2I were discarded randomly to permit equal-n analysis of group data across conditions. Each class was taught by a different three-member team of instructors, with both instructor-to-team and team-to-class assignments made on a random basis.

The experiment was conducted during the Prescribed Load List (PLL) Annex of the 76C course. This annex consisted of 79 hours of instruction divided into 15 blocks covering tasks required for maintaining a PLL in support of unit operational requirements. Example tasks included: identification of repair parts, preparation of requests for issue and turn-in of parts, receipt and storage of parts, and taking parts inventory. Blocks 1-7 and 9-14 consisted of task-specific, lecture-based instruction followed

by a practical exercise (PE) after each block. Blocks 8 and 15 were dedicated to testing. Trainees had to score at least 85% correct on each test to progress through the course without interruption. Those not attaining criterion on their first attempt could take each test again, provided that they attended an intervening remedial study hall.

Procedure. Before starting the PLL Annex, separate classes were divided into groups containing either 1, 2, or 4 randomly assigned members. Cooperative learning occurred during the PE of each instructional block. Group members worked together to arrive at agreed-upon answers which they recorded in their own PE booklets. These booklets were then scored and knowledge of results provided on the speed and accuracy of responding. Trainees were tested individually at Blocks 8 and 15. Both tests required performance of tasks similar, but not identical, to those on the PEs. Before beginning the PLL Annex, trainees were told they would be working in groups of various sizes during the PEs, tested later individually, and rewarded either independently or as a group depending on their treatment condition. They were not allowed to remove training materials from the classroom, and were asked not to discuss course content after class.

Under independent reward, trainees received either a "GO" or "NOGO" based on their individual test scores and were rewarded (i.e., allowed to proceed to the next instructional block without attending a remedial study hall) independently of one another. Trainees not attaining criterion had to attend study hall before making a second attempt at the test. If successful, the trainee rejoined his fellow groupmates for the next instructional block. If unsuccessful, he was recycled to a later nonexperimental class.

Under group reward, groupmates received either a GO or NOGO based on whether or not all attained criterion. If all were successful, then all were rewarded. If one or more members failed to reach criterion, then all, including those that did reach criterion, returned to study hall where passing members helped the failing member(s) restudy for a second test attempt. For all conditions, only first-attempt test scores were analyzed.

After completing the PLL Annex, trainees who had worked cooperatively on the PEs indicated via questionnaire whether they preferred to work the PEs alone or in a group. All had worked individualistically on PEs during a prior 36-hour annex covering use of the Army Master Data File (AMDF) and, therefore, had experienced both individualistic and cooperative learning.

Results and Discussion

To determine whether performance differed among conditions at the start of the PLL Annex, a one-way analysis of variance (ANOVA) was performed on individual trainee error scores obtained at completion of the preceding AMDF annex. This ANOVA revealed no significant differences, $F < 1$, with the rejection region for this and all other analyses set at .05. Thus, subsequent performance differences to be reported among conditions were not the result of any differences present before the PLL Annex began.

Practical Exercises. To evaluate PE performance prior to each test, total error and time scores were calculated separately for PE Subsets 1-7 and 9-14. Then separate 2 (Reward) X 3 (Size) between-subjects analyses of variance (ANOVAs) were performed on error and time scores added across each subset for each group. Mean total error scores for each subset are shown in Figure 1 and mean completion time scores are shown in Figure 2.

Error analyses revealed significant main effects of group size for PEs 1-7, $F(2, 114) = 16.89$, and 9-14, $F(2, 114) = 34.09$. Individual comparisons done by the least significant difference method, revealed that errors were inversely related to group size for both subsets.

Analysis of time scores for PEs 1-7 revealed significant size, $F(2, 114) = 32.09$, and reward effects, $F(1, 114) = 5.68$, and a Size X Reward interaction, $F(2, 114) = 3.09$. Simple effect comparisons revealed that times increased with each increment in group size under group reward, but flattened out once group size reached two members under independent reward. In addition, pairs and quads took more time under group reward than their counterparts under independent reward. Analysis of time scores for PEs 9-14 revealed significant size, $F(2, 114) = 30.55$, and reward effects, $F(1, 114) = 5.89$, but no Size X Reward interaction. Thus, larger groups took longer to coordinate their answers under both reward conditions.

In summary, the PE data indicate that (a) groups were more accurate than individuals, (b) errors were inversely related to group size, but unrelated to reward, and (c) PEs took longer to complete under group reward than under independent reward.

Tests. Test performance was analyzed to determine individual trainee achievement. Mean error and time scores were computed for each pair and quad. These within-group means were then compared with the raw scores from trainees in the single-member groups. This procedure yielded 20 scores for each of the six conditions. The means of the 20 error scores for Tests 1 and 2 are depicted in Figure 3, and the time score means for the two tests are depicted in Figure 4.

To determine whether overall group performance on the PEs affected later test scores of individual group members, each dependent variable was analyzed separately using 2 (Reward) X 3 (Size) factorial ANOVAs identical to those performed earlier. Analysis of Test 1 errors revealed a significant reward effect, $F(1, 114) = 7.57$, and a Reward X Sixe interaction, $F(2, 114) = 4.31$. Analysis of simple effects from the interaction revealed that errors decreased as group size increased under group reward, but were unrelated to group size under independent reward. Differences, however, were not reliable until group size reached four members. Analysis of time scores revealed no significant effects.

Analysis of Test 2 scores revealed a significant reward effect, $F(1, 114) = 9.53$, and a Reward X Size interaction, $F(2, 114) = 4.82$. Analysis of simple effects revealed that errors decreased under group reward, but increased under independent reward as group size increased. The mean numbers of errors committed under group reward by the pair and single-member groups did not differ, but were greater than those committed by the quad

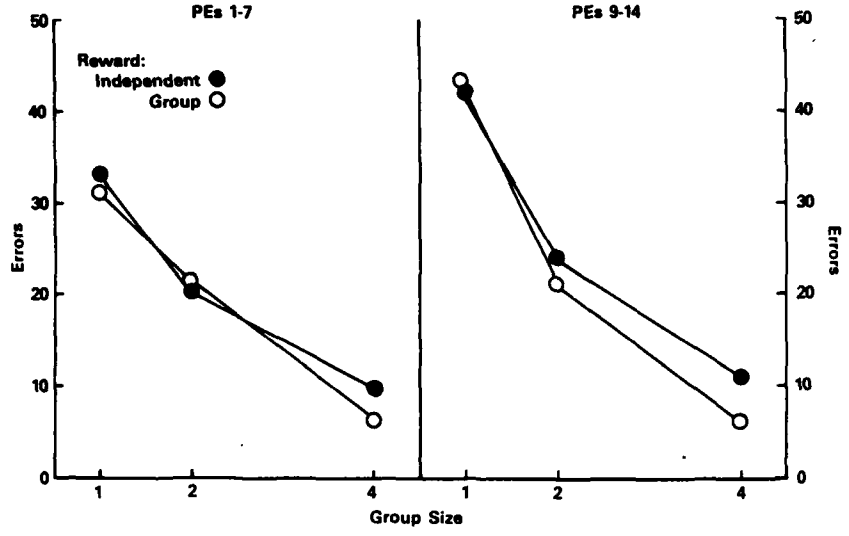

Figure 1. Mean number of total errors committed on PE subsets.

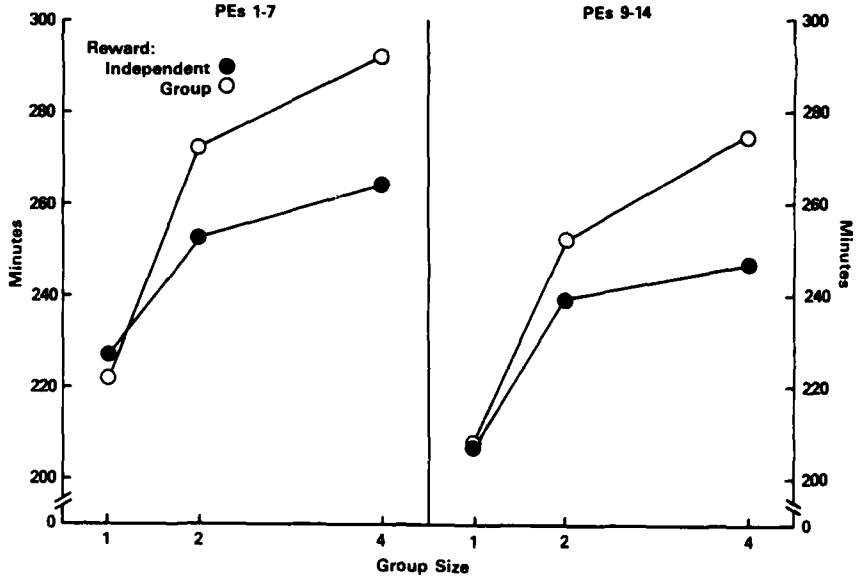

Figure 2. Mean total completion times for each PE subset.

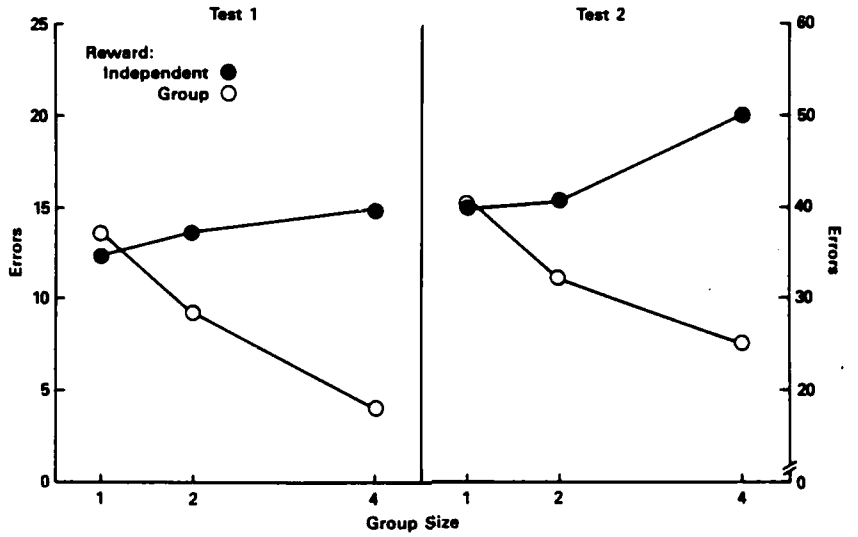

Figure 3. Mean number of errors committed on each test.

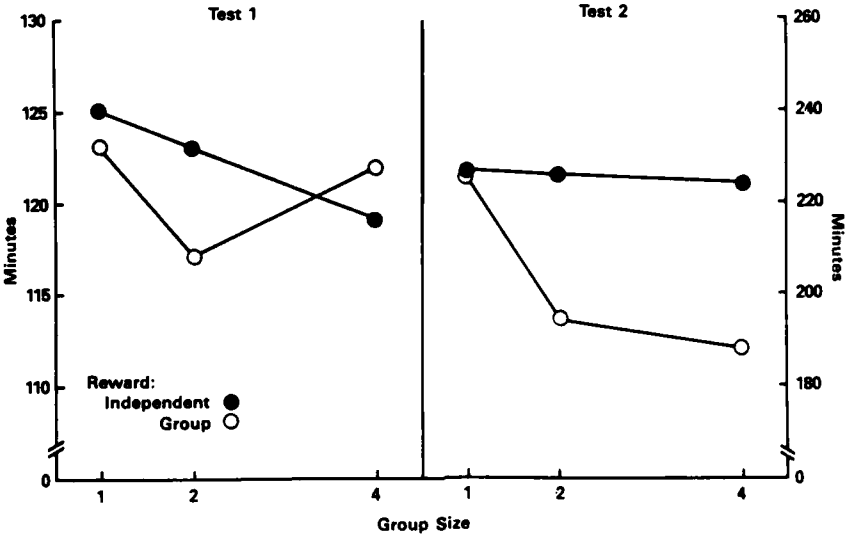

Figure 4. Mean test completion times.

groups. The pair and single-member groups under independent reward displayed comparable accuracy, but committed fewer errors than the quad groups. Once again, only when group size reached four members were reliable performance differences found between the two kinds of reward.

Analysis of Test 2 times revealed significant reward, $F(1, 114) = 33.71$, and size effects, $F(2, 114) = 10.10$, and a Reward X Size interaction, $F(2, 114) = 7.96$. Analyses of simple effects revealed that test completion times decreased as group size increased under group reward, but remained stable under independent reward. Most of the time decrease found under group reward occurred as groups increased from one to two members, with no further decrease occurring as groups increased from two to four members. Time differences were also found between reward conditions for both pairs and quads.

Questionnaire Responses. Questionnaire data obtained from individual trainees revealed that 72% of those who had worked in pairs and 70% of those who had worked in quads preferred to work cooperatively. No difference in preference was found on the basis of group size, $\chi^2(1, n = 240) < 1$. There was, however, a significant relationship between preference and reward. Ninety-one percent of the trainees who had worked under group reward preferred to work cooperatively compared to only 51% of those who had worked under independent reward, $\chi^2(1, n = 240) = 46.47$.

In summary, analyses of the test and questionnaire data revealed that (a) cooperative learning only promoted individual achievement when coupled with group reward, (b) achievement varied directly with group size under group reward, but inversely with group size under independent reward, (c) differential effects of reward were most evident with quads, although pairs did show some time advantage at Test 2, and (d) trainees preferred to work cooperatively on the PEs regardless of group size, provided that a group reward contingency was enforced.

These results reveal the importance of group reward for obtaining individual achievement gains under cooperative learning. It is unclear, however, why group reward was so effective. On the one hand, it may have encouraged effective communication among group members, as suggested earlier. Results of past research (14) showing that trainees in cooperative groups help each other substantially more when they are rewarded as a group than when they were not, support this argument. On the other hand, group reward may have simply motivated group members to learn more on their own because the rest of the group was depending on them to do so. Hulten & DeVries (10) have found that greater peer pressure exists for members to do well under group reward than under independent reward. Thus, enhanced individual motivation to learn rather than effective within-group communication could have been responsible for individual achievement gains found under group reward. If true, then group reward should promote comparable individual achievement under both a cooperative task, where group members help one another, and an individualistic task, where group members work alone and are not allowed to intercommunicate. If within-group communication is necessary for group reward to be effective, then greater individual

performance gains should be found with a cooperative task than with an individualistic task because the latter precludes within-group communication.

EXPERIMENT 2

Experiment 2 was designed to differentiate between the motivation and communication hypotheses offered above as possible explanations for the beneficial effects of group reward on individual achievement under cooperative learning. Task structure was varied to include both cooperative and individualistic learning tasks under both group and independent reward contingencies. Under the individualistic task, trainees learned on their own without input from fellow groupmates; under the cooperative task, within-group communication was allowed. If increased motivation is the key to enhanced individual achievement, then no performance differences should be found on the basis of task differences because motivation to learn should be the same under both individualistic and cooperative procedures. If within-group communication is the key, then individual achievement should be greater when trainees work cooperatively because only a cooperative task allows groupmates to communicate.

The present experiment also varied reward to include independent along with group contingencies under both individualistic and cooperative task conditions. Manipulation of both reward and task within the same experiment provided an opportunity to examine further their relative importance in promoting individual achievement.

Method

Design, subjects, and procedure. Four treatment conditions were formed by the factorial combination of two kinds of reward, i.e., independent (I) vs group (G), and two kinds of task, i.e., individualistic (I) vs cooperative (C). These four conditions are designated CG, IG, CI, and II, with the first letter referring to task and the second letter to reward. Groups contained four members in all conditions except II where formal grouping was unnecessary. Data from Conditions 4G, 4I, and 1I of Experiment 1 were used for Conditions CG, CI, and II of Experiment 2, because these three conditions were slated to be treated the same in Experiment 2 as they were in Experiment 1. Eighty male trainees from two additional 76C classes were divided into quads to provide the data necessary for Condition IG. Group members in this condition worked alone on the PEs, but were rewarded as a group for their individual test performance. Because trainees in Condition IG worked individualistically on the PEs, their performance scores were averaged within groups and compared with PE scores achieved through mutual agreement in the cooperative learning conditions. Test scores for all groups were analyzed the same as in Experiment 1. Instructor-to-team and team-to-class assignments were made on a random basis except for Conditions CG and IG which were taught by the same team of instructors.

Results

Practical Exercises. A one-way ANOVA performed on individual trainee error scores obtained at completion of the preceding AMDF Annex revealed no differences among conditions prior to the start of the PLL Annex, $F < 1$. To determine PE performance prior to each test, total error and time scores were calculated separately for PE Subsets 1-7 and 9-14. Separate 2 (Task) X 2 (Reward) between-subjects ANOVAs then were performed on within-group error and time scores added separately for each condition across each subset. Figure 5 shows these mean error scores and Figure 6 shows the mean time scores.

Analysis of errors revealed a significant task effect for PEs 1-7, $F(1, 76) = 35.13$, and 9-14, $F(1, 76) = 37.78$, with fewer errors committed when trainees worked cooperatively. A significant reward effect was also found for PEs 9-14, $F(1, 76) = 7.42$, revealing that accuracy was greater under group reward than under independent reward. Thus, enforcement of a group reward contingency improved the accuracy of PE performance for both kinds of tasks, at least for PEs 9-14, but working cooperatively produced superior response accuracy regardless of the reward contingency enforced.

Analysis of completion times revealed significant task, $F(1, 76) = 40.53$, and reward effects, $F(1, 76) = 9.38$, for PEs 1-7 along with similar task, $F(1, 76) = 35.6$, and reward, $F(1, 76) = 11.93$, effects for PEs 9-14. For both subsets, completion times were faster when trainees worked alone and when reward was given on an independent basis.

Tests. Test scores were examined to reveal individual trainee achievement under the four treatment conditions. Mean error and time scores for Conditions CG, IG, and CI were derived by computing the mean within-group scores for each quad. These within-group mean scores were then included with the raw scores for trainees in Condition II to yield 20 scores for each condition. Error score means for Tests 1 and 2 are shown in Figure 7 and time score means for the two tests are shown in Figure 8.

Both dependent measures were analyzed via separate 2 (Reward) X 2 (Task) between-subjects ANOVAs identical to those used earlier. Analysis of Test 1 errors revealed a significant reward effect, $F(1, 76) = 16.65$, and a significant Reward X Task interaction, $F(1, 76) = 3.95$. Analysis of simple effects from the interaction revealed that trainees in Condition CG performed best, followed by those in Conditions IG and II, which did not differ from one another, with trainees in Condition CI performing the worst of all. Thus, group reward effectiveness was dependent upon task, in that group reward was most beneficial when trainees learned cooperatively.

Analysis of Test 2 errors also revealed a significant Reward X Task interaction, $F(1, 76) = 5.45$, and an ordering of simple effects almost identical to that found on Test 1. The performance differences favoring Condition CG over IG on both tests suggest that a cooperative task is necessary for promoting individual achievement under group reward, and thus provide support for the communication hypothesis. The lack of a difference between Conditions II and IG indicates that differential

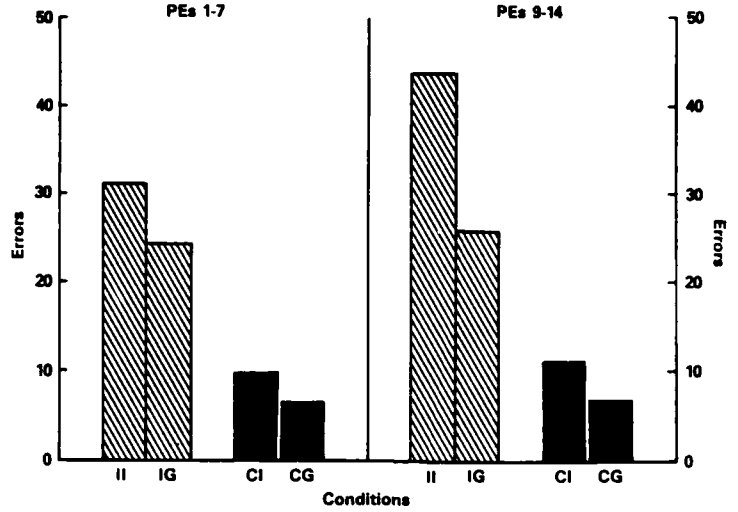

Figure 5. Mean number of total errors committed on PE subsets under each condition (II=individualistic task/independent reward; IG=individualistic task/group reward; CI=cooperative task/independent reward; CG=cooperative task/group reward).

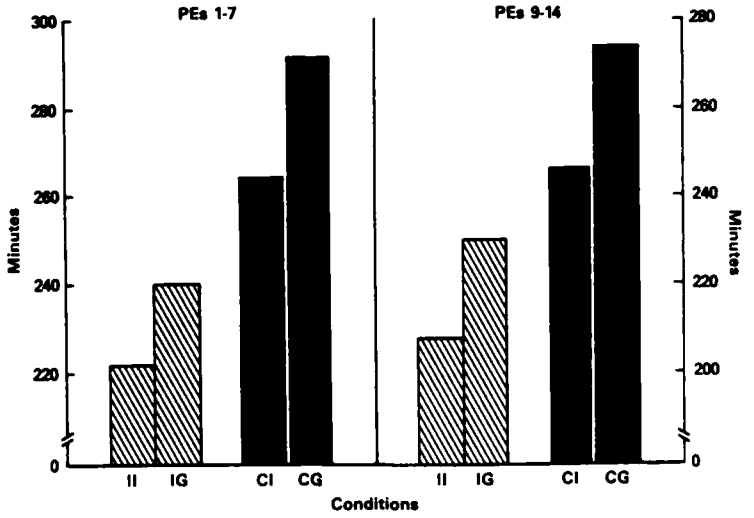

Figure 6. Mean total completion times for PE subsets under each condition (II=individualistic task/independent reward; IG=individualistic task/group reward; CI=cooperative task/independent reward; CG=cooperative task/group reward).

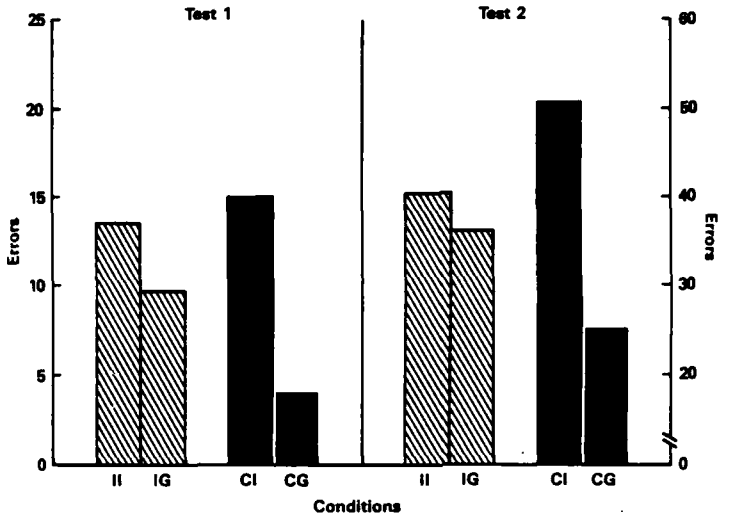

Figure 7. Mean number of errors committed on each test under the four conditions (II=individualistic task/independent reward; IG=individualistic task/group reward; CI=cooperative task/independent reward; CG=cooperative task/group reward).

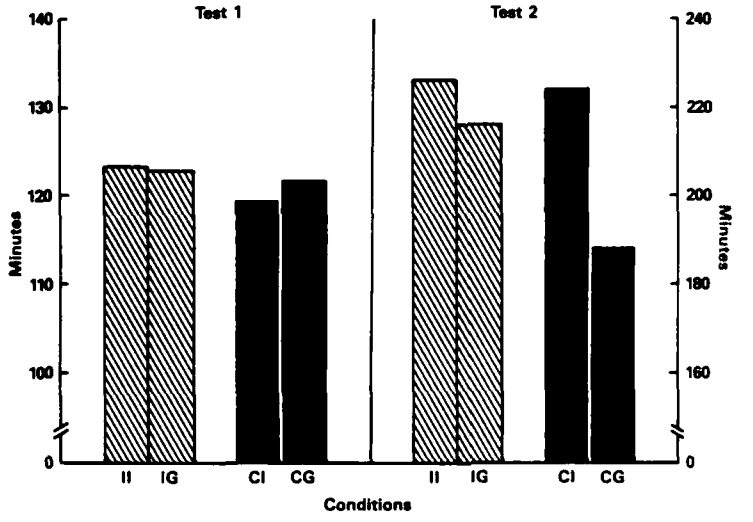

Figure 8. Mean test completion times under each condition (II=individualistic task/independent reward; IG=individualistic task/group reward; CI=cooperative task/independent reward; CG=cooperative task/group reward).

achievement should not be expected under either kind of reward when trainees learn on their own.

Analysis of time scores revealed no significant effects for Test 1, but significant effects of reward, $F(1, 76) = 24.60$, and task, $F(1, 76) = 10.01$, in addition to a Reward X Task interaction, $F(1, 76) = 7.2$, for Test 2. Analysis of simple effects provided additional support for the communication hypothesis in that faster completion times were found for Condition CG than for the other three conditions which did not differ from one another. Thus, trainees in Condition CG not only responded more accurately but also faster during testing than trainees in the other three conditions.

GENERAL DISCUSSION

This research sought to determine whether cooperative learning promotes individual achievement, and if so, identify conditions under which a consistent benefit can be expected. The test results of Experiment 1 indicate that cooperative learning is no better, and sometimes worse, than individualistic learning unless a group reward contingency is enforced for individual performance. This supports Slavin's (16) claim that group reward is necessary for cooperative learning to be effective. Test results also indicate that individual achievement varies directly with group size under group reward, with maximum benefits occurring with groups containing four members. Under independent reward, increases in group size have either no effect or a detrimental effect on individual trainee test scores.

Performance on the PEs suggests that an inverse relationship exists between errors and group size irrespective of reward. This was expected for two reasons. First, groups generally outperform individuals when a group project is considered. And second, answer sharing was ensured to some extent by requiring pairs and quads to provide agreed-upon answers on the PEs regardless of the reward contingency applied later for individual test performance.

Completion time scores varied directly with group size and to a greater extent under group reward than under independent reward. Presumably, the extra time taken by cooperative groups was necessary to coordinate answers and larger groups took longer to effect this coordination. This would account for the extra time required by pairs and quads under independent reward.

Why, however, was even more time taken under group reward? Presumably, this extra time was used for explaining or elaborating upon selected answers. This added time for explanation could account for the superior individual achievement found under group reward. Cognitive processes, such as elaboration and retrieval, are necessary for deeper understanding and effective storage of information into memory. These processes occur through dialogue and interaction with others (2). Although it is tempting to interpret the superior achievement found under group reward as merely the result of added time taken on the PEs, this interpretation does not

hold for the finding that independently rewarded pairs and quads also took more time than single-member groups, and yet failed to display any additional improvements in individual test performance.

The results of Experiment 2 indicate that group reward benefits are the result of within-group communication that occurs during cooperative learning, rather than the result of increased motivation to learn on the part of individual group members. Although it was not possible to record the nature of group interactions within the operational military classroom, they probably took the form of peer tutoring. Devin-Sheehan (6) has reported that tutoring improves the academic performance of tutees, and in some instances, of tutors as well. Buckholdt and Wodarski (4) have argued that receiving trainee-generated explanations is particularly effective for learning, because trainees tend to use language that other trainees understand and tend to correctly interpret each other's nonverbal cues about whether or not a concept is understood. Sharan (13) has shown that cooperative learning methods that allow peer tutoring are especially effective in promoting performance of low-level cognitive tasks. The kind of supply-related tasks taught to entry-level soldiers in the present research would fall into this category. And lastly, Webb (19) has found that the giving and receiving of answers (with explanations) are the best predictors of individual achievement in cooperative learning tasks, whereas receiving no answer or merely a terminal answer with no explanation is negatively associated with achievement gains.

Although the present experiments used group reward to encourage within-group communication, any cooperative procedure that ensures effective communication among group members should promote individual achievement. Thus, group reward may not be necessary when this communication is brought about by other means. Dansereau (5), for example, has shown that structuring interaction within cooperative groups by giving members specific assignments to orally summarize and elaborate upon to-be-learned materials can effectively promote individual achievement in the absence of group reward. The present research suggests that if group interaction is left unstructured, then group reward can be used to encourage the interaction among group members necessary for promoting individual achievement gains when trainees work cooperatively.

In conclusion, what should be especially encouraging to the Army instructor or trainer about the results of this research is that individual achievement gains can be obtained through unstructured cooperative learning without modifying training materials, compromising the goals of criterion-referenced evaluation, or increasing training resources. Of course, one important factor affecting the successful implementation of changes in any instructional or operational training program is trainee acceptance. In this regard, preference responses obtained in Experiment 1 suggest that cooperative learning will be well received provided it is coupled with group reward.

REFERENCES

1. Anderson, N.H. (1961). Group performance in an anagram task. Journal of Social Psychology, 55, 67-75.
2. Baker, L. (1979). Comprehension monitoring: Identifying and coping with text confusions (Tech. Rep. No. 145). Urbana, IL: University of Illinois, Center for the Study of Reading.
3. Beane, W.E., & Lemke, E.A. (1971). Group variables influencing the transfer of conceptual behavior. Journal of Educational Psychology, 62, 215-218.
4. Buckholdt, D.R., & Wodarski, J.S. (1978). The effects of different reinforcement systems on cooperative behaviors exhibited by children in classroom contexts. Journal of Research and Development in Education, 12, 50-68.
5. Dansereau, D.F. (1083). Cooperative learning: Impact on acquisition of knowledge and skills (Tech. Rep. No. 586). Alexandria, VA: U.S. Army Research Institute for the Behavioral and Social Sciences.
6. Devin-Sheehan, L., Feldman, R.S., & Allen, V.L. (1976). Research on children tutoring children: A critical review. Review of Educational research, 46, 355-385.
7. Dossett, D.L., & Hulvershorn, P. (1983). Increasing technical training via computer assisted instruction. Journal of Applied Psychology, 68, 552-558.
8. Fox, D.J., & Lorge, I. (1962). The relative quality of decisions by individuals and by groups as the available time for problem solving is increased. Journal of Social Psychology, 57, 227-242.
9. Hill, G. (1982). Group versus individual performance: Are N = 1 heads better than one? Psychological Bulletin, 91, 517-539.
10. Hulten, B.H., & DeVries, D.I. (1976). Team competition and group practice: Effects on student achievement and attitudes. (Rep. No. 212). Johns Hopkins University, Baltimore, MD: Center of Social Organization of Schools.
11. Humphreys, B., Johnson, R.T., & Johnson, D.W. (1982). Effects of cooperative, competitive, and individualistic learning on students' achievement in science class. Journal of Research in Science Teaching, 19, 351-356.
12. Laughlin, P.R., & Sweeney, J.D. (1977). Individual to group problem solving. Journal of Experimental Psychology: Human Learning and Memory, 3, 246-254.
13. Sharan, S. (1980). Cooperative learning in small groups: Recent methods and effects on achievement, attitudes, and ethnic relations. Review of Educational Research, 50, 241-271.
14. Slavin, R.E. (1980a). Effects of student teams and peer tutoring on academic achievement and time on-task. Journal of Experimental Education, 48, 252-257.
15. Slavin, R.E. (1980b). Cooperative learning in teams: State of the

art. Educational Psychologist, 15, 93-111.
16. Slavin, R.E. (1983). When does cooperative learning increase student achievement? Psychological Bulletin, 94, 429-445.
17. Slavin, R.E., & Karweit, N. (1981). Cognitive and affective outcomes of an intensive student team learning experience. Journal of Experimental Education, 50, 29-35.
18. Steiner, I.D. (1966). Models for inferring relationships between group size and potential group productivity. Behavioral Science, 11, 273-283.
19. Webb, N.W. (1984). Stability of small group interaction and achievement over time. Journal of Educational Psychology, 76, 211-224.
20. Yager, S., Johnson, D.W., & Johnson, R.T. (1985). Oral Discussion, group-to-individual transfer, and achievement in cooperative learning groups. Journal of Educational Psychology, 77, 60-66.

SCALE-UP PRODUCTION AND PURIFICATION OF DIISOPROPYLFLUOROPHOSPHATASE FROM TETRAHYMENA THERMOPHILA

Bruce G. Harper, PhD, Ms. Leonora P. Midgley, I. Gary Resnick, PhD, and Wayne G. Landis, PhD, U.S. Army Dugway Proving Ground, Dugway, Utah, 84022-5000 and Chemical Research and Development Center, Aberdeen, Maryland 21010-5423

INTRODUCTION

Enzymatic hydrolysis of diisopropylfluorophosphate (DFP) was first reported by Mazur in 1946 (15). DFP is regarded as the prototype of a class of organophosphorus compounds which inhibit acetylcholinesterase (AChe) (6). The term DFPase is used to identify a class of enzymes which hydrolyze DFP and other organophosphorus compounds, such as soman (GD, 1,2,2-trimethylpropyl methylphosphonofluoridate), tabun (GA, ethyl N,N-dimethylphosphoramidocyanidate), and sarin (GB, isopropyl methylphosphonofluoridate) (3, 6, 8).

Thru the years, two general types of DFPases have been identified. The first, termed "Mazur-type DFPase", represents enzymes isolated from mammalian tissues (hog kidney, rat liver) and microorganisms (Escherichia coli, Tetrahymena thermophila)(11, 15, 16). This type of DFPase has the following characteristics: 1) molecular weight between 45,000 and 65,000 daltons, 2) several fold stimulation of enzyme activity in the presence of 10^{-3} M Mn^{++} ion, 3) hydrolyzes soman faster than DFP, and 4) loses activity with precipitation in ammonium sulfate (3, 6, 7, 8, 9). The second class DFPase, "squid-type DFPase", is isolated from the head ganglia and nerve fibers of squid (1, 3, 4). Its characteristics are: 1) molecular weight about 26,000 daltons, 2) slight inhibition in the presence of Mn^{++}, 3) hydrolyzes DFP faster than soman, and 4) maintains enzyme activity with ammonium sulfate fractionation (1, 3, 8, 11).

The naturally-occurring substrate for DFPase in the environment has eluded identification (3, 7). Nevertheless, DFP-hydrolyzing enzymes have several potential uses. Among them are: 1) detection of organofluorophosphate chemicals, 2) non-corrosive decontamination of nerve agent materials, specifically skin, wound or potable water contamination where more harsh decontamination procedures are inappropriate, and 3) controlled detoxification of environmental pollutants (insecticides). The enzyme has

been covalently attached to agarose beads, while still maintaining DFPase activity. Enzymatic hydrolysis of DFP on an agarose DFPase (squid-type) column was directly proportional to the loss of AChe-inhibiting ability (5). Further studies of tetrahymena DFPase with a surfactant indicates substantial activity and stability of the enzyme (12). These properties are ideal for construction and production of an enzyme "reactor" for the purpose of neutralizing and destroying organophosphorus compounds.

This work demonstrates that Tetrahymena thermophila can be produced to high densities in 200 L fermentation batches, with the successful collection and purification of a Mazur-type DFPase.

MATERIALS AND METHODS

Culture/Growth Conditions:

Tetrahymena thermophila was maintained in medium containing 0.5% Proteose Peptone, 0.5% Tryptone, and 0.2% yeast extract (Difco, 30°C) (11). Antibiotics (50 µg/ml streptomycin sulfate, 50 units/ml penicillin G) were added during fermentation runs to inhibit bacterial contamination.

Fermentation Scale-up: A 5% vol/vol inoculum ($3X10^5$ cells/ml) was used to seed a 15 L or 250 L fermentor (containing 10 L and 200 L of medium respectively. Agitation was kept at less than 100 rpm to prevent breakage of the fragile protozoa. A silicone based antifoam (GE 60) was used to control foaming. Tetrahymena was collected during the late log phase with the use of a flow-through centrifuge (IEC #450, 1150 RCF) with a flow rate of 1 L per min.

Dry weight and viable cell count were both used to measure tetrahymena growth. Three 100-ml samples of culture were collected, centrifuged, washed in saline, and then dried (50°C) to obtain the dry cell weight. A viable cell count was made with a humidified counting chamber. The total number of tetrahymena in a 10-µl dilution of cell culture could be counted.

Enzyme Assay: DFPase activity was determined by measuring the increase in fluoride ion concentration using an Orion 901 ion analyzer and a fluoride-sensitive electrode. The enzyme assay buffer consisted of 400 mM KCl, 50mM NaCl, and 5 mM bis-tris-propane (pH 7.2 with 3×10^{-3} M DFP [Sigma]). A 100-µl sample of enzyme was added to 5 ml of assay buffer at 37°C and the reaction rate was followed for 5-15 mins (5, 6, 11).

Enzyme Purification: Tetrahymena cells were concentrated from the fermentation fluid with the flow-through centrifuge, and then centrifuged

to a pellet (5,000 RCF, 15 min). The pellet was stored (-20°C) until needed. After one freeze-thaw cycle, the cells were sonicated (Branson sonifier #350, micro-tip probe, step 5, 50% duty, 3 min) and centrifuged (10,000 RCF, 20 min). The cell paste was washed twice to insure maximum recovery of the enzyme. The cellular extract fluids were combined, and the enzyme was salted-out with an ammonium sulfate precipitation procedure (4°C). The DFPase was collected in the 50%-75% saturated ammonium sulfate fraction (4), and the precipitated proteins were stored (4°C) until further purification.

The ammonium sulfate-precipitated proteins were desalted and further purified by gel filtration liquid chromatography. An equal volume of water was added to the salted proteins to resolubilize the enzyme. The sample was filtered (Millipore pre-filter, AP25 025 00) to remove insoluble proteins. A 3-ml sample was applied to a Sephadex G-100 column (2.5 X 30 cm) and eluted with 0.025 M Tris-HCl (pH 7.5, linear flow rate of 17.7 $cm.hr^{-1}$). Protein concentrations were measured with the Lowry technique (14) using bovine serum albumin as a standard. Enzyme activity was determined as above. The chromatographed protein fractions with high enzyme activity were pooled and lyophilized.

RESULTS:

Tetrahymena thermophila was easily adapted to grow (from 500 ml Fernbach flasks) into 200-L fermentation batches. A few minor adjustments in fermentation conditions had to be made when going to larger volumes. As can be seen from Fig. 1, Tetrahymena thermophila is highly aerophilic. Oxygen was found to be a limiting growth factor and is rapidly depleted in a 200-L fermentation batch without constant sparging. A 20% oxygen saturation was adequate to achieve high growth rates (generation time less than 3 hr). Three liters of tetrahymena culture can easily be collected in one centrifuge run (Beckman JA-10 rotor, 6-500 ml buckets, 20 min). This method would not be feasible with 200 L of culture fluid, which would require the constant use of three centrifuges for more than 22 hr. A Sharples high-speed, high-volume fermentation centrifuge (12,000 RCF) could not be used since it was too harsh for the protozoa and would crush them, releasing the intracellular DFPase. The first attempt to overcome this collection problem was to use a hollow fiber tangential flow concentration system (Amicon, Model DC10a). In theory, with a 0.1-μm cartridge (H5MP01-43), one should be able to concentrate even fragile cells; however, tetrahymena was easily fractured and the DFPase was diluted into the culture fluids. An attempt to break the cells and remove the cell debris with the 0.1-μm cartridge, and then concentrate the enzyme in the culture fluids with a 30K dalton molecular weight cut-off cartridge (H5P30-43) also proved fruitless. The silicone antifoam used in the fermentor to control foaming contributed to slow processing times, rendering the procedure time

Figure 1. Photomicrograph of Tetrahymena thermophila

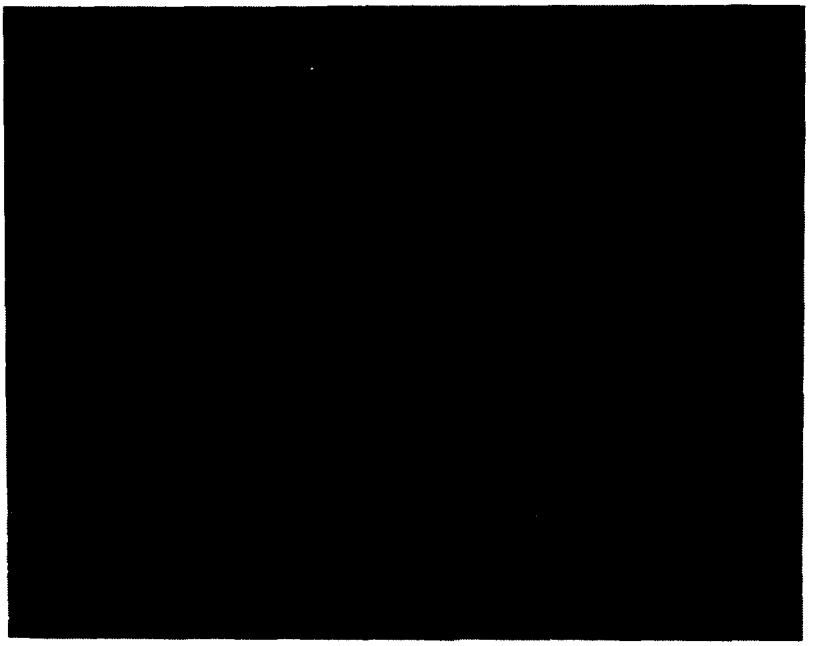

Photomicrograph of Tetrahymena showing the aerophilic nature of the organism clustering near an air/liquid interface (bubble).

inadequate. The collection problem was corrected with a variable speed, flow-through centrifuge, which can concentrate 30 L of culture to a volume of 400 ml within 30 min.

Under optimum conditions a total cell count of 5×10^5 cells/ml was harvested in late log phase growth 26 hours post inoculation (Fig 2). This has a corresponding dry cell weight of 1.5 g/L. Generation time for Tetrahymena thermophila in the fermentor was determined to be 2.8 hr (specific growth rate of 0.25/hr). Following sonication and ammonium sulfate treatment, the precipitated proteins (50%-75% fraction) were desalted and purified further with size exclusion chromatography.

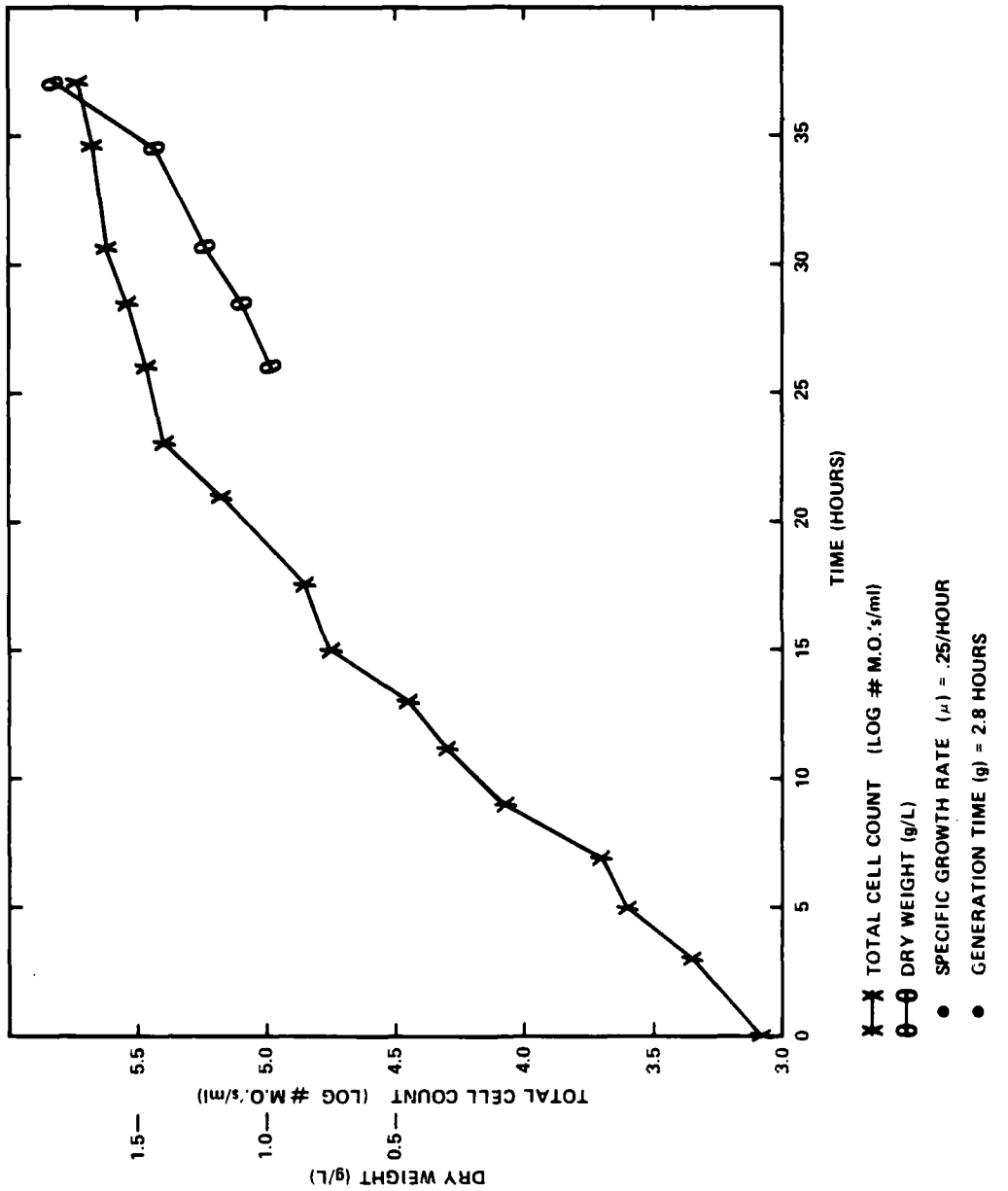

Figure 2. Tetrahymena Growth Curve

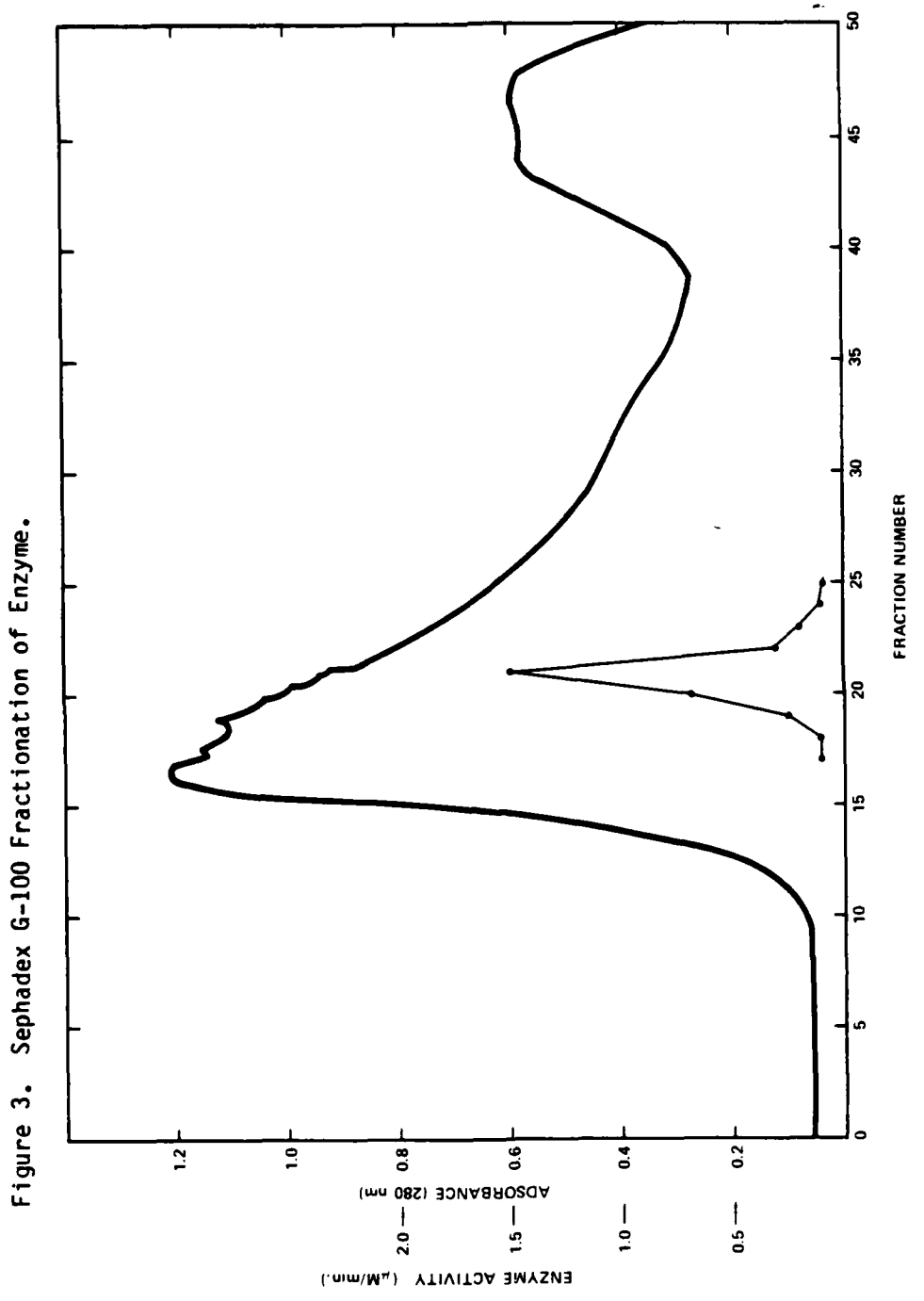

Figure 3. Sephadex G-100 Fractionation of Enzyme.

TABLE 1 Purification of DFPases from Tetrahymena thermophila

FRACTION	VOLUME ml	PROTEIN mg/ml	ACTIVITY μM/ml/min	TOTAL ACTIVITY μM/min	SPECIFIC ACTIVITY μM/mg/min	YIELD %	PURIFICATION
1) Supernatant fluid from 2 liters of cells, after 10K spin	26.0	34.5	0.32	8.33	0.0009	-	-
2) 50-75% saturated ammonium sulfate fraction, resuspended in buffer	3.1	33.8	1.36	4.22	0.0403	50.6	4.3
3) G-100 fractions							
19	4.5	1.8	0.09	0.41	0.050	4.9	5.3
20	4.5	1.5	0.17	0.77	0.115	9.2	12.4
21	4.5	1.3	0.47	2.12	0.365	25.5	39.2
22	4.5	1.2	0.08	0.36	0.067	4.3	7.2
4) Lyophilized Material[a]	NA	22.0	1.47	NA	0.400	NA	44.4

[a]Pooled fractions from 15-20 G-100 column runs, lyophilized and reconstituted with water (10X concentration).

Fig. 3 is a profile of the proteins eluted from a Sephadex G-100 column, indicating the fractions which have DFPase activity. A maximum 39-fold increase in specific activity was achieved, with a total enzyme yield of 25%. The fractions collected with high enzyme activity were stored (-20°C), pooled, and lyophilized in batches (800 ml volumes). Approximately 2 g of DFPase (specific activity of 4,000 μM/g/hr) were collected from a 200-L batch fermentation.

DISCUSSION

Availability of large quantities of DFPase would provide opportunities for determining the feasibility and possible use of the enzyme for: 1) detection of organofluorophosphate chemicals, 2) non-corrosive decontamination of nerve agent materials, and 3) detoxication and control of environmental pollutants. In an effort to demonstrate the availability of DFPase in quantity, Tetrahymena thermophila was grown in 200-L fermentation batches and treated to extract and purify the enzyme for use in additional studies. It is important to realize that a balance must be maintained between purification of the enzyme and percent yield of product. Purification steps which recover a maximum amount of the enzyme and have a lower specific activity must be weighed against purification techniques which result in a high specific activity but a lower recovery of total enzyme. In a large scale process, enzyme recovery must be maximized to be economically feasible. Hoskin and Long were able to show a 1300-fold purification of squid-type DFPase using ammonium sulfate and ion-exchange chromatography (DEAE cellulose), but lost 95% of the enzyme in the process. With a Mazur-type enzyme we were able to show a 40-fold increase in specific activity using ammonium sulfate, G-100 chromatography and lyophilization, and recover 45% of the enzyme. The specific activity achieved (4,000 μM/g/hr) is more than sufficient to perform other tests, such as enzyme stability on solid substrates and decontamination/neutralization of organofluorophosphate chemicals.

Landis et al (10) achieved a 16-fold purification of tetrahymena DFPase with gel filtration (S-200) and a 1,000-fold purification using DEAE Sepharose. Gel electrophoresis of the best purified extract shows at least six bands. Further analysis of the protein fractions (with and without Mn^{++}, ratio of enzyme activity with DFP and soman as substrates) hints at the possibility of five proteins in tetrahymena with DFPase activity (13).

Our preliminary work with DFPase and ion-exchange chromatography yielded negative results; we could not recover enzyme activity from the separated proteins. Perhaps this was due to the ammonium sulfate precipitation procedure and concurrent loss of an enzyme cofactor which was removed with ion exchange chromatography. Additional research and effort

is needed to increase the yield of enzyme activity. Research has also been initiated to produce monoclonal antibodies with specific affinity for DFPase (or DFPases). This would permit a rapid one-step purification of the enzyme using affinity chromatography, and would allow purification of the individual DFPases for enzyme kinetics and properties.

ACKNOWLEDGEMENTS: This work was supported by TECOM Project No 8-CO-410-000-002, requested by CRDC. We wish to thank Ms. Carol Nudell for countless hours running tedious enzyme assays.

BIBLIOGRAPHY.....DFPASE....ASC PAPER

1. Garden, J. M., S. K. Hause, F.C.G. Hoskin, and A. H . Rousch. 1975. Comparison of DFP-Hydrolyzing Enzyme Purified from Head Ganglion and Hepatopancreas of Squid (Loligo pealei) by means of Isoelectric Focusing. Comp. Biochem. Physiol. 52C:95-98.

2. Hofmann, E., and G. Cleffmann. 1981. External Factors Limiting the Multiplication Potential of Tetrahymena. J. Cell Sci. 50:407-418.

3. Hoskin, F.C.G., 1971. Diisopropylphosphofluoridate and Tabun: Enzymatic Hydrolysis and Nerve Function. Science 172:1243-1245.

4. Hoskin, F.C.G., and R. J. Long. 1972. Purification of a DFP-PHydrolyzing Enzyme from Squid Head Ganglion. Arch. Biochem. Biophysics. 150:548-555.

5. Hoskin, F.C.G., and A. H. Roush. 1982. Hydrolysis of Nerve Gas by Squid-Type Diisopropyl Phosphofluoridate Hydrolyzing Enzyme of Agarose Resin. Science 215:1255-1257.

6. Hoskin, F.C.G., and R.D. Prusch. 1983. Characterization of a DFP-Hydrolyzing Enzyme in Squid Posterior Salivary Gland by use of soman, DFP and Manganous Ion. Comp. Biochem. Physiol. 75C:17-20.

7. Hoskin, F.C.G., M.A. Johns and K.E. Steinman. 1984. Two Enzymes for the Detoxication of Organophosphorus Compounds-Sources, Similarities and Significance. Fund. Appl. Toxicol. 4:S165-172.

8. Hoskin, F.C.G., and K.E. Steinman. 1985. Naturally-Occurring DFPases. In Proceedings of Triservice Workshop on Enzymatic Decontamination, Ft. Detrick, Maryland.

9. Landis, W.G., and R.E. Savage, Jr. 1984. Initial Characterization of a Soman Hydrolyzing DFPase in Tetrahymena thermophila. In Army Science Conference Proceedings, West Point, New York.

10. Landis, W.G., D.M. Satanek, G.S. Hart, M.V. Haley, D.W. Johnson, and R.E. Savage. Jr. 1984. Kinetics and purification of a Diisopropyl-fluorophosphate-Hydrolyzing Activity in the Protozoan, Tetrahymena Thermophila. M.D. Rausa (ed.), in proceedings of Scientific Conference on Chemical Defense, CRDC SP-85006:633-637.

11. Landis, W.G., R.E. Savage, Jr., and F.C.G. Hoskin. 1985. An Organofluorophosphate-Hydrolyzing Activity in Tetrahymena thermophila. J. Protozoology 32:517-519.

12. Landis, W. G., H.D. Durst, R.E. Savage, and B.G. Harper. 1986. The Tetrahymena-DFPases: Elucidation, Characteristics, Utility as Non-Corrosive Decontaminants, and Therapeutic Potential. In Army Science Conference Proceedings, West Point, New York.

13. Landis, W.G., H.D. Durst, D.M. Haley, M.V. Haley, D.W. Johnson, R.M. Tauber, and R.E. Savage,Jr. 1985. Tetrahymena-DFPase: Activity, Kinetics, and Separation. M.D. Rausa (ed.), in proceedings of the 1985 CRDC Scientific Conference on Chemical Defense. CRDC-SP-(In press).

14. Lowry, O.H., N.S. Rosebrough, A.L. Farr, and R.J. Randall. 1951. Protein Measurement with the Folin Phenol Reagent. J. Biol. Chem. 193:265-275.

15. Mazur, A. 1946. An Enzyme in Animal Tissue Capable of Hydrolyzing Phosphorus-Fluorine Bond of Alkyl Fluorophosphates. J. Biol. Chem. 164:271-289.

16. Mounter, L.A., R.F. Baxter, and A. Chanutin. 1955. Dialkylfluorophosphatases of Microorganisms. J. Biol. Chem. 215:699-704.

DEVELOPMENT OF A GENETICALLY ENGINEERED MALARIA VACCINE FOR MAN(U)

WAYNE T. HOCKMEYER*, LTC, JAMES F. YOUNG, Dr., W. RIPLEY BALLOU, MAJ, ROBERT A. WIRTZ, MAJ, IMOGENE SCHNEIDER, Dr., LOUIS H. MILLER, Dr., RICHARD BEAUDOIN, Dr., CARTER L. DIGGS, COL
WALTER REED ARMY INSTITUTE OF RESEARCH, WASHINGTON, DC, 20307-5100
SMITH, KLINE AND FRENCH, SWEDELAND, PA, NATIONAL INSTITUTES OF HEALTH AND NAVY MEDICAL RESEARCH INSTITUTE, BETHESDA, MD

Malaria is one of the great global health problems. Although it was first clinically recognized and described by Hippocrates, it remains today a principal endemic disease threat for nearly two billion people. The World Health Organization estimates that as many as three million people die of this disease every year. Military forces have repeatedly succumbed to malaria and the US Army first encountered casualities due to malaria during the Revoluntionary War. This pattern has been repeated in every major conflict since that time. In many campaigns, malaria casualities greatly outnumbered battle casualities. Nonetheless, efforts to control this disease were considered promising in the 1930's and 1940's with the advent of modern insecticides and new therapeutic drugs. Malaria control and eradication programs were agressively pursued throughout the world. Though not realized at the time, they reached their zenith by the early 1960's. Mosquito vectors became resistant to insecticides and the parasites which cause the disease no longer responded to the new drugs. The U.S. military, with some 45,000 cases of malaria in troops in Vietnam, encountered serious problems with chloroquine resistant malaria. Because of these setbacks, scientists armed with new techniques in immunochemistry and molecular biology have increasingly been turning their attention to the development of vaccines to control this ancient enemy. Strategy for development of an effective malaria vaccine is based on an understanding of the life cycle of the parasite. The most promising effort to date is directed at the sporozoite, the parasite stage transmitted by Anopheline mosquitoes and which initiates infection in man. An effective sporozoite vaccine would have the intrinsic advantage of completely

preventing infection. However, since immunity to the sporozoite has no effect on the stages found in the blood which cause clinical manifestations of malaria, a single sporozoite escaping the primed immune system could cause disease. Complementary efforts thus exist to develop a vaccine against the asexual erythrocytic stages. This effort is hindered by the number and complexity of antigens displayed on the surface of these stages and determining which of these proteins is capable of eliciting a protective immune response. Lastly, many of these asexual parasite surface antigens are strain variant and are thus not ideal vaccine candidates.

The concept of sporozoite immunity has been evolving for more than 15 years. Irradiated sporozoites have been used to successfully immunize and protect rodents, non-human primates and even a small number of human volunteers (1-3). Sporozoite immunity is related to development of antibodies to a protein found on the surface of sporozoites termed the circumsporozoite (CS) protein. These CS proteins have been found on all malaria parasites, including Plasmodium falciparum, the most significant of human malaria parasites (4). Nonetheless, techniques using irradiated sporozoites were not practical for anything but experimental purposes. Sporozoites can be laboriously obtained only from infected mosquitoes and can't be cultured in vitro. Thus, development of a whole organism attenuated or sub-unit vaccine was not possible.

Then, virtually overnight, the advent of new techniques in molecular biology resulted in a rapid shift to attempts to clone genes encoding the CS proteins. Success followed quickly. This was first accomplished with P. knowlesi, a monkey malaria parasite (5). Within a few months, in a collaborative effort involving scientists from the National Institutes of Health and the Walter Reed Army Institute of Research, the CS gene of the human malaria parasite P. falciparum was cloned and sequenced (6). Subsequently, we and others have cloned additional CS protein genes including that for another human malaria parasite, P. vivax (7-9). Although CS proteins have been shown to be structurally analagous, they differ in their primary amino acid sequence. The P. falciparum CS protein has a sequence typical of a membrane protein with an NH_2 signal peptide and a COOH terminal anchor sequence. The most striking feature of the protein is a large repeat region composed of 37 identical Asn-Ala-Asn-Pro tetrapeptides interspersed with 4 Asn-Val-Asp-Pro repeats. Because monoclonal antibodies (Mabs) and serum from humans immunized and protected against sporozoites react with this immunodominant repeat region, it was considered an important vaccine target. Flanking the repeats were two smaller sequences conserved among P. falcparium, P. vivax, and P. knowlesi. We termed these sequences region I and region II and

suggested they might be conserved for an important biological function. As such, they too were considered important vaccine targets.

Faced with at least three regions of the CS protein which might form the basis for a useful malaria vaccine, we felt that studies designed to determine which of these might be most efficacious were important. Accordingly, we synthesized peptides from the repeat and conserved regions of the P. falciparum CS protein having the sequences shown in Table 1 (10).

Table 1. Sequence of synthetic P. falciparum CS protein peptides. Synthetic peptides included 8-, 10-, 12-, 14-, and 16- residues of the repeat region as well as the conserved regions I and II sequences as described (6). Ballou et al., (1985). Copyright AAAS.

Residues	Sequence
8	NPNANPNAC-
10	NANPNANPNAC-
12	NPNANPNANPNAC-
14	NANPNANPNANPNAC-
16	NPNANPNANPNANPNAC-
Region I	-CKHKKLKQPGDG
Region II	-TEWSPCSVTCGNGIQ

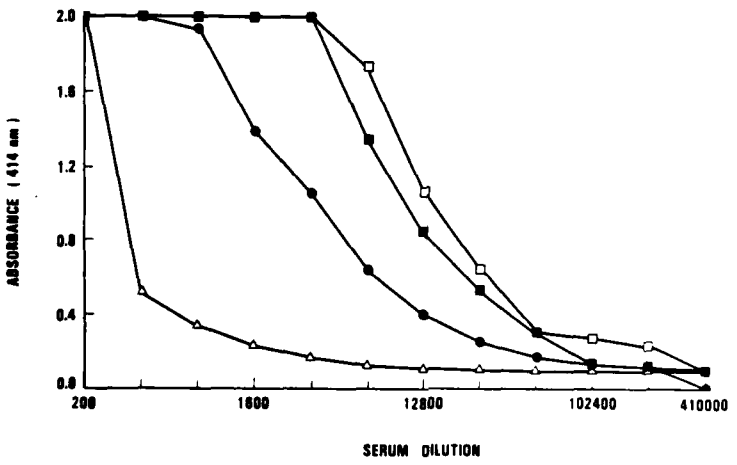

Fig 1. Immunogenicity of synthetic P. falciparum CS peptides. Antiserum to 16-residue repeat peptide (●); antiserum to region I peptide (■); mouse antiserum to region II peptide (△); rabbit antiserum to region II peptide (□). Ballou et al (1985). Copyright AAAS.

These peptides were conjugated to bovine serum albumin (BSA), thryoglobulin or keyhole limpet hamocyanin (KLH) and used to immunize rabbits or C57 BL/6 mice. The animals were bled 7 days after the last booster injection and tested in an ELISA for antibody against the respective peptide antigens. As shown in Figure 1, each of the peptides made detectable antibody responses in mice though the response to region I and the repeat peptides was better than to region II. However, high titer antibody to region II was produced in rabbits. Antibody responses to the repeat peptides were uniformly high and independant of the length of the peptide. The peptide antisera were further tested in an indirect fluorescent antibody (IFA) assay for reactivity against sporozoites (10). Antisera to region I and the repeat region but not to region II reacted with sporozoites (data not shown).

Although the results described above were encouraging, they did not address the critical question of whether such antibody posseses any biological activity indicative of in vivo protection. Sera from animals and man immune to sporozoites produce a circumsporozoite precipitin (CSP) reaction and inhibit sporozoite invasion (ISI assay) of a human hepatoma cell line in vitro. Both the CSP and ISI assays are thought to be good correlates of protection in vivo (11-13). As shown in Table 2, only antisera raised against the repeat region peptides produce strong CSP reactions and inhibit sporozoite invasion of hepatoma cells. Antisera to region I and II produced no activity.

Immunogen	CSP	% Inhibition
8 residues	23/25 (+)	100
12 residues	13/25 (+)	NT
16 residues	21/25 (+)	100
Region I	0/25 (0)	0
Region II	0/25 (0)	0

Table 2. Circumsporozoite precipitin (CSP) reactivity and percentage inhibition of sporozoite invasion (ISI) of HepG2-A16 hepatoma cells by mouse antisera to repeat and region I peptides, and rabbit antiserum to region II peptide in vitro. The (CSP) reactions were performed as described (14). Twenty-five random sporozoites were examined for each serum sample and the number of CSP positive organisms is indicated. The degree of CSP reactivity is shown in parentheses (0, no CSP reactivity detectable; 2+, a granular precipitate on the surface of the sporozoites; 4+ a long thread-like filament at one end of the sporozoites. Inhibition of sporozoite invasion was performed as described (13).

Inhibition was the percentage reduction of sporozoite invasion by antisera to the synthetic peptides compared to normal mouse serum controls when CS reactive Mab 2F1.1 (6) gave 100 percent inhibition of sporozoite invasion at a dilution of 1:20. NT = not tested. Ballou et al 1985. Copyright AAAS.

These data were encouraging in that they clearly established that the repeat region of the CS protein and not the conserved sequences were the important vaccine target. The fact that anti-repeat peptide antibodies were biologically active clearly established the feasibility of development of an anti-sporozoite malaria peptide sub-unit vaccine. Peptide vaccines are not without potential problems including limita tions on the amount of peptide that can be conjugated to the carrier. This may limit ones ability to generate an adequate anti-peptide antibody response. Other problems include increased reactogenitiсy, sensitization of the host leading to increased clearance of the antigen and lastly the phenomenon of epitope specific suppression (15). This has been observed with peptides from streptococcal M protein and with diphtheria peptides conjugated to tetanus toxoid (16). As an alterna-tive, we decided to attempt to produce a malaria vaccine using recombinant DNA technology.

Since the peptide studies clearly indicated that the repeat region of CS protein was important in eliciting protective antibodies, we excised a Xho II fragment containing 16 tetrapeptide repeats from the CS gene and ligated it into the Bam HI site of the pAS1 λ PL E. coli expression plasmid (Fig. 2).

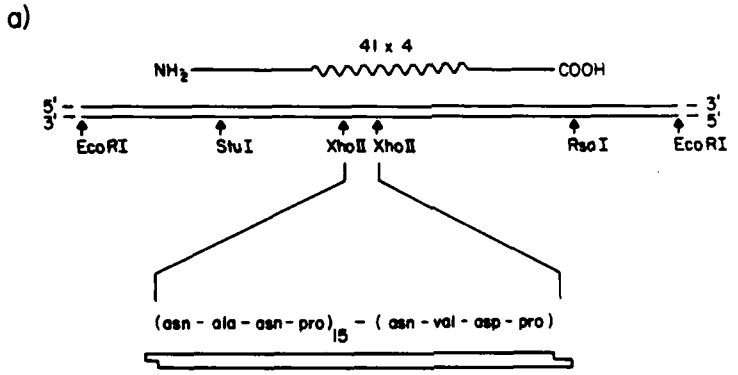

Fig. 2 A. Schematic representation of the Eco RI insert from the λ mPf1 (6) containing the CS gene and a diagram of the protein encoded by this gene showing the 41 tetrapeptide repeats as a wavy line. The 192 -bp Xho II fragment encodes for 15 Asn-Ala-Asn-Pro tetrapeptide repeats and one Asn-Val-Asp-Pro repeat, as shown.

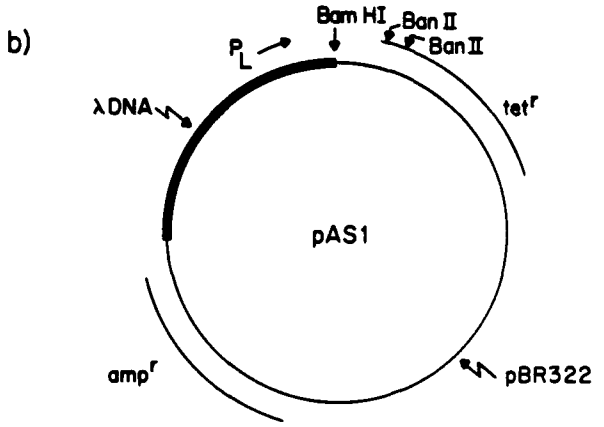

Figure 2 B. Diagram of the pAS1 E. coli expression plasmid (18,19). The segments of DNA derived from λ phage and pBR322 are indicated. The complete ampicillin resistance region (Amp^r) and part of the Tet^r are from pBR322. Expression of genes inserted into the Bam H1 site is under control of theλP_L promoter, whose transcription is controlled by a cI repressor protein. Vector constructs are therefore transformed and maintained in a cI^+ lysogenic host (MM294I+) to prevent expression of protein that may be toxic to the host strain. To control expression, the plasmid is transferred into a lysogen carrying a temperature-sensitive c1857 repressor (20). Bacteria can then be grown in the absence of expression (32^oC, repressor active) and then shifted to 42^oC to inactivate the repressor and turn on transcription from the P_L promotor (21). Young et al (1985). Copyright AAAS.

Three proteins were subsequently produced in E. coli and designated as $R16tet_{32}$, $R32tet_{32}$ and $R48tet_{32}$ (17). These proteins had 15, 30 or 45 (Asn-Ala-Asn-Pro) tetrapeptide repeats and 1, 2, or 3 (Asn-Val-Asp-Pro) repeats respectively (Fig. 3). All three proteins contained 32 amino acids derived from the tetracycline resistance gene of the pAS1 plasmid. These proteins were purified to homogeneity from bacterial extracts and used for immunogenicity studies.

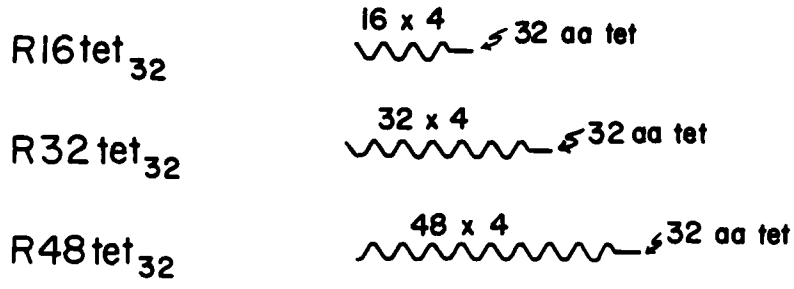

Fig. 3. Summary of three CS protein derivatives produced in E. coli. The wavy lines represent the immunodominant tetrapeptide repeat unti and the number of repeats in each construct is indicated over this line. The $R16tet_{32}$, $R32tet_{32}$, and $R48tet_{32}$ contain 16, 32, or 48 repeats respectively, fused to 32 amino acids from an open reading frame in the Tet^r region. Young et al (1985). Copyright AAAS.

The three purified CS protein derivatives produced in E. coli were used to immunize C57Bl/6 mice. They were administered as three 50ug injections 4 weeks apart. The proteins were given either without adjuvant (plain), with aluminum hydroxide or emulsified in complete Freund's adjuvant (CFA). The animals were bled 4 weeks after the last booster injection and the serum from each group pooled. These sera were then tested by ELISA for anti-sporozoite antibody. As shown in Fig. 4, the large $R32tet_{32}$ and $R48tet_{32}$ proteins were very immunogenic and produced high titer antibody responses even without adjuvants. The smaller $R16tet_{32}$ was less immunogenic. As would be predicted, adjuvants enhanced the antibody response of all three proteins. Reciprocal titers up to 102,000 were observed with at least one of the proteins.

Fig. 4. Antibody responses of mice to purified recombinant P. falciparum CS proteins R16tet$_{32}$, R$_{32}$tet$_{32}$, or R48tet$_{32}$ were determined by ELISA using as antigen a 16 amino acid synthetic peptide consisting of four repeats of the P. falciparum CS protein (Asn-Ala-Asn-Pro) (6, 10). Assays were run in triplicate and the means and S.E.M. were calculated. In all instances the S.E.M. was less than 0.09. Symbols for the antisera are: ◆ R16tet$_{32}$, ◇ R32tet$_{32}$; ■ R48tet$_{32}$. Animals were immunized with (A) proteins in CFA; (B) proteins with aluminum hydoxide; or (C) proteins in PBS without adjuvant. Young et al (1985). Copyright AAAS.

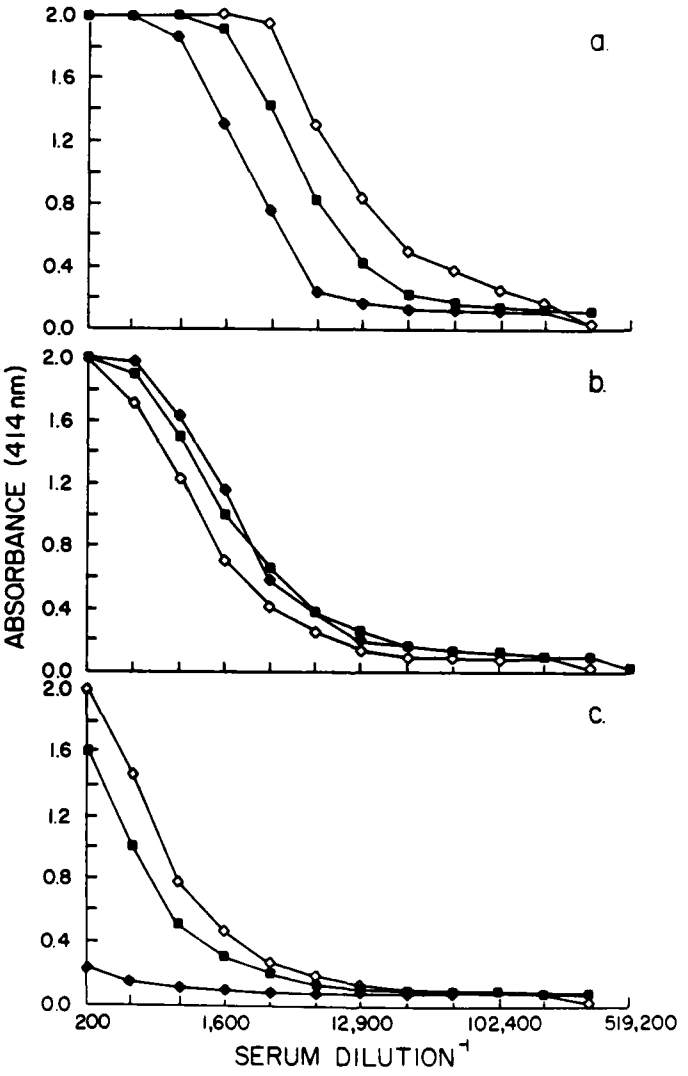

These sera reacted strongly against authentic CS protein when tested by IFA against P. falciparum sporozoites (data not shown). As indicated in Tables 3 and 4, these sera produced strong CSP reactions and blocked sporozoite invasion of hepatoma cells in vitro. As indicated previously, both the CSP and ISI assays are considered predictive of in vivo protection. Antibody responses have been followed in these animals for 8 months after their last injection of vaccine (22). Alum adjuvanted R32tet32 vaccinated animals still exhibit high titer antibody responses with strong CSP and blocking activity. Taken together, these data indicate that the recombinant $R32tet_{32}$ is a promising malaria vaccine candidate.

Adjuvant	Reactivity of antisera to		
	$R16tet_{32}$	$R32tet_{32}$	$R48tet_{32}$
None	0/25 (-)	17/25 (2+)	21/25 (4+)
CFA	23/25 (4+)	21/25 (4+)	21/25 (4+)
Aluminum hydroxide	25/25 (4+)	25/25 (4+)	16/27 (2+ to 4+)

Table 3. Circumsporozoite precipitin (CSP) reactivity of mouse antisera to $R16tet_{32}$, $R32tet_{32}$, or $R48tet_{32}$. The CSP reactions were performed as described (14). (See Table 2) Young et al (1985). Copyright AAAS.

Adjuvant	Percentage of inhibition by antisera to		
	$R16tet_{32}$	$R32tet_{32}$	$R48tet_{32}$
None	46	95	92
CFA	76	92	94
Aluminum hydroxide	100	100	96

Table 4. Inhibition of sporozoite invasion was performed as described (13). (See Table 2) Young et al (1985). Copyright AAAS.

DISCUSSION

These studies partially describe an effort conducted over the past 2 years to develop an efficacious malaria vaccine. Though the CS protein on the surface of sporozoites was known to be a good immunogen, sporozoites could not be cultured in vitro and thus, development of an attenuated whole organism vaccine was impossible. This problem was successfully circumvented by cloning the gene encoding the CS protein. Knowing the amino acid sequence, synthetic peptides were employed to determine which portion of this 412 amino acid protein was the most appropriate vaccine target. In a protein this large, many possibilities existed. We considered at least three, of which only the repeat region was found to be promising. Using recombinant DNA techniques, three CS derived proteins were produced in E. coli, purified, and tested for immunogenicity. One of these, $R32tet_{32}$, produced high titer biologically active antibody. Using DNA probes, we have also determined that the CS gene, and specifically the repeat region, is conserved in a wide variety of geographic isolates (23). Since $R32tet_{32}$ vaccine is based on the repeat region, we expect it to protect against P. falciparum from any area of the world.

Many factors were considered in development of this vaccine. Among the more obvious were issues of immunogenicity, requirements for adjuvants, effect of boosting and duration of antibody response. By necessity, this is often determined emperically. We believe the present approach may offer some predictability to vaccine design which can be used in other situations. We chose the recombinant rather that the synthetic peptide approach so that we could produce large proteins. Larger molecules are often more immunogenic than smaller ones. Though not completely understood, larger molecules can satisfy requirements for immunogenicity which include the presence of antigenic sites capable of recognition by immunoglobulin molecules on the surface of B cells, agretopic sites for major histocompatibility (MHC) elements, and epitopes conserved during antigen processing which bind subsites on T cell receptors (24). Peptide vaccines require a carrier protein to provide T cell sites to allow for secondary antibody response. In contrast, $R32tet_{32}$ contains such subsites within the repeat region. The actual length and amino acid sequence of the subsite is currently being determined. One could realistically expect to design into the construction of an expression vector such subsites to insure high level antibody responses for any protein of interest.

Other factors may also be important for future vaccine design. $R32tet_{32}$ contains 32 amino acids derived from the tetracycline resistance gene of the plasmid. Because of the vector construction, this is a unique fusion protein never before produced. We originally

thought it could provide a T cell site - a factor which might have been critical had one not been contained within the repeat region. Tet_{32} however, is important for an entirely different reason. Because of its amino acid composition, it is highly charged and binds avidly to alum, an adjuvant which has a long history of safe use in man. When alum was used with this vaccine, it increased not only antibody titer but also the duration of antibody response. As with T cell sites, incorporation of Tet_{32} in the expression system will assure production of candidate immunogens which can be readily adjuvanted.

Alum adjuvanted $R32tet_{32}$ malaria vaccine has been manufactured and extensive pre-clinical testing in mice, rabbits and monkeys has recently been completed. These studies show that it is safe and highly immunogenic. An investigational new drug (IND) application has been approved by the Food and Drug Administration to test this vaccine in human volunteers. These first human malaria vaccine trials have begun.

REFERENCES

1. R. J. Nussensweig, J. Vanderberg, and H. Most, Mil. Med. 134, 1176 (1969).
2. D. F. Clyde et al., Am. J. Trop. Med. Hyg. 24, 397 (1975).
3. K. H. Rieckmann et al., Trans. R. Soc. Trop. Med. Hyg. 57 (Suppl. 1). 261 (1979).
4. P. Potocnjak et al., J. Exp. Med. 151, 1504 (1980).
5. G. N. Godson et al., Nature 305, 29 (1983).
6. J. B. Dame et al. Science 225, 503 (1984).
7. T. F. McCutchan et al: Science 230, 1381 (1985).
8. V. Enea et al., Proc. Natl. Acad. Sci. USA 81, 7520 (1984).
9. D. Arnot et al., Science 230, 815 (1985).
10. W. R. Ballou et al., Science 228, 996 (1985).
11. E. Nardin et al., J. Exp. Med. 156, 20 (1982).
12. N. Yoshida et al., Science 207, 71 (1979).
13. M. R. Hollingdale et al., J. Immunol. 132 909 (1984).
14. J. Vanderberg, R. S. Nussensweig, and H. Most, Mil. Med. 134, 1183 (1969).
15. L. A. Chedid et al., Infect. Imm. 35, 417 (1982).
16. M. P. Schutze et al., J. Immunol. 135, 2319 (1985).
17. J. F. Young et al., Science 228, 958 (1985).
18. M. Rosenberg, Y. Ho. A. Shatzman, Methods Enzymol. 101, 123 (1983).
19. A. Shatzman, Y. Ho., M. Rosenberg, in Experimental Manipulation of Gene Expression, M. Inouye, Ed. (Academic Press, New York, 1983), pp. 1-14.
20. R. Sussman and F. Jacob, C.R. Acad. Sci. Ser. A 254, 1517 (1962).

21. J. F. Young et al., Proc. Natl. Acad. Sci U.S.A. 80, 6105 (1983).
22. R. A. Wirtz et al., Exp. Parasit. Manuscript submitted (1986).
23. J. L. Weber and W. T. Hockmeyer, Mol. Biochem. Parasitol. 15, 305 (1985).
24. J. Berzofsky, Science 229, 932 (1985).

A SYNTHETIC BONE REPAIR MATERIAL (U)

*JEFFREY O. HOLLINGER, D.D.S., Ph.D., LTC AND JOHN P. SCHMITZ, D.D.S., MAJ
UNITED STATES ARMY INSTITUTE OF DENTAL RESEARCH
WASHINGTON, DC 20307-5300

Nearly 18 percent of the battlefield injuries involve the face and jaws. A simple fracture merely requires stabilization to allow for healing. However, when injuries to the face and jaws are severe, the extensive bony damage requires treatment with bone implants and grafts.

Many different types of materials have been used for the purpose of repairing, replacing, and augmenting bone. At the present time, autografts are the favored modality of treatment used by maxillofacial surgeons (1). Unfortunately, there are numerous disadvantages associated with autogenous grafting, such as, 1-failure rates ranging from 13-30 percent, 2-inability to recover sufficient autogenous bone to meet the needs of the host, 3-technical inconvenience, 4-trauma to the patient as a consequence of a second surgical procedure, 5-potential morbidity at the recipient donor sites, 6-high cost due to the need for numerous principal and ancillary personnel, and 7-considerable time away from duty as a consequence of a long recovery period (2,3,). Bone allografts, alloimplants, demineralized bone, and collagen gels have been used in attempts to rectify these problems, often with mixed results (3-8). Furthermore, bone alloimplant material (bank bone), the second most frequently used treatment, has a failure rate exceeding that of the autogenous graft (9).

Due to the shortcomings of the traditional bone repair agents, the United States Army Institute of Dental Research developed a material that may be a viable alternative. It is a synthetic consisting of a combination of biopolymers and calcification inducer.

The biopolymers of poly-alpha-hydroxy acids (a class of polyesters) have garnered much interest in the medical and dental fields in the last 10 to 15 years. The poly-alpha-hydroxy acids of polyglycolic acid (PGA) and polylactic acid (PLA) were initially developed for biodegradable suture materials (10-12). They are commercially available as Dexon® and Vicryl®. Different formulations of the PLA and PGA also have been used experimentally for osseous repair and reconstructive procedures (13-17).

Considerable attention has been focused on the cell derived organelle

known as the type II matrix vesicle for its role in initiating calcification (18-20). Intensive investigation of the structure of the matrix vesicle has revealed that its trilaminar membrane possesses a high content of acidic phospholipid (21,22). It has been shown that a protein-acidic phospholipid (proteolipid) complex similar to that of the matrix vesicle can cause calcification (the formation of hydroxyapatite) both *in vitro* and *in vivo* (23-25).

The purpose of this investigation, therefore, was to determine if the combination of PLA and PGA plus a proteolipid would affect bony wound repair.

MATERIALS AND METHODS

Preparation of the Synthetic Implant Materials for Rats and Dogs

The acidic phospholipid, phosphatidylinositol 4,5 diphosphate, was combined with a commercially available lysozyme (mucopeptide-N-acetylmuramoyl-hydrolase) in a volume ratio of 2:1, producing a proteolipid complex (PL) (25). A commercially synthesized copolymer, 50:50 poly (D,L)-lactide co-glycolide (inherent viscosity of 0.92 and weight average molecular weight of 80K Daltons), was solubilized in methylene chloride at a 1:12.5 weight volume ratio. The synthetic copolymer was precipitated with anhydrous methanol (1:1 volume ratio) and forced into Teflon molds to produce 140 2.0mm x 1.25mm implants for insertion into bone wounds in rats. Copolymer proteolipid implants were prepared in a similar manner; however, the precipitated copolymer was combined with the proteolipid (PL) (1 percent by weight proteolipid to copolymer). The geometry of the cured combination was identical to the plain copolymer. Copolymer PL implants also were prepared for dogs and these implants were of a dimension 20mm x 17mm x 8mm. All bone repair agents were cured at 50 degrees C, 5 millitorr, for 48 hours to remove residual solvents. Sterilization was accomplished using ethylene oxide at 30 degrees C, 4-5 psi, for 6 hours followed by degassing for 24 hours to remove all residual ethylene oxide and any possible ethylene glycol and ethylene chlorohydrin residuals.

Preparation of Experimental Rats

One hundred and eighty Walter Reed strain of rats (random males and females, average weight 200-300gm) were anesthetized with intraperitoneal sodium pentabarbital, USP, at a dosage of 3-5mg/100mg body weight. The 180 rats were divided into 3 groups of 60 each: Group A received the copolymer PL, Group B received copolymer implants, and Group C served as the untreated controls.

The diaphyses of the right and left tibias were selected as the implant and control sites. Areas over the diaphyses were shaved and scrubbed with povidone iodine for five minutes. A 1cm incision was made

on the anterolateral surface of each tibia and following reflection of soft tissues, a circular defect (1.95mm) was prepared through the cortical plate with a bone trephine and sterile water coolant. Copolymer PL implants (120 in number) were inserted into each tibia of the 60 rats; the second group of 60 rats received 120 plain copolymer implants; the 120 control wounds in the remaining 60 rats were left untreated. All surgical sites were closed in layers with 3-0 Dexon suture. At 3,7,14,21,28, and 42 days, 10 animals from each of the 3 groups were sacrificed with intraperitoneal sodium pentobarbital, USP, and control and experimental sites were retrieved.

Preparation of the Experimental Dogs

Twenty-five (60-70 lbs) random sex, foxhound dogs were conditioned for two weeks and adult skeletal maturity was authenticated by radiographic evidence of closure of epiphyses of the distal femur and proximal tibia. Animals were verified to be healthy by routine physical examinations and accepted veterinary diagnostic testing.

Prior to surgery, dogs were kept off food and water for 24 hours and benzathine penicillin (150,000 units) was administered intramuscularly (IM) for prophylaxis. Preoperatively, acepromazine (5mg) and atropine (1mg) were given IM and subcutaneously, respectively. An intravenous (IV) line was established in the left hind leg and Ringer's lactate (1cc/min) was infused during the entire procedure and until the animal was responsive. After induction with sodium pentathal (20mg/kg, IV), dogs were intubated and maintained at a surgical plane of anesthesia with two percent halothane and N_2O/O_2 50:50 (1 liter/min).

The 25 dogs were divided into 2 groups: 18 for bilateral extraction of mandibular premolars and first molars in the resection sites and 7 without extractions. Alveoloplasties were performed and soft tissue was closed in layers with 3-0 Dexon. Antibiotic coverage consisted of 150,000 units of Bicillin IM for 5 days. Both groups of animals were maintained on a soft dental diet for the duration of the experiment. Animals were allowed to heal for 6-8 weeks before being scheduled for surgical resections.

After 6-8 weeks and following a surgical scrub of the shaved skin with povidone iodine, the dog was draped and the mandible was approached through an external submandibular incision. The mid body of the mandible was degloved facially and lingually and the neurovascular bundle was ligated and a 17mm discontinuity (cortex to cortex) was created using a Hall air drill, 703 bur, and copious sterile water for irrigation. All animals received identical bilateral defects and the left sides served as controls, whereas the right sides received the synthetic bone repair implants (copolymer PL) of the identical dimension to the ablated segment (17mm x 17mm x 8mm). Implants were secured with 21 gauge stainless steel ligature wire. Proximal and distal mandibular fragments were fixated on each side

with tubular stainless steel bone plates and four self tapping screws. A water tight seal of the intraoral mucosa for the extraction group was accomplished with 3-0 Dexon and the submandibular tissues were closed in layers with 4-0 Dexon. Antibiotic coverage and soft dental diet were identical to that previously described. All animals were examined clinically and radiographed every four weeks at the surgical sites. A dental X-ray technique was used for obtaining lateral mandibular radiographs (kvp, 90;mamp, 3; time, 0.3 sec). At each time period of 4,8,12,24, and 40 weeks, 5 animals were sacrificed with T-61® euthanatizing solution and specimens were recovered and processed for histomorphometry (to be described).

Analysis of Rat Specimens

The experimental and control sites were retrieved from the rat tibias using a dental 703 bur in a rotary handpiece with ample water irrigation. Approximately 2mm of contiguous bone was recovered with the implants and controls and these were placed into individually labeled vials containing 70 percent ethanol. Specimens were embedded in polymethyl methacrylate, sectioned at five micrometers, and stained with a modification of the Masson-Goldner trichrome stain to facilitate histomorphometric analysis. Each specimen was analyzed in a meandering fashion across the wound from top to bottom. Each 10 animal group of rats provided 100 pooled fields from which histomorphometric measurements could be made on trabecular bony volume, mean trabecular diameter, and bone remodeling cells.

Data from the histomorphometric analysis of the same variable (i.e., volumetric density, VV) from the same treatment and temporal groups were pooled to yield a mean. The pooled mean for each variable plus and minus its standard error of the mean was used to construct a bar graph.

A two-way analysis of variance was used to test, 1-the main effects of the treatment groups (differences between the three treatment groups averaged over the six time periods), 2-the main effects of the time periods (differences between the six time periods averaged over the three treatment groups), and 3-possible interaction between treatment group and time (whether the time curves were essentially parallel). Effects having an observed significance level (p value) less than five percent (based on the F test value) were considered to be statistically significant.

Analysis of the Experimental Dog Specimens

At 5 post-implantation times (4,8,12,24, and 40 weeks) 5 animals were euthanatized with T-61®. The number of extraction to nonextraction animals varied from 3:2 to 4:1, respectively.

At the time of necropsy, experimental and control areas were surgically removed en bloc. A 100 micrometer slice was retrieved from the center of the specimen (sagittal plane) using a Buehler Isomet Low Speed Saw

and the slice was placed into 70% ethanol, embedded in polymethyl methacrylate, sectioned at three and one-half to four micrometers and stained with a modification of Masson-Goldner trichrome stain to facilitate histomorphometric analysis (Fig.1).

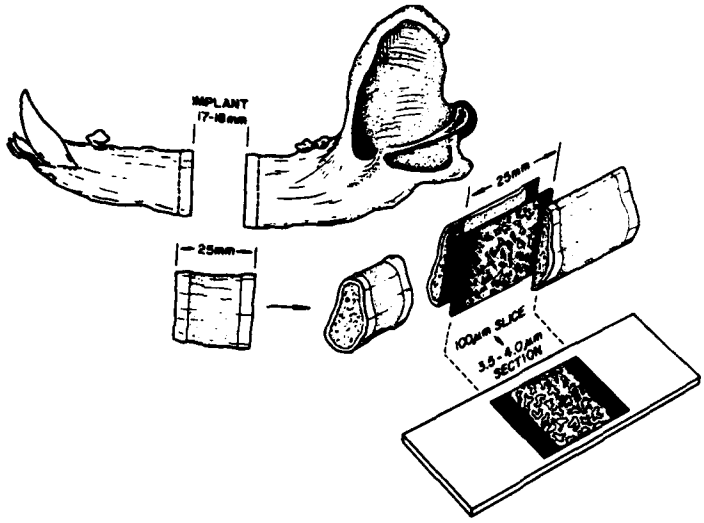

Fig.1.
Mandible prepared for histomorphometry.

A 22mm x 10mm window was placed over each prepared slide specimen to standardize and define the assessment perimeter. Using a 1.25X objective and an eyepiece greticle in a Zeiss 10X eyepiece, a grid was superimposed over each specimen that defined the fields to be measured within that perimeter. Therefore, within a 220mm^2 area (22mm x 10mm) it was possible to measure 2 fields that included approximately 50 grid squares per field (Fig.2).

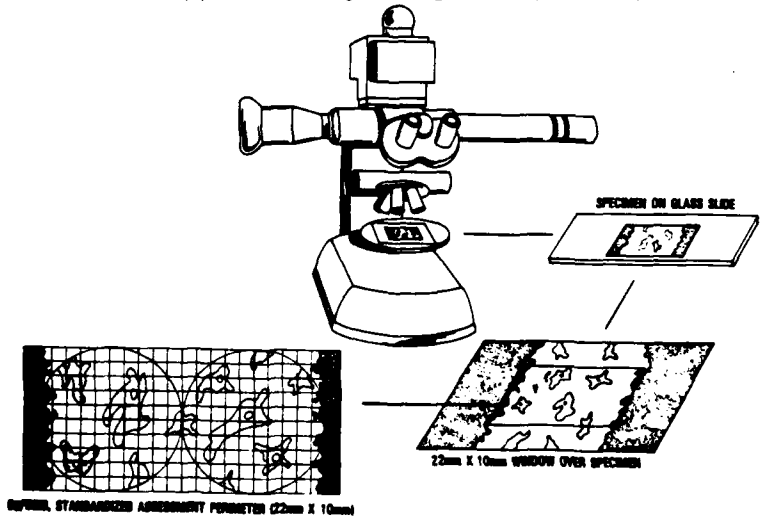

Fig.2.
Specimen evaluations using a standardized perimeter.

Measurements were made of the two-dimensional bony trabeculae in each field using a Zeiss Image Analysis System with Osteoplan® (version 4.1) to derive three-dimensionality, i.e., the first order derived quantity of trabecular volume (TV) (mm^3 trabecular bone/mm^3 bone tissue).

For each necropsy time (4,8,12,24, and 40 weeks), means and standard deviations (across 5 animals after taking the mean of the duplicate measurements) were computed for implants and controls. Overall differences in mean TV between implants and controls and effects of necropsy time were tested using analysis of variance procedures for a two factor repeat measure design. The paired t-test was used for making individual comparisons of implant and control means at each necropsy time.

RESULTS

Histomorphometric and Statistical: Rats

Histologically, early experimental and control wounds (three and seven days) displayed the expected compliment of acute inflammatory cells that are associated with injury. Numerous polymorpholeuconeutrophyls (PMNs) and occasional small round cells were apparent; they diminished in number by 14-28 days for treatments and controls. By 14 days, osteoblasts and minimal osteoid could be seen in the Groups A (copolymer PL), and B (copolymer), and C (controls). Over the course of the experiment, there did not appear to be an adverse tissue reaction to the synthetic bone repair materials. There was no evidence at any time of abundant giant cell formation or inflammatory cells associated with a chronic adverse tissue response to foreign material.

The overall trends in osseous healing frequently displayed only subtle differences when observed by routine histological assessment; however, when histomorphometric variables of volumetric density (VV), mean trabecular diameter (D-TRAB), and discrete bone cell types (osteoblasts, OBI; osteoclasts, OCI) were quantitated, it was apparent that statistically significant differences did exist between treatments and between time periods. The histomorphometric data that were derived for each of the variables that were measured are summarized in bar graphs I-IV.

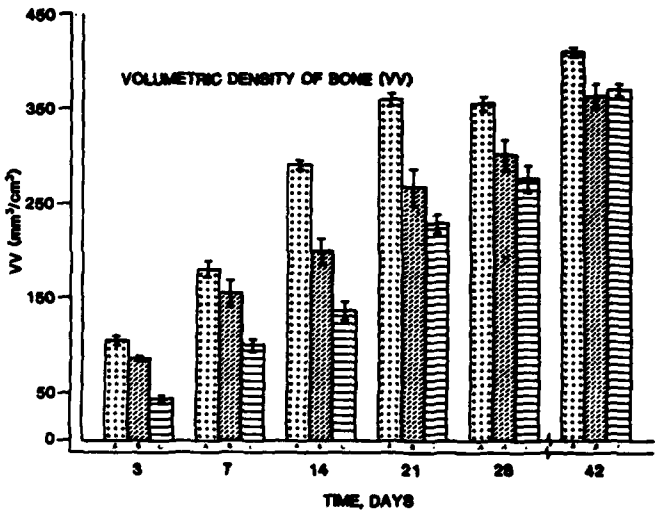

Graph I

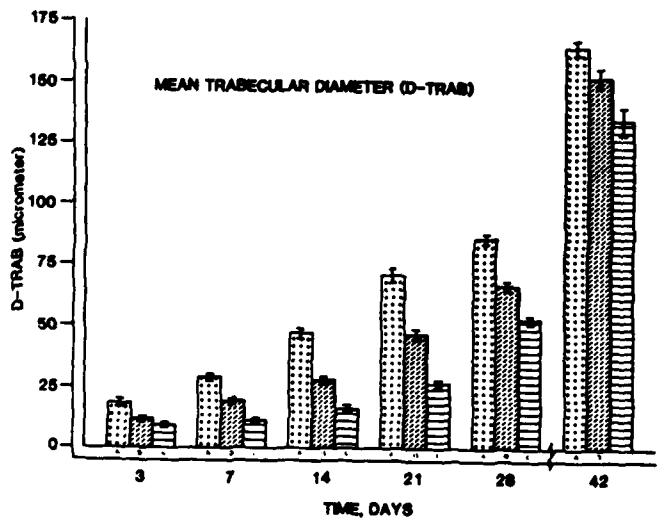

Graph II

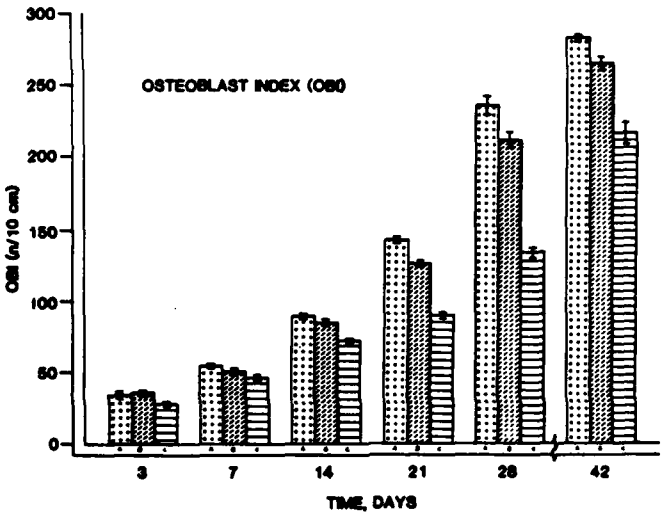

Graph III

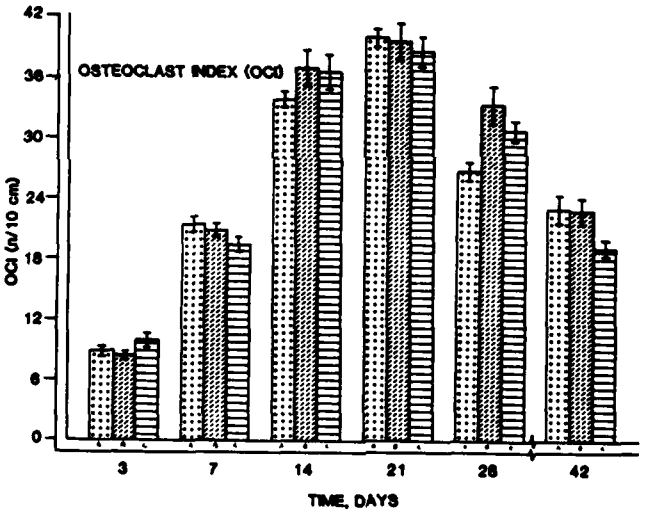

Graph IV

For most time periods, the elements of bone repair for Group A were greater than Group B which were greater than Group C. Furthermore, over time (day 3 through day 42), the same relationship were true. The only divergence in response was from the OCI (osteoclast index), which displayed an initial rise followed by a decline. This was to be expected.

for this pattern follows the remodeling phase of bony wound healing.

The statistical analyses comparing different experimental treatments and control over time revealed that (for most variables) there were significant differences between the three treatment groups over the six time periods ($p<0.05$) and there were significant differences between the six time periods averaged over the three treatment groups ($p<0.05$). The results of the two-way analysis of variance are summarized in the table on this page.

TABLE

RESULTS OF THE TWO-WAY ANALYSIS OF VARIANCE

VARIABLE	MAIN EFFECTS OF TIME		MAIN EFFECTS OF TREATMENT	
Volumetric Density of Bone (VV)	F• 65	p^1	F• 21	p^2
Treatment Contrasts				
AvsB				
AvsC				
BvsC				
Mean Trabecular Diameter (D-TRAB)	180		27	
AvsB				
AvsC				
BvsC				
Osteoblast Index (OBI)	54		6.9	
AvsB				
AvsC				
BvsC				
Osteoclast Index (OCI)	7.6		2.4	
AvsB				
AvsC				
BvsC				

Key

• - F confidence level of 95% or greater.

p^1 - Represents the comparison of time groups averaged over the treatment groups, where $p<0.05$.

p^2 - Represents the comparison of treatment groups averaged over the time groups, where $p<0.05$.

For all four variables the degrees of freedom were equal to two for treatments, five for time, and the residual (within cell) was equal to 162.

Clinical and Radiographic: Dogs

Clinical problems (i.e., abscess formation, loosening of fixation device) developed in eight dogs; however, following treatment by standard procedures (drainage, irrigation, debridement, antibiotics, tightening or replacement of fixation devices) the animals responded favorably and were able to continue in the experiment. Overall, the clinical observations were relatively unremarkable.

The general pattern of events at the mandibular wound sites eventually resulted in the formation of varying amounts of bone. Radiographically, osseous regeneration at the implant sites produced a complete osseous bridging by 40 weeks. At the control sites, evidence of bone formation was observed in 2 out of the 5 animals at 4 weeks post surgery. Only 1 dog failed to produce a complete osseous bridge by 40 weeks.

Histomorphometric and Statistical: Dogs

Graph V summarizes the effects of treatment (implant versus control) and necropsy time on trabecular volume (TV). Analysis of variance demonstrated an overall effect of treatment with differences between temporal groups. In both the implant and control sites, mean TV increased overtime, reaching a plateau at approximately 24 to 40 weeks. For each necropsy time (temporal group), the TV of the implanted sites exceeded the controls ($p<0.05$ using the paired t-test).

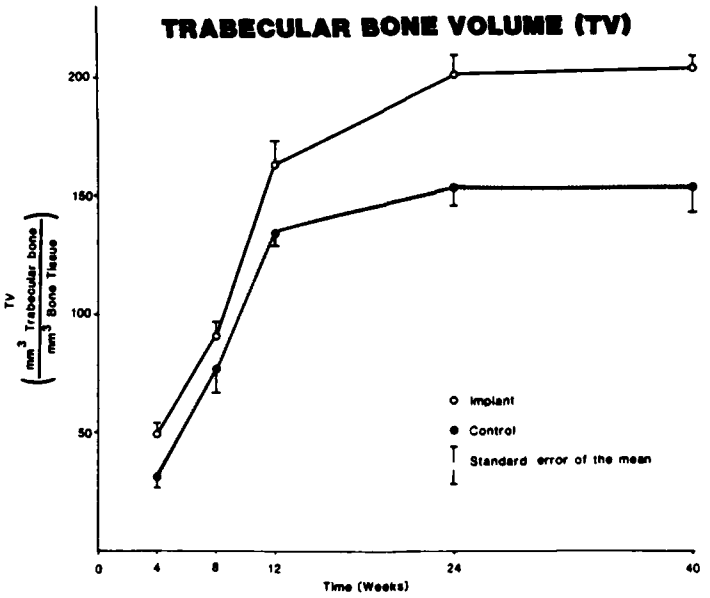

Graph V

DISCUSSION

Materials such as bone grafts and implants, collagen gels, ceramics, bone derivatives, and biopolymers are some of the many agents which have been employed by orthopedic and maxillofacial surgeons for initiating osseous repair or for replacing bone. Failure to achieve beneficial results with these materials has not been necessarily a consequence of imprudence, but rather due to deficiencies in the repair and replacement agents. A combination of the synthetic biopolymers PLA and PGA in conjunction with the PL described, appears to offer promise as an alternative to the more common, conventional materials.

A convenient experimental site had been selected in the rat for evaluating the new material. Although it was not of a critical size (that is, a non-healing osseous wound), we were concerned principally with determining how a bony wound would respond when the synthetic implant was inserted into a test site. It was not, therefore, important that the 1.95mm diaphyseal control would heal; but rather, did the synthetic copolymer PL enhance or delay osseous repair?

The dog experiment involved a bony wound that also was not a critical size defect (CSD). (The importance of a CSD has been reviewed and described for bone repair studies (26).) Again, we were not interested in an "all or none" phenomenon; rather, what was the effect of the synthetic on the rate of bone formation at a wound site?

The factors contributing to the superiority of healing at the experimentally treated implant sites reside with the properties of the implant's constituents. It has been mentioned that the proteolipid (PL) complex establishes a unique chemical environment conducive to calcium and phosphate precipitation, nucleation, and subsequent crystal growth (25). Moreover, the implication is that the locally introduced proteolipid was tantamount to surrogate extracellular matrix vesicles, the structures whose limiting membranes are heavily endowed with an acidic phospholipid component virtually identical in chemical composition to the PL. The extremely critical function of matrix vesicles in the calcification scheme has been described at length (20,22,27,28).

The contribution made by the synthetic biopolymers may be appreciated by understanding their process of biodegradation. The PLA and PGA biopolymers degrade in the body by the process of non-specific hydrolytic scission that results in the generation of lactic and glycolic acids (29-31). The lactic acid becomes incorporated in the Krebbs' cycle and is excreted by the lungs as carbon dioxide and water. Glycolic acid dimers, trimers, etc., are enzymatically degraded by esterases and carboxypeptidases (32) and are converted to glycolic acid monomers which either can be excreted in the urine or enzymatically converted by glycolate oxidase to glycoxylate. This moiety reacts with glycine transaminase and the glycine that is produced can be used in the Krebbs' cycle after transformation to pyruvate. The introduction of lactic and glycolic acids into the Krebbs'

cycle results in the generation of adenosine triphosphate (ATP), the body's energy currency. This extremely important commodity is essential for normal physiologic functions, and it is especially important for tissue repair.

For the rat experiment, two types of synthetic implants were used, one contained the proteolipid, while the other was the plain copolymer. Despite the evidence indicating that the plain copolymer engendered a more rapid rate of bone repair than untreated controls in endochrondral wounds (the tibial sites) in the rats, we did not opt to prepare unembellished copolymers for the mandibular discontinuities in the dogs. The choice of the synthetic copolymer plus PL was made because the histomorphometric data from the rat experiment determined the superiority of the copolymer PL implant over the synthetic by itself. We did not use plain PL in either the rat or dog experiments because it has a paste-like consistency.

The positive bone healing response produced by the combination synthetic bone repair material may be hypothesized as a being a consequence of several factors. We have mentioned that the PL may function as surrogate matrix vesicles. The significance of the synthetic biopolymer for bone formation may be due to a number of possible factors. The cells that are needed for repairing injured bone require a lattice or framework upon which they can begin to function. This requirement is known as anchorage dependence. The biodegradable synthetic biopolymer that we selected for our experiments possesses a linear molecular configuration that can provide bone cells with sites upon which they may anchor. Moreover, the importance of collagen in bone formation has been attributed to its geometry and surface charge (33,34). There may be a parallel affect from the linearly arranged macromolecules comprising the synthetic repair material. Furthermore, as the repair agent degrades by nonspecific hydrolytic scission of its ester bonds, there is a shift in local pH. This shift could affect calcification inhibitors (i.e., proteoglycans, glycosaminoglycans) and could act in a beneficial way to promote release from the host site of certain polypeptides (i.e., bone morphogenetic protein and skeletal growth factors) that could enhance osseous repair (35). These polypeptide factors have been described as being agents capable of increasing both osteoblast progenitor cell proliferation and subsequent bone formation rate.

The synthetic bone repair material developed by United States Army Institute of Dental Research may benefit orthopedic and maxillofacial surgeons because it is tissue tolerant and may be readily available as an off-the-shelf type of bone substitute. Additionally, it is osteoconductive and may be conveniently shaped into a variety of geometries at the time of surgery (36).

We believe that the biodegradable synthetic polymers such as PLA and PGA can be useful carriers for bone repair compounds. Therefore, in the next phase of maxillofacial bone repair experiments, synthetic polymers will be studied in combination with ossification inducing agents rather than calcification inducers such as the PL.

CONCLUSIONS

Evaluation of the hypothesis that a synthetic bone repair biopolymer of PLA:PGA plus PL could facilitate bony wound repair in rats and dogs was accomplished by histomorphometric, clinical, and radiographic techniques. The results of these evaluations indicate that the combination synthetic is superior to the plain copolymer in engendering bony regeneration in rats. In dogs, the combination material was useful in stimulating bony wound repair. Results from both experiments suggest that the synthetic material may be an alternative to the agents commonly employed for osseous repair and reconstruction.

BIBLIOGRAPHY

1. Tuli SM, Singh AD: The osteoinductive property of decalcified bone matrix. J Bone Joint Surg 60B:116-123, 1978.
2. Gregory CF: The current status of bone and joint transplants. Clin Orthop Related Res 157 259-273, 1981.
3. Urist MR: Practical applications of basic research on bone graft physiology, In Evans, B (editor): Instructional Course Lectures, Am Acad Orthoped Surg 25:1-26, The CV Mosby Co., St. Louis, 1976.
4. Osborn DB, Lilly GE, Thompson CW, Jost T: Bone grafts with surface decalcified allogeneic and particulate autologous bone:report of cases. J Oral Surg 35:276-284, 1977.
5. Mulliken JB, Glowacki J, Kaban LB, Folkman J, Murray JE: Use of demineralized allogeneic bone implants for the correction of maxillocraniofacial deformities. Ann Surg 194:366-372, 1981.
6. Gross BD, Nevins A, Laporta R: Bone induction potential of mineralized collagen gel xenografts for bone replacement. Oral Surg 49:21-26, 1981.
7. DeVore DT: Collagen heterografts for bone replacement. Oral Surg 36:609-615, 1973.
8. North AF, DeVore DT: Reconstituted collagen xenograft for the repair of oroparanasal defects:an experimental study. J Oral Surg 38:181-187, 1980.
9. Urist MR:Bone transplants and implants, In Urist, MR (editor): Fundamental and clinical bone physiology. J.B. Lippencott Co., Philadelphia, 1980, p357.
10. Cutright DE, Hunsuck EE: Tissue reaction to the biodegradable polylactic acid suture. Oral Surg 31:134-159, 1971.
11. Frazza E, Schmitt EE: The value of absorbable suture. J Biomed Mater Res 1:43-58, 1971.
12. Kulkarni RK, Pani KC, Neuman C, Leonard F: Polylactic acid for surgical implants. Arch Surg 93:839-843, 1966.
13. Cutright DE, Hunsuck EE, Beasley JD: Fracture reduction using biodegradable material, polylactic acid. J Oral Surg 29:393-397, 1971.

14. Cutright DE, Hunsuck EE: The repair of fractures of the orbital floor using a biodegradable material, PLA. J Oral Surg 33:28-37, 1972.
15. Getter L, Cutright DE, Bhaskar SN, Augsburgh JK: A biodegradable intraosseous appliance in the treatment of mandibular fractures. J Oral Surg 30:344-348, 1972.
16. Nelson JF, Stanford HG, Cutright DE: Evaluation and comparison of biodegradable substances as osteogenic agents. Oral Surg 43:836-843, 1977.
17. Olson RJ, Roberts DL, Osborn DB: A comparative study of polylactic acid, gelfoam and surgicel in healing extraction sites. Oral Surg 53:441-449, 1982.
18. Anderson HC: Introduction to the second conference on matrix vesicle calcification. Metab Bone Dis Rel Res 1:83-87, 1978.
19. Mulrad A, Bab A, Deutsch D, Sela J: Occurrence of actin-like protein in extracellular matrix vesicles. Calcif Tis Int 3(4):376-381, 1981.
20. Wuthier RE: A review of the primary mechanism of endochrondral calcification with special emphasis on the role of cells, mitochondria, and matrix vesicles. Clin Orthop Rel Res 169:219-242, 1982.
21. Vogel JJ, Boyan-Saylers BD: Acidic lipids associated with the local mechanisms of calcification, a review. Clin Orthop Rel Res 118:230-241, 1976.
22. Wuthier RE: Lipid composition of isolated epiphyseal cartilage cells, membranes, and matrix vesicles. Biochem Biophys Acta 409:128-139, 1975.
23. Boyan-Saylers BD, Boskey AL: Relationship between proteolipids and calcium phospholipid-phosphate complexes in Bacterionema matruchotii. Calcif Tis Int 30:167-174, 1980.
24. Ennever J, Boyan-Saylers BD, Riggan JL: Proteolipid and bone matrix calcification in vitro. J Dent Res 56:967-970, 1977.
25. Hollinger JO: In vivo calcification induced by a proteolipid complex (lysozyme-acidic phospholipid). Biomater Med Devices Artif Organs 10(2):71-83, 1982.
26. Schmitz JP, Hollinger JO: The critical size defect as an experimental model for cranio-mandibulofacial nonunions. Clin Orthop Rel Res, In Press, 1986.
27. Vogel JJ, Boyan-Saylers BD, Campbell MM: Protein-phospholipid interactions in biologic calcification. Metab Bone Dis Rel Res 1:149-153, 1978.
28. Yaari AM, Shapiro DM: Effect of phosphate and phosphatidyl serine-mediated calcium transport. Calcif Tis Int 34:43-48, 1982.
29. Bovey FA, Winslow FR: Macromolecules: An Introduction to Polymer Science, Academic Press, NY, 1979.
30. Chu CC: The in vitro degradation of poly (glycolic acid) sutures - effect of pH. J Biomed Mater Res 15:795-804, 1981.

31. Kronenthal RL: Biodegradable polymers in medicine and surgery. In Kronenthal RL, Oser Z, Martin E (editors): Polymers in Medicine and Surgery. Plenum Publishing Corp, NY, 1975, pp 119-137.
32. Williams DF, Mort E: Enzyme - accelerated hydrolysis of polyglycolic acid. J Bioengin 1:231-238, 1977.
33. Reddi AH, Huggins CB: Influence of geometry of transplanted tooth and bone on transformation of fibroblasts. Proc Soc Exp Biol Med 143:634-637, 1973.
34. Reddi AH, Huggins CB: Cyclic electrochemical inactivation and restoration of competence of bone matrix to transformed fibroblasts. Proc Natl Acad Sci USA 71:1648-1652, 1974.
35. Urist MR, DeLange RJ, Finnerman GAB: Bone cell differentiation and growth factors. Science 220:680-686, 1983.
36. Hollinger JO, Battistone, GC: Biodegradable bone repair materials: synthetic polymers and ceramics. Clin Orthop Rel Res, In Press, 1986.

SUPERCONDUCTING AUGMENTED RAIL GUN (SARG) (U)

*C. G. HOMAN
W. SCHOLZ
U.S. ARMY ARMAMENT RESEARCH AND DEVELOPMENT CENTER
CLOSE COMBAT ARMAMENTS CENTER
BENET WEAPONS LABORATORY
WATERVLIET, NY 12189-4050

INTRODUCTION

Electromagnetically launched (EML) projectiles offer the possibility of projectile muzzle velocities considerably greater than can be achieved with cannon or rocket technologies.

The most promising of EML concepts is the rail gun system due to its inherent simplicity. The development of rail gun technology, presently in its infant stage, presents many new problems which must be solved in order to complete its successful weaponization.

The major problem areas include system efficiency, Joule heating effects, switching, and power supplies. Secondary areas of concern include rail damage, projectile design, and structural integrity.

System efficiency represents the most important area since it impinges directly on all areas mentioned above as well as the important subsidiary requirements of reduction of system weight and size. Important developments have already been made on some portions of the rail gun system. The most notable in recent years is the development of compact homopolar generators (HPG). Improvements in HPG design have increased the energy stored/volume ratio by more than 30 times with a concomitant improvement in energy stored/mass ratios. Further increases in power supply performance are expected to increase these ratios by perhaps another factor of two. Thus, spectacular increases in system efficiency will occur in other portions of the rail gun system.

Figure 1 schematically suggests that such improvement might be sought in the rail gun (or barrel) itself. The rail gun represents the electromechanical load of the system and techniques must be found to increase

actual launch efficiency by increasing projectile velocity to barrel length, by increasing projectile velocity to launch current ratios, and by reduction of residual magnetic field losses at the completion of launch. Several designs have been proposed including segmented barrels and normal augmentation coils placed in series with rails. Such systems suffer from either increased difficulties of switching and timing (segmented) or increased demands on power supplies. Indeed, we have shown that normally augmented rail guns (NARG) have approximately the same efficiency as unaugmented guns under constant current operation. The increase in system performance by NARG systems is counterbalanced by increasing the source work (1).

The initial study of the application of superconducting principles to rail gun design clearly showed that quantum improvements could be achieved by adding an adjunct superconducting coil operating in the persistent mode and closely coupled magnetically with the normally conducting rails (1). Superconducting rails, which could have a significant effect in a space-based system but would present extraordinary commutation problems in a terrestrial system, were not analyzed. In this paper we will briefly describe the previous analyses (1-3), present new theoretical developments, and report on the development of the superconducting augmented rail gun (SARG) demonstrator at Benet Weapons Laboratory.

THEORETICAL ANALYSIS

The SARG concept uses the physical principle of magnetic flux trapping of a superconducting coil. This principle may be derived by the application of Faraday's law to a closed superconducting coil of length ℓ, i.e.,

$$\oint \underline{E} \cdot d\underline{\ell} = -\frac{d\phi}{dt} = 0 \quad \text{(Superconducting Coil)} \tag{1}$$

where $\underline{E}$ is the induced electric field and ϕ is the magnetic flux threading the area enclosed by the coil.

Equation (1) is only valid for a superconducting coil, since the resistivity of a superconductor is effectively zero. By comparison, the best normal conductor, copper, has a resistivity of the order of 10^{-6} ohm cm.

Using Eq. (1), we analyzed the SARG system shown schematically in Figure 1. For the constant rail current mode of operation, we were able to show that the mechanical energy W_M, the magnetic field energy W_m, and the work required from the electrical source W_S, could be expressed by (1)

$$W_M = \tfrac{1}{2} LI^2 + MII_{SO} - \tfrac{1}{2} \frac{M^2 I^2}{L_S} \tag{2}$$

$$W_m = \tfrac{1}{2} LI^2 - \tfrac{1}{2} \frac{M^2 I^2}{L_S} \tag{3}$$

$$W_S = LI^2 + MII_{SO} - \frac{M^2 I^2}{L_S} \tag{4}$$

In these expressions, L is self-inductance of the rail circuit; I is the normal current in the rail circuit; M is the mutual inductance between the rail and augmentation coils; I_{SO} is the initial supercurrent in the augmentation coil; and L_S is the self-inductance of the augmentation coil.

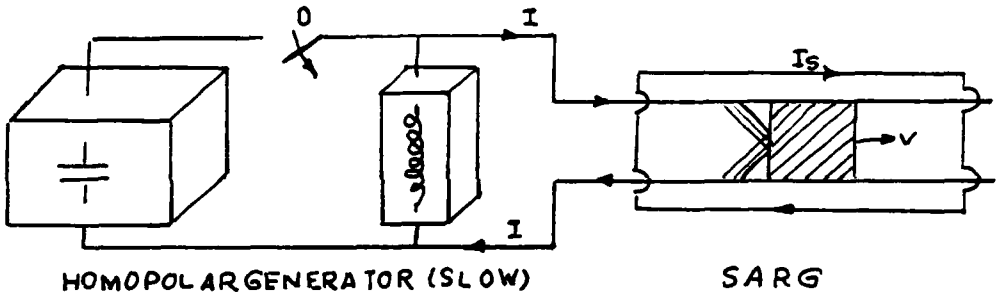

Figure 1. Schematic Circuit of Rail Gun With an Adjunct Superconducting Augmentation System (SARG).

Substitution of the relationship

$$M \equiv k\sqrt{LL_S} \tag{5}$$

in Eqs. (2) through (4) yields

$$W_M = \tfrac{1}{2} LI^2(1-k^2) + kII_{SO}\sqrt{LL_S} \tag{6}$$

$$W_m = \tfrac{1}{2} LI^2(1-k^2) \tag{7}$$

$$W_S = LI^2(1-k^2) + kII_{SO}\sqrt{LL_S} \tag{8}$$

where k is the magnetic coupling constant and $0 \leq k \leq 1.0$.

In the derivation of Eqs. (1) through (8), we have neglected the normal resistance of the rail circuit for mathematical convenience and for a clearer explanation of the physical principles involved.

By comparison, the simple unaugmented rail gun (SRG) operating under constant current conditions yields

$$W_M = \tfrac{1}{2} LI^2 \tag{9}$$

$$W_m = \tfrac{1}{2} LI^2 \tag{10}$$

$$W_S = LI^2 \tag{11}$$

If we define the ideal launch efficiency (ILE) as ILE = W_M/W_S, then

$$\text{ILE} = \tfrac{1}{2} \quad \text{(SRG)} \tag{12}$$

$$= \tfrac{1}{2} \frac{(1-k^2) + 2k\, I_{SO}/I\sqrt{L_S/L}}{(1-k^2) + k\, I_{SO}/I\sqrt{L_S/L}} \quad \text{(SARG)} \tag{13}$$

again, neglecting frictional and resistance effects. Figure 2 shows the variation of ILE as a function of k.

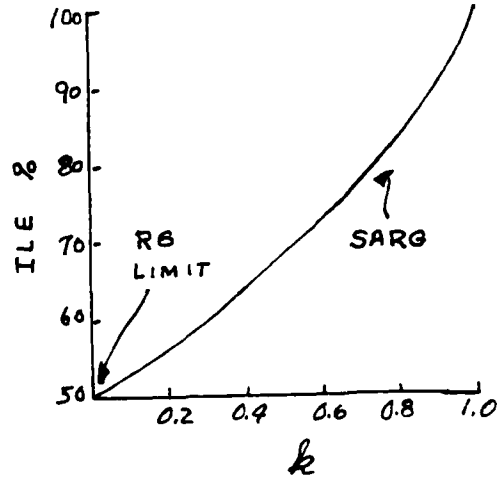

Figure 2. Variation of Ideal Launch Efficiency (ILE) as a Function of Magnetic Coupling Constant k for the Case When $I_{SO} = I$ and $L_S = L$.

So far we have dealt with ideal systems by neglecting resistance and frictional effects. We can adopt the procedure outlined by Hammond (4), i.e., the system is analyzed using idealized components and then the dissipating elements are introduced. For our particular system, we note that the idealized circuit of the simple rail gun is a linear circuit in which the magnetic and mechanical energy are each equal to half of the work supplied by the source at constant current. For a nonideal system, the frictional and resistive losses can be included as a part of kinetic energy W_M. Then we may write

$$W_M = \tfrac{1}{2} m_p v_p^2 + \frac{I^2 R \Delta t}{2} + f \tag{14}$$

where m_p and v_p are the projectile's mass and muzzle velocity, respectively; $R/2$ is the mean value of the total room temperature rail resistance; and Δt is the projectile transit time. The second term on the right of Eq. (14) is the energy loss due to current flow in the rails assuming no rail heating. The factor f contains dissipative terms due to rail heating, Joule heating, friction, etc., which are extremely difficult to analyze. Intuitively, we feel that the energy loss due to increased resistance and heat losses from rail heating will dominate f. The heating of the rails will vary as I^2, thus we expect that f will also vary as I^2 to a good approximation.

The actual launch efficiency (LE) defined as

$$LE \equiv \frac{\tfrac{1}{2} m_p v_p^2}{W_s} \quad \text{(SRG)} \tag{15}$$

can be determined experimentally. Thus using the experimental results of EMACK (5), we estimate that LE = 25 percent and we can find using Eq. (9) that

$$\frac{W_M}{2} \approx \tfrac{1}{4} LI^2 \approx \frac{I^2 R \Delta t}{2} + f \quad \text{(SRG)} \tag{16}$$

In order to extend this analysis to a SARG system, we note that the adjunct superconducting augmentation system is essentially nondissipative. We assume that a SARG launcher being powered at constant current from the power source will have a dissipative term

$$f_{SARG} = f_{SRG} \cdot \frac{(I_{SARG})^2}{(I_{SRG})^2} \tag{17}$$

and that an expression of the form of Eq. (16) may be written using the appropriate W_M (Eq. (6)).

This assumption cannot be justified on the basis of SARG being a linear circuit, since Eqs. (6) and (7) clearly show that equipartition does not occur in SARG. However, the magnetic energy of a SARG operating at constant current depends only on the specific inductances of the circuit and thus is a function of system geometries only. Therefore, the dissipative terms are clearly related to the kinetic energy team.

SARG DEMONSTRATOR

In order to demonstrate the principle of superconducting augmentation, Benet Weapons Laboratory (BWL) and Los Alamos National Laboratory (LANL) are collaborating in the construction and test of a SARG demonstrator.

LANL is constructing and testing a small rail gun system consisting of a 1 meter long, 3/8-inch square bore rail gun powered by a 5 Kv, 1444 μf capacitive energy source through a 6 μH pulse shaping inductance. A 4 gram projectile should reach a muzzle velocity of at least 600 m/sec in this gun. Beginning in March 1986, LANL is launching fifty projectiles at various power levels and measure muzzle velocities with flash x-ray techniques. Statistically significant velocity results will be reported for the various power levels.

Benet is modifying a 4 Tesla superconducting dipole magnet system, supplied by DOE from the ESCAR Magnet Program, to a warm bore configuration. The modified magnet coupled with Benet's 20 watt liquid helium (LHE) refrigerator system constitute the adjunct augmentation system. The augmentation system will be completed and tested in FY86.

The SARG system will be assembled from these components and tested in FY87. The assembled SARG will have relatively low magnetic coupling ($k \sim 0.4$) due to the particular design of the ESCAR magnet system. However, a properly designed SARG system discussed below should be able to achieve coupling constants greater than 0.9.

The present demonstrator system should yield a 50 percent increase in muzzle velocities and more than 50 percent increase in actual launch efficiencies at equivalent power supply levels.

Cryogenic testing of the ESCAR magnet system by DOE indicates cryogenic loads of less than 5 watts at 4.5 K using closed-cycle refrigeration and with heat loads approaching launch conditions. Thus, the capability of providing adequate refrigeration from small scale, commercially available

units is feasible. This point is central to the weaponization of SARG systems.

PROTOTYPE SARG WEAPONS

The weaponization of SARG launchers will require solutions to technical problems unique to these new systems. Benet is particularly concerned with those problems associated with direct fire or close combat weaponization. Typical specifications of such a system are shown in Table I.

TABLE I. TYPICAL SPECIFICATIONS FOR THE WEAPONIZATION OF A SARG LAUNCHER

Total Mass of Projectile and Sabot	> 3 kg
Projectile Muzzle Velocities	> 3 km/sec
Projectile Energy	> 13.5 MJ
Barrel Length	< 8 m
System Weight (including vehicle)	< 55 tons
Firing Rate	> 1 Hz

Additional problems associated with a SARG-type system include improvement in coupling coefficients, cryogenic requirements, superconducting magnet quench due to eddy current heating or exceeding the critical temperature, magnetic field or current of the superconductor used, and the mechanical integrity of the augmentation system itself.

A feasibility study was performed to determine if a SARG-type system could meet these specifications using existing technology. That is, what would be the most feasible configuration of a rail launcher using components and technologies presently available.

Before describing the results of the analysis, we will present some solutions to problems directly concerning SARG configurations.

The magnetic quenching of a properly designed superconducting coil occurs primarily by eddy current heating of the copper matrix material in commercially available superconducting wire. The present state of the art cable when ramped with current from an external source can sustain 60 Hz cycling without quenching. This translates into a half period of about 8 msec which represents the limit of its use in a rail gun application. Since transit times of the rail gun described here are in the order of 4 msec, use of a superconducting coil ramped with current from an external source is not possible with present technology.

However, in the SARG configuraiton, the augmentation coils are a closed loop with persistent supercurrents. Hence, SARG augmentation coils are ramped by the magnetic field of the rails. This is an entirely

different physical situation from current ramping. Unfortunately, no experimental data exists for this situation; however, considering the magnetic flux conservation stated in Eq. (1), one would expect that eddy current heating would be substantially reduced. Of course, a coil completely composed of superconducting filaments would have no eddy current heating. Coils made from commercially available cable require at least 10 percent of the cable volume to be copper matrix for conduction, fabrication, and mechanical reasons. The half period for magnetic ramping of a 90 percent superconducting - 10 percent copper matrix cable coil was estimated to be at least a factor of two less than the current ramp case (6). This estimate suggests a SARG-type system in which the supercurrent is ramped by the magnetic field of the rails may be marginally possible.

To further reduce the possibility of magnetic field ramp quenching, we analyzed the "ballasted" SARG circuit. The "ballasted" SARG is constructed by placing an additional superconducting coil in series with the augmenting coil which is <u>not</u> magnetically coupled with either the augmentation or rail coils. Such a configuration is shown schematically in Figure 3.

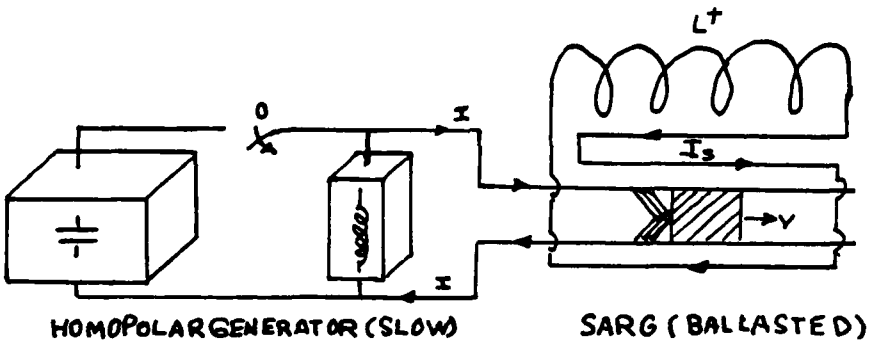

Figure 3. Schematic Circuit of "Ballasted" SARG.

Now the inductance of the superconducting circuit L^* is $L^* = L^+ + L_s$, where L^+ is the inductance of the "ballast" coil and L_s is the inductance of the augmentation coil. Also, if $L^+ >> L_s$, then

$$L^* = L^+ + L_s >> L_s \tag{18}$$

and

$$M = k\sqrt{LL_s} \tag{19}$$

We have previously shown (1) for the "ballasted" SARG that

$$W_M = \tfrac{1}{2} LI^2 + LII_{so}\frac{M}{L} = \tfrac{1}{2} LI^2\left[1 + \frac{2I_{so}}{I} k\sqrt{\frac{L_s}{L}}\right] \quad (20)$$

$$W_m = \tfrac{1}{2} LI^2 \quad (21)$$

$$W_s = LI^2 + LI_{so}I\frac{M}{L} = LI^2\left[1 + \frac{I_{so}}{I} k\sqrt{\frac{L_s}{L}}\right] \quad (22)$$

Evaluation of the supercurrents shows

$$(I_s)_{SARG} = I_{so} = \frac{IM}{L_s} \quad (23)$$

and

$$(I_s)_{BALLASTED\ SARG} \approx I_{so} \simeq \text{Constant} \quad (24)$$

Thus, the ramping of the supercurrent which occurs in SARG may be significantly reduced in the ballasted SARG condition.

In order to evaluate the three systems involved, we used the procedure outlined in Eqs. (14) through (17) to determine f for each system; Eqs. (6) through (8) for SRG; Eqs. (9) through (11) for SARG; and Eqs. (20) through (22) for the "ballasted" SARG to determine system parameters. Assuming a constant projectile energy of 14 MJ, these parameters are tabulated in Table II.

TABLE II. RESULTS OF THE THEORETICAL ANALYSES OF THREE CONFIGURATIONS OF RAIL LAUNCHERS (RAIL GUN, SARG, AND BALLASTED SARG). THESE CALCULATIONS WERE PERFORMED HOLDING PROJECTILE VELOCITY CONSTANT.

	I(MA)	I_{so}(MA)	$\frac{1}{2}m_p v_p^2$(MJ)	$I^2R\Delta t/2+f$ (MJ)	W_m(MJ)	W_s(MJ)	Act Eff %
Rail Gun	3.9	NA	14	14	28	56	25
SARG	3.1	0.61	14	8.5	3.2	25.7	54
Ballasted SARG	2.2	0.44	14	4.2	8.6	26.8	52

In these calculations, we assumed that I was constant, $L = 3.6\times10^{-6}$ Henry, $R = 2.4\times10^{-4}$ ohms, and the transit time Δt = 4 msec from the

experimental EMACK test results (5). In addition, we assumed the conservative values of k = 0.9, L_s = 10 L, and I = 5 I_{so} for the augmentation system.

These results indicate that the actual efficiency of an augmented system is more than twice that of a simple rail gun. The ballasted SARG is the superior design for the following reasons.

1. The current required is 30 percent less than SARG and 44 percent less than SRG. Thus, heating loads and cooling requirements are significantly lowered.

2. For approximately the same size source and efficiencies, the ballasted SARG has significantly higher magnetic field energy than SARG which must be dissipated. However, this energy is dissipated after launch and may be more efficiently disposed in either a properly designed muzzle resistor or may actually be partially recovered. The magnetic field energy is only 30 percent of the SRG configuration.

It is important to note that the kinetic energy used is sufficient to launch penetrator type projectiles (3 kg) at velocities greater (3 km/sec) than achievable by current cannon.

Some important tradeoffs must be considered. For example, the increased complexity of superconducting coil and cryogenic requirements for the augmented systems are offset by increased efficiency and lower rail heating.

The increased efficiency means that smaller homopolar generators (or other power supplies) may be used to power the launcher system. Present HPG's weigh, with their ancillary equipment, approximately five tons and can deliver about 1 MA to a rail gun system load. Thus the power supply requirement, assuming an increase in HPG efficiency of 25 percent would lead to power supply weights of over 15 tons for an SRG and over 12 tons for SARG, compared to about 9 tons for the ballasted SARG case.

One must consider the additional weights of the augmentation system including the cryogenic and power modules. From our preliminary experimental results on the SARG demonstrator, we can estimate cooling loads of about 10 watts at 4.5 K. Thus, the ancillary equipment to the augmented systems should weigh less than two tons.

The weight of the augmentation ancillary equipment will be offset by the reduced cooling requirement of the rail gun when operated in these modes, since less than 30 percent of the waste heat generated by an SRG launch is developed in a ballasted SARG launch.

CONCLUSION

Application of superconducting technology to the augmentation of simple rail guns can yield significantly improved efficiency. This improvement is achieved by reducing both the magnetic field normally dissipated at the end of launch and the barrel Joule heating losses.

This study also indicates that it is practical to achieve weapon quality launchers using current state of the art technology with mobile gun systems.

REFERENCES

1. C. G. Homan and W. Scholz, "Evaluation of Superconducting Augmentation on a Rail Gun System," ARRADCOM Technical Report No. ARLCB-TR-83016, Benet Weapons Laboratory, Watervliet, NY, June 1983.

2. C. G. Homan and W. Scholz, "Evalulation of Superconducting Augmentation on Rail Gun Systems," IEEE Trans. on Magnetics, Mag-20, 1984, p. 366.

3. C. G. Homan and W. Scholz, "Application of Superconductivity to Pulse Power Problems," Proceedings of the Fourth IEEE Pulsed Power Conference, (T. H. Martin and M. F. Rose, eds.), 1983.

4. P. Hammond, Energy Methods in Electromagnetism, Clarendon Press, Oxford University Press, NY, 1981, Chapter 6.

5. D. W. Deis and D. W. Scherbarth, "EMACK Electromagnetic Launch Commissioning," IEEE Trans. on Magnetics, Mag-20, 1984, p. 245.

6. T. Pollock, Private Communication, Intermagnetics General Corporation, Guilderland, NY, 1986.

CATALYTIC AIR PURIFICATION FOR COLLECTIVE PROTECTION

*CHEN C. HSU, DR.
JOSEPH V. PISTRITTO, MR.
U.S. ARMY CHEMICAL RESEARCH AND DEVELOPMENT CENTER
ABERDEEN PROVING GROUND, MD 21010-5423

ASC whetlerite charcoals and other modified forms have been used exclusively in the military environment since World War II [1]. Because of the weaknesses associated with ASC whetlerite carbon such as finite life time, rapid degradation under hot and humid conditions, and desorption of toxic gases and vapors, fundamental studies and engineering tests on ASC whetlerite charcoals have been attempted to improve their performance. Parallel to this effort, alternative means for air purification by using modern technology have been sought. Between 1961 and 1966, Philco/Ford Motor Company and AiResearch Manufacturing Company [2-3] were awarded two research contracts by the U.S. Army to study the catalytic and thermal decomposition of toxic agents. The first phase of these contracts involved the development of the catalyst Pt/Al2O3 and kinetic and mechanistic studies of thermal and catalytic decomposition of DMMP. The second phase of the work was extended to GB, HD, and VX. Results from this study indicate that complete catalytic decomposition of GB and HD was achieved at temperatures around 673 K and 548 K, respectively. In the absence of a catalyst the thermal decomposition took place at temperatures higher than 673 K and 548 K, respectively. More importantly, it demonstrated a complete destruction of GB for 82 hours at concentrations of 10, 40, and 120 microgram/l at 400 CFM flow rate [4]. Four albino rats survived on the air purifier discharge during the 82-hour continuous endurance test [4].

A survey was recently conducted by Life Systems, Inc. to assess the feasibility of various methods of air purification for their Chemical Agent Removal Subsystem (CARS) [5].

Results of this assessment indicate that in addition to cyclic regenerative adsorption (temperature swing and pressure swing adsorption) of ASC whetlerite charcoals, two other methods of air purification were identified to have a high probability of success. They are, in order of decreasing probability, catalysis and plasma discharge. The U.S. Army has been pursuing the application of these three methods to air purification. Following this direction, a literature survey was conducted to identify the catalysis technology developed for air purification in the period from 1966 to the first quarter of 1983 [6].

Two important catalytic processes are considered essential to catalytic air purification: dealkylation and oxidation. Catalytic dealkylation, also known as catalytic cracking, involves a chemical process to break up large molecules into small fragments on the active acidic sites of dealkylation catalysts, i.e., alumina, alumina-silica, and silica-magnesia, etc. An example of such a reaction can be illustrated by the catalytic dealkylation of isopropyl methylphosphonofluoridate (GB or Sarin) with Pt/Al2O3 catalyst at 673 K, in which GB is broken into smaller molecules such as methylphosphonofluoridic acid and propylene. Such a process may be very useful for air purification provided that these smaller molecules possess less toxicity than the precursor. Catalytic oxidation, including catalytic combustion, on the other hand, involves a chemical process facilitating oxidation reactions between oxidizable materials and oxygen molecules. Examples of the catalytic oxidation reaction are as follows [2].

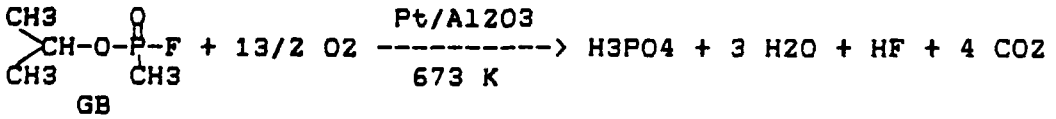

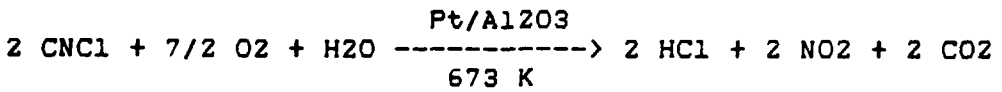

The above chemical equations clearly illustrate that catalytic oxidation reactions bring about oxidation products notably smaller in molecular size and lesser toxicity in all cases.

As promising as the catalytic air purification system appears, improvement is needed in two major areas: the reduction of the light-off temperature and the increase of the life of catalysts [7]. To the former, an Army contractor is conducting the development of low-temperature oxidation catalysts, to the latter, we are performing investigations into the catalyst deactivation mechanisms. The following is a summary of the recent progress in these areas.

CATALYTIC DECOMPOSITION EFFICIENCY OF HAZARDOUS CHEMICALS

Catalytic decomposition efficiency was determined using commercially available oxidation catalysts and experimental oxidation catalysts being developed by Signal Research Center under an Army contract. The details of the evaluation of these catalysts are as follows.

(a) Commercial Oxidation Catalysts - while low-temperature (<250°C) oxidation catalysts are being developed, the commercial oxidation catalysts such as those used in the auto catalytic converter were evaluated with simulants. An oxidation catalyst manufactured by Degussa Corporation in New Jersey was tested with dimethyl methylphosphonate (DMMP) with a concentration of 100 ppm. The catalyst used for this evaluation contains 0.16 wt% Pt and 0.01 wt% Rh supported with alumina. The DMMP vapor was generated from an influent supply unit of an automated catalyst evaluation system constructed by Life Systems, Incorporated, in Ohio. The flow rate of the reactants (mixture of DMMP and dried air) was 27 l/min and the reaction temperature was controlled at 400°C. The influent and effluent gas species were analyzed alternately by an automated valving system installed on a Hewlett Packard gas chromatograph (GC) system model 5790A. Simultaneously, the influent and effluent gases were collected in gas cells and analyzed by Fourier transform infrared spectrometer (FTIR) for species identification. The results of the tests indicated that a decomposition efficency of 96% of DMMP was achieved during the first 18 hours of reaction [8].

(b) Experimental Oxidation Catalysts - Signal Research Center in Illinois, formerly UOP, Inc., is under an Army contract to develop low-temperature (<250°C) oxidation catalysts. The main objectives of this contract are to reduce the light-off temperature below 250°C, to abate the vulnerability of S, P, and halogens poisoning, and to increase the ease of catalyst regeneration. At the present time, a literature search and the first series of tests of the new catalysts are complete. From the results of the literature search, Pt was selected as the active metal, gamma alumina, chemically modified alumina, and titania as washcoats, and the straight-channel monolith with the density of 400 and 600 cell/in^2 as the catalyst support. Five catalysts were prepared based on the parameters mentioned above with high and low Pt content. Initially, the prepared catalysts were tested against four chemicals simultaneously at a flow rate of 1 l/min, 250°C at 5 and 90% relative humidity (RH). The concentrations of the four chemicals were 10, 1000, 30, and 10 ppm for DMMP, hydrogen cyanide (AC), cyanogen chloride (CK), and phosgene (CG), respectively. Based on the test results, two best catalysts, high Pt content with 600 cell/in^2 monolith support and with either chemically modified alumina (CMA) or titania washcoat, were selected. These two catalysts were further tested with three chemicals (AC, CG, and CK) separately at 75, 150, and 250°C with 5 and 90% RH. The conclusions from the individual chemical tests can be summarized as follows [9].

(1) Both catalysts completely decomposed CG at 150 and 250°C; however, only CMA completely destroyed CG at 75°C. The results of effluent analyses using GC/MS and ion chromatography inidicate that the probable destruction was due to catalytic hydrolysis which formed carbon dioxide and hydrogen chloride.

(2) Both catalysts completely decomposed CK at 150 and 250°C, but only titania was highly effective (>97%) over 2 hours at 75°C. The results of effluent analyses also indicated that CK destruction was due to catalytic hydrolysis which formed carbon dioxide and ammonium chloride.

(3) Titania was much more effective than CMA for AC destruction at 250°C with 90% destruction efficiency for 2-hour reactions at 90% RH and greater than 60% efficiency at 5% RH. The results of effluent analyses indicated that carbon dioxide and nitrogen were formed from the catalytic reactions.

These two selected catalysts were subjected to deactivation tests at 250°C and 5 and 90% RH. The test results are summarized as follows:

(1) Both catalysts maintained at least 93% DMMP conversion at 90% RH after 6 hours of continuous test.

(2) CMA maintained about 86% DMMP conversion at 5% RH after 6 to 8 hours of test.

(3) Titania catalyst showed AC conversion greater than 88% for 8 hours at 90% RH and 250°C.

The conclusion from these deactivation tests can be stated (a) at low humidity and 75°C, CMA was superior to titania catalyst for DMMP conversion, and (b) at high humidity and 250°C, titania was better than CMA catalyst for DMMP conversion.

Based on the test results for the catalysts being developed we arrived at the following conclusions: (1) Pt on CMA is superior to the titania catalyst at low humidity for DMMP conversion, (2) Pt on titania is superior for AC and DMMP conversion at high humidity, (3) both catalysts are effective for hydrolytic decomposition of CG and CK, (4) AC is hydrolyzed and oxidized by both catalysts, and (5) DMMP is partially oxidized by both catalysts. It should be noted that the catalyst with low Pt content and alumina washcoat representative of the catalyst developed during the 1960's was least effective in destruction efficiency when compared with other catalysts being developed.

ELUCIDATION OF CATALYST DEACTIVATION MECHANISMS

Although the above catalytic reactions were well studied, because of the emphasis on the evaluation of the decomposition

efficiency, data on the formation of transient species were not available. This prevents detailed analyses of catalytic reaction kinetics and mechanisms. Such information, however, is important for the understanding of deactivation mechanisms which is the key to the catalyst optimization. Recent advances in laser spectroscopy allow one to detect transient species in catalytic reactions, including both fluorescing and non-fluorescing radicals [10-12]. We have used laser-induced fluorescence (LIF) and multiphoton ionization/mass spectrometry (MPI/MS) techniques for the detection of the transient and stable products from the reaction of DMMP and trimethyl phosphite (TMP) on Pt and Pt/Rh (90/10%) surfaces in the temperature range of 1100 - 1300 K. The free radicals PO and OH (with addition of oxygen) were observed by LIF [13-16]. The desorption activation energies for PO from Pt and Pt/Rh surfaces were determined for the first time to be 59±2 and 50±2 Kcal/mole, respectively. The activation energy of PO from the Pt surface is comparable to that of NH desorption (66 Kcal/mole) [17]; however, it is twice that of NO desorption from Pt single crystal surfaces [18-20]. These high activation energies are related to the cause of phosphorus deactivation of the catalyst. The MPI/MS study revealed no methyl radical formation. Electron impact/mass spectrometry (EI/MS) showed the formation of CO and water with a trace amount of carbon dioxide from the catalytic reactions of DMMP and TMP on Pt and Pt/Rh surfaces [15]. A brief description of the experiment follows.

The experimental apparatus and procedure used in this work have been described previously in detail [10-11]. Briefly, PO and OH radicals desorbing from the Pt and Pt/Rh surfaces were detected by means of resonance LIF using a CMX-4 flashlamp pumped tunable dye laser. The B-X transition in PO was excited by the laser operating with Rhodamine 640, frequency doubled into the 325 nm region. The fundamental output of the laser was removed by a copwing 7-59 filter. The laser beam entered and exited the cell through long baffled sidearms with Brewster windows designed to minimize scattered light. LIF from the region 2 cm below the catalyst was passed through a Corning 7-60 filter and focused onto an RCA 31034 photomultiplier. The laser beam exiting the cell was detected by a photodiode whose output was used to monitor laser energy

and to trigger the detection electronics. Both these outputs were displayed in real time and averaged in a dual channel Nicolet 1174 signal averager. Typically, 128 laser shots were integrated and then the laser power was accumulated.

For the LIF measurement of PO, the laser was tuned to the vicinity of the known 325 nm Q-branch bandhead of the B-X transition [21] and then fine tuned for maximum signal. Similarly, for the OH measurement the laser was tuned to the A-X transition at 308 nm [21].

The Pt (99.99% pure) and Pt/Rh wire catalysts, 20 cm long and 0.5 mm in diameter, were coiled flat spirals suspended approximately 1 cm below the gas inlet and 2 cm above the laser beam. Temperature of the catalysts was controlled by passing a variable current through the wire. The current through and voltage drop across the wire were measured to determine the wire's resistance at a given current. The ratio of this resistance to that at room temperature (measured and calculated) was then compared with the literature to determine the temperature at a given current.

The Pt and Pt/Rh wire catalysts was activated prior to each experiment by a vacuum bakeout at about 1300 K followed by passage of several torr of oxygen over the Pt and Pt/Rh surfaces for several minutes at comparable temperature. This reactivation was found to be essential for significant signal to be observed.

DMMP (Aldrich, 97% pure) and TMP (Aldrich, 99+% pure) were used after trap-to-trap distillation. Both compounds were diluted in Ar (typically 0.005%) at least 24 hours before use to allow for complete mixing. In the desorption activation energy measurements, experiments typically a 3 torr background pressure of Ar was established with 25-100 mtorr of the diluted sample then added. Mixing occurred about 50 cm from the cell in a metal line heated to about 323 K. This was necessary to facilitate the flow of DMMP which sticks to the walls of inlet tubings.

Based on the experimental results described above, the possible catalytic decomposition mechanisms of DMMP and TMP on Pt and Pt/Rh surfaces can be represented as follows.

$$\underset{\text{DMMP}}{(CH_3O)_2CH_3PO(a)} \longrightarrow 2CH_3O(a) + CH_3(a) + PO(a) \quad (1)$$

$$\underset{\text{TMP}}{(CH_3O)_3P(a)} \longrightarrow 3CH_3O(a) + P(a) \quad (2)$$

$$\longrightarrow 2CH_3O(a) + CH_3(a) + PO(a) \quad (2a)$$

$$CH_3O(a) \longrightarrow CO(g) + 3H(a) \quad (3)$$

$$CO(a) \longrightarrow CO(g) \quad (4)$$

$$CH_3(a) \longrightarrow C(a) + 3H(a) \quad (5)$$

$$PO(a) \longrightarrow PO(g) \quad (6)$$

Addition of oxygen effectively generates O(a), leading to the occurrence of the following key oxidation processes:

$$CO(a) + O(a) \longrightarrow CO_2(a) \longrightarrow CO_2(g) \quad (7)$$

$$H(a) + O(a) \longrightarrow OH(a) \quad (8)$$

$$OH(a) + H(a) \longrightarrow H_2O(a) \longrightarrow H_2O(g) \quad (9)$$

$$OH(a) \longrightarrow OH(g) \quad (10)$$

$$PO(a) + (X-1)\,O(a) \longrightarrow POx(a) \quad (11)$$

Since PO was detected weakly and only for a short period after the introduction of TMP into the system with a freshly cleaned Pt wire catalyst, reaction (2a) is believed to be a major channel of the TMP decomposition reaction which effectively deposits P on the catalysts resulting in the elimination of active sites. This is also supported by the fact that TMP can be used as a source of P for InP semiconductor preparation [22]. The presence of P on the Pt and Pt/Rh surfaces was also substantiated by the appearance of PO LIF-signals when oxygen was admitted to the system after TMP was completely shut off and pumped out.

AD-A173 639 PROCEEDINGS OF THE ARMY SCIENCE CONFERENCE (1986) HELD 2/4
AT WEST POINT NEW.. (U) DEPUTY CHIEF OF STAFF FOR
RESEARCH DEVELOPMENT AND ACQUISITIO.. 20 JUN 86
UNCLASSIFIED F/G 5/2 NL

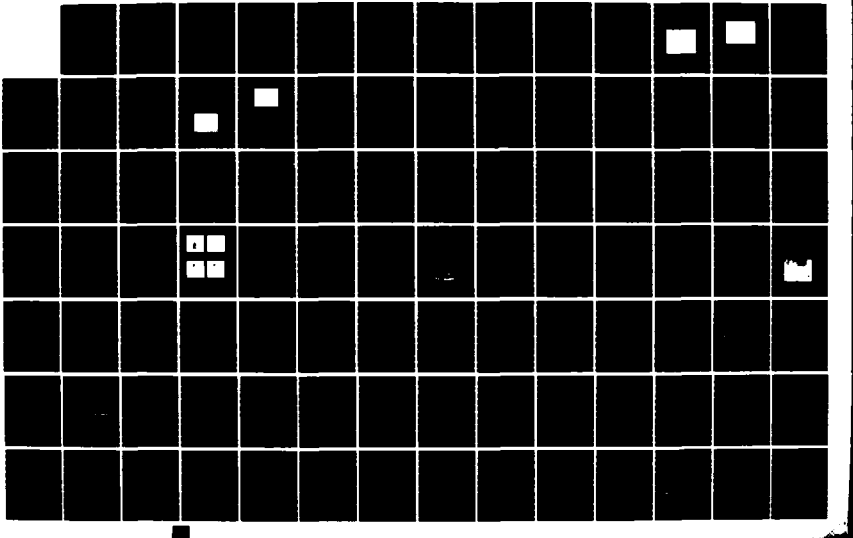

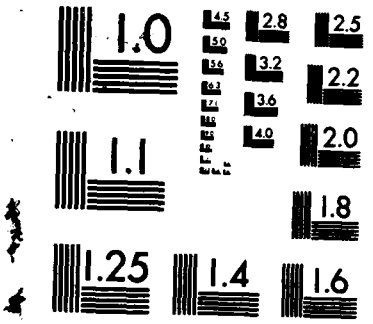

MICROCOPY RESOLUTION TEST CHART
NATIONAL BUREAU OF STANDARDS-1963-A

The production of CO and water on the EI/MS data had apparent activation energies of 9 and 15 Kcal/mole respectively over the Pt/Rh catalyst. Carbon dioxide production was temperature independent at the test temperature. However, neither the formation of methoxy radical by LIF nor the formation of methyl radical by MPI/MS was detected through an extensive search, indicating that either Pt-methyl and Pt/Rh-methyl radical bonding is too strong to desorb or the methyl radicals on the Pt or Pt/Rh surfaces react with the adsorbed H atoms.

DISCUSSION

The success of catalytic air purification development is largely dependent on the reduction of the light-off temperature to increse the catalytic activity and of the poisoning effect to alleviate the risks associated with logistics and safety and to prolong the life of catalysts. It appears that the first objective has been achieved by comparing the performance of the catalyst developed in the 1960's with the newly developed catalysts [9]. Although P poisoning mechanisms were elucidated [13-16], poisonings due to S and halogens are yet to be studied. The understanding of the deactivation mechanisms will enable design of either a chemical process for catalyst regeneration or a chemical scrubber system in the upstream before a catalytic reactor. In light of the potential threat of the penetrants of the carbon filter from our adversaries, catalytic air purification systems indeed represent one of the best alternatives for collective protection.

CONCLUSIONS

Two new oxidation catalysts, one with CMA washcoat and the other with titania washcoat in conjunction with high Pt content and 600 cell/in^2 monolith support, have shown high destruction efficiency of AC, CG, CK, and DMMP at temperatures equal to or lower than 250°C. Such a performance efficiency has surpassed the performance of the catalysts developed in the 1960's.

In the study of catalyst deactivation, PO radicals were detected during the catalytic decomposition of DMMP and TMP over Pt and Pt/Rh wire catalysts above 1100 K by laser-induced fluorescence. The detection of the PO radical clearly indicates that both compounds can be effectively destroyed by the Pt and Pt/Rh catalysts at elevated temperatures. The activation energies for the desorption of PO from Pt and Pt/Rh surfaces were determined for the first time to be respectively 59±2 and 50±2 Kcal/mole. These high desorption energies of PO radicals account for the P deactivation.

MPI/MS and EI/MS studies identified CO, water, and carbon dioxide as catalytic reaction products. Combining all the results obtained, the decomposition mechanisms including the P deactivation mechanisms of DMMP and TMP were proposed.

The concept of using catalytic oxidation for air purification was demonstrated to be feasible in the 1960's [4]. Such feasibility was further strengthened by the recent efforts to increase the competitiveness to the carbon filtration systems in terms of lowering the light-off temperature and increasing the life of catalysts [8-9,13-16]. In view of the indiscriminatory destruction capability and efficiency along with the potential threat due to the penetrants of the carbon filter being developed by our adversaries, catalytic air purification systems are indeed considered one of the best alternatives for collective protection.

ACKNOWLEDGMENTS

Dr. George R. Lester of Signal Research Center, Illinois, Drs. Ming C. Lin and Charles S. Dulcey of Naval Research Laboratory, Washington, DC, and Mr. Bruce Fauth of the Military Academy, West Point, New York, are gratefully acknowledged for their contributions to the new oxidation catalyst development, cooperative work in elucidating the catalyst poisoning mechanisms, and evaluating the commercial oxidation catalysts, respectively.

REFERENCES

[1] Summary Technical Report of Division 10, Vol. 1, "Military Problems with Aerosols and Non-Persistent Gases," 1946.

[2] F. J. Cheselske, A. Wheeler, S. W. Weller, R. W. Baier, P. H. Dutch, and F. B. Weiler, "Study of Catalytic and Thermal Decomposition of Toxic Agents," Contract DA18-035-AMC-279(A), Final Report, Book 1, CB-67-2378-10.1, October 1970.

[3] R. W. Baier, W. M. Graven, H. D. Linhardt, R. C. Oliver, D. L. Peters, and S. W. Weller, "Feasibility Study of Catalytic Methods of Air Purification," Final Report, Publication No. C-2767, Philco/Ford Motor Company, Contract DA-18-108-CML-6671(A), 26 August 1964.

[4] R. R. Steves, "Design, Fabrication, and Evaluation of First 400 CFM Catalytic Air Purifier Model," Contract DA18-035-AMC-279(A), Book 1, CB-67-2378-12.1, March 1971.

[5] M. Manning, "Evaluation of Thermal Methods for Use in the CARS," Task Assignment Report, ICAIR Task Assignment No. 118, ICAIR Systems Division, Life Systems, Inc., 1981.

[6] C. C. Hsu and J. V. Pistritto, "Air Purification By Catalysis - A Literature Survey," Proceedings of the 1983 Scientific Conference on Chemical Defense Research, Aberdeen Proving Ground, MD, 15-18 November 1983.

[7] J. W. Milius, J. S. Greer, and A. J. Juhola, "Advanced Collective Protection System Design Studies," Final Comprehensive Report, Mine Safety Appliances Company, ED-CR-74016, Contract DAAA15-71-C-0498, July 1974.

[8] C. C. Hsu and J. V. Pistritto, "Analysis of Catalytic Oxidation Products with FTIR," SPIE, Vol. 553, 1985 Fourier and Computerized Infrared Spectroscopy (1985).

[9] G. R. Lester, "The Development of Oxidation Catalysts for Air Purification," presented at the 1985 Scientific Conference for Chemical Defense Research, Aberdeen Proving Ground, MD, 19-22 November 1985.

[10] L. D. Talley and M. C. Lin, "Laser Diagnostics of OH Radical Formation in the H2 + N2O Reaction on Pt," AIP Conf. Proc., vol. 61, Aspects of the Kinetics and Dynamics of Surface Reactions, p. 297 (1980).

[11] G. S. Selwyn, G. T. Fujimoto, and M. C. Lin, "Catalytic Removal of NH and NH2 Free Radicals by Polycrystalline Pt and Fe Surfaces," J. Phys. Chem. 86, 760-765 (1982).

[12] T. G. DiDluseppe, J. W. Hudgens, and M. C. Lin, "Multiphoton Ionization of CH3 Radicals In The Gas Phase," J. Phys. Chem. 86(1), 36-41 (1982).

[13] C. C. Hsu, J. V. Pistritto, C. S. Dulcey, and M. C. Lin, "Catalytic Removal of Dimethyl Methylphosphonate Studied by Laser Induced Fluorescence," Proceedings of the 1984 Scientific Conference for Chemical Defense Research, Aberdeen Proving Ground, MD, 13-16 November 1984.

[14] C. C. Hsu, C. S. Dulcey, and M. C. Lin, "Thermal Desorption of PO Radicals from Polycrystalline Pt Surfaces in the Catalytic Decomposition of Dimethyl Methylphosphonate and Trimethyl Phosphite," the Ninth North American Meeting of the Catalysis Society, Abstract, Houston, Texas, 17-21 March 1985.

[15] C. S. Dulcey, C. C. Hsu, J. V. Pistritto and M. C. Lin, "The Catalytic Removal of DMMP and TMP Studied by Laser Induced Fluorescence and Multiphoton Ionization-Mass Spectrometry," Proceedings of the 1985 Scientific Conference on Chemical Defense Research, Aberdeen Proving Ground, MD, 19-22 November 1985.

[16] C. S. Dulcey, M. C. Lin, and C. C. Hsu, "Thermal Desorption of the PO Radical from Polycrystalline Pt Surfaces," Chem. Phys. Lett. 115(6), p. 481 (1985).

[17] G. S. Selwyn and M. C. Lin, "Production of the NH Radical from the Catalytic Decomposition of NH3 on Polycrystalline Pt and Fe Surfaces at High Temperatures," Chem. Phys. 67, 213-220 (1982).

[18] J. L. Gland and B. Sexton, "NO Adsorption on the Pt(111) Surface," Surf. Sci. 94, 355 (1980).

[19] J. A. Serri, M. J. Cardillo and G. E. Becker, "A Molecular Beam Study of the NO Interaction with Pt(111)," J. Chem. Phys. 77, 2175 (1982).

[20] C. T. Campbell, G. Ertl and J. Segner, "A Molecular Beam Study of the Interaction of NO with a Pt(111) Surface," Surf. Sci. 115, 309 (1982).

[21] M. A. Clyne, "Laser-Induced Fluorescence Electronically Excited States of Small Molecules," in Dynamics of the Excited States, Ed. K. P. Lawley, John Wiley & Sons, 1982.

[22] Patent by Nippon Telegraph and Telephone Public Corp. Chem. Abs. 96, 498 (1982).

IYER

RADIATION CASTING OF ENERGETIC MATERIAL FORMULATIONS WITH BINDERS

SURY IYER, DR.
ENERGETICS AND WARHEADS DIVISION, ARMAMENT ENGINEERING DIRECTORATE
US ARMY ARMAMENT RESEARCH AND DEVELOPMENT CENTER, DOVER, NJ 07801-5001

INTRODUCTION

Present energetic material cast loading procedures in munitions involve multiple steps and slow cooling. Charges produced using this process still develop defects and separation from the casing.

In order to eliminate the above shortcomings, there exists a need to search for new loading and processing methods which are simple and will provide better charge quality. Radiation casting (or radiation curing) is one process with such potential.

Casting of energetic material slurries with liquid monomer (or semifluid prepolymer) binders can be accomplished using penetrating radiation. Radiation causes polymerization and cross-linking of the fluid binder and provides a rigid cast. Radiation curing is new in energetic material technology and shows good promise for useful applications. During the course of this work, it was also found to be scientifically challenging (see below).

The feasibility of this method was demonstrated (1, 2) by incorporating 1,3,5-trinitro-1,3,5-triaza-cyclohexane (RDX) in a polymethylmethacrylate (PMMA) matrix via x-irradiation of methylmethacrylate (MMA) in a slurry with RDX. Similarly by employing gamma-radiation, rigid casts of RDX-PMMA and RDX-trimethylolpropane trimethacrylate (TMPTM) polymer were obtained.

The radiation curing of monomeric binders in presence of energetic materials containing nitro groups posed a scientific challenge to accomplish (2). For example, MMA in slurries with RDX particles could not be polymerized using radiation, the reason being that the nitro explosive compounds are good radical inhibitors and free radicals are intermediates in polymerization. After several studies the problem was overcome

by the following technique, viz., by providing a protective coating consisting essentially of a polyhydric alcohol (e.g. glycerol) on RDX particles. It is believed that the polyhydric alcohol ties up the nitramine groups via hydrogen bonding and thereby renders them inactive for inhibiting the radiation polymerization process. Any chosen coating substance for the energetic material should be, of course, insoluble in the monomer being polymerized.

Various energetic material and binder systems were investigated using the radiation curing method. Thus, RDX was successfully radiation cured with energetic liquid mixtures containing radiation polymerizable monomers. High velocity burn rate propellant Hivelite was found to cure well with MMA. Other energetic materials have also been found to be radiation curable with monomers. Furthermore, new diacetylenes containing energetic nitro groups were developed as binders for energetic materials. BKWR-thermo-hydrodynamic equation of state calculations (TIGER Code) were performed on HMX with cured energetic liquid binder mixtures. In addition, an 80/20 slurry of RDX/MMA was successfully in-situ radiation cured in an M42 shaped charge munition. The cured cast was examined by remote sectioning of the munition. This paper describes the details of these results.

Radiation curing provides several benefits (3). It can be performed at ambient or subambient temperatures. This is important for energetic materials which are sensitive to heat. Since the material to be cured can be exposed to or removed from the radiation field at will, it provides a good control to the curing process. For those systems where short "pot life" is a problem when cured conventionally (using heat and catalyst), radiation helps to provide indefinite pot life by virtue of the fact that no reaction occurs when there is no radiation field. Also, radiation leaves no catalyst residues (since no catalyst is used) as in a thermal process. Penetrating radiation, e.g., x-rays or gamma-rays, goes through the entire depth in a bulk and brings about polymerization in spatial uniformity. This makes the creation of any localized hot regions (arising out of the exothermic polymerization reaction) less likely than in a catalyst induced thermal process.

Radiation curing has been shown (3, 4, 5) to produce a stronger bond between polymer binder and filler than chemical curing. Thus in glass-fiber resin binder systems, it produces a stronger adhesion bond and increases the tensile strength of cured systems by a factor of up to 2.8 (4). In concrete-polymer composites (MMA, trimethylolpropane trimethacrylate, styrene) it provides 12-38% increase in compressive strength and similar increases in tensile strength and elastic modulus as compared with chemically cured systems (5).

EXPERIMENTAL SECTION

Radiation Sources

Both x-rays and gamma-rays were employed for curing. X-rays were generated from a Norelco MG 150 Industrial x-ray unit equipped with a 150 kV beryllium window tube. The operating conditions were: 40 kV and 20 ma current. The radiation dose rate at the location of the sample was 2.3×10^4 rads/hr (measured by standard $FeSO_4$ - Fricke Dosimeter (6)). The cross-sectional size of the beam was 2-1/2 in. x 3 in. and gram quantities of the sample were irradiated. For gamma-irradiations, a nominal 10 kilocurie cobalt-60 radioactive source with a dose rate at the sample location of 1.0×10^5 rads/hr was used.

Curing Procedure

Curing in simple shapes was accomplished by x- or gamma-irradiation of the energetic material - uncured binder mixtures in simple containers. The curing was satisfactorily obtained both in presence and absence of air. The radiation curing doses were: 80/20 RDX - MMA, 0.5 megarad (in absence of air), 1.4 megarads (in presence of air); 80/20 RDX - trimethylolpropane trimethacrylate, 1.0 megarad (in presence of air); 80/10/10 RDX-FEFO-trimethylolpropane triacrylate, 1.4 megarads (in presence of air); 80/20 Hivelite-methylmethacrylate, 1.4 megarads (in presence of air). Samples were also cured on a shaped charge cone. A 60° copper cone belonging to an M42 shaped charge grenade was used. The cone was glued tightly to a pyrex glass tube as shown in Fig. 1. The energetic material - uncured binder mixture was poured over the cone, the glass tube capped, and the material cured by exposing to gamma-rays. The necessary radiation doses were same as those for curing simple shapes.

Characterization of Cured Composites

In addition to x-radiography (100 kev x-rays) and optical microscopy, the cured samples were further physically characterized via scanning electron microscopy (SEM) and x-ray analysis. In SEM analysis, the samples were sputter coated with gold (to prevent sample charging) and analyzed using Amray Co. Model 1000 VTC scanning electron microscope. In x-ray diffraction, intensity (I) versus 2θ patterns were obtained using Norelco-Philips x-ray diffractometer and k_α radiation with nickel filter (to remove k_β). The instrument was operated at 35 kV and 15 ma current. Coefficients of linear expansion of radiation cured samples were measured in a Perkin-Elmer Model TMS-1 thermomechanical analyzer.

RADIATION CURING OF RDX/PMMA ON A SHAPED CHARGE CONE

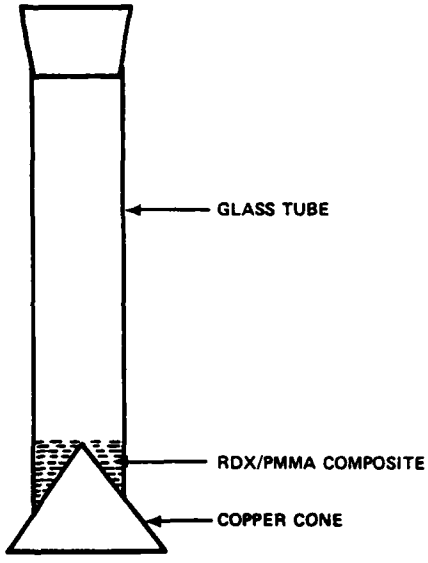

Figure 1. RDX/MMA is Radiation Cured to Obtain RDX/PMMA

Measurements of Mecnanical Properties

A fully computerized high rate mechanical testing system (MTS) was used under low load rate to obtain stress-strain plots for different samples tested. Samples were about 1/2" in diameter and 1" long. From the stress-strain plots, the values of compressive strength and rupture strain were obtained.

Detonation Velocity Measurements

These were determined by the known procedure (7). Samples with 3/8-inch diameter and 2-1/2-inch length were confined in steel (1 in. o.d., 3 in. long). RP-80 detonator was used as an initiator. Six pins were located, pin to pin 3/8 inch apart. The time taken for the detonation to travel across pins was measured and the velocity calculated.

IYER

Theoretical Calculations

Theoretical detonation pressures and velocities were calculated using the TIGER Code (BKWR-thermo-hydrodynamic equation of state calculations (8)). Propellant properties were calculated as per OSRD Report 935 (9).

RESULTS AND DISCUSSION

80/20 RDX - Polymethylmethacrylate System

Physical Characterization. X-irradiation or gamma-irradiation of RDX-MMA composite generated a product which was hard and machinable. For analysis purposes, small sections of the hard mass were made by turning it in a minilathe.

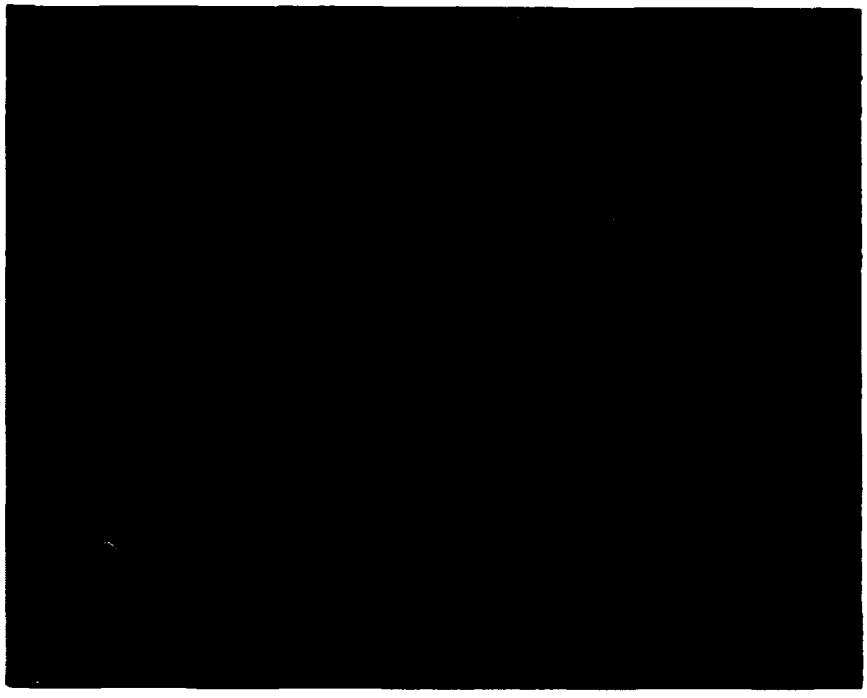

Figure 2. SEM of Freshly Cut Surface of RDX/PMMA Composite Showing Good Wetting Between the Filler and the Binder

Radiography (100 keV x-rays) of the whole (unsectioned) composite showed that it was continuous, uniform, and free from any gross physical defects. Examination of a freshly cut section of the composite using an

optical microscope (magnification, 61.5) showed that the surface was free from voids and cracks. Figure 2 shows an SEM picture of RDX-PMMA composite. It can be seen from the figure that the radiation-cured cast is free from voids, and furthermore, there is good wetting between the explosive RDX and PMMA binder.

Figure 3 shows a machined RDX/PMMA cast on an M42 shaped charge copper liner. It can be seen that the cast is very strongly adherent to the cone surface.

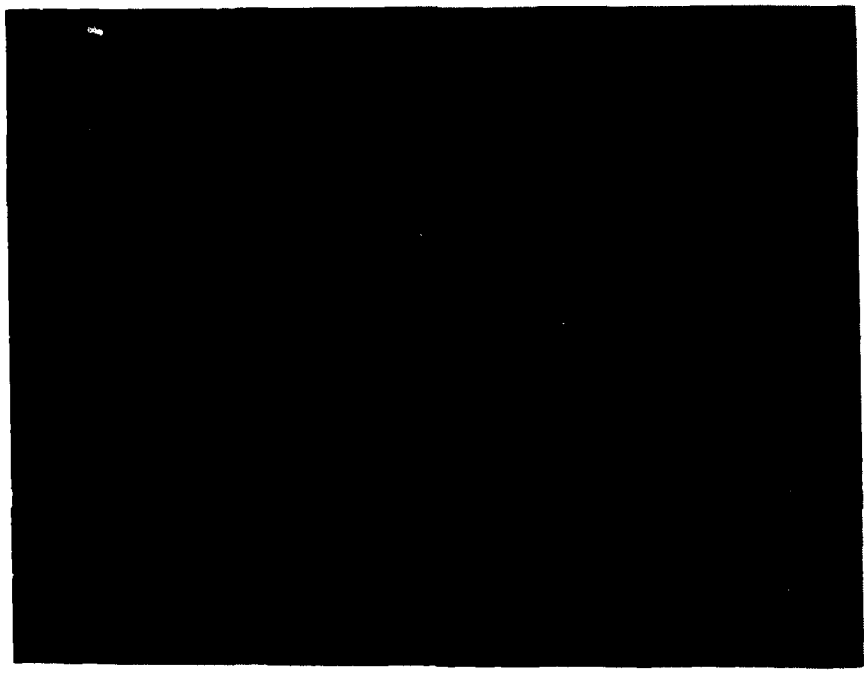

Figure 3. Radiation Cured RDX/PMMA on Copper Cone from M42 Shaped Charge Munition. The Cured Composite is Machined at the Top for Observation

Figure 4 shows the x-ray diffraction data for RDX, PMMA, and the RDX-PMMA composite. It can be seen that the I versus 2θ pattern for the composite is same as that for RDX, PMMA itself showing no peaks. This indicates that the structural identity of RDX is unchanged as a result of going into the polymer matrix.

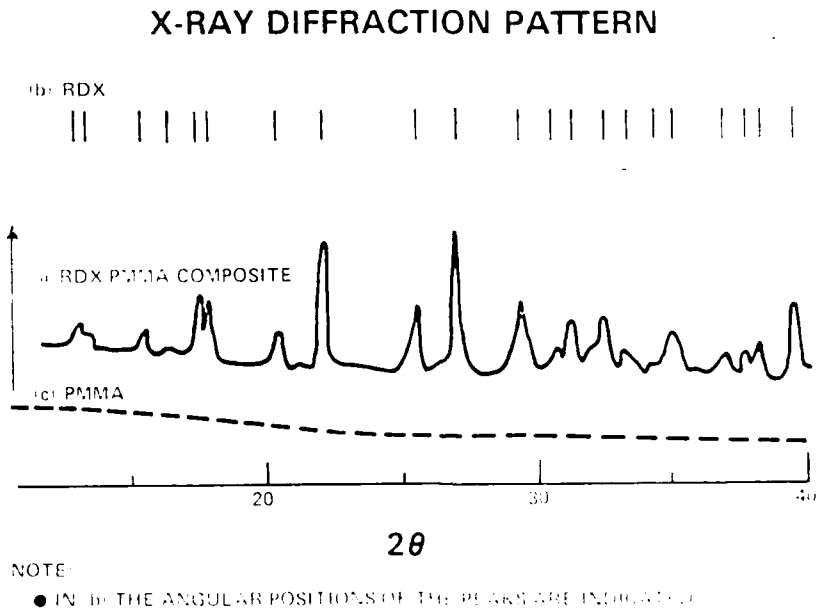

Figure 4. X-ray Diffraction Pattern of RDX/PMMA Composite

Material and Explosive Properties. Table 1 shows the measured value of detonation velocity, compressive strength, and rupture strain for RDX-PMMA composite. Average detonation velocity for the radiation cured material at cast density of 1.53 g/cm^3 is 7.70 mm/μs. The radiation cured material possesses also good mechanical strength. It is, for example, about 2-1/2 times stronger (ratio of compressive strengths) than Composition B and can withstand much larger strains (2% versus 0.24%). The value of Young's modulus (compressive) for RDX-PMMA measured in the work is 3 x 10^5 psi.

Table 1. Properties of RDX/PMMA Composite (80/20)

	Detonation Velocity[a] (mm/μs)		Compressive Strength (psi)		Strain at Rupture
Radiation Cured RDX/PMMA	7.78 7.73 7.58	(1.55)[b] (1.53) (1.52)	4300	(1.53)[b]	2.0%
Comp B	7.73	(1.66)	1759 (PATR 4587)[c]		0.24%

[a]3/8 in. diameter 2-1/2 in. long samples confined in steel (1 in. OD 3 in. long); [b]Densities in parentheses; [c]Reference (10).

RDX-FEFO-TMPTA System

Significant progress has been made in developing a radiation curable binder solution containing an energetic ingredient. Thus, mixtures comprising RDX, energetic FEFO (liquid; FEFO: Bis (1, fluoro -2,2-dinitroethyl formal)) and TMPTA (another liquid; TMPTA: trimethylolpropane triacrylate) in 80/10/10 proportion were successfully radiation cured to obtain uniform and hard composites. The binder system was prepared by mixing uniformly TMPTA with an equivalent weight of FEFO. As the binder system is initially a liquid, slurry loading is easily accomplished. The introduction of FEFO at the expense of the inert (e.g. 80/20 RDX/PMMA) improves the energy content of the energetic material composition.

TIGER calculations of detonation velocity and detonation pressure were performed for the RDX/FEFO/TMPTA system. The heat of formation and the theoretical maximum density (TMD) of the composite were calculated from the respective values and the relative proportions of the components. The heat of formation for TMPTA was estimated from the bond additivity method to be -269.1 Kcal/mole (11). The detonation velocity for the system was also measured. The data are presented in Table 2.

Table 2. Properties of Radiation Cured 80/10/10 RDX/FEFO/TMPTA System

Density	Detonation Velocity (mm/μs)		Detonation Pressure (kbars)
	Calculated	Observed	Calculated
1.73*	8.44	--	302
1.56	--	7.71	--

*TMD.

Coefficient of Thermal Expansion

The measured value of the thermal coefficient for radiation cured 80/10/10 RDX/FEFO/TMPTA is: $\alpha = 140 \times 10^{-6}$ inch/inch°C. The α - value for Al and low density polyethylene are: 24 and 180×10^{-6} in the same units (12). These values show that the intermolecular bonding in this composite, which is an indicator of the elastomeric behavior in polymer materials is similar to that in polyethylene. The addition of FEFO seems to have conferred elastomeric behavior to the RDX/FEFO/TMPTA composite. The expansion and contraction profiles (through the JANNAF cycle) were also quite smooth showing the absence of any abrupt dimensional changes.

HMX-Energetic Liquid Mixtures

BKWR-thermo-hydrodynamic calculations of cured HMX-energetic liquid mixtures are summarized in Table 3.

Table 3. Performance Calculations of HMX-Binder Systems

System	TMD (g/cm^3)	Detonation Velocity (mm/μs)	CJ-Pressure Kbars
HMX-FEFO-TMPTA (80/10/10)	1.81	8.71	327
HMX-FEFO-TMPTA (80/15/5)	1.82	8.86	343

The detonation velocity and CJ-pressure values for HMX-FEFO-TMPTA systems show that they have potential for high energy yielding formulations. For example, 80/15/5 HMX-FEFO-TMPTA System would have a power output comparable to the best castable military system to date, viz. 75/25 octol which has a detonation velocity of 8.48 mm/μs (1.81 g/cm^3) and CJ-Pressure equal to 342 Kbars (1.82 g/cm^3) (13).

Ammonium Nitrate (AN)-Polymer System

A composite of dried 78% AN and 22% MMA was successfully radiation cured (using gamma-radiation). The weight of the cured composite exposed to ambient humidity remained constant up to 142 hours, thereby showing no moisture pick-up. Under the same conditions, plain AN was deliquescent. Radiation curing thus shows potential for preparing relatively cheap AN based military charges which would be free from hygroscopicity problems.

Propellant Systems

The use of radiation for curing some propellant formulations would offer several advantages. For example, radiation curing can be performed at ambient or subambient temperatures. Combustible cartridge formulations which are at present cured at above room temperatures have been found to be extremely vulnerable to heat. This difficulty can be greatly reduced if radiation is used at ambient temperatures instead of heat to cure them.

Radiation Curing of Hivelite-Binder System

Hivelite represents a family of compounds based on salts of decaborane blended with a variety of oxidizers such as potassium nitrate. Hivelites serve as ingredients of very high burning rate (VHBR) propellants (burning rates in the range 1-100 m/s) (14). Hivelite 300511 is a composition made from cesium boron hydride ($Cs_2B_{10}H_{10}$) as the fuel and potassium nitrate as the oxidizer. The very high burning rates in these compositions arise due to the characteristic high exothermicity associated with the combustion of boron hydrides.

VHBR propellants are considered and tested for application as travelling charges (15). An ideal travelling charge is one which does not separate from the base of the projectile for the entire duration of the internal ballistic process. For this purpose, it is highly desirable to find ways to make the propellant charge adhere well to the projectile base. Travelling propellant charges could also suffer from problems of disintegration and bulk break up while burning. Radiation cured casts have a very strong metal adhering property (Figure 3). In addition, their mechanical strength is also superior. These properties could be useful in countering the problems of travelling charges mentioned above.

In order to test the feasibility of radiation curing Hivelite formulations, a slurry of 80/20 Hivelite 300511/MMA was subjected to gamma-radiation. The slurry cured very nicely to a solid and strong cast. Radiation curing dose was 1.4 megarads (see experimental).

Experiments are underway to test the strong metal adhering behavior of these radiation cured casts. These tests will measure the compressive force necessary to shear the joint surface of the metal with the radiation cured cast.

Acetylenic Propellant Binders

Polymers of diacetylenes (see below) could be very desirable binders for propellants.

$$n\ X - CH_2C \equiv C - C \equiv C\ CH_2 - X \xrightarrow{\text{radiation}} \left[=\overset{\overset{CH_2X}{|}}{C} - C \equiv C - \overset{\overset{CH_2X}{|}}{C} =\right]_n$$

X could be - ONO_2, $CH(NO_2)_2$ or $C(NO_2)_3$

The calculated thermochemical properties for these substituted diacetylenes are shown in Table 4.

Table 4. Thermochemical Properties for Diacetylenes

	X = ONO_2	$-CH(NO_2)_2$	$-C(NO_2)_3$
Isochoric Flame Temperature, °K	4,038	3,496	4,406
Force, Ft - lbs/lb	505,517	442,085	423,796

The preparation of the above diacetylene with X = $-ONO_2$ was attempted from 2,4-hexadiyne in methylene chloride at 5°C. The product which was not purified with a final distillation (because of the high instability of the compound) showed the presence of $-ONO_2$ groups in its infrared spectrum. Radiation-curing experiments of this binder with propellants and explosives are in progress.

Radiation Curing in Military Hardware

80/20 RDX-liquid MMA was successfully in-situ cured in an M42 shaped charge munition. The cured cast in the M42 was sectioned using remote saw and controls. Figures 5 and 6 show microscopic view of these sections. These show uniform casts as well as no shrinkage nor separation of the charge from the walls of the munition case or the shaped charge liner. This is a very important feature of the process in that it should lead to reduced round-to-round variation in the target penetration performance of the M42 munition.

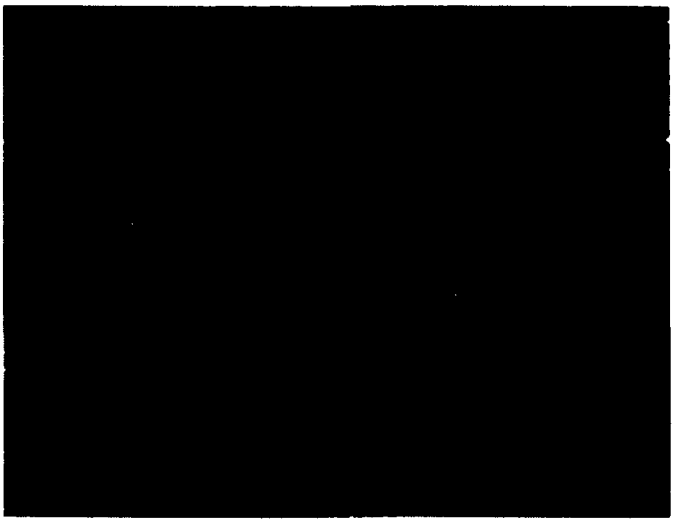

Figure 5. Radiation-cured RDX/PMMA in M42 Munition; Magnification: 8
A: Steel wall; B: RDX/PMMA Cast; C: Copper Liner

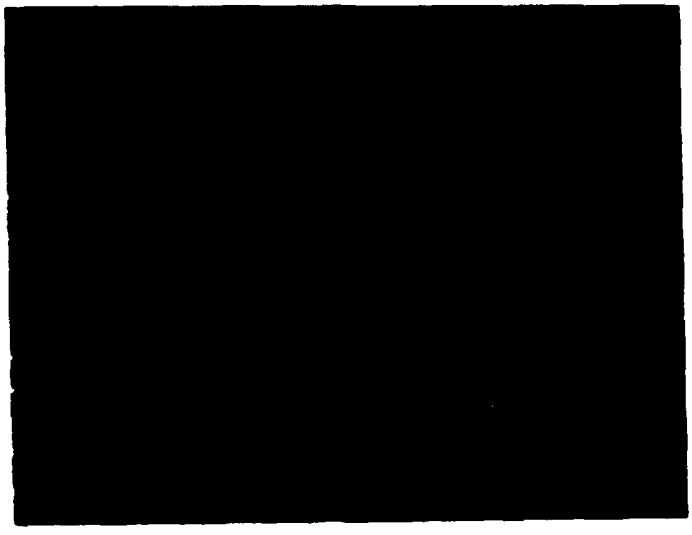

Figure 6. Radiation-cured RDX/PMMA in M42 Munition; Magnification: 31
A: RDX/PMMA cast; B: Copper liner

CONCLUSIONS

Casting of energetic material-liquid monomeric binder mixtures using radiation provides cured composities which are hard, void-free, and mechanically strong. Furthermore, the casts adhere very strongly to metals on which they are cured. Thus, this new technique, which was found to be scientifically interesting as well, has shown potential to furnish improved munition charges. The casting can be performed at ambient temperatures and directly in the casing. In this manner, this procedure lends easy adaptability to a rather simple process of munition loading and thus can be very valuable.

REFERENCES

1. S. Iyer, ICT International Annual Conference, Fraunhofer Institute for Propellants of Explosives, Karlsruhe, West Germany, p. 321, 1981.

2. S. Iyer, US Patent 4,343,664, 1982.

3. A. Charlesby, "Atomic Radiation and Polymers," Pergamon Press, Oxford, p. 424, 1969.

4. S.I. Omel'chenko et al, Intern Polymer Science and Technology, 8, (2) p. T65, 1981.

5. M. Steinberg et al, Multicomponent Polymer Systems - ACS Adv. in Chem. Series, 99, p. 556, 1971.

6. J.W.T. Spinks and R.J. Woods, "An Introduction to Radiation Chemistry," J. Wiley & Sons, NY, p. 106, 1964.

7. I. Akst and J. Hershkowitz, Picatinny Arsenal Technical Report 4987, 1976.

8. M. Cowperthwaite and W.H. Zwisler, "TIGER: Computer Program Documentation," SRI Publication Z106, 1973.

9. J.O. Hirshfelder and J. Sherman, OSRD Report 935, 1942.

10. T.S. Costain and R.V. Motto, Picatinny Arsenal Technical Report 4587, 1973.

11. S.W. Benson, "Thermochemical Kinetics," J. Wiley & Sons, NY, 1968.

12. R.A. Flinn and P.K. Trojan, Engineering Materials and Their Applications," Houghton Mifflin Co., Boston, II Ed., p.672, 1981.

13. B.M. Dobratz and P.C. Crawford, "LLNL Explosives Handbook," p. 19-103, 1985.

14. R.A. Fifer, "Workshop Report: Combustion of Very High Burning Rate (VHBR) Propellants," 18th JANNAF Combustion Meeting, Vol. II, Chem. Propuls. Inf. Agency, 1981.

15. I.W. May et al, "Thrust Characterization of VHBR Propellants, ibid.

RESULTS FROM RAILGUN PLASMA-ARMATURE INVESTIGATIONS

*KEITH A. JAMISON, DR.
JOHN D. POWELL, DR, MIGUEL MARQUEZ-REINES, MR, AND HENRY S. BURDEN, MR
USA LABCOM, BALLISTIC RESEARCH LABORATORY
ABERDEEN PROVING GROUND, MD 21005-5066

INTRODUCTION AND BACKGROUND

Electromagnetic propulsion has recently been receiving considerable attention for strategic applications, but offers many potential benefits for tactical applications as well. Of the many types of EM propulsion, the plasma-driven railgun holds great promise and has received the most thorough study. A key component in the railgun is the electrical armature. The requirements of an armature, whether it is solid metal or plasma, for any application are multifaceted. The armature must be capable of conducting megampere currents for times on the order of milliseconds and must also collect this current from a conducting rail while traveling at high velocity. The enormous magnetic forces applied to the projectile are accrued in the armature and it must not fail under the resulting stress. A plasma armature offers a solution to all these requirements, with the principal disadvantages being extremely high temperature and, prior to this work, notable lack of knowledge concerning the properties of accelerating plasmas under conditions appropriate to railguns. In this paper we report our effort to study, both theoretically and experimentally, the properties of plasma armatures.

The railgun is a device which utilizes the Lorentz force to accelerate objects to high velocities. The concept of the railgun is not new and dates back to the early 1900's (1). Several waves of interest have peaked and diminished in the past but with limited success in developing a device which could serve as a weapon. In the late 1970's, a major milestone was reached when researchers at the Australian National University demonstrated that velocities up to six kilometers per second (2) could be obtained using a plasma-armature railgun powered by a homopolar generator with an intermediate inductive store. Later, experiments performed jointly by Los Alamos and Lawrence Livermore National Laboratories (3) showed that velocities as high as ten kilometers per second could be obtained with a plasma-armature railgun. Work in decreasing the size and weight of the power source required to operate railguns has recently shown remarkable progress.

the gun system and the logistics train. A variety of non-weapon applications have also been suggested, ranging from research tools for the study of very high impact pressures to mechanisms which could produce thermonuclear fusion by impact of special materials. Perhaps the most publicized application for EM guns is in the Strategic Defense Initiative. Our interests, however, have focused on the tactical air-defense application, and this application has guided the basic research on EM guns intended to bring the railgun concept to a level where development can begin.

Of central importance to the operation of the railgun is the armature. The armature is an electrically conducting device which must carry large currents from rail to rail. There are several very stringent requirements placed on the armature because of the difficult task it must perform. First, the energy dissipated in the armature must be a small fraction of the total energy if the railgun is to be efficient. Second, the armature which actually incurs the large magnetic forces and transmits them to the projectile, must not fail under strain nor due to ohmic heating. Third, the armature must maintain good electrical contact with both rails even when traveling at a very high velocity. Finally, the mass of the armature should be small since its kinetic energy cannot be recovered or exploited in a useful way.

Solid and plasma armatures have both been used successfully in railguns in the past. The plasma armature is usually metal vapor, ohmically heated by the electric current until nearly all of the constituent atoms are ionized. Unlike the solid armature which may fail due to heating, it transfers force to the projectile hydrostatically and is not sensitive to mechanical strain. The mass of the plasma is estimated to be quite small so that very little energy is wasted in accelerating the armature to the same velocity as the projectile. As a gas, the plasma can make very good contact with the rails so that the high-velocity sliding electrical contact is not a problem. On the negative side, the electrical conductivity of plasma armatures is much below that of solid armatures. Thus, severe ohmic heating poses a problem both with regard to efficiency and with regard to thermal erosion of the gun tube. All plasma railguns have, in fact, shown significant damage to the bore surfaces after firing and usually require refurbishment of the bore between shots. A final disadvantage of the plasma armature is that its initiation requires high voltage and relatively high power; the levels required are not at present well known or understood. Consequently, the switch gear in the power source needed to control this voltage and power is not well defined. The solid armature has been successfully used only at velocities up to about 1600 meters per second. Since we are basically interested in higher-velocity applications, this limitation has been the principal motivation for our plasma-armature investigations.

A railgun in its simplest form is a pair of parallel conducting rails as shown in Fig. 1. A power source supplies a large pulse of electrical energy to the rails causing a very high electrical current to flow down one rail, cross from rail to rail through the armature, and return along the other rail. The region between the rails extending from the armature and back towards the power source contains the magnetic field associated with this current. The interaction of the magnetic field with the current in the armature produces the Lorentz force which accelerates the armature and projectile in Fig. 1 to the right. In practice, the rails make up only half of the bore surface with insulating sections comprising the remainder of the bore. Usually, there is some sort of very high-strength containment structure which holds the conducting and insulating sections together during the acceleration of the projectile. In the small BRL railgun, for example, which has a one-half inch square bore and is one meter in length, the containment is accomplished by two one-meter-long pieces of angle iron held tightly with large clamps.

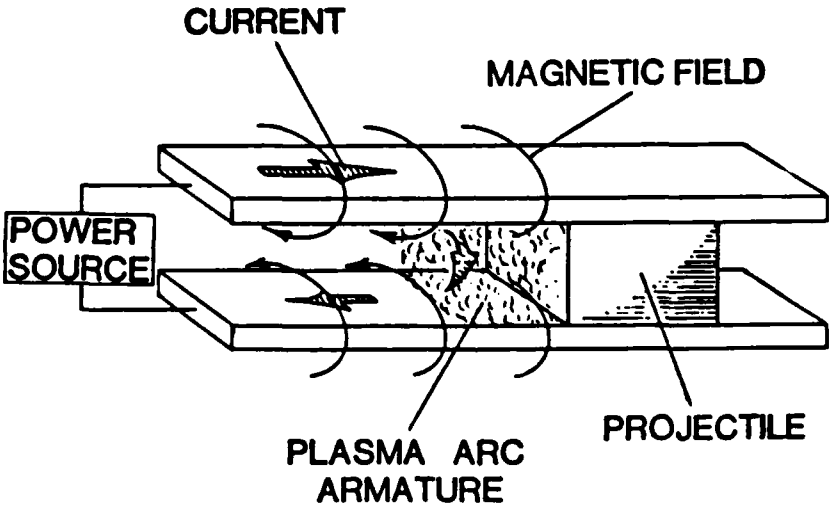

Figure 1. Schematic view of plasma-armature railgun.

Since the accelerating force is applied to the armature and projectile by a massless magnetic field and a nearly massless electrical current, acceleration to very high velocities may be possible. We view the potential for launching very-high-velocity projectiles to be the principal payoff in developing electromagnetic propulsion for a future weapons system. The role of an anti-aircraft gun, for example, seems a natural one for EM propulsion since short time of flight from the gun to the target may have very real benefits in increasing the probability of a projectile hitting the target. Many other applications have been suggested for EM guns, all with some advantages such as elimination of propelling charges from both

The purpose of our investigations is to study theoretically and experimentally the properties of plasmas under conditions appropriate to railgun armatures. Through a thorough understanding of these properties, it is hoped that we can minimize the disadvantages of plasma armatures discussed above and provide design data for future railgun systems. With our models we are able to calculate, for example, the thermodynamic properties and electromagnetic fields associated with the plasma and infer what erosive effects these properties might have on the rails and projectile. Our experimental work, which consists of diagnostic measurements of the plasma properties, is intended to validate the theoretical predictions and to prove concepts where too many variables may exist for modeling to be meaningful. We now turn to a discussion of some of our recent results. The discussion here is intended to be more qualitative and descriptive than the detailed results presented elsewhere (4-8).

THEORETICAL MODELING

The thrust of our theoretical efforts has been to develop first one-dimensional (4), and later two-dimensional (5), models for assessing the thermodynamic and electrodynamic properties of the plasma. In the one-dimensional calculations these properties are assumed to vary only along the direction of acceleration, whereas in the two-dimensional case,variations are also accounted for in a direction normal to the rail surface. The latter calculations have in particular led to improved estimates of the density and temperature within the plasma.

In both models a number of assumptions are employed to make the calculations as tractable as possible. The most important assumption is that the properties of the plasma are steady in the frame of reference that accelerates with the projectile. Thus, the results can be expected to be valid for describing the plasma properties only when the acceleration process is well underway, and not for describing early-time effects such as plasma initiation. In addition it is assumed that the plasma does not interact with the rails (other than by radiating energy onto their surfaces), that the mass of the plasma remains constant, and that the current furnished by the power supply is constant in time. Time variations can be allowed in the calculations, but the results will be valid only in the quasi-static sense. Energy transport within the plasma and to the exterior boundaries is assumed to occur only by radiation, with ordinary conduction being neglected owing to the short time scales involved. At temperatures characteristic of railgun plasmas, this assumption can be easily justified. The energy radiated away from the plasma per unit time is assumed to be balanced by the energy dissipated due to ohmic heating so that a steady state is maintained. Finally, it is assumed that the plasma is, at most, doubly ionized with higher degrees of ionization not accounted for. Again for the temperature ranges of interest, this assumption is reasonable.

The calculations are somewhat tedious and we indicate here only a qualitative description of the technique involved. We are interested in determining as a function of position within the plasma the magnetic induction field, the electric field, the current density, the temperature, the pressure, the mass density, and the concentrations of singly and doubly charged ions. The solution must also yield the length of the plasma measured along the acceleration direction as well as the magnitude of the acceleration. Information sufficient to determine these parameters is contained within Maxwell's equations, the hydrodynamic conservation equations, the Saha equations which predict the ionization state, an equation of state, and appropriate expressions for the plasma conductivity and radiation mean free path.

After considerable analysis, we have derived a set of coupled algebraic and differential equations, the solution of which yields the unknowns discussed above. In some limiting cases, exact analytic solutions of the equations can be obtained, and these solutions are useful for deriving approximate scaling relations which indicate how plasma properties vary with gun size and acceleration characteristics. In general, however, numerical solutions must be employed and considerable effort has been expended in developing the appropriate numerical techniques.

We now turn to a discussion of some of the specific results from our model calculations. In particular, we emphasize those aspects that have led to predictions concerning the performance of the railgun or the erosive effects of the plasma on the rails.

One of the most important considerations in the assessment of the feasibility of railguns is how efficient they are or how the energy furnished by the power supply eventually becomes distributed. For constant-current, steady-state operation, our models, which neglect losses in the rails, indicate that the energy is distributed as follows. At the end of the acceleration process less than one-half of the energy is transformed to kinetic energy of the plasma and projectile and an equal amount is stored in the magnetic field. The remaining energy is dissipated in the plasma due to ohmic heating. The fraction of the energy dissipated depends sensitively on the acceleration characteristics, especially the current, and can vary from a small fraction at high currents to a very large fraction at low currents. If, however, the rail current decays to zero by the time the projectile reaches the muzzle, the energy stored in the field can be recovered. The disadvantage of this mode of operation is that the gun must be designed to withstand early acceleration forces, much larger than the average, which offset the later, small forces; this effect would duplicate a problem common in conventional guns.

In railgun experiments at BRL, an intermediate inductive store is used to provide current to the rails. The time constant is less than half the total acceleration time so that the current is nearly zero when the projectile reaches the muzzle. To account for this effect in the model calculations, we have represented the current as decaying exponentially and assumed that the plasma properties vary quasi-statically. The ratio, as the current reaches zero, of the energy dissipated in the plasma to the total kinetic energy is given by

$$\frac{E_D}{E_k} = \frac{16\ m}{\mu\ i_0^2\ \sigma\ \ell\ L'\ \tau} \quad . \tag{1}$$

In this relation m is the combined mass of the plasma and projectile, μ is the magnetic permeability, i_0 is the initial current, σ is the plasma conductivity, ℓ is the plasma length along the acceleration direction, L' is the railgun inductance gradient, and τ is the current decay constant. The derivation is based on the assumption that the product $\sigma\ell$ is nearly independent of time; this assumption can be justified theoretically from scaling relations derived in our two-dimensional model calculations.

As a specific example of the application of Eq. (1), we consider a typical BRL experiment in which a 2.5 g projectile is accelerated to about a kilometer per second in two milliseconds. The initial pulsed current i_0 and the decay constant τ were measured and found to be 170 kA and 752 μs, respectively. Experimental values of the muzzle voltage, current, and plasma length (at any time) were then used to estimate $\sigma\ell$, and we obtained a value of 560 mho. When all these results are then used with the experimental value of L', namely, 0.5 μH/m, Eq. (1) yields $E_D/E_k \simeq 5$. Consequently, in this case, a rather large amount of energy is dissipated and cannot be usefully recovered. The result indicates the importance of operating at high currents since, according to Eq. (1), the ratio E_D/E_k decreases very rapidly as i_0 increases.

We now consider results from our two-dimensional, steady-state model which indicate how thermodynamic properties within the plasma vary as a function of position. We emphasize in particular the hydrostatic pressure, because of the large force it exerts on the insulating side rails as well as on the rails themselves; and the temperature, because of its obvious thermal-erosion effects. These calculations were undertaken using as input parameters for our numerical calculations data roughly appropriate for the railgun used by Rashleigh and Marshall (2) in their pioneering experiment. In that experiment, a 3 g projectile was accelerated in a railgun with a square bore 1.27 cm on a side to about 6 km/s using a pulsed current of about 300 kA (assumed constant during the acceleration time). The length of the plasma was estimated to be about 10 cm.

In Fig. 2 is shown the pressure profile in the plasma which, by assumption, remains constant in time. The figure is drawn so as to represent the pressure exerted on the side rails, at a point approximately 100 cm down the gun tube, as the plasma flies by. It is of some interest to note that, despite the fact that the calculation is two-dimensional, the pressure is nearly constant along a line normal to the rail surface. That the pressure should be nearly constant in the other dimension can be argued on physical grounds and was partial justification for our earlier one-dimensional calculations.

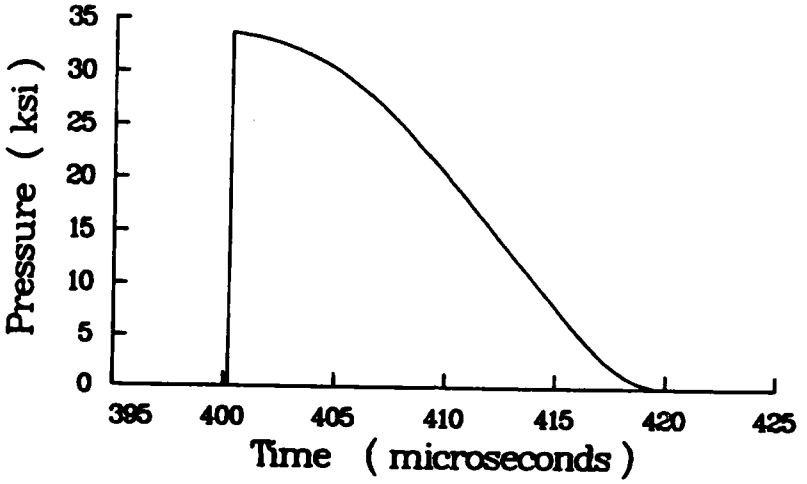

Figure 2. Pressure exerted at a point on the side rails as a function of time.

As can be seen in the figure, the pressure rises monotonically from zero at the back of the plasma to about 33 ksi near the projectile surface. Furthermore, the point in question on the insulators must be able to withstand high pressures for times of the order of 0.1 ms, regardless of the total acceleration time. The large, time-dependent variation of pressure across the plasma results, of course, from the plasma being totally confined by the magnetic field so that it accelerates along with the projectile.

A similar plot of the temperature is shown in Fig. 3. Here, however, two-dimensional effects are important and it is for this reason that our two-dimensional calculations have led to much improved estimates of the temperature within the plasma. What is shown in the figure are lines of constant temperature plotted as a function of ξ, the distance from the back of the plasma to the projectile in units of the total plasma length and η, the distance from the lower toupper rail in units of the rail separation. As can be seen there is a high concentration of thermal energy near the

projectile surface with very steep temperature gradients near the boundaries. The high temperature near the projectile results from the high mass density there which in turn causes the radiation mean free path to be very small. Consequently, energy dissipated in that part of the plasma is radiated away with greater difficulty. However, within a few mean free paths of the boundary, the photons can "see" the surface and are radiated outward easily. Therefore, the temperature drops dramatically in a very small distance.

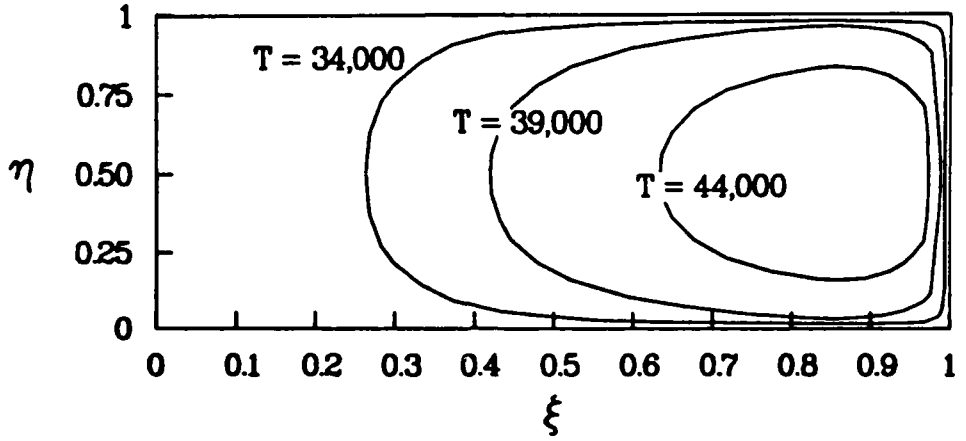

Figure 3. Lines of constant temperature, in degrees Kelvin.

As is evident from the figure, temperatures associated with plasmas in railguns are very high compared to propellant temperatures in conventional guns. The plasma is confined to a very small region, and travels at a high velocity. These conditions should alleviate problems associated with rail erosion. In an effort to evaluate thermal-erosion effects on the rails more precisely, we have developed a model (8) to determine how much of the rail surface actually melts during the time the plasma is in contact with a particular point on the rails. The model employs results from our previous two-dimensional calculations, particularly for determining the temperature near the plasma-rail boundary. It is assumed that energy is transferred from the plasma to the rails by radiation only.

Numerical solutions of the governing equations have been carried out for a number of cases of interest. However, the most extensive calculations have been undertaken to analyze railgun experiments at BRL, since we have available from these experiments data to use as input in the model as well as data with which to compare the results. Results of our calculations indicate a fair amount of damage near the breech end of the gun, but very little or none farther down the gun tube. For example, at a point 16 cm from the breech, the model predicted that about 60 μm of the rail

surface melted during the time of contact (about 60 μs). At a point 50 cm down the gun tube, however, the model predicted no melting at all. The damage is greatest near the breech because of the increased dwell time there, as well as because the temperature drops as the current decays in the later stages of acceleration. The dwell-time problem can be alleviated somewhat by injecting the projectile into the breech with some initial velocity.

EXPERIMENTAL FINDINGS

Our experimental facilities consist of two small test-bed railguns with power supplies and an array of data recording equipment. The first railgun is one meter in length and has a half-inch square bore. It is powered by a capacitor bank with an intermediate inductive energy store (6). The capacitor bank is capable of storing 60 kJ of electrical energy; just under half of this is available to the railgun magnetic field following the switching of current into and out of the intermediate energy store. The 2.5 gram, lexan-block projectiles, whose flight and terminal effects are not of interest here, are used only to provide an accelerative load for the armature. Typically, during the less than 2.0 milliseconds the projectile spends in the barrel, we can reach velocities of 1500 m/s. The second railgun is a small materials tester which is six inches in length and designed to accept rectangular slabs of materials to be examined for the effects of exposure to plasma armatures. The materials tester is powered by a capacitor discharge that is damped by a limiting resistor to prevent voltage reversal on the capacitor bank. The materials tester utilizes the same "projectile" as the one-meter gun. The low projectile velocity, typically 400 m/s, provides a 300 microsecond dwell time for the plasma, allowing deposition of about 250 joules of thermal load per square centimeter on the test-material surface.

Although electromagnetic launchers may produce a loud report, a significant muzzle flash, and a supersonic projectile and are frequently referred to as guns, it is important to remember that performance is a direct function of a rudimentary electrical circuit operated in a pulsed mode; consequently, the most important parameters relating to the railgun's performance are measured electrically. Knowledge of the current and voltage in the various components is essential prior to any diagnostic analysis of the armature performance. Because of the enormous power levels involved, current measurements are made with Rogowskii coils, which are not physically connected to the circuit; voltage measurements are made with resistive dividers. Both of these probes transmit their output to digital oscilloscopes set to begin recording when the firing sequence is initiated. Typical records of the railgun current and the voltage across the breech from rail to rail are shown in Fig. 4. The abscissa of the plot is time in microseconds; for this case, the projectile acceleration time was about 2 milliseconds and the velocity was just over 1 km/s.

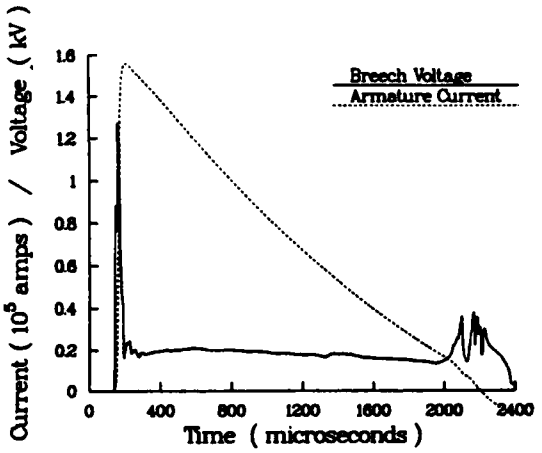

Figure 4. Gun voltage and current.

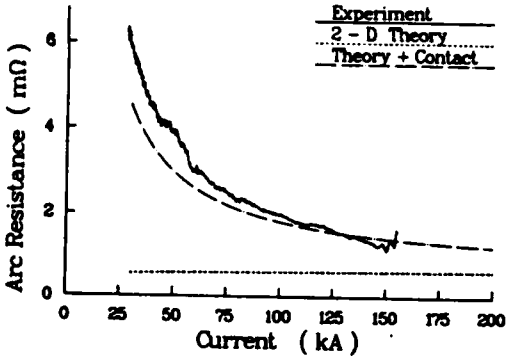

Figure 5. Observed armature resistance.

The resistance of the plasma may be found by taking the ratio of breech voltage, after correction for inductive effects, to current. This generally significant inductive correction, related to projectile velocity and changing current, amounted to only 6% for the trace of Fig. 4. The plasma resistance is shown plotted as a function of current in Fig. 5. The dotted curve is the armature resistance predicted by approximate scaling relations from our two-dimensional model, described above. If a sometimes postulated, fixed "contact potential" of 120 volts is added to the armature voltage from the model, the computed resistance will then follow the dashed curve. Since properties of a plasma are quite sensitive to its thermodynamics, one expects a higher resistance for the less dense, low-current plasma armatures. The resistance decrease with higher currents illustrates again that a small-scale device such as our laboratory railgun is destined to be highly inefficient. Typically, four percent or less of the electrical energy stored in the capacitors prior to the shot is converted to kinetic energy of the projectile. The ohmic losses by the armature account for about 30 percent of the initial stored energy. While this ratio of dissipated to converted energy is quite large, the evidence that a higher-energy system will suffer far smaller losses is clear. By doubling our current level, for example, the ratio of energy lost to kinetic energy extracted is expected to drop to about one as can be seen from our previous analysis. In general, the efficiency of plasma armatures increases with increasing projectile velocity.

If the armature voltage and the current distribution in the plasma armature are known, a one-dimensional plasma-conductivity distribution may be

calculated. Prior to our efforts, no measured or theoretical estimates of even the plasma length existed. We developed and utilized an experimental technique to determine not only the length of the plasma armature but also the distribution of current throughout the armature. This distribution is not directly measurable; however, it may be derived from the relatively easy measurement of the fluctuating magnetic field produced as the conducting plasma armature passes a fixed point. Figure 6 provides a schematic view of the setup. The curve shown, whose origin is referenced to the rear of the projectile, represents the current density distribution in the plasma armature. Note that the small, multi-turn loops for measuring the rate-of-change of the magnetic field (B-dot) are so oriented as to link

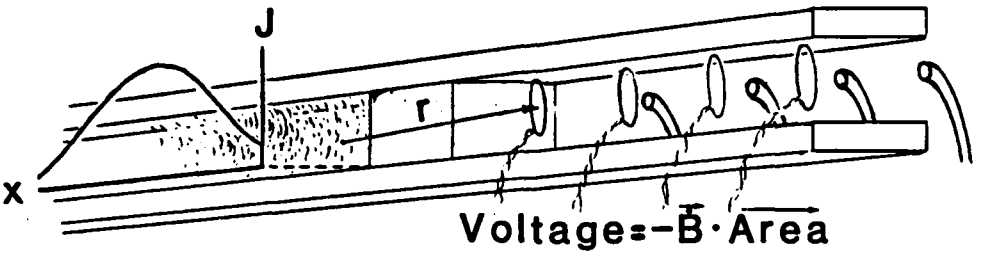

Figure 6. Locations of plasma armature, B-dot loops and fiber-optic ports.

only flux produced by currents flowing vertically, from rail to rail, through the armature; the loops are insensitive to flux produced by current flowing along the rail. To obtain the shape of the current distribution curve, an iterative process was developed in which a comparison of the calculated and observed B-dot signals serves as a criterion for choosing a J(x,t) which best models the actual distribution of armature current. Armature total current vs. time and time of armature arrival at each of four fiber optic ports spaced along the sidewall are measurements which constrain the currents and velocities of the calculated case to duplicate those of experiment.

The current density distribution was assumed uniform from rail to rail and from sidewall to sidewall. Along the rails the functional form of the distribution J(x,t) could be assigned arbitrarily except that the current density integral over the distribution was always made to match the measured instantaneous total rail current. The chosen form had a distinct effect on the calculated peak heights, peak spacing, and curve slope at zero crossing, emphasizing the sensitivity of the relationship between shape of the distribution and the B-dot signals.

Several different mathematical forms of the current density distribution were tried, but a Guassian curve, truncated off-peak by a vertical line representing the current/projectile interface, gave the best results.

Its shape, suggested by our theoretical prediction (5) for the current distribution, could be controlled by adjustable parameters until it gave calculated B-dot signals in excellent agreement with the data from the B-dot loops on the gun. Figure 7 shows the data from the loops and the calculated signature based on our optimized J(x,t).

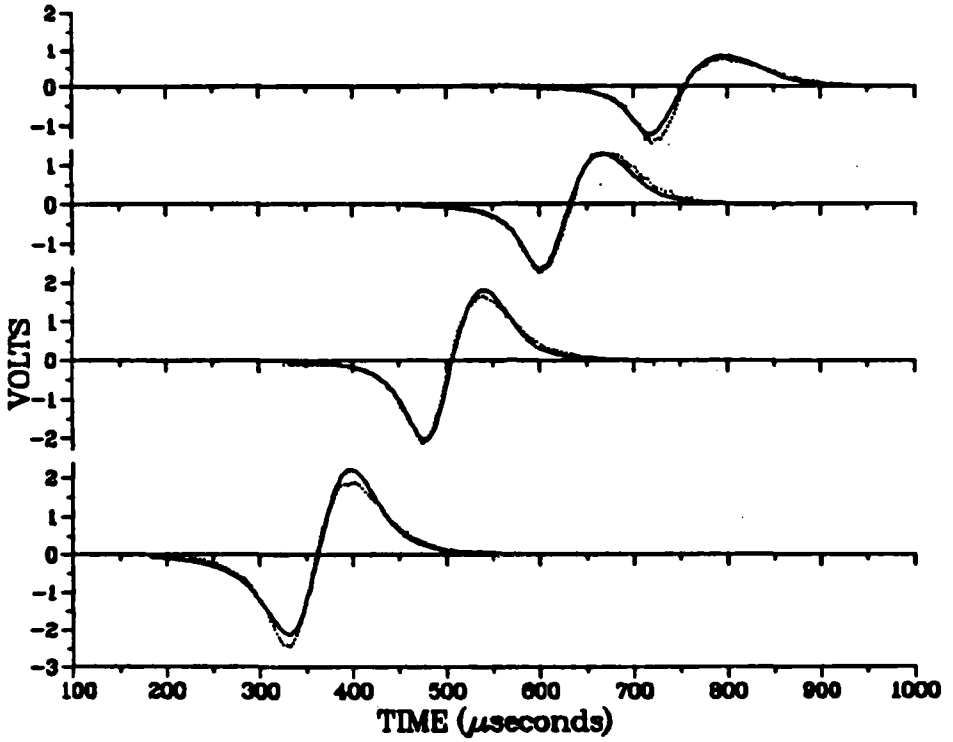

Figure 7. B-dot data as measured (solid) and as calculated (dotted).

The fitting process allowed the armature to lengthen as the current amplitude decreased. This mechanism provided the flexibility needed to cause the fitted distribution to expand at a rate consistent with the gun current decay observed during the armature's travel past the coil and, incidentally, to duplicate almost perfectly observed B-dot asymmetries. In tests of the iterative process, calculations starting with very different initial parameter values always converged to similar final values. For our railgun, as the current decays throughout the acceleration event (see Fig. 4), we observe an armature expanding in time. The average armature length is found to be 4.4 cm for a current of 100 kA and 9.6 cm for 50 kA. This time variation in the length correlates inversely with the total instantaneous current.

The current-density distribution is a function of both space and time. As such it may be graphically displayed with the time fixed and position as the independent variable (snapshot view). Figure 8 shows a sequence of four, fixed-time snapshots of armature current density. The shaded curves depict the distribution giving the best fit to the data of Fig. 7. Current density, predicted by the two-dimensional model for a plasma containing 8.0 mg of aluminum and matched to the experimental case in instantaneous total armature current and position, is shown by solid lines. That armature mass, otherwise unknown, was chosen arbitrarily to give reasonable agreement with the curves extracted from our measurements and was assumed independent of the changing current. Both the functional form of the current density distribution and the armature length scaling support the theoretical predictions.

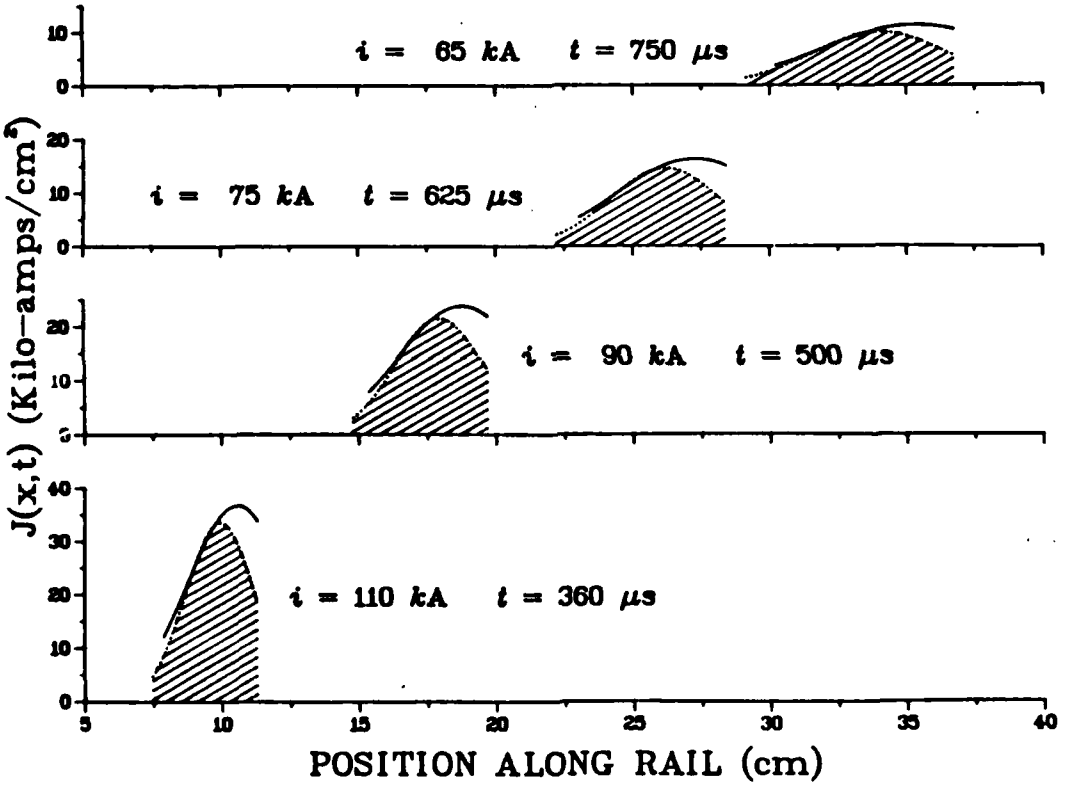

Figure 8. Current density predicted by model (solid) and deduced from measurement (shaded).

In nearly every experiment we observe fluctuations in the fiber-optic light-intensity signals which are on the order of the resolution limit of the fibers; the larger size of the B-dot coils limits the fineness of the

structures within the distribution which they can resolve, so the smoothness of the B-dot trace does not rule out the possibility that rapid spatial fluctuations in the current density are present. Theoretical and experimental work is being directed to study this phenomenon which would strongly influence rail erosion.

Recently, we have been focusing our efforts on non-steady phenomena in railgun armatures. One of the most easily recognized non-steady processes is the initiation of a plasma armature. Typically such initiation utilizes ohmic heating by a large current to vaporize a thin, metallic-foil conductor. If current conduction is established in the vapor, it will become ionized and a plasma armature will form. Nearly all experiments monitoring the initiation process show an initial high voltage across the rails which plummets as the process advances. In Fig. 9, the muzzle voltage vs. time for our materials-tester railgun, illustrates this effect over the first 20 μs. The small peak observed at 50 μs was caused by the collision, 10 cm down-bore from the foil, of the free-running plasma with the projectile. We are developing a one-dimensional, time-dependent model to analyze both the initiation process and the resistance rise during a plasma/projectile collision.

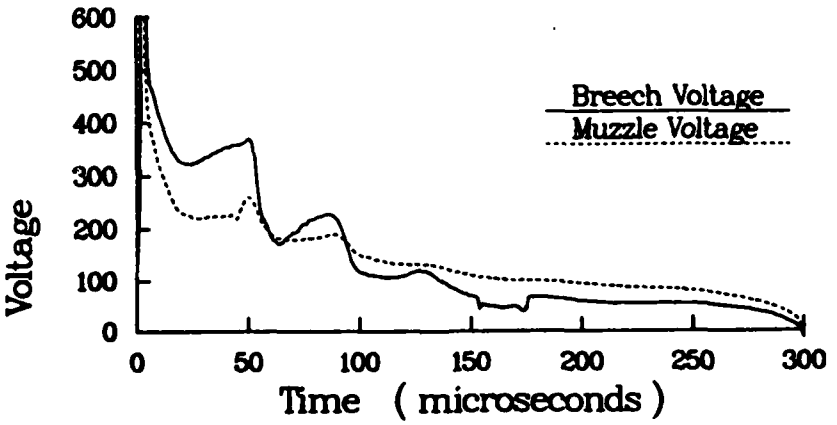

Figure 9. Breech and muzzle voltages from 6-inch railgun.

CONCLUSION

This paper describes the present findings in a continuing program of experimental and theoretical research on the high-pressure, high-temperature, accelerating plasmas unique to the chambers of EM guns. Our measurements of the time and spatial dependence of the current density of a plasma armature support, with slight differences, the theoretical predictions of a

two-dimensional model. With this model we can predict pressures, conductivity, and heat transfer that affect barrel life after steady-state operation has been achieved. The experimental effort has defined areas requiring further investigation; in particular, in the transient startup period. A theoretical understanding of this regime is particularly important because the time-dependent effects are most important during the early phase of acceleration when current is high, velocity is low, and exposure time of a section of rail is long. Presently, time-dependent theory is being developed to provide a model for the startup period. In addition, it should provide information on the changing electrical loads that will be presented to the switch and power source for rep-rated systems; and it should be able to calculate the hydrodynamic loads on the gun barrel.

In summary, we have undertaken basic investigations of plasma armatures. The results from this work are providing valuable information for the design of future railguns. We are continuing to investigate armature properties significant to the design of all components of future EM weapons systems.

REFERENCES

1. A.L.O. Fauchen-Villeplee, Canons Electrique, Paris, 1920.

2. S.C. Rashleigh and R.A. Marshall, J. Appl. Phys. 49, 2540 (1978).

3. R.S. Hawke, A.L. Brooks,F.J. Deadrick, J.K. Scudder, C.M.Fowler, R.S. Caird and D.R. Peterson, IEEE Trans. Magn. MAG-18, 821 (1982).

4. J.D. Powell and J.H. Batteh, J. Appl. Phys. 52, 2717 (1981).

5. J.D. Powell and J.H. Batteh, J. Appl. Phys. 54, 2242 (1983).

6. K.A. Jamison and H.S. Burden, BRL Report No. ARBRL-TR-02520 (1983).

7. K.A. Jamison, M. Marquez-Reines and H.S. Burden, IEEE Trans. Magn. MAG-20, 403 (1984).

8. J.D. Powell, IEEE Trans. Magn. MAG-20, 395 (1984).

ADAPTIVE PHASED ARRAY RADAR, ARTIFICIAL NEURAL NETWORKS, AND OPTICS (U)

*JOHN L. JOHNSON, DR.
DON A. GREGORY, DR.
RESEARCH DIRECTORATE, RESEARCH, DEVELOPMENT, AND ENGINEERING CENTER
U.S. ARMY MISSILE COMMAND, REDSTONE ARSENAL, ALABAMA 35898-5248

INTRODUCTION

In this paper the similar functions of adaptive phased array and artificial neural networks are reviewed and their common optical solutions are discussed. The rate equation for the antenna weights and the covariance matrix of adaptive phased arrays are compared to the neural slab equation and the synaptic connection strength matrix of an artificial neural network model. It is shown that the mathematics are nearly identical except for a few key differences. These differences are traced to the basic goals of each system: the purpose of the radar system is to null out a given input distribution while that of the neural model is to identify and discriminate various input distributions. The second part of the paper considers some of the optical techniques appropriate for each system. Other optical approaches are developed and shown to be compatible with adaptive phased arrays and/or artificial neural network models.

PART I: A COMPARISON

Consider the adaptive phased array system given in Widrow's basic 1967 paper[1]. Its objective is to null unwanted inputs for a given look angle. It applies adaptive weights W_n to each antenna input X_n and minimizes the error between a reference signal d_o and the weighted input sum. The adaptation of the weights occurs between return radar pulses and is repeated for each new desired look angle.

The Widrow one-mode system shown in figure 1 is solved by an iterative least-mean-square algorithm which adapts the antenna weights so that the error signal is minimized. Here, j indicates the jth iteration in time. This linear system is described by the set of relations

$$S_n(j) = X_n(j) + d_o(j)e^{i\delta n},$$

$$\varepsilon(j) = d_o(j) - \sum_{m=1}^{N} S_m(j)\, W_m(j) \qquad (1)$$

$$W_n(j+1) = W_n(j) - 2\, k_s \varepsilon(j)\, S_n(j)\ ,$$

where δ_n is the phase shift at the n^{th} antenna element and establishes the desired look angle and k_s is a system constant which must be negative to ensure stable convergence of the weights. These expressions can be combined in a form appropriate for comparison to the neural network mode

$$W_n(j+1) = W_n(j) - 2|k_s| \sum_{m=1}^{N} \overline{S_m(j)\, S_n(j)}\, W_m(j) + 2|k_s|\, d_o(j)\, S_n(j)\ . \qquad (2)$$

Here, absolute values have been used on k_s to emphasize the signs of the contributing terms. The expectation value notation of reference one has suppressed for clarity. The overbar term indicates the covariance matrix factor.

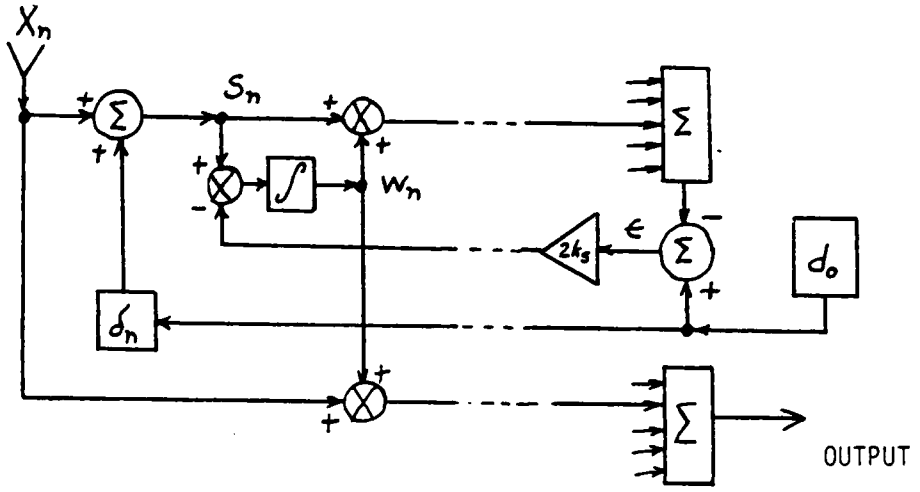

Figure 1. WIDROW ONE-MODE SYSTEM

The artificial neural network model of Grossberg[2] consists of a slab of interconnected elementary cells which receives an input distribution and generates a response distribution (figure 2a). Its objective is to adapt its output activity according to its past history of inputs. Generally, the system becomes more responsive to its most-used pathways. It also can learn to ignore inputs which are nonthreatening and which interfere with its preselected basic pattern of behavior.

Each cell (figure 2b) generates a thresholded positive real output signal S, and receives similar signals. It can apply internal weights, adaptive or fixed, and sum its weighted inputs as either inhibitory or excitatory signals. This sum drives an internal activity variable 'x' against a threshold to produce the output. The internal activity also is used to slowly increase the weights of the inputs which most often yielded an output. The adaptation occurs on a much slower time scale than the instantaneous operation of the rest of the cell.

Grossberg finds that in order to achieve stability against recycled noise in a network of cells that the outputs must be a nonlinear function of the internal activity. The threshold function is a simple nonlinear function; in general, any sigmoid relation is acceptable. The complete slab model is then described by a system of first order coupled differential equations relating the output signal, input signal, internal activity level, the adaptive weights and the two different time scales of cell response and adaption:

$$\dot{X}_n = - A_n X_n + \sum_{k=1}^{N} W_{kn} S_{kn} - \sum_{k=1}^{N} C_{kn} S_k + I_n$$

$$\dot{W}_{kn} = - D_{kn} W_{kn} + B_{kn} S_k \left[X_n \right]^+$$

$$S_n = \left[X_n - \Gamma \right]^+$$

$$A \gg D \qquad (3)$$

Γ, A, B. C, D are positive constants

$$[u]^+ = \begin{cases} u , & u > 0 \\ 0 , & \text{otherwise} \end{cases}$$

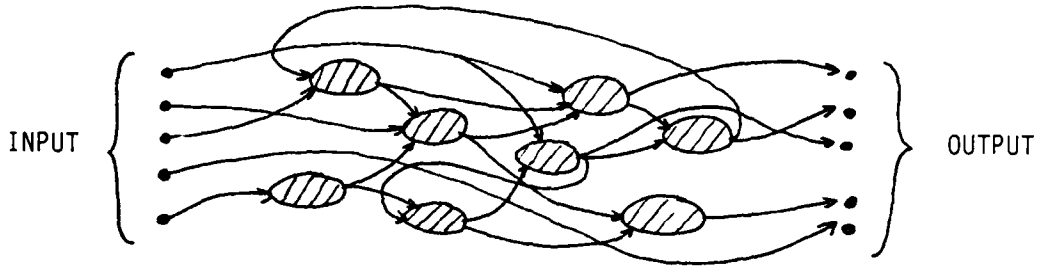

Figure 2a. NEURAL NETWORK SLAB MODEL

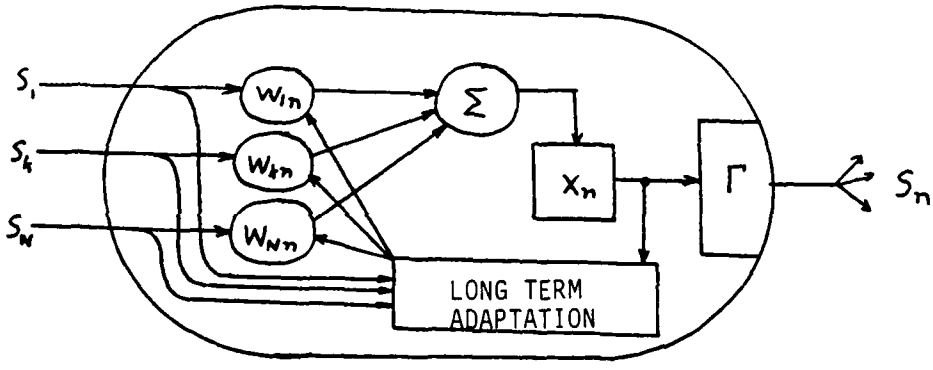

Figure 2b. CELL MODEL

Consider the special case of a single isolated cell with N inputs. One input S_1 also is chosen as a hardwired inhibitory input. An additional external control pulse I is used to turn on the system so that the adaptation of the weights can proceed. Equation (3) becomes

$$x_n = AX + \sum_{m=1}^{N} W_m S_m - C_1 S_1 + I$$

and

$$\dot{W}_m = -DW_m + B S_m [x]^+ \tag{4}$$

When the cell is operating, the weight equation can be expanded on an intermediate time scale Δt: $\frac{1}{A} < < \Delta t < < \frac{1}{D}$. Then

$$W_n(t+\Delta t) = (1-D\Delta t) W_n(t) + \frac{B}{A} \sum_{m=1}^{N} S_m(t) S_n(t) W_m(t)$$

$$- \frac{B}{A} C_1 S_1 (t) S_n(t) \tag{5}$$

Equations (2) and (5) show the strong functional similarity of the adaptation processes in the two systems. There are important differences. Table 1 summarizes the two systems.

The adaptive radar system used complex numbers and linear functions to null out the input distribution while becoming more tuned to the reference distribution. The neural model becomes more responsive to its input pattern and can be inhibited by some of its inputs. It uses positive real signals and nonlinear functions. Both systems account for stability and noise considerations. Both systems use the same type of terms in their processing functions. This last fact can be used to infer that common solutions to the implementation of the processes required by both systems can in principle be applied. An important constraint on this is the vastly different time scales on which the systems operate. Radar systems, although having a strong functional similarity to the isolated cell neural model, must operate much more quickly. Even with this constraint neural model research can be viewed as a possible source of processing techniques that could prove useful in implementing future adaptive radar systems. An example is given in the last section of this paper.

TABLE 1. COMPARISONS

ADAPTIVE RADAR USES COMPLEX NUMBERS AND LINEAR FUNCTIONS

NEURAL MODEL USES POSITIVE REALS AND NONLINEAR FUNCTIONS.

BOTH SYSTEMS ACCOUNT FOR STABILITY AND NOISE CONSIDERATIONS

OBJECTIVE OF EACH SYSTEM IS OPPOSITE.

COMPARE COEFFICIENTS:

ADAPTIVE RADAR	1	$-2\|k_s\|$	$+ 2\ \|k_s\|\ d_o(j)$
NEURAL MODEL	$1 - D\,\Delta t$	$+ B/A$	$- B/A\ C_1\ S_1(t)$

ADAPTIVE RADAR	"NEVER" FORGETS	NULLS OUT THE INPUT VECTOR	BECOMES MORE TUNED TO REFERENCE
NEURAL MODEL	SLOWLY FORGET	BECOMES MORE RESPONSIVE TO THE INPUT VECTOR	IS INHIBITED BY SOME INPUTS

PART II: OPTICAL PROCESSORS

Optical processing, with its high speed and massive parallelism, is particularly appropriate for real-time computations which have a large data input field, a multipoint algorithm, and a small number of output channels. It is less appropriate for lengthy algorithms requiring serial operations. Multiplication, time delay, integration, matrix and vector operations have been demonstrated optically.

The optical processor discussed here implements several operational principles of a neural model of an adaptive pattern classifier[2,3], chosen as an example because it embodies fundamental subnetworks imbedded in many neural network designs. Its value beyond optical image processing lies in the extremely general information processing features of these subnetworks. The performance data reported here centers on the general purpose subnetworks.

The adaptive pattern classifier is a two-slab system. Each output site of each slab connects to several sites of the other slab through adaptive channels. Each site also receives a distributed activity pattern, or image, through hardwired connection points. Each site sends an inhibiting signal to its local neighbors and has a positive feedback loop from itself back to itself.

An input image S_1 to the first slab is stored in short-term memory by the positive feedback loops. It is intensity normalized and contour enhanced by the local competitive inhibiting subnetwork which is basically a laplacian operator. The slab output R_1 goes to the second slab which is regionally activated by a code-word reference image S_2. Sites receiving both R_1 and S_2 adapt their connection weights, thus tuning the S_2 pattern to the R_1 overlap. The output of the second slab R_2 returns to the first slab and adapts the connection weights in the overlap of R_2 and S_1. The adaption process is on a slower time scale than the rest of the slab activity. Other inputs and code-word references can likewise be correlated by further training sessions. Code stabilization is achieved by yet another subnetwork. It selectively inhibits further adaption in slab regions which have already been used to encode previous input patterns. At the same time it also activates other nearby unused sites so they become available to encode the new input by the adaptation process. For example, the thresholds could be raised or lowered in the appropriate regions, thus suppressing or enhancing the individual sites' ability to produce an output. Since adaptation only occurs at sites producing output the variable threshold could protect previous adaptations while permitting the system to adapt to the new inputs. Detailed discussions of the adaptive pattern classifier and its subnetworks are given in references 2

and 3.

The subnetworks of interest are the recurrent shunting on-center/off-surround intra-slab connections and the local adapted interconnection pattern from one slab to the other. The two slabs communicate with each other only through the adaptive interconnections. A site on one slab receives signals from a limited region of the activity pattern on the other slab. If we consider the site to be a small area rather than a single point, then the receiving region can be viewed as a demagnified partial image of the activity pattern patch being transmitted to it.

This suggests a way to implement these subnetworks using two-dimensional modulators. Let the memory adaption be contained in a relatively small two-dimensional local neighborhood of each processing site. Basically, this uses some of the two-dimensional modulator surface for memory at the expense of spacial resolution of the input and output scenes. However, if one has a $10^3 \times 10^3$ pixel image and if a 10×10 block is used for adaptive memory functions, one still has a $10^2 \times 10^2$ effective pixel image capability.

Consider the optical processor shown in Figure 3. The system has three input images, F, G, and H, and an output intensity image detected at R. The images F and G are identical displays of the same scene. H is a radially symmetric transmittance mask with a central opaque spot when the system is used to perform image intensity normalization and edge enhancement. In the correlation mode of operation, H includes an additional transparency of a reference scene (memory) or liquid crystal television transmittance mask which displays the reference scene.

The incoherent television image F is imaged by a lens L_1 through a plane polarizer P_1 onto the read side of the LCLV. The resultant image reflected from the LCLV is directed by a beamsplitter through plane polarizer P_2 and imaged by lens L_2 onto the output plane. This image is the processor output R. The write side of the LCLV is illuminated using another television image G. This incoherent image passes through the mask H located at the aperture of lens L_3 and is re-imaged near, but not exactly on, the write side of the LCLV. This image is deliberately defocused by an amount Δ, shown in Figure 3. The polarizer P_2 is set parallel to P_1. This is 90 degrees from the usual crossed polarizer setting[4]. Normally, an intense "write" light results in an intense "read" light. This is not true when P_1 is parallel to P_2. An intense "write" light will now inhabit the reflectivity of the "read" side of the LCLV. The complete operation of the LCLV is described in detail elsewhere[5].

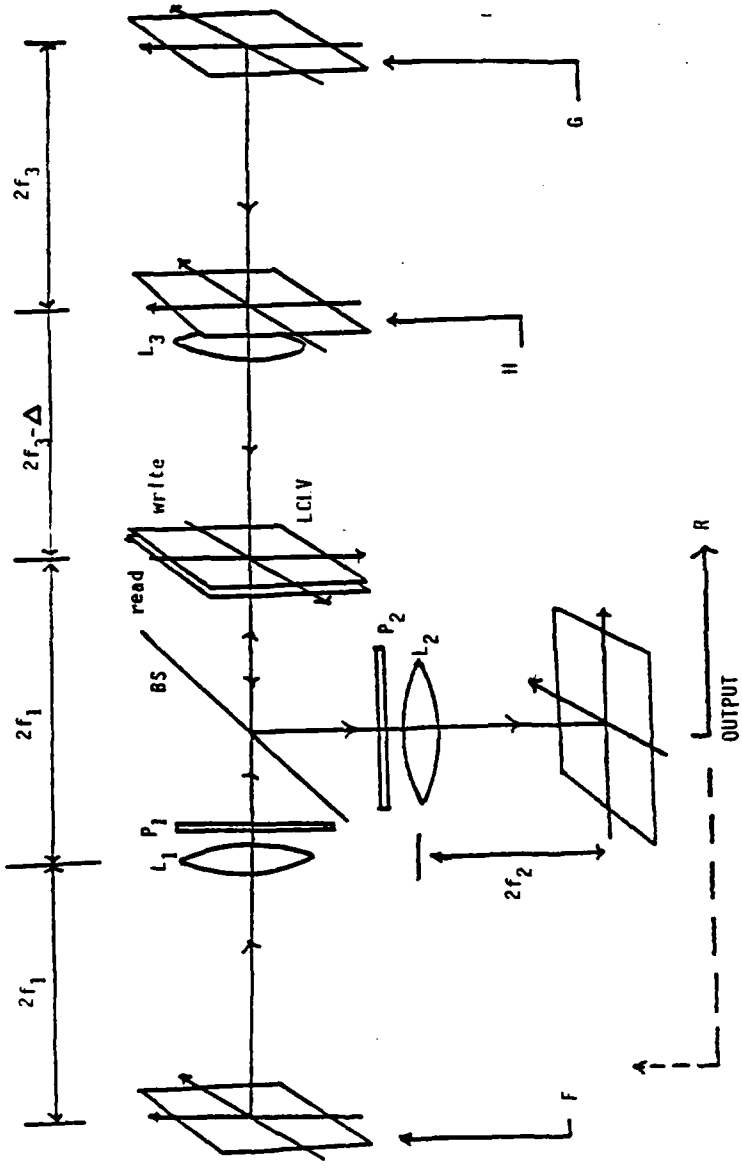

Figure 3. OPTICAL PROCESSOR

If the mask H is a simple stop with a central opaque spot, the system functions as an intensity normalizing and edge enhancing pre-processor. The intensity normalization is due to the inhibition mode of the LCLV. The photograph of Figure 4 shows a typical input scene, a model tank. The photograph was taken from a television monitor which was displaying the output from a television camera and lens combination placed at the output plane R. The writing intensity from the image at G was blocked, thus the reflected image F was not inhibited (normalized). The LCLV responded with a high reflectivity. The writing light was then unblocked and a 2 cm opaque central spot stop placed in front of the 5 cm diameter lens L_3. The reflectivity of the LCLV was then inhibited and the resulting intensity normalized image is shown in the photograph of Figure 5.

A demonstration of edge enhancement has been done using two circular spots as an input scene. One spot was more reflective and thus appeared brighter than the other. A photograph of the input scene is given in Figure 6. The contrast difference is obvious. A measurement of this difference was obtained using a video image digitizer. The contrast ratio (the maximum intensity divided by the minimum) was obtained by determining the average intensity of the bright spot and of the darker spot. The contrast ratio of Figure 6 is about 2.5. The ratio was measured again after the image of the two spots was processed. The results are shown in Figure 7. The contrast ratio was about 5.0, a significant improvement. The improvement is due to the fact that the system allows each spot to inhibit the other but not itself, and the brighter spot thus further suppresses the dimmer spot more than it itself is suppressed. This competitive dominance effect increases the ratio of the intensities of the two spots. This occurs for all nearby pairs in an image, resulting in an overall contrast enhancement.

The correlation function of the system requires that the reference (memory) image also be displayed at the location of H in Figure 3. This may be accomplished using a transparency of the reference image or by using an LCLV modified for the purpose. Essentially, the modification would involve removing the factory attached polarizers and holding the display screen vertical with fabricated supports. This has successfully been done for a different application.[6] Input scenes are then applied to the correlator by displaying them simultaneously as the same television image at F and G.

The intensity on the write side of the LCLV is now a convolution[7] of the LCLV reference image and the defocused image G. If G contains the reference image, the intensity on the write side becomes a broad maximum with a depresssion in the center (an annular distribution). The central depression is due to the opaque spot in H. The LCLV is operated in its inhibition mode. This low broad distribution will be centered on all the

Figure 4. OUTPUT IMAGE WITHOUT INTENSITY NORMALIZATION

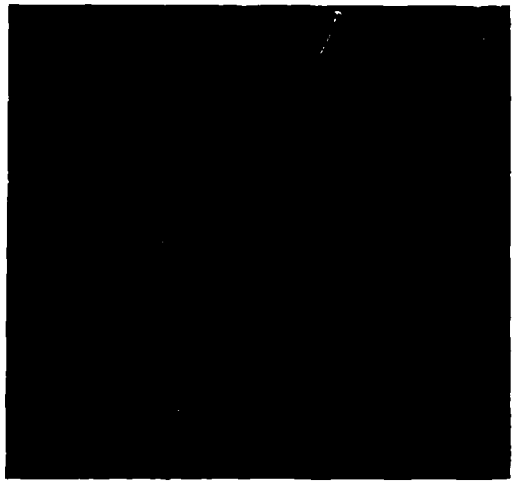

Figure 5. OUTPUT IMAGE WITH INTENSITY NEURALIZATION

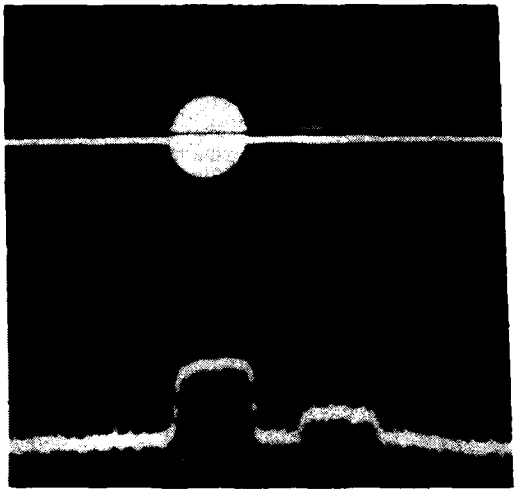

Figure 6. OUTPUT IMAGE WITHOUT CONTRAST ENHANCEMENT

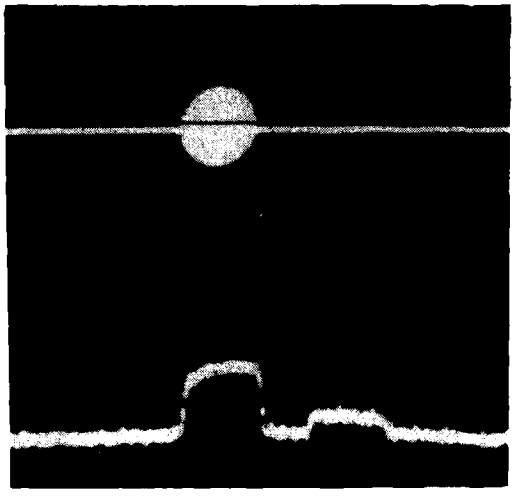

Figure 7. OUTPUT IMAGE WITH CONTRAST ENHANCEMENT

target images matching the reference. As the system intensity normalizes and edge enhances, the targets will suppress the surrounding regions while at the same time they themselves are relatively enhanced and sharpened. The inhibiting convolution can occur anywhere on the entire active region of the LCLV, therefore, it can continue to enhance a target undergoing a non-rotating lateral translation in the scene and will track a moving target. The system is thus able to detect, identify, and track targets. The correlation (recognition) may be observed at the output plane R, either directly or with the aid of a television camera and monitor.

The connection of this optical system with the neural model is as follows: the shunting on-center/off-surround subnetwork is implemented by the LCLV inhibition mode and the aperture mask with the central opaque spot. The recurrent feedback, not yet incorporated in the laboratory setup, can be obtained by mixing the output R with the input F. The adapted memory distribution is the reference scene applied at H, and the basic processing slab site is the demagnified region on the LCLV illuminated by G and convolved with the reference at H.

The connection with adaptive phased array radar can be seen by recognizing that the total two-dimensional radar array represents the Fourier transform of the radar image being received. If the array distribution is up-converted to visible light through EO modulators, it can be Fourier transformed into a visible image by an optical lens. Use this image as the scene input at F. For the G-input, add in a bright reference spot image transform at the desired look angle. Inspection of the pilot signal and its array element phase shifts of eq (1) shows that it Fourier transforms as an array-modulated spot of light at the desired look angle. Use the basic on-center/off-surround H mask with the central opaque spot. The pilot signal image in G will suppress its local neighborhood, and the overall scene distribution will inhibit itself to a normalized edge enhanced output. The total effect is that the system response is greatly suppressed everywhere except at the desired look angle. Thus, when the radar return pulse comes through, it passes through the system with a much greater response then the remaining distribution. Note that the read side of a light valve does not degrade the response time characteristic of oscillations in the light signal illuminating the read side. The output image R can then be summed by a condensing lens to a single detector as is done by radar networks, or could be further optically processed by thresholding and windowing to further increase the relative return signal strength.

This new concept of an optical processor for adaptive radar supports the basic argument of this paper that the similarity of adaptive phased array and artificial neural networks can be exploited in their common meeting ground of optical processing systems.

REFERENCES

1. B. Widrow, P. E. Mantley, L. J. Griffiths, and B. B. Goode, "Adaptive Antenna Systems", IEEE Proc. 55, No. 12, p. 2143, (1967).

2. S. Grossberg, Studies of Mind and Brain, Reidel Pub. Co., Dordrecht, Holland, (1982).

3. D. Hestenes, "How the Brain Works: The Next Great Scientific Revolution", 3rd Workshop on Maximum Entropy and Bayesian Methods in Applied Statistics, University of Wyoming, 1-4 August 1983.

4. W. Bleha, L. Lipton, E. Wiener-Avnear, J. Grinberg, P. Reif, D. Casasent, H. Brown, and B. Markevitch, Opt. Engr. 17:371, (1978).

5. J. Grinberg, A. Jacobson, W. Bleha, L. Miller, L. Fraas, D. Boswell, and G. Myer, Opt. Engr. 14:217, (1975).

6. D. Gregory, Appl. Opt., 15 February 1986 (in print).

7. J. Goodman, Introduction to Fourier Optics, p. 163, McGraw-Hill Book Company, NY (1968).

DEVELOPMENT OF AN EXPERIMENTAL MANIPULATOR ARM FOR APPLICATIONS IN THE CLOSE COMBAT MISSION AREA (U)

MR. DONALD E. JONES* AND MR. GLENN S. FRIAR
U. S. ARMY ARMAMENT RESEARCH, DEVELOPMENT AND ENGINEERING CENTER
CLOSE COMBAT ARMAMENTS CENTER
BENET WEAPONS LABORATORY
WATERVLIET, NY 12189-4050

INTRODUCTION

History shows that the United States Army has considered the application of automated loading devices for tank main armament for sometime. Tannenbaum and Fuller (1), in a review of activities in the 1942-1952 period, conclude that shifting military concepts allowed little time for completing automatic loading developments. They cite poor reliability of prototypes and the bulk and complexity of such equipment as further deterring acceptance. More recently, Holly (2), surveyed international autoloading endeavors. He states that modern equipment has significant potential for enhancing future weapon systems. He enumerates the attributes for such equipment and calls for the application of state-of-the-art technology. His survey identifies the need for including design guidelines and total functional requirements for such equipment in a well-integrated development with the close combat weapon system for a successful application.

Neither of the current M60 or M1 US tanks employ mechanization for ammunition handling. In contrast, both the T64 and T72 Soviet tanks do. Differences in the two country's approaches are apparent. The US designs apply fixed ammunition, good ergonomic design of crew stations, and four-man crews. The Soviet designs apply three-man crews, separate loading ammunition, and very cramped crew space. In fact, incidences of crew injury from the autoloader are reported (3). Nevertheless, the Soviets have utilized autoloaders in their main battle tanks for nearly a generation and they (autoloaders) are attributed as greatly improving their MBT's firepower (4).

Current investigations in the area of tank main armament systems at Benet Weapons Laboratory, (5-8) approach main gun ammunition loading as a materials handling problem. The movement of ammunition to, through, and from the combat vehicle can be facilitated through the use of modern technology. The source and form of the incoming product (the ammunition), the nature of the cache of the product on the vehicle, the transfers of the product within the vehicle, and the disposal of the unused elements of the

product from the vehicle are major elements of the process. The application of hard and flexible automation technologies, including robotics, are considered appropriate to the problem.

This paper presents efforts directed toward the development of a tank main armament ammunition handling system. The development centers on the potential use of a robot-like manipulator arm to accommodate the loading of large caliber ammunition into the main gun. Following a statement of the problem being addressed, the workspace for the application is defined. Kinematic synthesis and dynamic analysis which were used to develop a design approach are presented. The considerations in converting the initial design to an experimental hardware device are given and areas of investigation for the device are summarized. Conclusions and recommendations for further study are given.

STATEMENT OF THE PROBLEM

To be an efficient and effective weapon system, the tank (Figure 1) must consume minimal resources (manpower and materials) while performing its mission. If mechanization can be accomplished for US tanks, potential improvements in the weapon system can be envisaged. The weapon system could require fewer crew and support personnel to perform its mission. The handling of ammunition could be done more consistently. A more reliable means for loading hazardous materials in a hostile environment may result. The rate at which the ammunition can be loaded into the main gun may be enhanced. Such considerations spurred further investigation of the ammunition handling for the main armament system for a main battle tank. The following paragraphs summarize the ammunition handling for the main battle tank and postulate the problem under consideration.

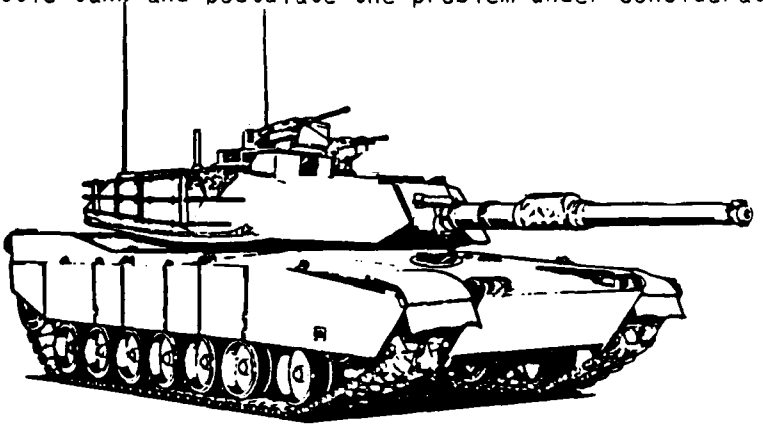

Figure 1. The M1A1 Abrams Main Battle Tank.

Ammunition for tank main armament is produced at manufacturing sites in the United States. Single cartridges are packaged in individual containers. Two packaged cartridges are placed in wooden boxes. The boxes are palletized for bulk shipment. Pallets may be aggregated in containerized modules (Milvans) for bulk handling. As the ammunition goes forward in the logistics train, the amounts of overpack, palletization, packing, and packaging are stripped off as reconfiguration occurs. Finally, at the combat vehicle, the individual cartridges are removed from their packaging and stored in racks in the tank.

There are two calibers of ammunition in current use by our tanks, 105mm and 120mm (9). In each caliber, there may be four to six different types of ammunition configurations. Each bare cartridge could weigh from 18 to 28 kilograms. Individual round packaging increases the unit weight to 22 to 32 kilograms. The length of the individual cartridges does not exceed one meter.

The human loader (10) removes ammunition from the racks in the tank and loads it into the main gun as directed by the tank commander. After the main gun is fired, the residue from the cartridge is ejected from the gun and the human loader must discard it from the tank. In the event that a cartridge has been loaded into the gun and it is not fired, the loader must clear the weapon and restow or dispose of the cartridge.

Within the tank, the crew is required to load the main gun to support a high rate of fire whether the vehicle is stationary or moving. Typically, loading at a cyclic rate of eight to twelve rounds per minute may be required. If the gun is tracking a target and/or is stabilized by the fire control system, the breech and chamber into which the ammunition is to be loaded is likely to be in constant motion relative to the tank-fixed coordinate system. While interruption of this constant movement may be made to load the ammunition, the crew must keep clear of the path taken by the moving gun, especially when it is fired, to avoid injury.

The general problem to be addressed is how to provide automation of the ammunition handling to enhance weapon system performance. Study (11) has shown that current flexible and hard automation technologies can be applied to the problem (12, 13). Commercial robotic devices, such as that shown in Figure 2, possess considerable flexibility in range of movement and ability to be programmed to perform variable tasks. These devices have been found very cost-effective in many industrial roles and have helped remove humans from hazardous work areas.

Can these or similar devices be effectively applied to the ammunition handling problem? The human loader weighs about 100 kg and occupies about 100 liters. He can retrieve ammunition from diverse and irregular shaped locations. He can operate in a limited workspace and compensate for

configuration changes. He can make on-the-spot decisions as the handling and loading process progresses. (What kind of ammunition should be retrieved? Is the breech open and clear? Is there impending danger in starting to remove a cartridge from the gun?) He can handle the myriad forms of ammunition and components required. Besides being a loader, the human can assist in other operations (e.g., diverse preventive maintenance and repair procedures or substitution for the driver). Automatic ammunition handling devices are anticipated to be dedicated and substantially single use equipment. They may weigh five or more times that of the human(s). Their maintenance will add to other operator and organizational duties. They operate more efficiently from fewer, regular, bulk magazines.

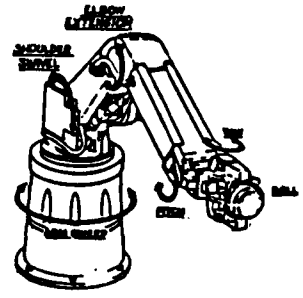

Figure 2. A Commercial Robot.

WORKSPACE

The materials handling problem to be addressed is bounded in one dimension by the manner of presenting the ammunition to the tank. Figure 3 shows the receiving of ammunition by the tank. At one end of the spectrum, individual ammunition cartridges can be introduced through openings or hatches. At the other, bulk packaged ammunition can be loaded on the vehicle.

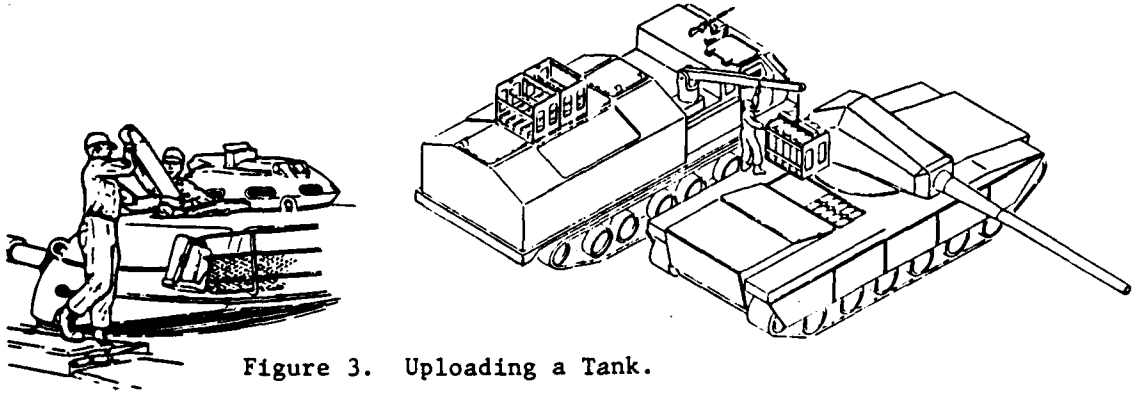

Figure 3. Uploading a Tank.

Within the vehicle, the potential spaces available for application of a manipulator are shown in Figure 4. They consist of: 1) a rectangular space located in the hull approximately one meter by two meters, 2) a cylindrical space located in the turret basket approximately two meters in diameter by one meter in length, and 3) an irregular overhead, rectangular shape in the turret which could extend and include portions of the bustle. The three volumes are contiguous although rotation between the turret and hull can occur and access between the two volumes may be provided in a half radian sector. They may contain ports, as described above, for introducing the ammunition. The volumes also contain other armament elements, crew, and weapon subsystems.

A concept for employing a robotic manipulator in this application is shown in Figure 5. The general volumes described above have been imbedded in a generic tank to show their relationships to the weapon system. This concept assumes a port in the hull, through which packaged ammunition is introduced into the tank. It also shows the gun into which the ammunition is loaded. A five degree-of-freedom manipulator is shown positioned in the turret basket which is capable of selecting a designated cartridge from one of the two caches, or magazines, and transferring it to the gun for loading. The manipulator may also be used to assist in receiving ammunition on board the vehicle or to perform gun clearing operations or maintenance. It must, however, avoid collisions with the gun, crew, and other objects. When the ammunition is transferred to the gun for loading, the docking with the breech of the gun must also be done with precision to permit other mechanisms to ram the cartridge into the gun.

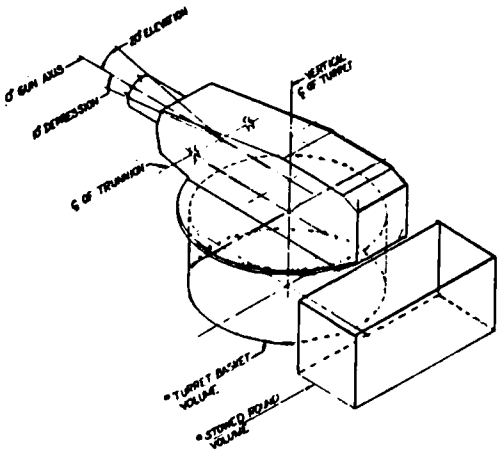

Figure 4. The Workspace.

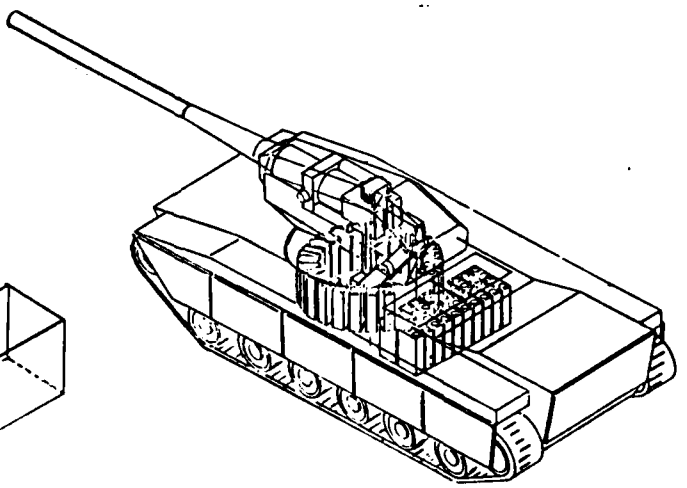

Figure 5.

A Concept for Manipulator Application.

KINEMATIC SYNTHESIS AND DYNAMIC ANALYSIS

With the concept advanced and the problem posed, the interactive process of engineering of a device to perform the required function was initiated. A five degree-of-freedom device which could potentially perform the required movements without collisions was synthesized (14). Its kinematic behavior was simulated for study using a commercially available computer code. Figure 6 portrays the three-dimensional graphics visualization provided by the code. Such visuals are useful in identifying interferences between manipulator, payload, and workspace. Preliminary characteristics for the manipulator were estimated. Assumptions concerning the trajectories and speed of movement were tested. A kinematic mapping of the concept was generated. Figure 7 depicts a typical output from the simulation. The torque required at joint number two (the shoulder joint) is depicted versus time. The trajectory lasts about 3.5 seconds and requires torques up to about 700 newton meters. The joint torque varies sharply with time. The plot suggests the need to increase torque from zero to peak value in about 100 milliseconds. However, such requirements need furher scrutiny before being implemented in the design. The general mapping, however, provides a basis for understanding the behavior of the mechanism.

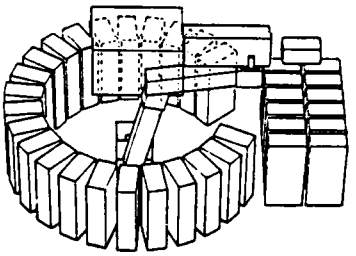

Figure 6. Graphics Simulation of a Manipulator.

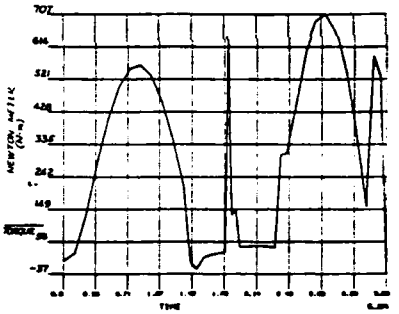

Figure 7. A Torque Plot.

An initial examination of the dynamic behavior of the mechanism was also made. The manipulator was modeled as a vibrating beam structure. It was found to have resonant frequencies in the range of 5 to 500 Hz. The structure was also modeled to estimate its deflection in response to a shock load. A 30 G ballistically - induced shock was found to cause a deflection on the order of 10 mm. These considerations have significant implications with regard to the control of the manipulator. The precision with which the device can be controlled will be influenced by its resonances and its deflections.

CONVERSIONS TO HARDWARE

With this general understanding of the concept, design of a manipulator was initiated. Figure 8 depicts the initial results of the designer's efforts. A five degree-of-freedom manipulator is shown. The waist joint is comprised of a large bull gear driven by a hydraulic motor and pinion. The motor weighs about 50 kilograms and requires a flow rate of approximately 100 liters of hydraulic fluid per minute to meet cycle rate requirements. The shoulder, elbow, and wrist joints are all rotary, hydraulic actuators of decreasing size and weight. The smallest weighs about 12 kg and requires less than a liter per minute. The latter four actuators are all directly coupled to the respective links to eliminate any backlash. The gripper is actuated with a small linear actuator. Each joint also has a rotary encoding device, mounted coaxially with the actuators. Plumbing and electrical details of the design are not shown. Obviously, the design is massive. It would weigh about 800 kg and require a peak power on the order of 30 kw to move a 50 kilogram payload from magazine to gun in three seconds. A better understanding of the design requirements and alternative strategies for actuation and control can be expected to significantly reduce the manipulator's weight and power needs.

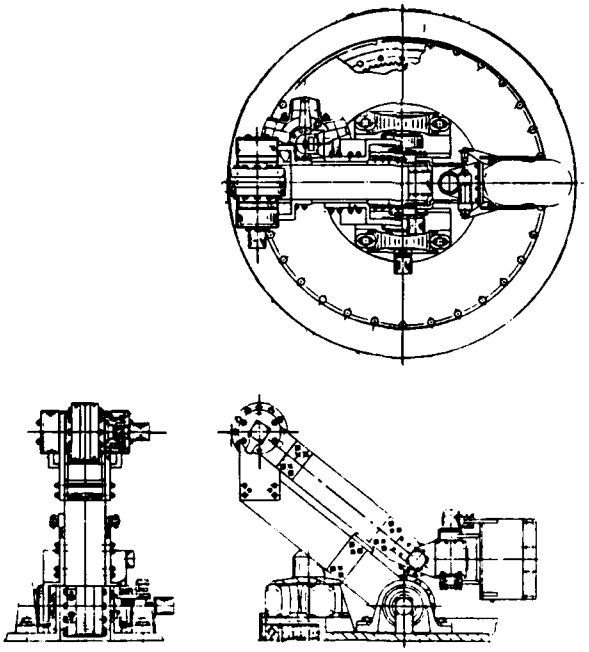

Figure 8. A First Generation Manipulator Design.

By this point in the development, the need for experimental hardware to confirm engineering estimates and further investigate the operation of such a device had been identified. Significant questions regarding the operation of the custom-designed manipulator centered on its control. Some preliminary work had been started in this area and will be discussed later. The decision to breadboard a three-degree-of-freedom manipulator was made. The breadboard would allow more complete engineering of the device, provide an opportunity to develop a better understanding of the control of the device, and permit experimentation concerning its operation in a confined workspace on a moving vehicle.

The breadboard three degree-of-freedom manipulator consists of shoulder, elbow, and wrist joints, and links to connect them, as in the device just described. Figure 9 shows the device which has been fabricated. It is mounted on a steel baseplate. The actuators are similar to those described above. The supports and links are all steel weldments and assemblies to ensure low backlash and minimal deflections. A simple gripper is attached. Rotary encoders on each joint measure position with 10-bit precision. They are connected to a small, special purpose microprocessor control. The control is also linked to servovalves for each actuator. Hydraulic lines connect each actuator and servovalve to the pump in the background. No special attempt was made to manifold and integrate the hydraulic lines with the structure. Instead, commercial, off-the-shelf components were used for breadboarding.

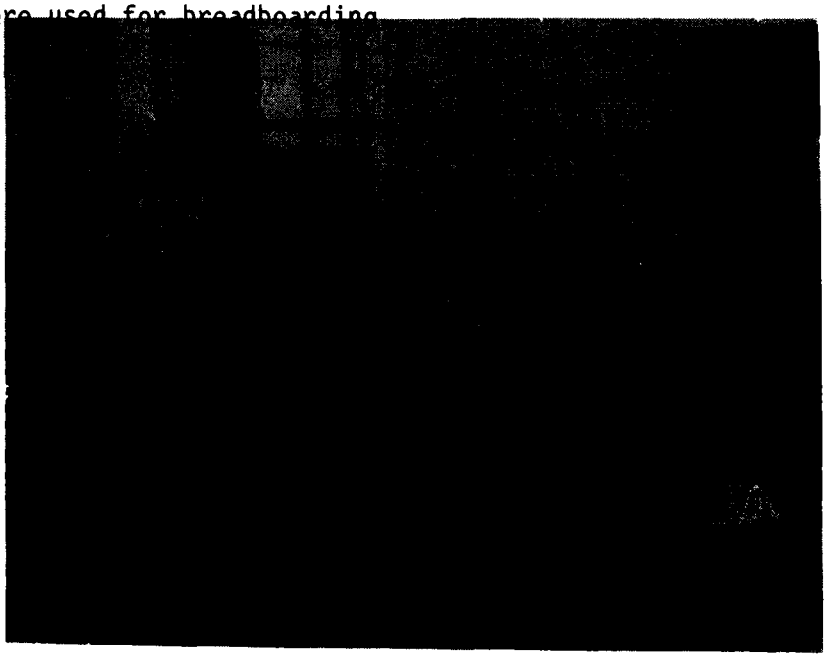

Figure 9. A Breadboard 3 D.O.F. Manipulator.

AREAS OF INVESTIGATION

Having synthesized a candidate manipulator representing some of the technologies applicable for robotics, our interest now turns to the question of whether the mechanism can be made to perform as originally conceived. Our interest centers on the application of control theory and the development of control strategies which will permit completion of the control specification. Guidelines for the device indicate that the following measures of performance may be applicable in specification:

1. Speed of operation
2. Precision and accuracy
3. Repeatability
4. Stability
5. Ability to operate in adverse environments
6. Capability of handling energetic and explosive materials.

The following paragraphs describe our investigations in these areas.

Our investigation began with the construction of a dynamic model of the device (15). Figure 10 shows the classic approach, as applied here. The coordinate system(s) and nomenclature are defined for a five degree-of-freedom manipulator. In the case shown, the Euler-Lagrange formulation relates the joint velocities and accelerations to the torques required to produce the motion. The coefficients in the equations embody the physical and mass properties of the device and the centripetal and Coriolis forces. In general, these coefficients depend on the joint angles and the equations become non-linear in nature. Boundary conditions for solution typically include initial and final positions, path or trajectory, velocities, accelerations, etc.

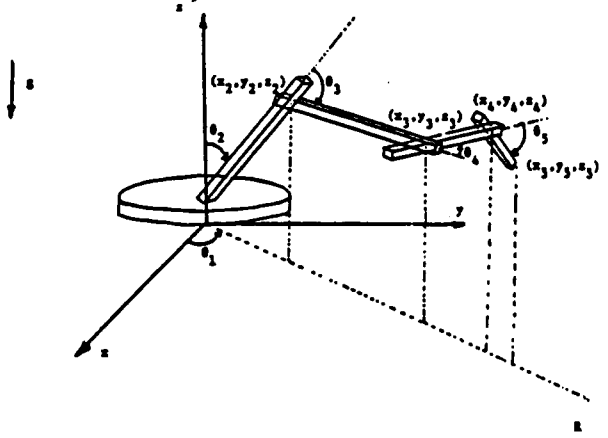

$$\tau_1 = D_{11}\ddot{\theta}_1 + D_{112}\dot{\theta}_1\dot{\theta}_2 + D_{113}\dot{\theta}_1\dot{\theta}_3 + D_{114}\dot{\theta}_1\dot{\theta}_4$$

$$\tau_2 = D_{22}\ddot{\theta}_2 + D_{23}\ddot{\theta}_3 + D_{24}\ddot{\theta}_4 + D_{211}\dot{\theta}_1^2 + D_{233}\dot{\theta}_3^2 + D_{244}\dot{\theta}_4^2 + D_{223}\dot{\theta}_2\dot{\theta}_3 + D_{224}\dot{\theta}_2\dot{\theta}_4 + D_{234}\dot{\theta}_3\dot{\theta}_4 + D_2$$

$$\tau_3 = D_{23}\ddot{\theta}_2 + D_{33}\ddot{\theta}_3 + D_{34}\ddot{\theta}_4 + D_{311}\dot{\theta}_1^2 + D_{322}\dot{\theta}_2^2 + D_{334}\dot{\theta}_3\dot{\theta}_4 + D_{324}\dot{\theta}_2\dot{\theta}_4 + D_3$$

$$\tau_4 = D_{24}\ddot{\theta}_2 + D_{34}\ddot{\theta}_3 + D_{44}\ddot{\theta}_4 + D_{411}\dot{\theta}_1^2 + D_{422}\dot{\theta}_2^2 + D_{433}\dot{\theta}_3^2 + D_{442}\dot{\theta}_2\dot{\theta}_4 + D_{443}\dot{\theta}_3\dot{\theta}_4 + D_{423}\dot{\theta}_2\dot{\theta}_3 + D_4$$

Figure 10. An Euler-Lagrange Model for the Manipulator.

An analysis of typical paths and path segments for the manipulator has provided an initial control strategy. Some segments could naturally be performed using optimal control for minimum time. Others appeared to require some form of feedback or hybrid control. Simulations imposing the control strategy were performed for selected cases. Figure 11 shows two planar path segments with nearly identical (but reversed) starting and ending points. In segment CD, the ammunition package is raised from the floor to the breech of the gun. In segment EC, the ammunition package is lowered from the gun to the identical location on the floor. Optimal control was applied for both segments. In segment CD, no collision occurs and the process is complete in 0.38 seconds. Segment EC is completed in 0.34 seconds, but the ammunition package collides with the breech, walls, and floor. Another less obvious result for segment EC is that the physical limits of the joint actuators are violated as a result of assumptions made to perform the simulation. This is an example of how the control strategy was developed for a stationary, undisturbed platform. This investigation did indicate that the transfer can be accomplished at the rate required.

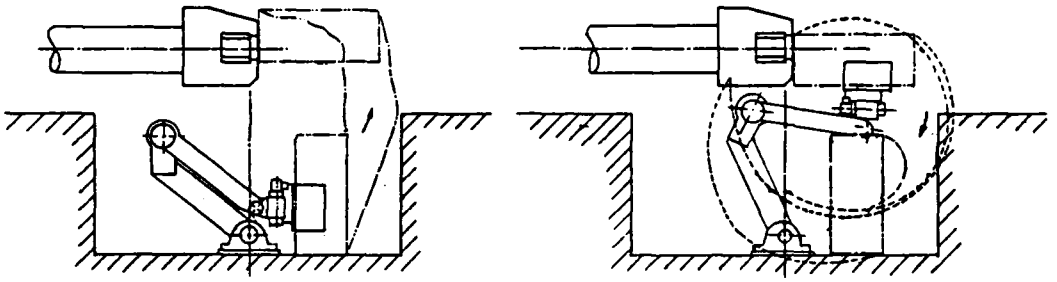

Figure 11. Optimal Control of Two Similar Path Segments.

Next, we examined the robustness of the control when subject to disturbances (16). For this investigation, a simplification was made. The manipulator was considered a one degree-of-freedom device with two links and a spherical-like joint. A feedback control strategy was used.

Figure 12 shows the control model. The math model for the manipulator is represented as a vector equation (the plant). A PID controller with velocity and gravitational corrections is applied. Path planning for the model amounts to choosing the shortest distance between origin and destination on a hemisphere. Behavior of the device was simulated for three types of disturbances:

1. The vehicle suddenly goes from a horizontal to an inclined translation.

2. The vehicle traverses a hill with increasing then decreasing slope.

3. The vehicle traverses an uneven (random) surface.

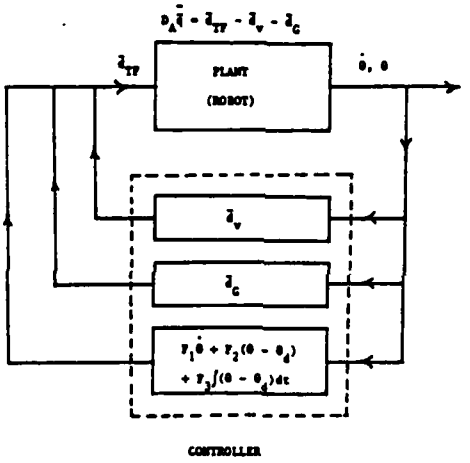

Figure 12. A Feedback Control Model.

Figure 13 shows an example of the controlled behavior. In the undisturbed case, trajectories are identical in both the world-fixed and robot-fixed coordinates. Some overshoot occurs at the end of the trajectory. The trace in the world coordinate system portrays the randomness and magnitude of the disturbances. In robot-fixed coordinates, it is evident that the controller has compensated for the disturbance with relatively little deviation in the trajectory from that in the undisturbed state. In this example, the controller seems to be robust enough to do the job.

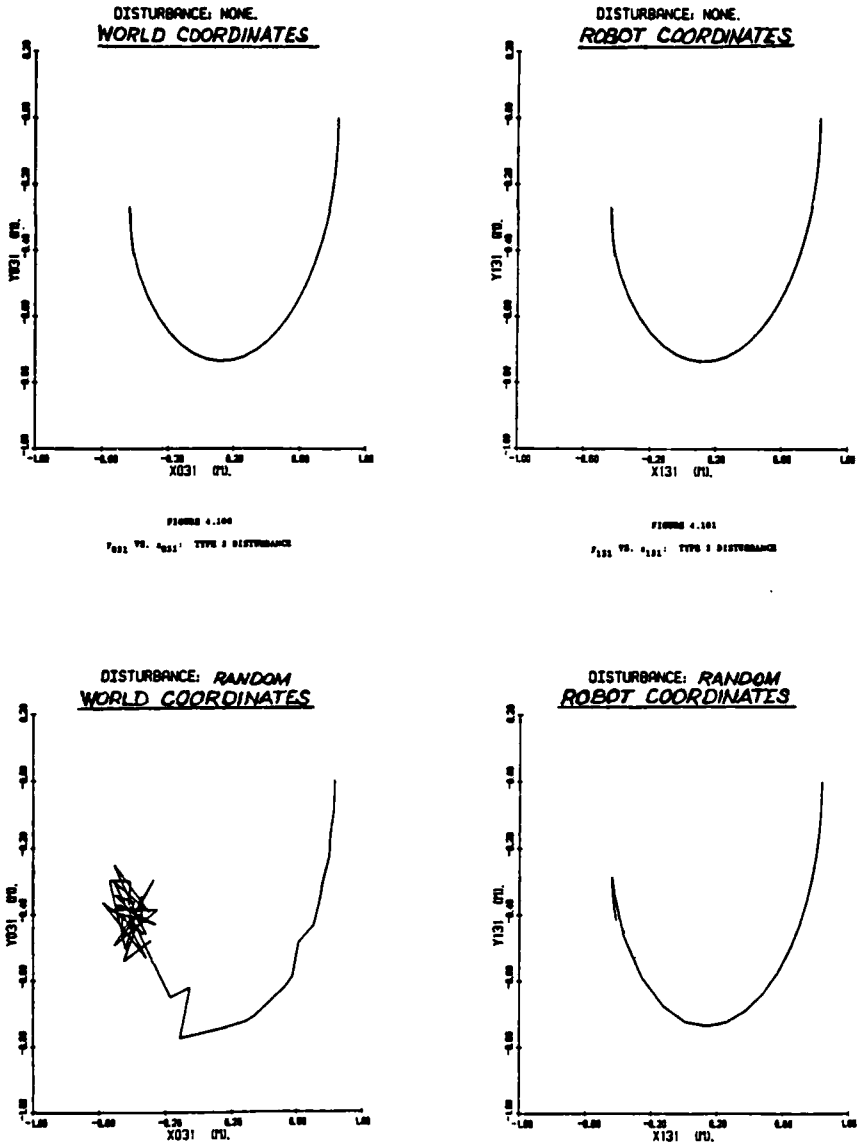

Figure 13 Trajectory Comparisons

CONCLUSIONS AND RECOMMENDATIONS

Robotics and automation have been identified as technologies that can be applied to the ammunition handling problem for combat vehicles in the Close Combat Heavy Mission Area. A concept for application has been advanced and initial, exploratory efforts have generated a breadboard manipulator for concept demonstration and further study.

The need for additional development of controls and control strategies is evident. The problems of operating the manipulator in a confined work space, at high speeds with precision is complicated further by the disturbances of a moving platform. Theoretical constructs can help develop an engineering solution to the control problem, but testing with the breadboard manipulator is needed to confirm predictions and focus the approach.

An arbitrary decision was made to apply hydraulics to the manipulator. Continued investigations should consider alternate approaches. Higher pressure hydraulic operating systems may help reduce weight and improve operating efficiency as they have in the aerospace industry. Maturation of the design to manifold the hydraulics may be beneficial. Electrical drive systems or hybrid systems may have advantages.

The first generation design of a custom robotic manipulator for application to ammunition handling on a main combat vehicle has proven to be large, heavy, complex and of unknown reliability. It was produced from standard materials and commercial components. Continued study should center on a more precise specification for such ammunition handling equipment requirements. As the problem becomes more fully understood, better alternative solutions should be developed which simplify and lighten the equipment while defining and confirming its reliable operation.

The automation of ammunition handling for the main battle tank provides an opportunity for further streamlining and mechanizing the handling of its ammunition supply. To accomplish such broad improvements requires a concerted effort. Design considerations must be sound and the ammunition and its packaging must be compatible with mechanization on the combat vehicle and the supply and transportation systems. Materials handling equipment may be required elsewhere in the supply system to support such an improvement. Further investigation and study should be conducted to this end.

REFERENCES

1. Tannebaum, Joseph and Fuller, S. H., "A History of Automatic Loading Equipment," Report No. RR-13, Ordnance Tank-Automotive Command, Detroit Arsenal, Center Line, MI, April 1960.

2. Holly, John W., CPT, "Automatic Ammunition Loading Systems for Large Caliber Weapons Mounted in Close Combat Armored Vehicles," TACOM Contractor Report No. 12898, US Military Academy, West Point, NY, September 1983.

3. Baxter, William P., Lt. Col., "Anatomy of the Soviet Main Battle Tank-T-72: An Impressive Rival," Army, Vol. 31(a), September 1981, pp. 29-32.

4. von Senger und Etterlin, F. M., Tanks of the World 1983, The Nautical and Aviation Publishing Company of America, Annapolis, MD, 1983.

5. Wildman, James E., "Conceptual Design for 120mm Improved Conventional Armanent System (ICAS) Autoloader," ARDC Contractor Report ARLCB-CR-84012, ARES, Inc., Port Clinton, OH, April 1984.

6. "Improved Conventional Armament System Autoloader," ARDC Contractor Report ARLCB-CR-84010, Emerson Electric Company, Electronics and Space Division, St. Louis, MO, April 1984.

7. Goodell, B. D. et al., "Conceptual Autoloader Design Study for Future Armament System For Combat Vehicles (FASCV)," ARDC Contractor Report ARLCB-CR-84011, FMC Corporation, Minneapolis, MN, April 1984.

8. Request for Proposal No. DAAA22-84-R-0143, Watervliet Arsenal, Watervliet, NY, 14 August 1984.

9. "Army Ammunition Data Sheets - Artillery Ammunition: Guns, Howitzers, Mortars, Recoilless Rifles, Grenade Launchers, and Artillery Fuzes," Technical Manual TM43-0001-28, Department of the Army, Washington, DC, April 1977.

10. "Soldier's Manual: 19E Armor Crewman," No. FM17-19E 1/2, Department of the Army, Washington, DC.

11. Jenkins, D. H. C. et al., "Autoloading in Tanks," International Defense Review, Vol. 17, No. 7, 1984, pp. 907-918.

12. Derby, S. J., "A Robotic Tank Autoloader," Proceedings of the Meeting of the Coordinating Group on Modern Control Theory (4th) Held at Rochester, Michigan on 27-28 October 1982, Part I, October 1982, AD-A128 964.

13. Derby, S. J., "Application of Robotics to Autoloaders," paper presented at the ARRADCOM Technical Conference, Large Caliber Weapon Systems Laboratory, Aberdeen, MD, July 1982.

14. Zakaluk, William A., "Conceptual Design and Analysis of a Robot Ammunition Loader," unpublished Master's Degree Thesis, Rensselaer Polytechnic Institute, Troy, NY, August 1983.

15. Wen, John and Desrochers, Alan A., "Control System Design for a Robotic Autoloader," Electrical, Computer, and Systems Engineering Department Report, Rensselaer Polytechnic Institute, Troy, NY, January 1984.

16. Joshi, Jagdish and Desrochers, Alan A., "Modeling and Control of a Mobile Robot," Robotics and Automation Laboratory Report, Rensselaer Polytechnic Institute, Troy, NY, 1985.

SURFACE PRESSURE MEASUREMENTS ON A 155MM PROJECTILE IN FREE-FLIGHT AT TRANSONIC SPEEDS (U)

LYLE D. KAYSER*, MR., WALLACE H. CLAY, MR.
AND WILLIAM P. D'AMICO, JR., DR.
US ARMY BALLISTIC RESEARCH LABORATORY
ABERDEEN PROVING GROUND, MARYLAND 21005-5066

I. Introduction:

A typical projectile in free-flight is simultaneously pitching, yawing, and spinning. This complex motion makes conventional ground testing difficult or sometimes impractical and provides an impetus toward use of instrumented free-flight models. Much progress has been made in the area of computational fluid mechanics and computational results have been helpful in evaluating projectile aerodynamics. Currently, it is not practical to computationally predict the complex projectile motion over a flight trajectory. The Army has used numerous experimental techniques for studying projectile motion. Conventional wind tunnel testing, including Magnus measurements, has been extensively used. Free-flight spark ranges have used the shadowgraph technique to measure projectile motion and extract aerodynamic coefficients. Within the past 20 years, developments in solid state electronics have permitted miniaturization and high-g survivability of electronic components. During this period, the Army has been active in developing on-board instrumentation and telemetry systems for projectile flight. The yawsonde (solar sensor) technique (1) has been extensively used to study the motion of projectiles over long flight paths. The yawsonde method obtains a time history of pulses from two solar sensors and yields yaw and spin characteristics. The yawing motion is a function of the relative phase of the two pulses and the spin frequency is approximately equal to the pulse frequency from either one of the solar sensors.

The high spin rates of projectiles present a significant challenge to experimentalists. Miller (2) developed a method for measuring pressures on a spinning model. His technique was a significant engineering achievement and provided results illustrating characteristics of the Magnus effect. However, long pressure stabilization times are needed and therefore require a steady state pressure and large amounts of tunnel time. Mark (3) demonstrated the feasibility of using telemetry for

measuring rapidly changing pressures on a wind tunnel model spinning at 300 rps. The measured pressures appeared to be reasonable, but there was a problem of signal phase with respect to model orientation which was later resolved by D'Amico (4). Mark (5) also obtained free-flight base pressure measurements on a gun-launched, non-spinning cone. The base pressure results were reasonable, but the lack of computational or experimental verification along with the high-g launch conditions make it difficult to assess the quality of the measurements. In-flight temperature measurements of liquid payloads have been reported in Reference (6). Whiting (7) also used telemetry to obtain laboratory pressure measurements on the end wall of a liquid filled cylinder which was spinning and coning simultaneously. Later, Hepner (8) conducted similar experiments in which amplified signals were transmitted across slip rings.

The loss of an instrumented projectile after its one and only flight may seem to present a significant disadvantage. However, one flight provides continuous data over the entire trajectory which includes a significant Mach number range at realistic Reynolds numbers and simultaneous pitching, yawing, and rolling motion. No cost comparisons have been made, but to duplicate the free-flight results from wind tunnel tests or by computation would require extensive programs.

The objective of the present program was to demonstrate the ability, or lack thereof, to obtain quality pressure measurements on a spinning, gun-launched projectile. To help achieve the objective, measurements were made only on a conical forebody for which computations could easily be made. The measured pressures can be verified when trajectory and yawsonde data are used as inputs to computational methods. Results are presented which illustrate not only the value of a local measurement but the capability of that measurement to describe in-flight behavior. Comparison of computed and measured pressures were found to be consistent.

II. Experiment:

The 155mm projectiles used for this test program were M687 shell with external geometry as shown in Figure 1. The projectile is 155mm in diameter, has a length of 6.13 calibers, and has a 0.25 caliber, 8 degree boattail. The conventional fuze was replaced with a sharp tipped cone which faired in with the 11.42 degree conical nose section. Two pressure port openings were located 1.594 calibers from the nose tip and were 180 degrees apart circumferentially. The projectile was also instrumented with a yawsonde system which utilized two solar sensors located 1.860 calibers from the nose tip and are 180 degrees apart. Each solar sensor has optical slits which are canted at different angles; as the projectile and sensor system rotate into the view of the sun, one sensor gives a positive voltage pulse and the other sensor gives a negative voltage pulse; the solar aspect angle is a function of the phase relationship of

the two pulses, which is determined by bench calibration. Reference (1) provides complete details of the yawsonde system. Figure 2 shows how the pressure transducers were located within the projectile. The local cone radius at the tap location was 49.9mm and the pressure ports were 1.59mm in diameter. Pressure transducers were located at two of the following radial locations: 0%, 36%, or 71% of the local cone radius from the projectile centerline.

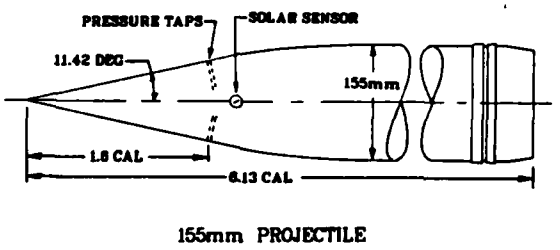

Figure 1. 155mm Projectile

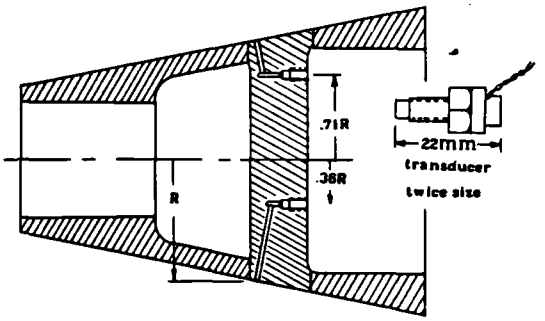

Figure 2. Pressure Ports and Transducer Mount

The pressure transducers used in these experiments were supplied by the Kulite Corporation and are miniature, solid-state semiconductor strain-gage sensors with a four element bridge circuit. The transducer is equipped with 10-32 threads and merely has to be inserted in a drilled and tapped hole--the approximate size can be seen from the sketch of Figure 2. The diaphragm end of the transducer along with the threaded section is 11mm long. The transducers are rated for 25 psia full scale; however, they are equipped with mechanical stops for an overload protection of 40 times the rated pressure. The transducer sensitivity to acceleration is very low and is quoted to be typically 0.0005% of full scale per g perpendicular to the diaphram and 0.0001% transverse to the diaphram.

The telemetry system was a three channel FM/FM system and a partial schematic is shown in Figure 3. Amplified voltages from the pressure transducers were used to modulate a 22 kHz and a 30 kHz voltage controlled oscillator (VCO). The yawsonde pulses were amplified and used to modulate a 70 kHz VCO. The outputs from the three VCO's were mixed and used to modulate a radio frequency transmitter (250 mHz, 100 mW). The transmitted signal was received by a Ballistic Research Laboratory (BRL) Instrumentation Station situated near the launch site. The carrier signals were demodulated by a telemetry receiver and the video outputs of the receivers were recorded on a high frequency response analog tape recorder. The video outputs of the telemetry receivers represent the recovered, mixed VCO signals.

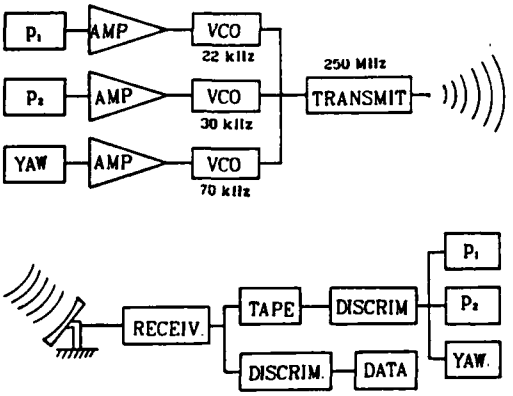

Figure 3. Telemetry System, Block Diagram

Four projectiles were fired in the test program and were designated as BRL 1839, -40, -41, and -42. The battery power of BRL 1840 was depleted during a delay caused by a misfire and no data were obtained from this flight. Just prior to loading the projectiles, power supply voltage was turned on and the transducer gages were shorted to provide a zero pressure equivalent. Then, the short was removed which permitted the transducers to measure the local ambient pressure. These pre-flight calibration signals were transmitted and recorded. The local ambient pressure and temperature were also recorded by independent measurement. Range radar was used to provide elapsed time, altitude, total velocity, and other trajectory parameters. Infrared sensors were used to detect muzzle blast for a time-zero indication.

Recorded data were discriminated using standard techniques. The raw signals were then low-pass filtered at approximately 250 Hz by precision analog filters; at the same time, the signals were amplified by a factor of 2.5. The exact filter frequency was adjusted so that the time delay was the same for each pressure, making relative phase of the signals correct. Pressure data were digitized by a VAX Laboratory Peripheral Accelerator, a sub-system for a VAX 11/730 computer, at a rate of 2,500 samples per second for each channel. For a spin frequency of 120 Hz, at least 20 samples per channel were recorded for each revolution of the projectile. Further computer processing was carried out which included applying calibration constants and digital filtering of selected data. Pressure measurements were non-dimensionalized by the constant value of sea-level atmospheric pressure.

III. Discussion:

For continuously changing pressures, there is concern that the pressure at the diaphragm may not be an accurate approximation to the pressure on the model surface. For rapidly fluctuating pressures the tubes must act as acoustic transmission lines and, if resonance occurs, the measured pressure can be in substantial error. Blake (9) shows that for tube lengths shorter than 0.25 wavelength the resonance should not affect the measurement. For a projectile spin rate of 120 Hz, the above criterion would permit tube lengths up to 0.7m, or for tube lengths of 50mm (maximum for this test) a maximum frequency of 1,400 Hz would be permitted. Viscous effects impede the flow in small pressure tubes and

therefore cause the pressure at the transducer to lag behind the pressure at the surface. Reference (10) provides a relationship for the stabilization time required for a given accuracy and a given step change in pressure. Using the criteria of Reference (10), "times" on the order of 30 microseconds were required for a one percent error, but since the actual pressure changes were not step changes, the required time should be even smaller. A pressure gradient can be supported in the pressure tubing of a spinning model by the centrifugal forces on the air column. The difference in pressure between the model centerline and the surface at the tap location is near one percent at the spin rate of 120 rps.

A transonic code by Reklis (11) was used to compute the pressure on the conical section of the projectile. Reklis used numerical techniques to solve the three-dimensional transonic small disturbance equation for slender bodies at angle of attack. The computation is based on a plane relaxation technique involving Fourier transforms to partially decouple the three-dimensional difference equations. An advantage of the technique is that only four circumferential computational planes (0, 90, 180, 270 deg) are needed. The code has been used extensively and performs particularly well over projectile forebodies. The computations are for steady flow, but nevertheless are used, with caution, to help evaluate the quality of the pressure measurements.

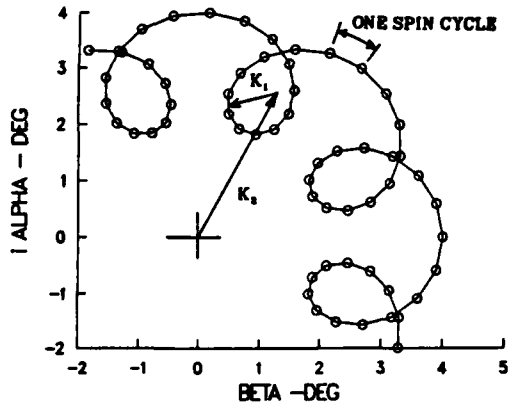

Figure 4. Typical Epicyclic Motion

Figure 4 is an illustration of the motion in the angle-of-attack plane of a spinning, statically unstable projectile which is precessing (slow mode) and nutating (fast mode). Other possible components of motion, such as those due to mass or geometric asymmetries are not illustrated. The time for the model to complete one spin revolution is indicated by the spacing between symbols. For the present investigation, there were approximately 16 spin cycles for each nutational cycle and approximately 8 nutational cycles for each precessional cycle. As the projectile goes through one spin cycle, each pressure tap will experience a windward and leeward pressure corresponding to the total angle of yaw. Therefore, pressure oscillations will occur near the spin frequency and the oscillations will be modulated in amplitude as the yaw magnitude changes throughout the nutational and precessional cycles.

IV. Results:

Pressures measured by each of the gages of round No. 1839 are shown in Figure 5 for a 10 second interval and are seen to be nearly equal (note the shifted ordinate scale for p_2). The data are too compressed to see oscillations due to spin, but in the early part of the flight the variations resulting from fast mode yaw are detected. Also, the decreasing amplitude of oscillation indicates damping of the fast mode yaw arm. The average pressure level at launch is seen to be about 20 percent greater than ambient pressure and it then steadily decreases as the projectile rises in altitude and decreases in velocity. Data for a smaller time increment (Figure 6) show the pressure oscillations due to spin and now clearly show the modulation in amplitude resulting from projectile nutational motion. Both pressures from Round No. 1839 are shown in Figure 7 for a small time interval and show the sinusoidal nature of the pressure oscillation. The absolute pressure levels are seen to be different by about 1.5 percent, which is quite good for a DC measurement using an FM/FM telemetry link, but the peak to peak values appear to be nearly equal. The oscillations are seen to be 180 degrees out of phase, as expected.

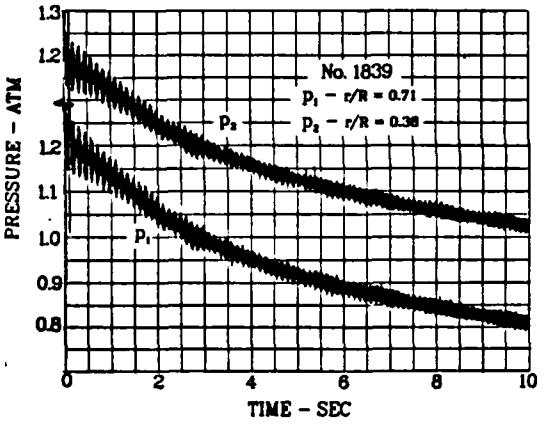

Figure 5. Ten-Second Pressure History

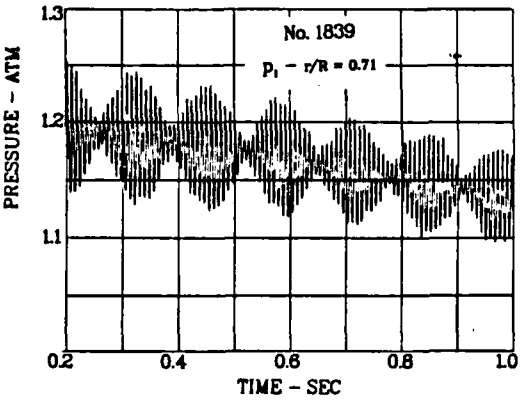

Figure 6. Pressure Oscillations

Trajectory data were obtained from position radar but were not obtained for approximately the first four seconds of flight due to time required for lock-on. Launch conditions were known and trajectory data for the four second interval were obtained by interpolation. The launch velocity was obtained from the launch spin rates obtained from the yawsonde data and from the known rifling twist rate. Standard atmospheric conditions were assumed to exist and were adjusted slightly for the sea level temperature and pressure as measured. With the assumed temperature profile, the velocity of sound could now be determined and with the

radar velocity data, the Mach number was computed. Altitude data and Mach number data are shown in Figures 8 and 9, respectively. The trajectory data for Round No. 1841 are somewhat different from the other two rounds.

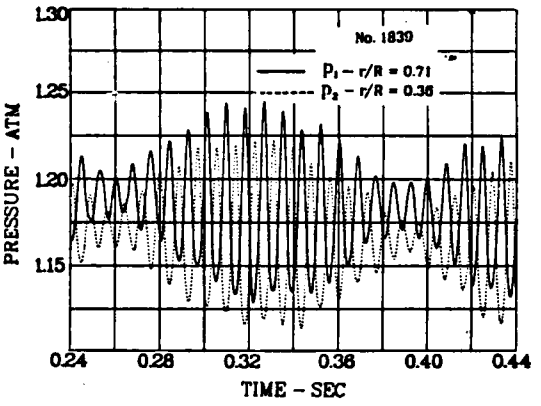

Figure 7. Comparison of p_1 and p_2

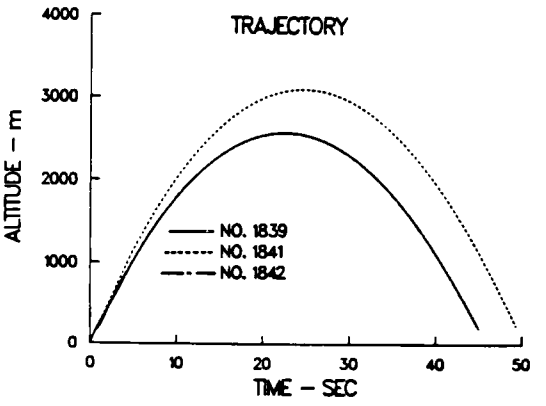

Figure 8. Trajectory Altitude

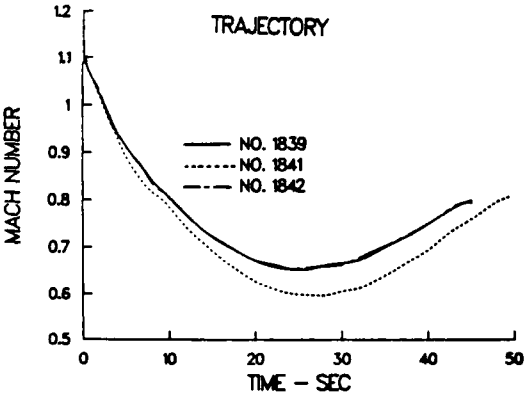

Figure 9. Trajectory Mach No.

The average of pressures at positive and negative angles of yaw should be *very nearly* equal to the zero-angle pressure. The pressure data were digitally low-pass filtered to remove the oscillations and leave only the slowly changing component due to velocity and altitude changes. A zero angle-of-attack computation was made for the Mach number range of the trajectory and compared with the measurements in Figures 10-12. Figures 10-11 (Rounds 1839, 1841) shows good agreement between the two pressures and the computation. Figure 11 (Round No. 1841) shows that the measured pressures p_2 agree with the computation a little better than the pressures p_1. The p_1 results are seen to be consistently biased slightly below the p_2 results. Figure 12 (Round No. 1842) shows both pressures to be lower than computed values and p_1 being slightly lower than p_2. Since all four of the above pressure histories agree with computation, it is believed that the measured values of Round 1842 are incorrect. The nature of the discrepancy indicates that the error may be due to a zero shift in the system.

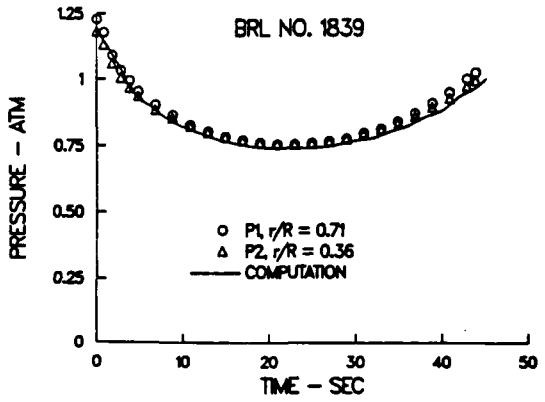

Figure 10. Altitude and Mach Number Effect on Pressure

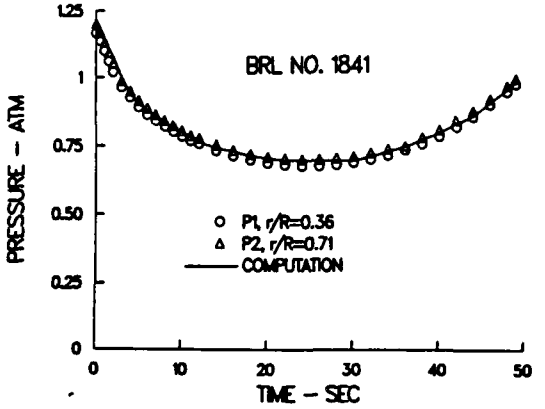

Figure 11. Altitude and Mach Number Effect on Pressure

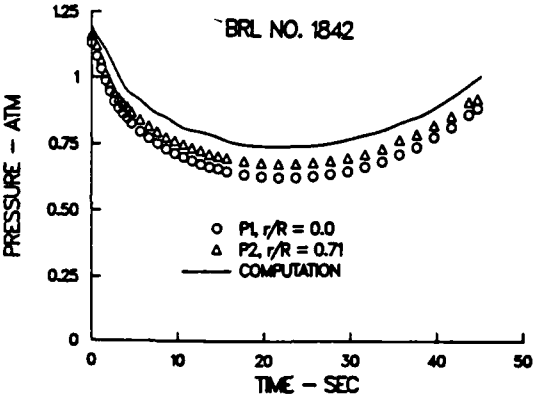

Figure 12. Altitude and Mach Number on Pressure

Figures 13-16 are samples of data obtained from the yawsonde solar sensors for round No. 1839. Figure 13 shows yaw data for the entire trajectory. The precessional behavior is readily seen from the largest oscillations and the fast mode yawing motion is barely seen as small perturbations on the precessional cycles in the early portion of the flight. The fast mode yaw damps out and is not visible at the end of the flight. The precessional frequency is seen to decrease as the projectile reaches apogee, at 22 seconds, and then increases in frequency toward the end of the flight as the altitude decreases. Figure 14 shows the first 10 seconds of yaw data which give a much clearer picture of the projectile behavior and indicates an epicyclic motion. Projectile spin is shown in Figure 15 and steadily decays over the entire flight. The yawsonde system actually measures an Eulerian spin which evidences oscillations due to the yawing motion. An estimate of the spin rate is obtained by averaging the oscillations. The above yaw data are solar aspect angles and do not show the true complex yaw angle but do show the projection of the epicyclic motion onto a plane. The correct complex motion (pitch and yaw behavior) can be extracted from yawsonde data (12) but will not be attempted at this time. For circular precessional motion, the yawsonde angles will be correct when precession is at a local maximum or minimum. The yaw data were

filtered to separate the nutational and precessional motions and are shown in Figure 16. The yaw angles at the time of a precessional maximum or minimum were taken as approximate values, since precession is not actually circular, for purposes of computation.

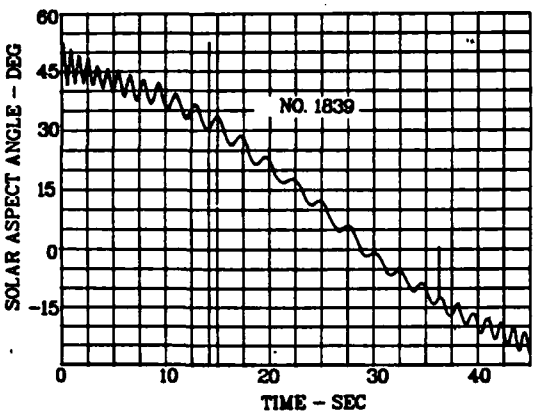

Figure 13. Yaw Behavior, 45 Sec

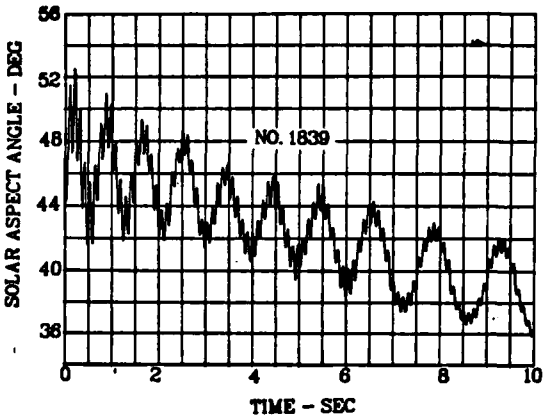

Figure 14. Yaw Behavior, 10 Sec

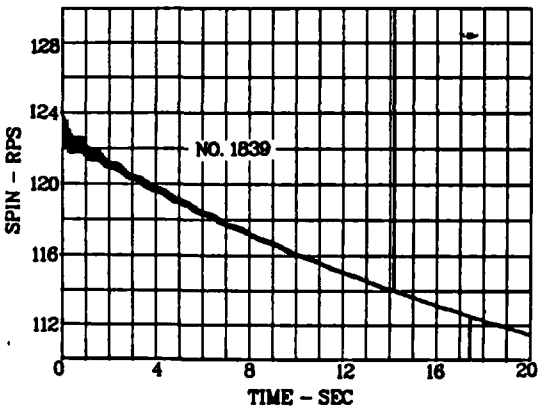

Figure 15. Spin History, 20 Sec

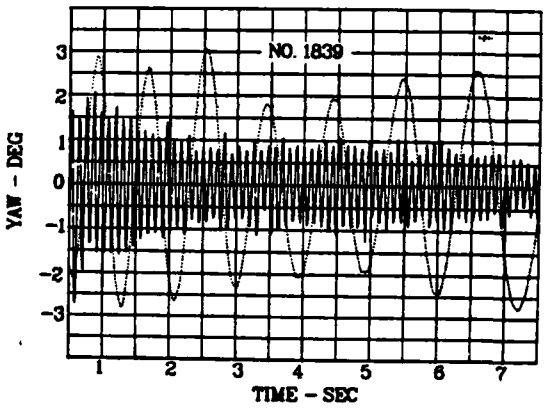

Figure 16. Nutational and Precessional Components of Yaw

A curve placed along the peaks of the pressure oscillations as shown in Figure 17, describes the degree of modulation due to changing yaw angle. The demodulation (envelope) makes a comparison of two oscillating pressures much easier as seen from the pressures of Figure 18 (No. 1839). The figure shows that both transducers sensed the same oscillating pressures and the minor differences give an indication of the experimental accuracy. A few computational results, for the approximate angles obtained as stated above, are also shown on Figure 18; the computed

values are slightly larger at both the peaks and valleys, but total excursion is nearly equal to the measured values. The difference between the measured and computed results are equivalent to about 1/3 degree in yaw and the agreement is considered to be very satisfactory since the angles obtained from the yawsonde results are only approximations.

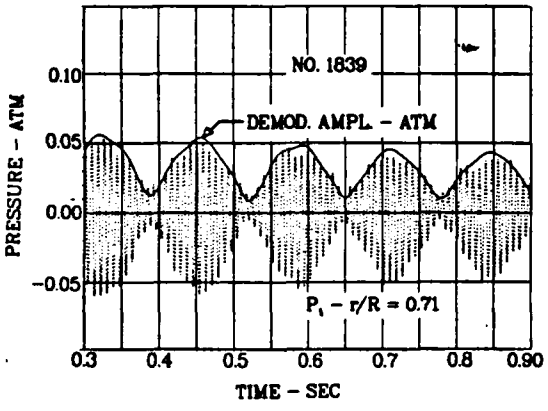

Figure 17. Oscillating Pressure and the Demodulation Amplitude

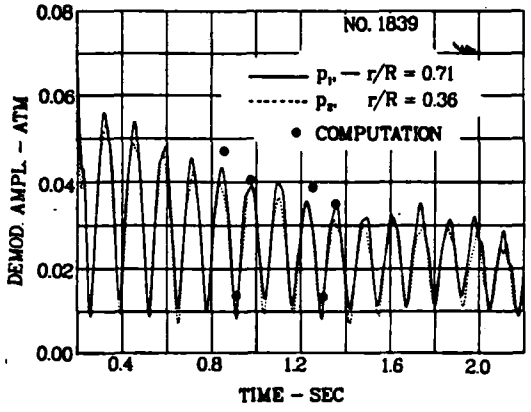

Figure 18. Demodulation Amplitude Computation and Experiment

The data of Figures 11 and 12 are examined further in Figures 19-22. Figure 19 compares oscillating pressures p_1 and p_2 for Round No. 1841. The peak-to-peak values are seen to be approximately equal in amplitude and the general behavior of both pressures is consistent. The highly expanded ordinate scale clearly shows the p_1 values to be 2-3 percent lower than the p_2 values. Figure 20 shows the demodulation amplitudes for the same pressures over a 2.0 second time span and the agreement is

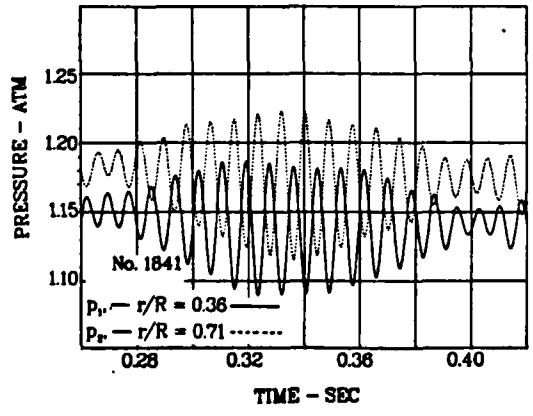

Figure 19. Comparison of p_1 and p_2

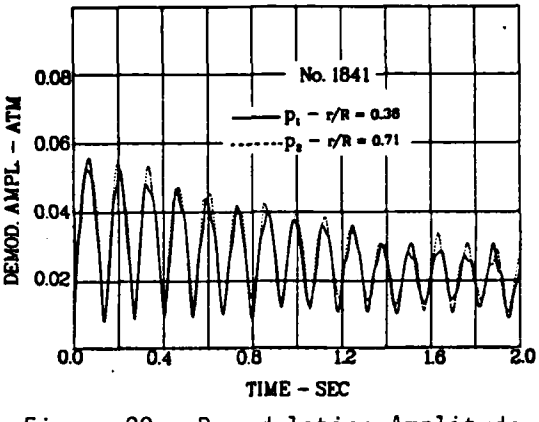

Figure 20. Demodulation Amplitude

considered to be generally good. Local discrepancies are seen to exist but there is no bias in the two sets of data which indicates that the gage sensitivity factors used in the data processing are correct. The 2-3 percent differences shown in Figure 19 must therefore be a zero offset. Figure 21 compares oscillating pressures p_1 and p_2 for Round No. 1842; the amplitudes of oscillation appear to be about equal but the absolute level differs by about 3 percent; again, the general behavior of both pressures is consistent. The decay of pressures during the first 100 milliseconds of the flight is evidently due to the projectile emergence from the muzzle gases. Figure 22 compares demodulation amplitudes for the same two pressures and the agreement is seen to be good over a 2.0 second time span and indicates correct sensitivities for both transducers. Therefore, the discrepancies shown above in Figure 12 must be primarily zero shifts.

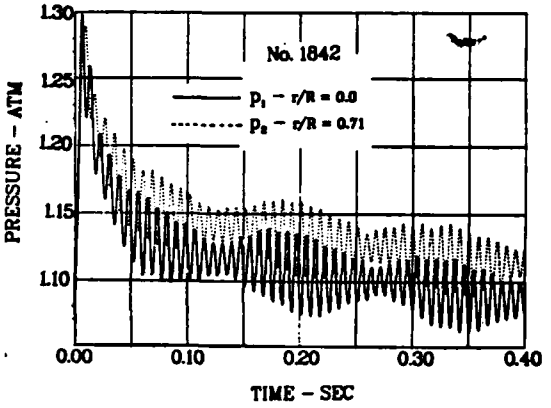

Figure 21. Comparison of p_1 and p_2

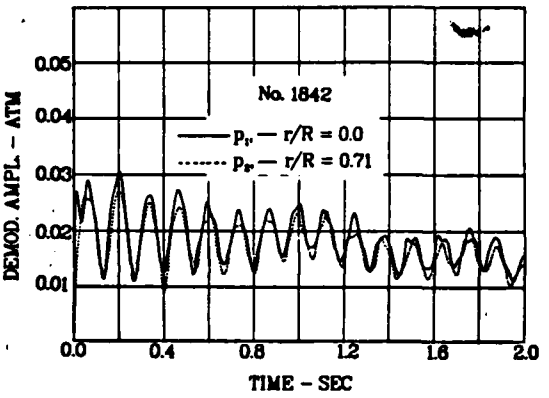

Figure 22. Demodulation Amplitude

Apparently the present instrumentation technique, gage and circuit calibration, needs to be refined to avoid zero shifting. It is believed that the zero shifting took place under the severe conditions of launch and suggests that in-flight calibrations could eliminate the affects of such changes.

Not all aspects of the experimental results have been fully investigated. For example, the demodulated data of Figures 18, 20, and 22 do not show a smoothly varying periodic nature as might be expected. This condition can also be seen in Figure 17 where the pressure peaks due to spin do not follow a smooth curve. This phenomenon may result from limitations in the measurement capability or it may be the result of small angular motions, other than nutation or precession, which occur at the spin rate. For example, a third yaw arm could result from a mass asymmetry or a small geometric asymmetry.

V. Conclusions:

1. Accurate pressure measurements are attainable from gun launched projectiles.

2. Computation and duplication of measurement were both needed to evaluate the quality of the results.

3. Transducer calibrations, zero crossing but not sensitivity, appear affected by high-g launch conditions and in-flight calibrations are needed.

4. Variations in amplitude of pressure oscillations describe the yawing motion of the projectile.

5. Additional aspects of flight behavior such as yaw of repose and yawing motion at spin frequencies should be investigated.

6. Though not fully assessed, pressure lag times or resonance are believed to not be a problem.

References:

1. Mermagen, W.H., "Measurements of the Dynamical Behavior of Projectiles Over Long Flight Paths," Journal of Spacecraft and Rockets, Vol. 8, No. 4, April 1971, pp. 380-385.

2. Miller, M.C., "Wind Tunnel Measurements of the Magnus Induced Surface Pressures on a Spinning Projectile in the Transonic Speed Regime," AIAA Paper No. 83-1838, Applied Aerodynamics Conference, July 1983.

3. Mark, A., "Pressure Measurements on a Spinning Wind Tunnel Model by Means of Telemetry," U.S. Army Ballistic Research Laboratory, Aberdeen Proving Ground, Maryland, Memorandum Report No. 2750, May 1977. AD A040909.

4. D'Amico, W.P., "Demonstration of a Technique for the Measurement of Surface Pressures on Spinning Wind Tunnel Models via Telemetry," U.S. Army Ballistic Research Laboratory, Aberdeen Proving Ground, Maryland, Memorandum Report No. ARBRL-MR-03017, April 1980. AD B047875L.

5. Mark, A., "Free-Flight Base Pressure Measurements on 8 Degree Cones," U.S. Army Ballistic Research Laboratory, Aberdeen Proving Ground, Maryland, Technical Report No. ARBRL-TR-02179, July 1979. AD A075365.

6. Clay, W. H., D'Amico, W. P., Mark, A., and Mermagen, W. H., "Measurements of Payload Temperature On-Board the XM687 155mm Binary Projectile," U.S. Army Ballistic Research Laboratory, Aberdeen Proving Ground, Maryland, Memorandum Report No. 2508, July 1975. AD B007023L.

7. Whiting, R. D., "An Experimental Study of Forced Asymmetric Oscillations in a Rotating Liquid-Filled Cylinder," U.S. Army Ballistic Research Laboratory, Aberdeen Proving Ground, Maryland, Technical Report No. ARBRL-TR-02376, October 1981. AD A107948.

8. Hepner, D. J., "Rotating Liquid Pressure Measurements for Low Reynolds Numbers," Paper presented at the 38th Meeting of the American Physical Society, University of Arizona, Tucson, Arizona, November 1985.

9. Blake, W. K., "Differential Pressure Measurement," Chapter 3 of Fluid Mechanics Measurements, Hemisphere Publishing Corp., edited by Richard J. Goldstein.

10. Volluz, R.J., Handbook of Supersonic Aerodynamics, Section 20, "Wind Tunnel Instrumentation and Operation," NAVORD Report No. 1488 (Vol. 6), January 1961.

11. Reklis, R.P., Sturek, W.B., and Bailey, F.R., "Computation of Transonic Flow Past Projectiles at Angle of Attack," AIAA Paper No. 78-1182, AIAA 11th Fluid and Plasma Dynamics Conference, Seattle, Washington, July 1978.

12. Whyte, R.H., and Mermagen, W.H., "A Method for Obtaining Aerodynamic Coefficients from Yawsonde and Radar Data," Journal of Spacecraft and Rockets, Vol. 10, No. 6, June 1973, pp. 384-388.

MODELING THE SPREAD OF LIQUID DROPLETS ON NON-IDEAL SURFACES

MR. JOEL M. KLEIN
U.S. ARMY CHEMICAL RESEARCH AND DEVELOPMENT CENTER
ABERDEEN PROVING GROUND, MD 21010-5423

I. INTRODUCTION

When a single droplet of liquid impacts on a solid surface, a number of simultaneous events begin. The liquid can be sorbed into the surface; it can evaporate into the environment; and it can spread on the surface. These processes are competitive. In order to describe the behavior of the droplet from the moment of impact until the last traces of the liquid have disappeared, one must propose a model that will account for all of these competitive and interacting phenomena.

The objective of the current research program titled "Drop Fate" is to propose a mathematical model that can be used to predict quantitatively the time history of a liquid droplet from the instant of its impact with a solid surface until the liquid no longer presents a hazard to exposed personnel. The program has been developed in response to a requirement to model the hazards created by liquid chemical warfare agents which are deposited on surfaces of interest to the military. Previous research has been conducted on the evaporation of droplets after deposition (1) and on the sorption of liquids into surfaces. (2) In each of these cases, it has been assumed that the process being studied occurs independently of any other competitive process. This assumption is needed to permit closed form solutions to the mathematical models that have been generated.

The spread of liquid droplets on solids is a topic of significant current interest. Within the past two years, two major review articles have been published discussing the theory of liquid droplet spread. (3-4) The appearance of these two papers, in turn, reflects the current research efforts being conducted in a number of laboratories throughout the world to gain an understanding of these interacting processes.

While the spread of liquids on highly polished surfaces (e.g., glass) has been reported and understood for years (5), the behavior of liquids on real world (i.e. non-ideal) surfaces is only poorly understood.

In order for a comprehensive mathematical model to be formulated describing the fate of a liquid droplet, it is necessary to develop a model which describes droplet spread on non-ideal surfaces. In this paper, I present some possible models that can be used and describe the experimental work that has been conducted to verify the selected model.

II. PROPOSED MODELS

The requirement for spontaneous spreading of liquid to occur on a solid surface is that there must be a driving force sufficient to overcome the surface tension forces of the liquid and to permit the formation of new liquid surface on the existing solid. Equations are formulated to describe the motion of the line formed at the three phase line, the intersection of the liquid droplet, the solid surface, and the environmental gas phase. (Figure 1) The forces that must be considered include gravity, friction, electrostatic, and free energy differences. The interaction of these forces is quite complex, and possible models can be proposed that will give different predictive equations depending on the assumptions made. Since the motion of the liquid proceeds on a molecular scale, a preferred model should describe the motion in terms of atomic and molecular parameters. However, the only properties of the materials that can be readily measured in the laboratory are bulk properties of the system. Accordingly, the models proposed here are stated in terms of these bulk properties and therefore have inherent simplifying assumptions.

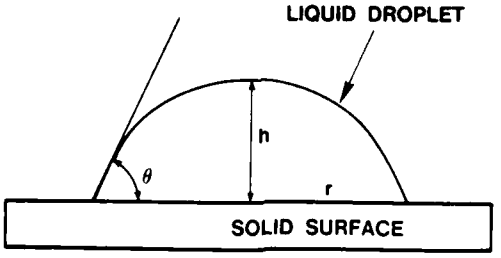

CONTACT ANGLE θ

FIGURE 1

The principal efforts in developing these models were made by Dr. Franklin Dodge and his colleagues at Southwest Research Institute. (6) For a complete description of the models and their derivations, one should refer to the final report prepared by Dr. Dodge. In Table 1, I present the generalized equation to describe the motion of the three phase line shown in Figure 1 along with the appropriate boundary conditions. Given this starting point, the initial conditions assumed for three possible models and the final proposed mathematical formulas for the spreading functions are presented in Tables 2-4.

TABLE 1

INITIAL SPREAD EQUATION

$$\mu \, \partial^2 V_r / \partial z^2 = \partial P(r,t)/\partial r$$

V_r = RADIAL VELOCITY
μ = LIQUID VISCOSITY
z = DROP HEIGHT
$P(r,t)$ = FLUID PRESSURE
t = TIME
h = DROPLET HEIGHT AT $t = 0$

SUBJECT TO BOUNDARY CONDITIONS

$$\partial V_r / \partial z = 0 \quad \text{AT} \quad z = h(r,t)$$

$$V_r = (\alpha/3h)\, \partial V_r / \partial z \quad \text{AT} \quad z = 0$$

α = SLIP COEFFICIENT

The first proposed model, called the Contact Line Velocity Model, begins with the assumption that the velocity of the three-phase contact line, shown in Figure 1, is proportional to the difference in cosine of the contact angle formed by the drop at the instant of contact and the angle formed after the droplet has spread. This proportionality includes a term containing such macroscopic parameters as the liquid vapor interfacial tension, σ_{LV} , and the viscosity of the liquid, μ . The result of this model is a predictive equation that relates the increase in droplet radius to time raised to the 1/7th power.

TABLE 2

CONTACT LINE VELOCITY MODEL

IN GENERAL $V_r = K[f(\cos\Theta_0 - \cos\Theta)]$ AT $h = 0$

$K \partial \gamma_{LV}/2\ Vol$

γ_{LV} = SURFACE TENSION
η = LIQUID VISCOSITY
Vol = INITIAL DROPLET VOLUME

FOR $\Theta_0 \simeq 0$

$$\dot{R} = K(1 - \cos\Theta)$$

AND FOR $\Theta \simeq 0$

$$\dot{R} = K\Theta^2/2$$

COMBINING WITH PREVIOUS DEFINITIONS

$$R = [7/2\ K\ (4\ Vol/\pi)^2 t + R_0^7]^{1/7}$$

WHICH PREDICTS AREA CHANGE PROPORTIONAL TO $t^{2/7}$

The second model, called the Spreading Force Model, is based on the assumption that the spread of the liquid droplet proceeds in the manner analogous to the frictional flow of a lubricant. The velocity of the contact line is again proportional to the cosine of the contact angle, but the model includes the spreading coefficient, s, and a friction term, α. The predictive equation that is generated by this model relates the increase in the spreading radius to time raised to the 1/10th power.

TABLE 3

SPREADING FORCE MODEL

$$\mu/R \int_0^R r\,(\partial V_r/\partial z)\Big|_{z=0}\,dr = S(1 - \cos\Theta)$$

WHERE S = SPREADING COEFFICIENT

WHICH YIELDS

$$R = \left[\frac{5S}{3\mu}\left(\frac{4\,V_0}{\pi}\right)^3\left(\frac{t}{\ln 2/\alpha\beta - 1}\right) + R_0^{10}\right]^{1/10}$$

β IS AN INTEGRATION CONSTANT

THIS PREDICTS THAT AREA CHANGE IS PROPORTIONAL TO $t^{2/10}$

By examining the spreading conditions on an atomic level, one can propose a model which is more generalized than the two previous models and which conceptually can account for non-ideal surfaces. Here, the motion considered is between atomic sites along the velocity line where n is the net number of sites involved. From analysis of this model, one can predict that the radius will increase in proportion to time raised to the 1/(3n+1). The general equation for the increase in radius given in Table 4 reduces to the Contact Line Velocity Model for the ideal case where two sites are involved.

TABLE 4

GENERALIZED MODEL

$$\partial R/\partial t = 2K\lambda \sin h [\sigma_{LV}/kT\,\Delta n\,(\cos\Theta_{eq} - \cos\Theta)]$$

HERE K IS NET NUMBER OF MOLECULES MOVING OUT RADIALLY
λ IS AVERAGE DISTANCE BETWEEN ABSORBTION SITES
Δn IS NET NUMBER OF SITES AFFECTED

THIS YIELDS

$$R = \{3K(n + 1/3)\,(4V_0/\pi)^n t + R_0^{3n+1}\}^{1/(3n+1)}$$

WHERE $n \leq 2$

IF n = 2, THIS IS THE CONTACT LINE VELOCITY MODEL

These three models, based on different conceptions of the spreading process, yield equations that are distinguished readily if controlled spreading tests are conducted. One need only examine the spreading rate observed as a function of time to identify the most probable model for future use. However, it is clear that the experiments must be conducted with care to insure that the results are meaningful. In an earlier experimental program, estimates were made on the spread of HD droplets placed on polyurethane painted steel plates. (Table 5). Although the paint used was the same for all twelve plates shown and the HD used was the same liquid in all cases, the spread was highly variable. These data emphasize the need for careful control of the experimental environment in any program used to identify a predictive model of the spreading process.

TABLE 5

SPREAD OF HD DROPLETS ON POLYURETHANE PAINTED STEEL

% of plate covered	
25 mg droplet	5 mg droplet
35	30
15	20
35	15
80	8
95	20
35	15

III. EXPERIMENTAL

The general experiment conducted to aid in identifying the appropriate model of the spreading process consisted of preparing the painted surface, characterizing it as described below, placing a single weighed droplet of the test liquid onto the surface, and following the droplet spread by videotaping the motion on the surface. The test surface was mounted in an environmental chamber (Figure 2) which permitted the surface to be conditioned before the spread experiment was conducted. The test plate was mounted on the pan of an electronic balance so that the loss of weight due to evaporation could be followed during the spreading motion experiment. To time the experiment, a digital clock was contained within the field of view of the video camera. The liquid droplet was placed on the surface from a syringe located outside the chamber. After the droplet was placed on the surface, the syringe was withdrawn from the field of view to avoid interference with video-taping. Measurement of the area at any time was accomplished by displaying the image of the droplet on a video monitor screen and tracing the image onto paper. A ruler was also included in the camera's field of view to give a distance scale. Planimeter measurements were made to obtain the area.

The materials and experimental conditions used in this test program are listed in Table 6. The paints were applied to primed steel plates in accordance with the appropriate Military Specifications. The plates, originally 4"X12", were cut to 4"X4" before use. Their surfaces were cleaned thoroughly by washing them in a surfactant solution using an ultrasonic bath. The plates were then rinsed with distilled water, alcohol, and distilled water again. After the final rinse, the plates were dried in a vacuum desiccator and stored there until ready for use.

SPREADING-DROP APPARATUS
(CUTAWAY VIEW)

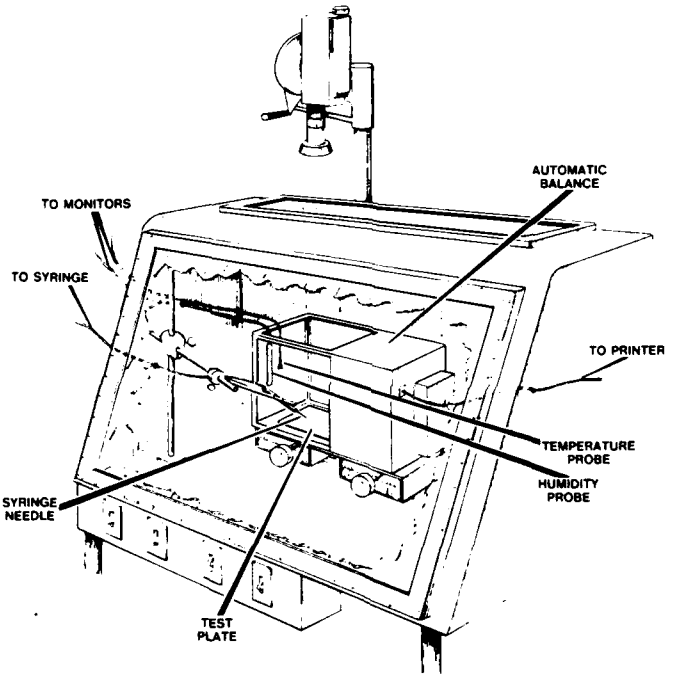

FIGURE 2

TABLE 6

CONDITIONS STUDIED IN CURRENT SPREADING RATE EXPERIMENTS

	(+)	(-)
Surface	Polyurethane Paint	Alkyd Paint
Liquid	Methyl Salicylate	Diethyl Malonate
Temperature	100^{o} F	70^{o} F
Humidity	80% RH	20% RH
Weight	25-30 mg	10-15 mg

To characterize the surfaces of the test plates, measurements were made of the distilled water contact angle at various points on the surface. A novel experimental procedure was developed to measure the contact angle on large plates. (7) By means of this test, the uniformity of the free energy on the test surface was insured. In addition, the critical surface tension was also determined by measuring the contact angle of a series of mixtures of ethanol and water, and the results were compared with values reported in the literature. (8) After treating the plates by the procedures described above, the water contact angle and the critical surface tensions measured were in good agreement with the values reported in the cited literature.

For each spreading rate experiment, one test plate was placed in the environmental chamber on the pan of the electronic balance. The chamber atmosphere was adjusted to the desired test conditions. After equilibrating, the test was begun by placing a single droplet onto the center of the test plate. The videotape unit was controlled by a timer programmed to make recordings for the first five minutes of the test and then at predetermined intervals up to two hours after the start of the test. If there was any weight loss during the progress of the experiment, this was recorded in addition to the other test data. Three tests were run for each set of conditions.

IV. RESULTS AND DISCUSSION

Thirty-two tests were run, sixteen each with two paint types. The area of the droplets was measured at two seconds, and measurement continued until the droplet could no longer be seen or for two hours, whichever occurred first. Typical results, averaged for the three runs, are shown in Figure 3 for comparable tests conducted with an alkyd paint and a polyurethane painted surface. The area covered by the droplet deposited on the alkyd paint was greater than that for the corresponding polyurethane sample, indicating that the spreading rate was greater for this paint.

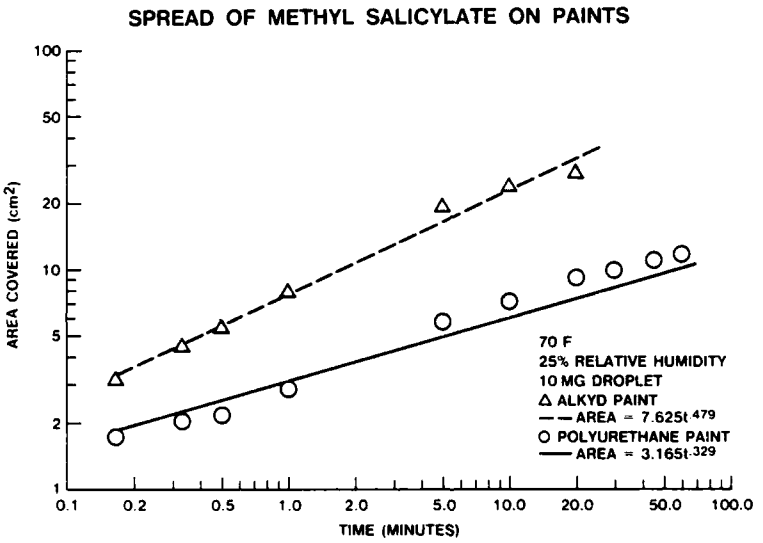

FIGURE 3

All the data were subjected to regression analysis to determine the coefficients in equation 1.

$$\log(\text{area}) = k + b*\log(\text{time}) \qquad (1)$$

The area of the spread was measured since some of the droplets did not give uniformly circular spreading patterns. The effect of reporting the results in terms of area is to multiply the exponent in each of the proposed models by 2. Listed in Table 7 are the values for k and b determined and the conditions for each of the tests. The high values (+) and the low values (-) are the same as those listed in Table 5.

Results of the experiments for the polyurethane painted plates are consistent with the models proposed earlier in Tables 2 and 4. Although the expected value for b (2/7 or .286) in the Contact Line Velocity Model is slightly lower than the values found for these tests (.339), it is not unreasonable to accept this simpler model as being correct for these data. The results can be subdivided into two groups based on the relative humidity (RH) present when the tests were conducted. Those tests at 80% RH had higher values of b than the comparable low humidity tests, indicating that the surface free energy was lowered by the increased presence of the water vapor promoting faster spread. The average value for b for the low humidity experiments was .326 and the value for the high humidity runs was .353. As predicted by these models, increases in droplet volume (weight) and temperature should result in increases in the coefficient k which is observed. It is also observed that changes in the surface tension of the test liquids are proportional to changes in the computed values of k.

For polyurethane paint, the model of the spreading process can be a good predictor of the expected behavior of the liquid droplets. On the other hand, the data analysis for alkyd painted steel is less clear. The value of k increases as the droplet weight and volume increase. However, the data do not reveal the same clear trends revealed in the polyurethane paint experiments. The values of b computed for these tests were always higher than those for the comparable polyurethane paint experiment and would appear to be consistent with the most generalized spreading model. If one uses the average value for b in these tests, one computes a value of n = 1.13 for the number of sites taking part in the spreading process (see Table 4).

One possible explanation for the results observed for the alkyd paint lies in an examination of the surface roughness of these paints. Cowsar and Speaker examined a series of alkyd and polyurethane painted samples and measured the roughness of the surface. (8) In general, they observed that the roughness of the polyurethane paints, expressed in terms of displacement of a test stylus from a flat plane in units of micrometers, ranged from 0-2 μm while the values for alkyd paint averaged around 3 m. In earlier models of the spreading process, the term rugosity (5) was introduced to account for this roughness; it is likely that the higher spreading rate observed for the alkyd paint can also be accounted for by this factor. No effort was made to compute this factor based on the available data. As more experiments are conducted with more liquids and surfaces, we will be in a better position to compute this factor in the model.

The need for a model of the spreading process arises from the fact that some of the processes controlling the rate of disappearance of a liquid are dependent on the exposed surface area. A typical figure of merit used is the "spread" factor which relates the maximum area of spread to the initial drop size. Although the spreading process is not independent of other competitive processes, many of the simulation computer programs currently used to model the time history of a liquid agent droplet employ a spread factor as one of the input parameters. The model that is reported here can give a prediction of the spread factor by relating the area at some time to the area at t = 0. By applying this approach, one predicts that the spread factor, s, is

$$s = t^b \qquad (2)$$

where t is the latest time of interest. This equation predicts that for a 60 minute time after deposition, the spread factor will be 3.2 if b = 2/7 as predicted for the model proposed here. Experimentally, typical spread factors can range from 2-4 for some agents of interest. (9) When combined with information on the time for spreading, these spreading models permit prediction of the spread factor for use in other simulations.

As seen clearly in equation 2, the models proposed here are open ended, implying that spreading will continue indefinitely. If sufficient liquid is present, spreading can continue until the edges of the surface have been reached. However, if competitive processes such as sorption or evaporation become the controlling processes, then the spreading will stop and the area covered will not increase. Indeed, in these experiments, I observed cases where the area decreased after a long time, indicating that evaporation of the liquid had begun to be a significant factor in the fate of that particular droplet. The overall objective of this program was stated to be the development of an integrated predictive model that will account for all the competitive processes. Currently, a program has been started to accomplish this integrated modeling. The present version of the spreading model can not account for the stopping of the spread.

Three models were proposed to describe spread. The results of my experiments have been analyzed and compared to each model. Although no clear case can be made for selecting the Contact Line Velocity Model or the Generalized Model presented earlier, it is apparent that the Spreading Force Model is not an adequate predictive model for systems such as those studied here. Since the other two models are very similar in terms of the parameters needed to describe the spread, it is convenient to select the Contact Line Velocity Model as the one to be incorporated into the overall droplet fate integrated model. By making

this selection, one need not make any assumptions on the number of atomic sites participating in the spread process as required by the generalized model. Any deviations from the predictions made by this assumption can be adequately explained by looking at the surface roughness factor discussed earlier.

V. CONCLUSIONS

A model to predict the spread of liquid droplets on non-ideal solid surfaces has been developed. The model includes terms for the viscosity, surface tension, and volume of the droplet. It is concluded that this model can be combined with previously derived models for evaporation and sorption of liquid droplets to permit derivation of an integrated droplet fate model.

TABLE 7

RESULTS OF REGRESSION ANALYSIS FOR EACH EXPERIMENT

Polyurethane Paint			Alkyd Paint	
k	b*	1 2 3 4**	k	b
2.476	.330	- - - -	5.634	.433
2.986	.367	+ - - -	8.866	.482
2.537	.317	- + - -	6.147	.447
2.952	.327	+ + - -	12.944	.492
3.384	.308	- - + -	6.249	.395
4.893	.305	+ - + -	14.210	.510
2.451	.352	- + + -	7.577	.396
3.899	.369	+ + + -	5.569	.420
3.165	.329	- - - +	7.625	.479
4.927	.336	+ - - +	12.465	.414
3.902	.374	- + - +	8.090	.462
3.436	.351	+ + - +	12.698	.529
2.754	.319	- - + +	8.758	.502
5.127	.310	+ - + +	9.400	.490
3.156	.418	- + + +	6.736	.413
5.390	.317	+ + + +	11.718	.431

* k and b are the coeffieients in equation 1.

** See Table 6 for values
1. Weight
2. Humidity
3. Temperature
4. Liquid

REFERENCES

1. Pickett, R.G. and Bexon, R. The Evaporation of Sessile or Pendant Drops in Still Air. J. Colloid and Interface Science 61, 336, (1977).

2. Sidman, K.R., et al. Absorption and Desorption of Organic Liquids by Paint Films. ARCSL-CR-82034. October 1982. Unclassified Report.

3. Maumur, A. Equilibrium and Spreading of Liquids on Solid Surfaces. Advances in Colloid and Interface Science 19, 75-102, (1983).

4. de Gennes, P.G. Wetting: Statistics and Dynamics. Review of Modern Physics 57, No. 3, Part 1, 827-863, (1985).

5. Adamson, A.W. Physical Chemistry of Surfaces. Fourth Edition. John Wiley & Sons, New York, 1982.

6. Dodge, F.T. Theoretical Model of the Spreading of Liquid Droplets on Solid Substrates. Contract DAAK11-84-C-0076. Final Report.

7. Klein, J.M. and Wasel, W.D. A Model Device for the Measurement of the Contact Angle Formed by Liquid Droplets on Solid Surfaces. CRDC Technical Memorandum In Press.

8. Cowsar, D.R. and Speaker, L.M. Interaction of Liquid Jets and Sprays with Supported Films and Drops: Substrate Characterization. ARCSL-CR-82032. October 1982. Unclassified Report.

9. Podall, R.T., et al. Exploratory Development of Contamination Monitoring Technology. Contract DAAK11-82-C-0099. Final Report.

STRUCTURAL INVESTIGATIONS AND ANALYSIS OF FRESH WATER BLUE-GREEN ALGAL (MICROCYSTIS AERUGINOSA AND ANABENA-FLOS-AQUAE) HEPATOTOXIC PEPTIDES BY TANDEM MASS SPECTROMETRIC TECHNIQUES.

*THAIYA KRISHNAMURTHY, DR.
LINDA SZAFRANIEC, MRS.
EMORY W. SARVER, DR.
CHEMICAL RESEARCH AND DEVELOPMENT CENTER
ABERDEEN PROVING GROUND, MD 21010-5423

INTRODUCTION

Some fresh water blue-green algal (cyanobacteria) blooms have been linked to loss of livestock and human health hazards in several countries.[1] Most of these reported cases have been attributed to a single species of cyanobacteria, known as Microcystis Aeruginosa. The growth of these toxic blooms is facilitated by increased environmental pollution as well as by a natural phenomenon (eutrophication) during which the amount of dissolved oxygen in fresh water is reduced as a result of the increase in the mineral and organic nutrients in a stagnant body of water.[1] The toxins isolated from the blue-green algal blooms were observed to be either hepatotoxic or neurotoxic.[1] Information on the structures and physico-chemical properties of these toxins is vital for their detection in natural fresh water supplies and for subsequent clean-up of contaminated sources.

The available information on chemical structures and properties of blue-green algal toxins is very limited. As a result, several investigations have been initiated recently in order to elucidate the structures and study the properties of these toxins.[1] In most instances, the blue-green algal toxins have been found to be small peptides with molecular weights in the range of 1,000 Daltons.[1] Botes et.al., have reported the structure for a hepatotoxin derived from a South African species of Microcystis Aeruginosa, which was deduced to be a cyclic peptide containing seven amino acids. This is the only reported, unambiguously established structure for any known blue-green algal toxin.[2]

We have recently investigated a hepatotoxin, termed as Akerstox, isolated from the natural blooms of Microcystis Aeruginosa in Akersvatn (Akers Lake), Norway. The toxin also was found to be a cyclic peptide with five common amino acids along with two uncommon ones. The identities of the latter and the sequences of all amino acids in the peptide were determined to be, -Ala-Leu-Masp-Arg-Adda-Glu-Mdha-, based on the fast atom bombardment tandem mass spectral data of the intact peptide, its derivatives, and chemical degradation products. This structural elucidation was accomplished in less than two days, using only picomole quantities of the intact peptides. The proton and ^{13}C nmr spectral data were also in support of this sequence. This toxic peptide was also observed in fresh water sources in Scotland, and the USA (Microcystis Aeruginosa) and Canada (Anabena flos-aquae). A lesser toxic peptide was also isolated from the latter source, and its structure was determined to be, Ala-Leu-Asp-Arg-Adda-Glu-Mdha-, by a similar approach.

The blue-green algal toxic peptides under thermospray ionization conditions formed both singly and doubly charged molecular ions. A similar phenomenon was observed in the case of other cyclic peptides as well.[3] This specific property was found to be applicable to develop a rapid tandem mass spectrometric method of analysis for these toxic compounds. This is very essential for the speedy detection and clean-up of the contaminated natural (drinking) waters to prevent any economic loss and/or disasters.

EXPERIMENTAL

Glass distilled HPLC grade solvents and ultra pure chemicals were used through out the investigation. The isolation and purification of blue-green algal toxic peptides and their amino acid analysis results have been described elsewhere in detail.[4] Peptide standard solutions were made up in methanol or in aqueous 5% acetic acid and stored in the refrigerator at $2^{o}C$.

Permethylation of Akerstox: The procedure developed by Roepstorff[5] for acetylation and permethylation of peptides was adapted. A standard solution containing 20 μg of the intact peptide was lyophilized in a test tube (6mm id x 50mm). The residue was dissolved in methanol (100 μl) and treated with acetic anhydride (50 μl) and left at ambient temperature for one hour. The solvent was removed under vacuum, and the tube containing the residue was flushed with nitrogen and sealed with teflon film.

Dimethyl sulfoxide was dried and distilled over CaH_2 and stored over CaH_2 in the refrigerator. A vial (5ml) containing potassium-t-butoxide (50mg) in DMSO (2 ml) was flushed with nitrogen and heated at 70°C for one hour. The resulting yellow solution containing a fluffy white precipitate was centrifuged and the supernatant was transferred to a small dry test tube. The tube was flushed with nitrogen and sealed with teflon film. An aliquot of the base was treated with 50 µl of triphenylmethane solution (10 mg/ml) in DMSO. A strong red color of the resultant solution was indicative of the presence of the anion of DMSO in the base solution.

The residue containing the acetylated peptide was dissoloved in DMSO (50µl) and treated with the base solution (50 µl). Methyl iodide (10 µl) was carefully added into the solution. The solution was kept at room temperature for 5 minutes and treated with 0.1M HCl (100 µl) and chloroform (250 µl). The solution was shaken carefully and the aqueous layer was separated and washed twice with chloroform (100 µl). The combined chloroform extracts were washed with water (2 x 100 µl) and dried over anhydrous Na_2SO_4. The solution was evaporated carefully under nitrogen and the product was used for mass spectral investigations.

Hydrolysis using trifluoroacetic acid: Peptide solution (40 µl) was treated with trifluoroacetic acid (100 µl) and left at room temperature overnight. The solution was lyophilized and the residue was used for investigations.

Esterification of the hydrolysate: A standard solution of 2N HCl in methanol was prepared by adding acetyl chloride (1.6 ml) dropwise with stirring to methanol (10 ml). The solution was left at room temperature for 10 minutes and used for esterification. The hydrolysate (10 µl) was treated with 2N methanolic HCl (200 µl) and left at ambient temperature for 3 hours. The reaction mixture was then lyophilized and used.

Deuteration, followed by esterification of the hydrolysate: The hydrolysate (10 µl) was treated with 2:1 Ac_2O/HCOOH (60 µl) and left at room temperature for 20 minutes. The solution was lyophilized and treated with D_2O (100 µl) and acetic anhydride (200 µl). The solution was lyophilized after 3 hours. The residue was treated with water (100 µl), lyophilized, and further treated with 2N MeOH/HCl (200 µl). The solution was lyophilized after 2 hours and used for further mass spectral investigations.

Mass spectral investigations: A triple quadrupole mass spectrometer assembled with standard Finnigan-MAT components and an Antek cesium ion gun[6]; and a standard VG model 7070EQ high field magnetic sector mass spectrometer with extended geometry and an 11-250 model data system were used in recording all main beam and CAD mass spectra. The samples in thioglycerol matrix were bombarded with 8 kv xenon or cesium ions. Glycerol and magic bullet matrices were also found to be adequate. The CAD spectra were obtained using argon and maintaining the collision gas pressure and collision energy at 2.2-6.0 mTorr and -30eV respectively.

Thermospray Ionization: A commercial Vestec Thermospray LC interface was used. The samples were introduced continuously at known intervals into the mass spectrometer source via the Thermospray using a 0.1M aqueous ammonium acetate buffer/methanol mixture. The ionized molecules were analyzed either by mass spectrometric or tandem mass spectrometric conditions.

The nmr spectral investigations: The ^{1}H and ^{13}C nmr spectra were obtained using a Varian XL-200 Superconducting FTNMR Spectrometer system.

RESULTS AND DISCUSSION

A hepatotoxic peptide was isolated from blue-green algal (Microcystis Aeruginosa) blooms found in the fresh water lake (Akersvatn) in Norway and purified by HPLC.[4] The peptide was termed as Akerstox based on its origin. The amino acid analysis of the purified peptide, using a Waters Pico-Tag amino acid system, indicated the presence of alanine (Ala), arginine (Arg), glutamic acid (Glu), leucine (Leu), and β-methylaspartic acid (Masp) in equi-molar quantities.[4] The identities and the relative ratios of the acids were established based on the comparison of retention times and areas of the eluted peaks with those of the authentic standards. Two peaks were observed for the β-methylaspartic acid standard, eluting at 2.2 and 2.7 minutes with the ratio of 7:1. The former peak was co-eluting with glutamic acid and hence the ratio of the peak eluting at 2.2 minutes was found to be higher than the other acids. The results of the amino acid analysis are shown in Figure 1.

The fast atom bombardment (FAB) mass spectra of the peptide were recorded in glycerol, or thioglycerol, or magic bullet (Figure 2.). Thioglycerol was found to be the most suitable matrix for recording the FAB mass spectrum of Akerstox. The protonated molecular ions were observed at m/z 995 along with the sodiated, pottasiated, and appropriate adduct ions. The molecular weight of the peptide was thus established to be 994 Daltons. Absence of sequence ions in the FAB spectra indicated the peptide to be cyclic.[7] The total masses of the identified amino acid fragments did not corroborate the observed molecular weight of the peptide. This denoted the presence of some other moieties as well in the molecule.

The collisionally activated dissociation mass spectrum of the protonated molecular ion, produced under FAB conditions was recorded (Figure 3). Several sequence ions as expected were observed in the spectrum. The presence of amino acids, earlier identified by amino acid analysis, were confirmed by the presence of daughter ions m/z 70 (alanine), 112 (leucine), 128 (glutamic acid and β-methylaspartic acid), and 156 (arginine). These ions were formed by the removal of protons from individual fragments (M-18) of the amino acids under the CAD conditions. Similarly, the daughter ions at m/z 84 and 312 indicated the possible presence of n-methyldehydroalanine (Mdha) and 3-amino-9-methoxy-2,6,8-trimethyl-10-phenyldeca-4,6-dienoic acid (Adda), respectively. Both these amino acids have been previously detected and confirmed by Botes et.al.,in a toxic peptide isolated from a South African species of Microcystis ~~Aeruginosa~~ in a most diligent manner by step-wise investigations.[2] The total masses of these five common and two uncommon amino acid moities were in agreement with the observed molecular weight of the Akerstox peptide. It was hence logical to take into consideration the presence of these two uncommon amino acids in this peptide, even though it was isolated from a different species of cyanobacteria. The amino acid moities thus identified in the Norwegian blue-green algal toxic peptide are shown in Figure 4.

The bonds cleave at various points under the CAD conditions, forming the sequence ions of the type $-N_nH-C_nHR_n-CO-$.[8] Ions indicating the sequence of the amino acids at various points were thus identified in the daughter spectrum as shown in Figure 3. Based on these observations derived from the daughter spectrum, the sequence of the amino acids in this cyclic peptide was determined to be:

Arg-Adda-Glu-Mdha-Ala-Leu-Masp

Table 1.
^{13}C NMR SPECTRUM OF AKERSTOX

AMINO ACID	ASSIGNMENTS
ALANINE	47.9 · 57.6 (1) · 17.4 (2)
ARGININE	47.8 · 57.6 (1) · 33.0 · 33.5 (2) · 26.0 · 26.9 (3) · 38.5 · 42.0 (4)
GLUTAMIC ACID	47.9 · 57.6 (1) · 26.0 · 26.9 (2) · 33.0 · 33.5 (3)
LEUCINE	47.9 · 57.6 (1) · 38.5 · 42.0 (2) · 26.0 · 26.9 (3) · 21.2 · 23.7 (4)
α-METHYLDEHYDROALANINE	126.7 · 146.4 (1) · 114.6 (2) · 36.5 · 42.0 (3)
METHYLASPARTIC ACID	47.9 · 57.6 (1) · 36.5 · 42.0 (2) · 16.6 (3)
ADDA	36.5 · 42.0 · 10.2 (1) · 47.9 · 57.6 (2) · 126.7 · 146.4 (3, 4, 5, 6, 7 and 9) · 45.2 (8) · 86.4 (9) · 58.7 (OMe) · 13.0 · 16.4 · 16.1 (Methyls)

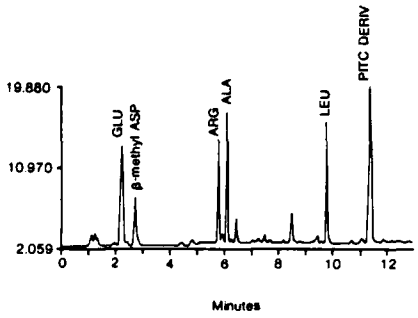

Figure 1.
AMINO ACID ANALYSIS OF AKERSTOX PEPTIDE

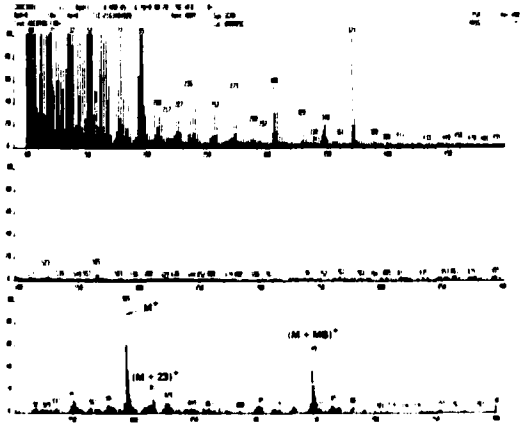

Figure 2.
FAB SPECTRUM OF AKERSTOX

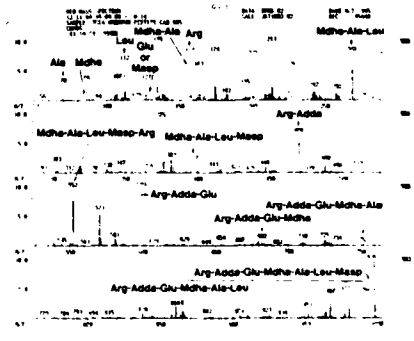

Figure 3.
FAB-MS/MS SPECTRUM OF AKERSTOX

Most of the sequence ions, calculated assuming the cleavage of the cyclic structure of the intact peptide at various points, were also identified in the CAD spectrum.

The 200 MHz ^{1}H nmr spectrum of the peptide in D_2O is shown in Figure 5. The ^{13}C nmr spectral parameters of the toxin in CD_3OD are listed in Table 1. The observed number of protons and carbons were consistent with the expected numbers for all seven amino acids present in the peptide. Despite the peak overlap observed at this field strength, several distinctive features of the spectra allowed confirmation of all of the amino acid moieties identified earlier by amino acid analysis and FAB-CAD mass spectrum. The observed ^{1}H and ^{13}C methyl resonances for leucine (^{1}H: 0.86; ^{13}C: 21.2, 23.7), alanine (^{1}H: 1.36; ^{13}C: 17.4), and β-methylaspartic acid (1H: 1.01; ^{13}C: 16.6) were supportive of the structures. The resonance at 3.96 in the proton spectrum was indicative of the glutamic acid moiety (C_α), and the peak at 158.6 in the ^{13}C spectrum confirmed the presence of arginine (C=N). The resonances for all the protons present in n-methyldehydroalanine were also observed (NCH_3: 3.40; $C=CH_2$: 5.59 and 5.96). In addition, the main features for the Adda moiety were confirmed from the ^{1}H and ^{13}C spectral data (^{1}H: CH_3'S, 1.01,1.01, 1.69; OCH_3, 3.26; H-4 & 7, 5.5-5.65; H-5, 6.35; aromatic protons, 7.3; and ^{13}C: CH_3'S, 13.0, 15.8, 16.1; C-8, 45.2; OCH_3, 58.7; C-9, 88.3). These results were in agreement with the high field ^{1}H and ^{13}C nmr spectral data reported for a hepatotoxin isolated from a South African species of Microcystis Aeruginosa.[2]

Several chemical modification and degradation reactions were conducted with the Akerstox peptide in order to confirm the above sequence. The daughter mass spectra of the products were in agreement with the one determined from the FAB-CAD spectrum of the intact peptide.

The intact peptide was subjected to acetylation followed by permethylation using dimethyl sulfoxide and sodium hydride following Roepstorff's method.[5] The daughter mass spectrum of the permethylated derivative of the acetyl-Akerstox is shown in Figure 6. The daughter ions m/z 112 and 381 were interpreted as due to the dimethyl-n-methyldehydroalanine and n-acetyl-dimethyl-Adda moieties. The sequence ions, of the permethylated amino acid moieties, observed in the daughter spectrum, were in agreement with the sequence determined for the amino acids in Akerstox (Figure 5).

Figure 4.
AMINO ACID MOIETIES IN AKERSTOX

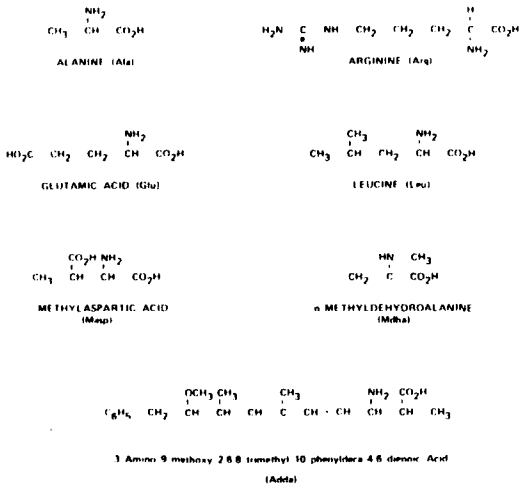

Figure 5.
PROTON NMR SPECTRUM OF AKERSTOX

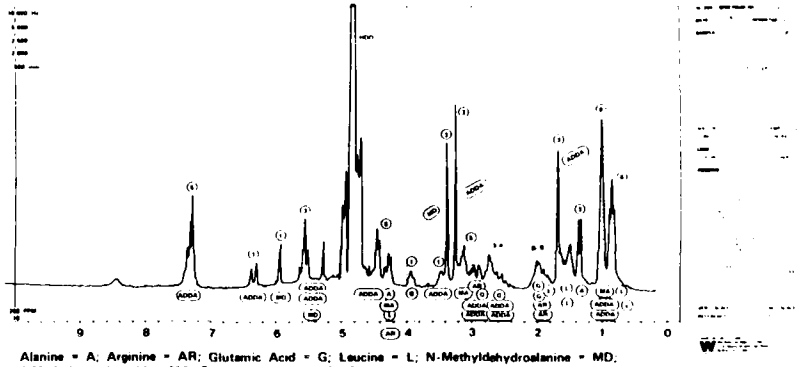

Alanine = A; Arginine = AR; Glutamic Acid = G; Leucine = L; N-Methyldehydroalanine = MD; β-Methylaspartic acid = MA; 3-Amino,9-methoxy,2,6,8-trimethyl,10-phenyldeca,4,6-dienoic acid = ADDA

Figure 6
CAD SPECTRUM OF PERMETHYLATED ACETYL AKERSTOX PEPTIDE*

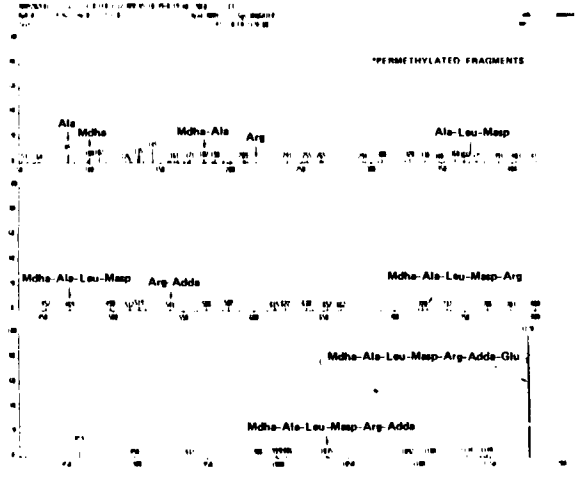

Figure 7.
CAD SPECTRUM OF HYDROLYSATE (m/z 930)

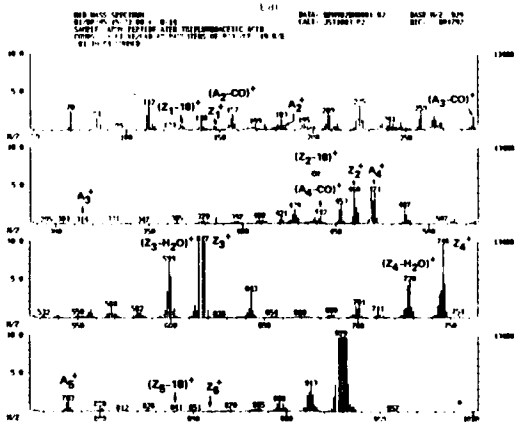

AD-A173 639 PROCEEDINGS OF THE ARMY SCIENCE CONFERENCE (1986) HELD 3/4
AT WEST POINT NEW..(U) DEPUTY CHIEF OF STAFF FOR
RESEARCH DEVELOPMENT AND ACQUISITIO.. 20 JUN 86

UNCLASSIFIED F/G 5/2 NL

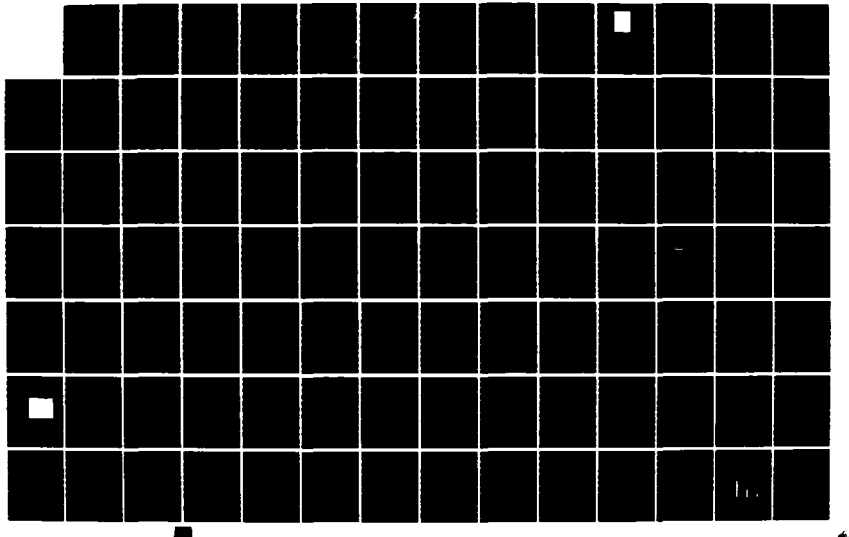

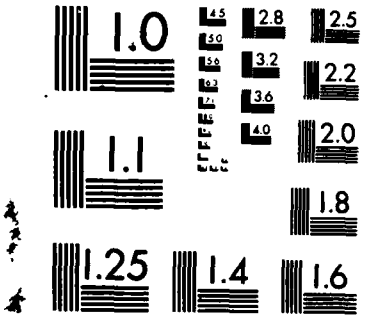

MICROCOPY RESOLUTION TEST CHART
NATIONAL BUREAU OF STANDARDS-1963-A

The intact peptide was hydrolyzed with trifluoroacetic acid. The FAB spectrum of the hydrolytic product showed two intense higher mass ions m/z 930 and 1013. The latter was due to opening of the ring in the cyclic peptide during hydrolysis. The former could be due to the degradation of the linear peptide (m/z 1013) formed during hydrolysis. Daughter spectra of m/z 930 and 1013 were recorded without subjecting the product through any chemical or chromatographic separations.

The CAD spectrum of m/z 930 is shown in Figure 7. Alanine and glutamic acid were found to be in the n-terminus and c-terminus, respectively. Based on the B and Y'' ions[9] observed in the daughter mass spectrum, the sequence of this hydrolytic product was derived as:

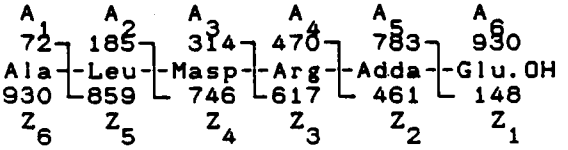

The daughter mass spectrum of the second hydrolytic product (m/z 1013) is shown in Figure 8. Careful inspection of the spectrum revealed the presence of two linear peptides in the hydrolytic product, formed by the cleavage of the bonds of the cyclic peptide either between n-methyldehydroalanine and glutamic acid or alanine and n-methyldehydroalanine. Based on the relative intensities of the sequence ions, it was concluded that the major product had alanine at the n-terminus and the minor one had n-methyldehydroalanine at the n-terminus. The former product being formed by the preferential cleavage of bonds at a tertiary carbon atom (alanine). The sequence ions for both products were identified as usual and were in agreement with the deduced sequence for the intact peptide. The amino acid sequences in both products were found to be as follows:

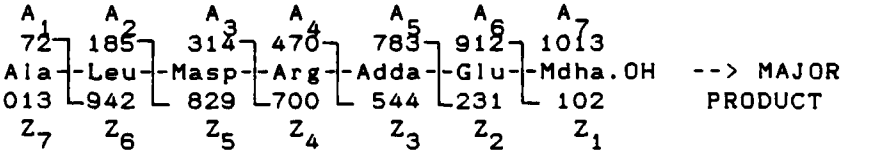

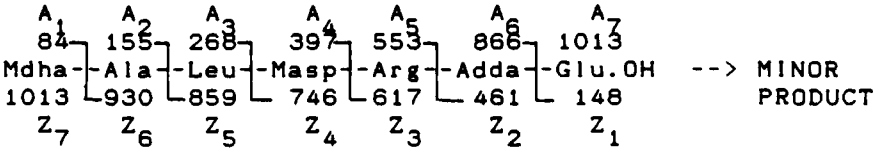

Figure 8.
CAD SPECTRUM OF THE HYDROLYSATE (m/z 1013)

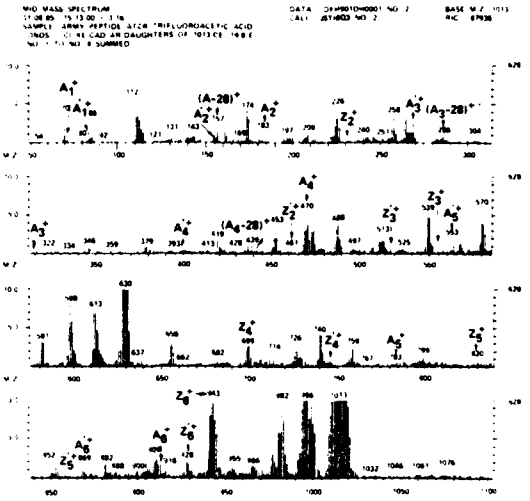

Figure 9.
CAD SPECTRUM OF METHYL ESTER (m/z 972)

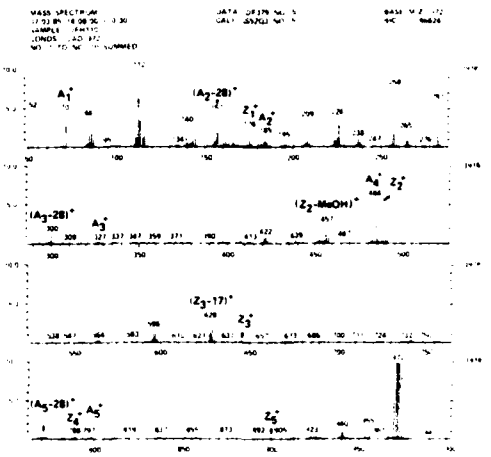

Figure 10.
CAD SPECTRUM OF METHYL ESTER (2)

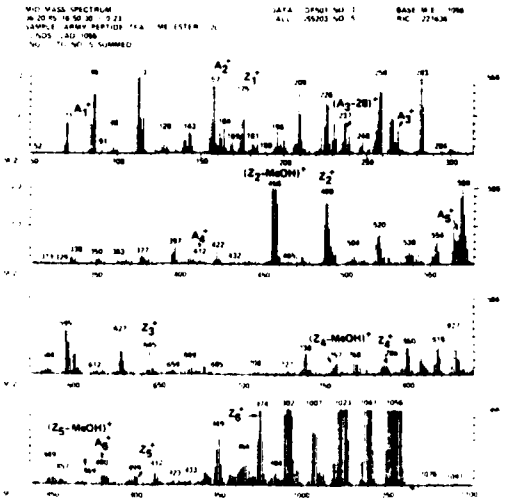

Figure 11.

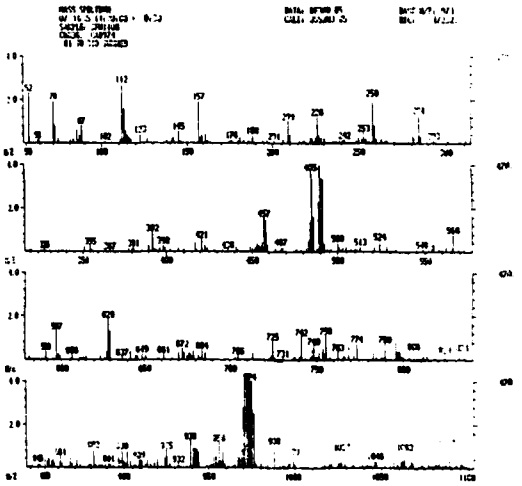

72	185	328	484	797	972
Ala -	Leu -	Masp (OMe) -	Arg -	Adda -	Glu (OMe)
972	901	788	645	489	176

The hydrolytic product mixture without any separation was esterified with 2M methanolic HCl in methanol. Two intense higher mass ions at m/z 972 and 1055 were observed in the FAB mass spectrum of the esterified mixture. The m/z of the former was in agreement with the m/z of the expected esterified product of the hydrolysate of molecular weight 929. The protonated molecular ion m/z 1055 could similarly be correlated with that of the hydrolytic product with m/z 1013.

The CAD spectrum of m/z 972 and 1055 are indicated in Figures 9 and 10, respectively. The observed daughter ions indicated the following sequences in the esters.

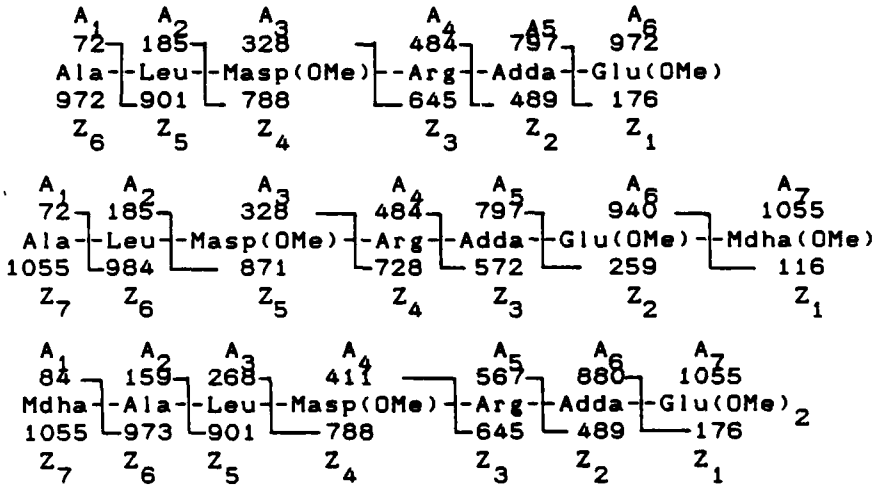

The types of linkages for the diacids in Akerstox, glutamic acid and β-methylaspartic acid, remained unknown at this point. Hence, the intact peptide was deuterated with D_2O and pyridine, followed by esterification with 2M methanolic HCl. The FAB spectrum of the deuterated and esterified product showed an intense ion at m/z 974, two masses higher than the ester of one of the hydrolytic products (m/z 972). This indicated the deuteration of two hydrogens located at the carbon(s) α to the acid groups. The daughter spectrum of m/z 974 is shown in Figure 11. The identified sequence ions are also shown in Figure 11. The sequence ion d_1-A_4 was observed at m/z 485, in comparison to m/z 484 in the corresponding protonated fragment, indicating the deuterium labelling at the α- carbon atom of β-methylaspartic acid. The d_1-(A_3-28) was also observed at m/z 301 instead of m/z 300, indicating the β-methylaspartic acid to be iso-linked with arginine. Similarly, the shift of

the Z_2 ion (m/z 490) by one mass higher than the corresponding protonated ion indicated that the α-hydrogen atom of the glutamic acid was not involved with the linkage of the moiety with Adda. The d_2-(Z_3-17) and d_1-Z_5 ions were observed at m/z 628 and 790 instead of correspondingly at m/z 627 and 788. Thus, glutamic acid and β-methylaspartic acid were unequivocally established to be iso linked in the intact peptide.

The glutamic acid and β-methylaspartic acid were determined to be iso-linked in the Akerstox based on the proton shifts of the C_α protons while changing the pH of the solution. The resonance at δ 3.96, attributed to proton at C_α glutamic acid, moved downfield by approximately 0.6 ppm when the intact peptide was treated with DCl. This indicated that the free carboxylic group was at the C_α position and confirmed the iso-linkage of glutamic acid. Similarly, on treatment with DCl, a doublet ($J \approx 3.6$ Hz) shifted from approximately 4.5 ppm to 4.73 ppm ($\Delta\delta$=+0.23). The only C_α proton resonance that was a doublet had been assigned to C_α of the β-methylaspartic acid moiety. Therefore, it appeared that the free carboxyl group of the Masp moiety was also at the C_α position and thus establishing it to be iso-linked. Even though there was a significant amount of peak overlap at 200 MHz, the other proton resonances were little affected by the addition DCl ($\Delta\delta$=0.09 or less). These results were in agreement with the results observed for the shifts of the proton resonances of the C_α of glutamic acid and β-Masp[2] present in the South African blue-green algal peptide, on addition of DCl.

The sequence of the amino acids in the Norwegian blue-green algal toxic peptide was thus established, as shown in Figure 12, using only nanogram quantities of the intact peptide. Generation of protonated molecular ions under the softer ionization conditions, followed by collisionally activated dissociation of the PMI has been found to be the most rapid, efficient way to determine the sequence of the amino acids in this cyclic peptide.

The peptides isolated from the blue-green algal (Microcystis Aeruginosa) blooms found in Scotland and Monroe, Wisconsin, USA were also investigated by a similar approach. Both were identical in structure to Akerstox peptide. Two peptides were isolated from the Canadian species (Anabena flos-aquae) and separated by HPLC. The sequences of amino acids in one of the peptides was also identical with Akerstox peptide. The sequence of the other one was determined to be:

-Ala-Leu-Asp-Arg-Adda-Glu-Mdha- .

The toxicity of this toxin was found to be lesser than Akerstox by one order of magnitude.[10]

Experiments were conducted to determine optimum conditions for the ionization of these peptides under softer conditions using Thermospray[3] LC/MS interface. The samples were directly introduced into the mass spectrometer via the Thermospray using 0.1M ammonium acetate buffer. The samples were introduced in the intervals of one to two minutes. The protonated molecular ions (m/z 995) were detected. The doubly charged molecular ions and the sodiated and pottasiated molecular ions were also detected under these conditions. All these ions underwent collisionally activated dissociation when they were reacted with argon at 2.6mTorr with a collision energy of 30eV. This would be applicable in developing methodologies for the rapid analysis of these toxic peptides either by mass spectrometric or by even more specific tandem mass spectrometric techniques. At present, experiments are being conducted to develop and to evaluate LC/MS, LC/MS/MS and more direct MS/MS methods of analysis for these toxic peptides in crude samples without any sample clean-up or preparations. Such rapid methods will be highly useful in detecting the contaminated drinking water sources even in battle situations and in subsequent treatment of the affected sources and clean-up of the contaminated sources.

Table 2.

THE 50 MHz ^{13}C NMR DATA OF AKERSTOX IN CD_3OD.

δ^a	ASSIGNMENT
13.0, 15.8, 16.1	CH_3 of Adda
16.6	CH_3 of Masp
17.4	CH_3 of Ala
21.2, 23.7	CH_3 S of Leu
25.9	C_γ of Leu
26.5	C_β of Glu
28.1, 29.5	C_β & C_γ of Arg
33.3	C_γ of Glu
37.6	C_β of Masp
38.4	NCH_3 of Mdha
38.9	C-10 of Adda
40.7	C_β of Leu
42.0	C_δ of Arg
42.0	C-2 of Adda
45.2	C-8 of Adda
53.0, 55.3, 56.9[b]	C_α's of Ala, Arg, Leu, Mdha, Glu, and C-3 of Adda
58.7	OCH3 of Adda
88.3	C-9 of Adda
114.4	C_β of Mdha
126.7, 137.0	C-4, C-7 of Adda
127.1	C-4 (in the Phenyl ring) of Adda
129.2, 130.5	C-2, C-3 (in the Phenyl ring) of Adda
133.9	C_α of Mdha
138.9	C-5 of Adda
140.5	C-1 (in the Phenyl ring) of Adda
146.4	C-6 of Adda
158.6	C=N of Ar
166.0, 172.3, 175.1, 175.4, 176.7, 176.8 177.1, 177.5, 179.3	Carbonyls

[a] Relative to $SiMe_4$ measured from internal CD_3OD and corrected by using δ ($SiMe_4$) = δ (CD_3OD) + 49.0 ppm.

[b] Not all resonances observed due to large solvent peak present in this region.

Figure 12.

NORWEGIAN BLUE-GREEN ALGAL HEPTATOTOXIN (AKERSTOX)

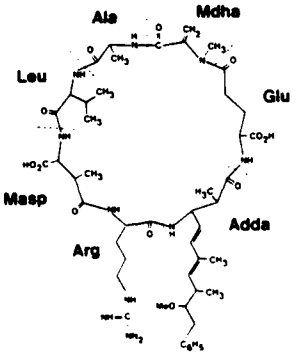

CONCLUSION

A Norwegian fresh water blue-green algal hepatotoxin has been deduced to be a cyclic peptide with a molecular weight of 994 Daltons and seven amino acid moieties. The sequence of the amino acids has been determined to be -Ala-Leu-Masp-Arg-Adda-Glu-Mdha-, by FAB-CAD(MS/MS) mass spectral technique. The same peptide was also detected in fresh water sources in Scotland, Canada, and the the USA by a similar approach. The sequences of amino acids in another, less toxic cyclic peptide found in Canadian waters was also determined to be -Ala-Leu-Asp-Arg-Adda-Glu-Mdha- by the same approach. Thermospray ionization followed by analysis either by mass spectrometric or tandem mass spectrometric methods was found to be adequate for the rapid and specific analysis of these toxins.

ACKNOWLEDGMENT

The authors gratefully acknowledge other contributors to this project: Prof. Donald F. Hunt and Dr. Jeffrey Shabanowitz, University of Virginia, Charlottsville, VA and Prof. Wayne W. Carmichael, Wright State University, Dayton, OH.

LITERATURE CITED

1. W.W. Carmichael and N.A. Mahmood, in "Seafood Toxins," E.Ragelis Ed., American Chemical Society Symposium Series 262, Washington, DC, 1984, p377.
2. D.P. Botes, A.A. Tuinman, P.L. Wessels, C.C. Viljoen, H. Kruger, D.H. Williams, S. Santikarn, R.J. Smith and S.J. Hammond, J. Chem. Soc. Perkin Trans. I, 2311-2318 (1984)
3. D. Pilosof, H. Y. Kim, D. F. Dyckes, and M. L. Vestel, Anal. Chem., 56, 1236-1240 (1984).
4. T. Krishnamurthy, W.W. Carmichael, and E.W. Sarver, in Toxicon (In press)
5. P. Roepstorff, Personal Communication.
6. D.F. Hunt, J. Shabanowitz, T.M. Harvey, and M. Coates, J. Chromatogr., 271, 93-105 (1983)
7. B. Tomer, F.W. Crow, M.L. Gross, and C.D. Koppler, Anal. Chem., 56, 880 (1984)
8. D. F. Hunt, J.R. Yates, J. Shabanowitz, S. Winston, and C. Hauer, in "Protein Sequencing by Tandem Mass Spectrometry," (in print)
9. P. Roepstorff, Biomed. Mass Spectrom., 11, 601 (1984)
10. T. Krishnamurthy and W. W. Carmichael, unpublished results.

DISPLAY AND CONTROL RESEARCH TO ENHANCE PERFORMANCE OF SHORT-RANGE AIR DEFENSE (SHORAD) FIRE UNIT PERSONNEL

GARY L. KURTZ
*JON J. FALLESEN
HUMAN ENGINEERING LABORATORY
U.S. ARMY LABORATORY COMMAND
ABERDEEN PROVING GROUND, MARYLAND 21005-5001

INTRODUCTION

A critical element of tactical doctrine is effective command and control (C^2). Nowhere else is this more true than in SHORAD. To effectively utilize air defense assets, SHORAD C^2 follows a policy of centralized management with the maximum possible decentralized authority to engage. To engage the threat at the maximum capability of SHORAD weapon systems, effective command and control is essential. Timely and accurate air-track and C^2 information must be provided to the SHORAD personnel. Such information allows a countering force to that of the threat's capabilities.

One intent of the SHORAD C^2 system will be to provide SHORAD personnel with targeting and command information. A substantial amount of information has been identified for meeting the system requirements. Determining which information is useful, when it is useful, which information is critical, and how to display it presents significant challenges in the design of the soldier-machine interface (SMI) at the fire unit subsystem.

SCOPE

An experimental SHORAD C^2 fire unit display and control unit was fabricated and used in a semicontrolled field test environment. The display presented air-track and command information. The task required fire unit teams of two personnel to search for and detect aircraft.

A series of four tests and one excursion test were conducted. The first test addressed the relative effectiveness of three different track alerting formats. The second test compared three ways of orienting the

display picture. The third test addressed three levels of track cueing accuracy. The fourth test addressed the utility of landmark display symbols. The excursion test gathered limited data on the use of binoculars with the test display.

OBJECTIVES

The purpose of the five tests was to obtain design data to contribute to the effectiveness of the future SHORAD C^2 system. The tests assessed the interaction between the soldier-operator and the visual display for aiding aircraft visual detection. The objectives for each of the tests were as follows.

Alerting Test. To determine the alerting format among three candidates which enables the greatest visual detection range.

Orientation Test. To determine the orientation format among three candidates which provided the greatest visual detection range.

Cueing Accuracy Test. To determine the accuracy among three levels which is sufficient for target cueing.

Landmark Test. To determine the utility of landmark display symbols for increasing visual detection range.

Excursion Test. To determine the utility of binoculars in conjunction with the test display for increasing visual detection range.

In the absence of differences in visual detection range for any of the tests, user preferences or perceptions were compared.

METHODOLOGY

Participants

Twelve enlisted males from the 1/67 Air Defense Artillery Battalion, served as test participants. Soldiers were assigned by their noncommissioned officer in charge (NCOIC) to six two-man teams, as either team chief or gunner.

SHORAD C^2 Test Display Device

A test display was fabricated primarily to present the test personnel with graphical air-track information (see Figure 1). The test display was

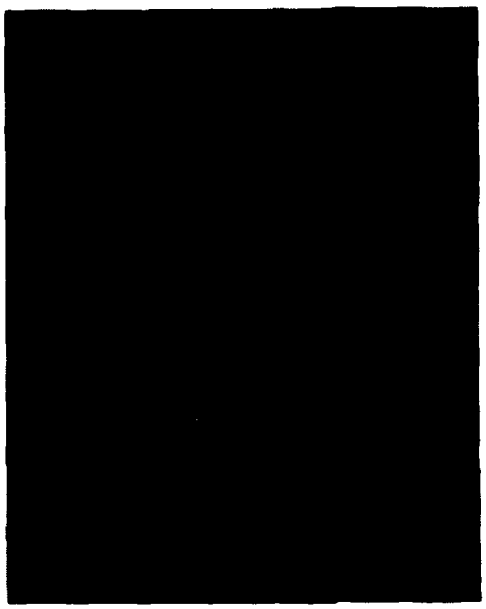

Figure 1. Experimental Fire Unit Display Device

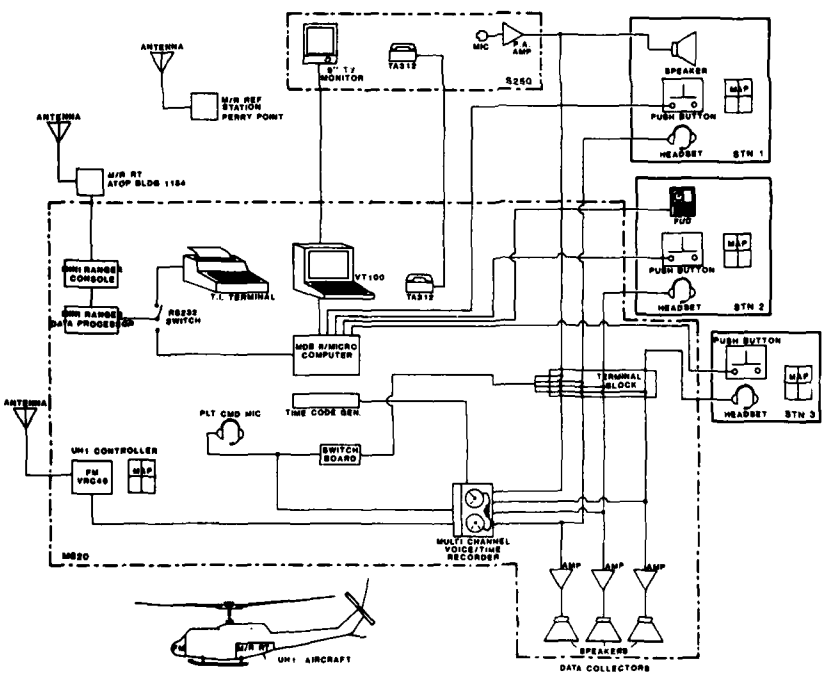

Figure 2. Functional Connectivity Diagram of Test Items

programmed to provide various display format presentations of information. The device used an electroluminescent (EL) display panel and a flat membrane, alphanumeric keypad to simulate a typical tactical display.

Alerting Test

In this test, three alerting formats were separately tested. Alerting Format 1 had a compressed 10-30 km range area with the inner 10 km providing an area for cueing track symbology. When an air track was inbound in the 10-30 km range, a 30-degree sector in the compressed range area was lit. An audible alert was sounded when the track first appeared and continued to sound until an acknowledgment response was made by the operator.

In alerting Format 2, a similar display was presented, except that an estimated time of arrival (ETA) was shown in the area of where the 30-degree sector was lit for Format 1 (see Figure 1). The ETA was presented in minutes until the air track would intersect a specified range from the fire unit or to the closest point between the specified and maximum range.

Alerting Format 3 used a 20 km range area with an air track shown as a symbol. An audible alert was sounded when the track symbol appeared (2). Format 3 was designed in response to survey information (3) which indicated a preference for no-range distinction between alerting and cueing information.

Orientation Test

In this test, three methods of displaying orientation azimuth on the display device were tested. One format presented the specification design which oriented the top of the display picture to north, east, south, or west, depending on which cardinal compass azimuth direction was closest to the primary target line (PTL) azimuth direction. The PTL is an azimuth direction from which threat aircraft have the greatest probability of appearing. It is also the center of the assigned azimuth search sector, which for these tests was 90 degrees. The search sector is indicated by the two dashed radial lines in Figure 1. A second format oriented the top of the display picture to north regardless of the PTL azimuth. A third format oriented the top of the display directly to the azimuth corresponding to the PTL azimuth (see Figure 1).

Cueing Accuracy Test

In this test, three levels of cueing accuracy were used. The finest level of precision available was within $\pm$2.5 degrees azimuth. No better

precision was available because of the scale of display picture elements (pixels) to real distance was 1 pixel = 100 meters. This level is referred to as the 0 degree condition.

The second level of precision was ±15 degrees and the third level was ±30 degrees. Level is the amount of azimuth difference between the track display symbol and actual track azimuth.

Landmark Test

In this test, six landmark symbol types were available for use (building, command post, fire unit, tree, water, and hill). All six could have been entered as single points, and the tree, water, and hill could be entered as a series of coordinates.

In the baseline format, no landmark symbols were used other than the fire unit position. In Figure 1, the fire unit position is indicated by the inverted T in the center of the graphic display. In the landmark format, landmarks were given to the test crews to use and were chosen from prominent features in the visible terrain and to coincide with the left and right search sector limits and along the PTL. These are indicated by the three square solid symbols in Figure 1.

Binocular Test

This test was conducted to attempt to determine the utility of binoculars for detection of aircraft in conjunction with the fire unit display. (Current doctrine recommends binoculars for target identification but not for detection [1 & 4]).

Test Site Setup

The test site was located near Locust Point on Spesutie Island, Aberdeen Proving Ground, Maryland. Three observation stations were placed at approximately 50 m apart. Station 1 provided Enhanced Manual SHORAD Control System (EMSCS) voice-tell air-track reports to a fire unit (FU) team. At Station 2, the experimental test display provided visual air track reports to the FU team. Station 3, referred to as autonomous, provided only the operation order with state-of-alert information to a FU team. Each station was assigned a PTL of 290 degrees grid azimuth. Camouflage netting was placed around each site to provide visual screening from one another.

A functional connectivity diagram of the major items of instrumentation is provided in Figure 2. Approximately 100 feet to the rear of Station 2 were the test instrumentation vans. An M820 expansible

van was used to house the Mini-Ranger tracking system, a microcomputer for test-display control and data collection, a multichannel voice recorder, manual data recording stations, and a radio for aircraft flight coordination. An S250 shelter was emplaced adjacent to the M820 van where a slaved television monitor was placed. The monitor showed SHORAD grid coordinates and headings for tracks which were voice broadcast to Station 1.

All stations had land-line communication to the test control van. At each station, there was a hand-grip push button to depress when a visual aircraft detection was made. These activations were recorded by the test computer and displayed on the computer monitor. The team chief followed the detection with a voice report.

The Mini-Ranger positioning system was used to locate the position of the test aircraft. The system was used effectively to simulate a tactical radar. The system was set up with two known reference points, each with a radar interrogator and transponder. One fixed reference station was placed at the Perry Point Veterans Hospital complex, and the other was co-located at the test site. A mobile unit on the instrumented helicopter contained a receiver-transmitter.

The Mini-Ranger system was operated in a tracking (i.e., x-y) mode. Slant range was usually available when the radar signal did not complete transmission to both reference stations. Normally, x-y position data were transmitted via an RS-232 output port to the test computer (MDB Micro/11). Through Fortran-based software, the computer processed the x-y coordinates provided by the Mini-Ranger system and used the resulting data to depict an aircraft symbol on the fire unit display. The computer also controlled the other operations of the test display as well as recording the activations of the detection push buttons and the aircraft positional data.

A multichannel voice recorder was used to record all voice communications which included voice detection reports and instructions from the simulated platoon command net, the simulated EMSCS early warning broadcast net, and FM communication to and from the instrumented aircraft. An IRIG-B format was used to time tag the audio tapes and served as the master clock for setting Mini-Ranger and the MDB Micro/11 computer.

Test Participant Procedures

The test participants first were given an overview of the tests and given an opportunity to ask questions. A consent-to-participate form was signed by all test participants. A background questionnaire was administered to obtain rank, duty position, and experience information.

Details on the conduct of the test were then provided. The nature of information provided to the three test stations was explained. The required tasks of SHORAD search and detection were reviewed. An overview of the experimental fire unit display and its characteristics were given.

Participants were then assigned to two-man teams by the NCOIC. Groups of flights were referred to as a "rotation"; each rotation related to a unique team and display format combination. During any one rotation, three of the six teams were assigned to predetermined stations on standby alert. A short training session was given to the team at Station 2 concerning operation of the test display. The training reviewed the display setup of the particular format which the team would be using.

Aircraft Flight Procedures

The start points for each flight were assigned over the 90-degree search sector. To determine the order of start points, they were placed into pairs of adjacent start points (1 & 2, 3 & 4, 5 & 6, 7 & 8, and 9 & 10). For each rotation, one start point from each pair was selected randomly. The start points began from 14 to 20 km away from the test site. On days of exceptional visibility, the 20-km start points were used.

Start points 1 through 10 and associated flight paths had approaches to the test site that varied from 0 to 2 km offset. The aircraft flew to its start point beyond visual detection range. When over the start point, a voice signal would be transmitted by the pilot to the instrumentation van. During the alerting test, all flights were flown at 700 feet mean above sea level (MSL). The aircraft maintained an indicated airspeed as close to 90 knots as possible. The aircraft continued inbound on the straight line approach until it was instructed to break off after all detections from the stations were made.

Experimental Design Approach

To minimize the number of combinations of the experimental conditions, a series of four experiments was planned in place of one complete factorial design for the four test issues. The order of the tests on the display formats was determined based on the issue's criticality and the even-ordering of the related tracks.

A decision-logic diagram was developed prior to testing. Its purpose was to make a forced-choice selection of the "best" format to carry forward to the next test, which would examine a different format parameter. For example, the first test compared three alerting formats.

The selection of one format was desirable to reduce the number of display conditions being tested in the orientation test.

In tests of cueing accuracy and landmark utility, complete representation of the experimental conditions for the respective test objective was made.

Alerting Test Methodology

Data for this test were collected on three consecutive days. To control extraneous variables, such as meteorological conditions, detection ranges for Station 3 (the autonomous station with limited early warning information) were subtracted from the detection ranges from station 2. Upon the conclusion of this test, a forced-choice question was asked of the test participants to determine the preference for the three formats.

Orientation Test Methodology

The alerting format determined to be "best" was used and held constant in the test of orientation formats. Data were collected over two days. Since orientation Format 1 had been used in the alerting test with each of the three alerting formats, the data were taken from the alerting test for orientation Format 1. Orientation Formats 2 and 3 were presented to the test participants in a counterbalanced order. Again, detection ranges for the automonous station were subtracted from those for the display station. Again, a forced-choice preference was requested of the test teams upon conclusion of the test.

Cueing Accuracy Test Methodology

To address the level of cueing accuracy, each team rotated to station 2 once to use the display during the test. Data were collected on two consecutive days. The three levels of accuracy were 0, ±15, and ±30 degrees. Four trials of either the ±15 or ±30 degree condition were presented, then one 0-degree trial, and then four trials of the third condition. Two trials of each set of four were in the clockwise direction (+) and two were counterclockwise (-). The presentation order of the 15 and 30 degree conditions were counterbalanced among teams and the direction (+ or -) was randomized. During the detections, the teams were asked to report whether the display cueing target matched with where they saw the visual target.

Landmark Test Methodology

Each team rotated to the display station once. Three trials with landmarks were made and two trials without landmarks were made. The

coordinates of the landmarks were entered by the test participants with assistance from a tester. The test participants were asked to give their preference for usage of the landmark symbols.

Excursion Test Methodology

In an excursion test, binoculars were available for use in aircraft detection in one of a pair of trials. Each team detected the aircraft for two trials at the display station.

RESULTS

Alerting Test

The detection range from the autonomous station was subtracted from the range of the display station. Descriptive statistics on the difference scores are provided in Table 1. A repeated measures, mixed-model analysis of variance (alerting format by start point by team) was performed on the difference scores. A significant effect ($F=10.15$, $df=2,9$, $p=.005$) on the alerting format was found. (A conservative F test was made with $df=1,5$ to account for compound symmetry. The observed F for the alerting main effect was greater than this critical F and, therefore, was significant at the most conservative level.)

There was no significant difference on the forced-choice preference among the test participants.

Orientation Test

A second analysis of variance (orientation format by start point by team) was performed on the detection range difference between the display and autonomous stations. Data from the alerting test (Format 2) for orientation Format 1 (north, south, east, west) were analyzed with data on formats 2 (north) and 3 (PTL) obtained in the orientation test. (Alerting format 2 was constant in the orientation test.) No main effect was found on orientation.

A unanimous preference for Format 3 (PTL) was indicated by the test participants. Descriptive statistics for orientation formats are provided in Table 2.

Cueing Accuracy Test

Detection ranges from the ±15 degree and ±30 degree conditions were decreased by the detection ranges for the 0 degree trials. Statistics

are presented in Table 3. Nine trials were flown for each team. An analysis of variance (cueing level by team) was performed on the difference score, and no significant cueing accuracy effect was found.

For each flight, the teams were asked to report if the display cueing matched with where the target was detected. A table was constructed where rows indicated whether there was a match, and columns represented the level of cueing accuracy (see Table 4). A significant effect was found indicating that more cues at the 30-degree level were perceived as not matching, while a high level (83%) of cues at 15 degrees were perceived as matching, even though there was a +/-15 degree error. All 0 degree offsets were correctly reported as matching.

Landmark Test

The landmark test used placement of symbols representing prominent features along the PTL and search sector boundaries. A repeated measures, mixed-model analysis of variance (landmark by team) was performed on the difference scores. No statistically significant effect was found for the utility of landmarks. There was a difference in detection range (relative to autonomous detection) of .8 km for using the landmarks (see Table 5). This difference was not significant given the magnitude of the variability. A χ^2 test indicated that there was a significant preference (χ^2=4.08, p=.05) for landmarks.

Binocular Excursion Test

A brief test of binocular usage in combination with the display device was conducted. Each team had trials when binoculars were available for use and when they were not. Although the difference in mean detection range between the two conditions was 1.8 km, the advantage for binoculars was not statistically significant (see Table 6).

Early Warning Methods

Detection range data were taken across all preplanned tests from the stations with different early warning methods (i.e., display device, EMSCS, and autonomous) (see Table 7). In a mixed model, repeated measures analysis of variance (early warning by test by team), significant early warning method and test differences were found. The detections in the alerting, landmark, and orientation tests were greater than those in the cueing accuracy test (as determined by simultaneous comparison). Detections at the display device condition were greater than those in the autonomous condition. The display was not significantly better than the EMSCS condition, and the EMSCS condition was not significantly different from the autonomous.

The display was preferred unanimously over the other methods of early warning.

CONCLUSIONS

The tests were successful in addressing the individual objectives. In each preplanned test, either a significant difference in range of detection for formats was found or a difference in format preference was established. To summarize, the following statements are made:

a. The ETA alerting format had greater detection ranges relative to autonomous detection than either of two other formats.

b. The orientation with the PTL at the top of the graphic display was unanimously preferred.

c. Reports on display agreement with the actual location of the aircraft indicated a tolerance for $\pm$15 degree error but intolerance for the $\pm$30 degree error.

d. The usage of landmarks was preferred by a significant margin to help register the display graphics to the visual scene.

RECOMMENDATIONS

There are many soldier-display interface issues yet to be addressed in the area of the SHORAD C^2 fire unit display. Repetitions of these test procedures (i.e., single target, controlled test environment, limited display features) would serve to address many human factors research issues quite adequately, such as utility of aircraft altitude information. Although the controlled, relatively benign test environment used here was satisfactory for addressing these initial display design questions, additional test parameters need to be introduced in future testing.

The general approach followed in the selection and testing of display formats was to limit the design to the absolute minimum information requirements. Design issues will undoubtedly require enhancements and modifications to the test display. The principles of ease of use and simplicity in display, as well as SHORAD crew decision making and workload capabilities, have to receive all due attention in trade-off considerations when adding information or increasing required operator input/control actions. The display must serve as an aid, instead of a burden to the soldier.

One area of operational concern is when there are multiple aircraft in near proximity. It will be critical that the SHORAD device aid the SHORAD crew i sorting out the aircraft in the distant visual scene. To further this end, additional research in the areas of required cueing accuracy, landmark utility, binocular utility, and decision aids will be beneficial. Issues should be addressed concerning how to present the required information, e.g., by adding modifiers to track symbols or by annotating the graphic display with tabular track information.

There are very important issues relating not only to the detection portion of the SHORAD weapon tasks as tested here, but also to the target identifications and engagement decision which the fire units must make. The most critical operational issues are the capabilities of the display for helping to discriminate aircraft parameters (flight paths, sectors, velocities, etc.) so that decisions can be made about the aircraft's identification and intentions. The decisions have to be made before the fire unit can no longer successfully engage. Investigations concerning the role that the display has in support of these tasks need to be conducted so that the utility of the SHORAD C^2 system and the effectiveness of the SHORAD weapon systems are maximized.

REFERENCES

1. Baldwin, R. D. (1973). Attempts to improve visual detection through use of search pattern and optical aids (HumRRO-TR-73-3). Alexandria, VA: Human Resources Research Organization.

2. Department of Defense (1983). Symbols for Army air defense system displays (DOD-STD-1477). Washington, DC: U.S. Government Printing Office.

3. Fallesen, J. J. (1985). Command and control (C^2) survey of short-range air defense (SHORAD) elements (Technical Memorandum 12-85). Aberdeen Proving Ground, MD: U.S. Army Human Engineering Laboratory.

4. Kurke, M. I., & McCain, C. N. (1957). Low power optical systems and aerial target detection (Technical Memorandum 5-57). Aberdeen Proving Ground, MD: U.S. Army Human Engineering Laboratory.

TABLE 1

Descriptive Statistics for the Alerting Test

Dependent Measure: Display detection - Autonomous detection											
						PERCENTILES					
Format	Mean	N	SD	Range	Min	5th	25th	Median	75th	95th	Max
Baseline	0.84	21	1.38	5.29	-1.72	-1.67	-0.03	0.34	1.91	3.50	3.57
ETA	1.87	27	2.60	13.46	-4.15	-3.41	0.72	1.49	3.09	8.02	9.32
20 km	0.33	28	1.57	8.21	-4.14	-3.19	-0.57	0.41	1.08	3.52	4.07
All Formats Combined	1.02	76	2.04	13.46	-4.15	-2.07	-0.06	0.86	1.90	4.67	9.32

TABLE 2

Descriptive Statistics for the Orientation Test

Dependent Measure: Display detection - Autonomous detection											
						PERCENTILES					
Format	Mean	N	SD	Range	Min	5th	25th	Median	75th	95th	Max
N,E,S,W	1.87	27	2.60	13.46	-4.15	-3.41	0.72	1.49	3.09	8.02	9.32
North	0.61	21	3.49	14.38	-7.86	-7.72	-0.80	0.77	2.27	6.46	6.52
PTL	1.57	23	4.08	19.41	-9.62	-8.03	-0.80	1.27	2.87	9.75	9.79
All Formats Combined	1.40	71	3.39	19.41	-9.62	-5.10	-0.10	1.16	2.85	8.36	9.79

TABLE 3

Descriptive Statistics for the Cueing Accuracy Test

Dependent Measure: Detection - 0 Degree Offset Detection											
						PERCENTILES					
Offset	Mean	N	SD	Range	Min	5th	25th	Median	75th	95th	Max
+/-15	-0.83	21	2.26	11.06	-6.16	-6.07	-1.38	-0.58	0.20	4.51	4.90
+/-30	-0.49	24	3.49	13.99	-9.10	-8.76	-1.40	0.14	1.38	4.86	4.89
Both Offsets Combined	-0.65	45	2.95	14.00	-9.10	-7.40	-1.38	-0.46	0.87	4.85	4.90

TABLE 4

Frequency of Reported Matches of Cueing Position to Detection Location

	Cueing Accuracy Offset Condition	
Perception	+/-15	+/-30
Match	19 (83%)*	4 (20%)
No Match	4 (17%)	16 (80%)

*Cell percentages represent cell frequencies divided by column frequencies.

Computed χ^2 = 12.19, df = 1
Critical χ^2 = 10.83, df = 1, ρ = .001

TABLE 5

Descriptive Statistics for the Landmark Test

Dependent Measure: Display detection - Autonomous detection

Landmarks	Mean	N	SD	Range	Minimum	Median	Maximum
Without	0.66	13	4.76	15.39	-6.80	-0.32	8.59
With	2.37	16	3.67	10.88	-0.92	0.94	9.96
Combined	1.60	29	4.20	16.76	-6.80	0.87	9.96

TABLE 6

Descriptive Statistics for the Binocular Test

Dependent Measure: Display-aided detection							
Binoculars	Mean	N	SD	Range	Minimum	Median	Maximum
Without	7.05	6	4.25	10.29	1.94	5.70	12.23
With	9.84	7	4.20	11.49	4.17	10.96	15.66
Combined	8.55	13	4.22	13.72	1.94	8.58	15.66

Wilcoxon rank sums test statistic = 35, z approximation = 0.9286, (Not significant)

TABLE 7

Descriptive Statistics for the Early Warning Methods

Dependent Measure: Detection						PERCENTILES					
Method	Mean	N	SD	Range	Min	5th	25th	Median	75th	95th	Max
Auton.	6.68	213	2.86	16.46	1.46	2.50	4.83	6.33	7.78	12.38	17.92
EMSS	7.32	213	3.04	16.03	1.09	2.82	5.14	6.92	9.32	12.73	17.12
Displ.	7.83	215	3.19	16.75	0.98	3.60	5.47	7.22	9.80	13.74	17.73
Combined	7.28	641	3.07	16.95	0.98	2.98	5.17	6.78	9.05	13.11	17.92

LAKHANI

ENLISTED MANPOWER COSTS OF THE BRADLEY FIGHTING VEHICLE AND THE M113: AN APPLICATION OF A PROTOTYPE ARMY MANPOWER COST (AMCOS) MODEL

HYDER LAKHANI
U.S. Army Research Institute
for the Behavioral and Social Sciences
Alexandria, Virginia 22333-5600

An objective of this paper is to provide a framework for determining all manpower cost of weapons systems, particularly for budgetary purposes early on in the acquisition cycle. Cost-effectiveness of alternative manpower mixes for particular weapons systems can be determined by evaluating a multitude of cost elements in a consistent framework. The Army Manpower Cost (AMCOS) model provides detailed and comprehensive information on recruiting, training, compensation, retirement, and separation costs for enlisted personnel. Too often, only basic pay is used as "the" cost of manpower in cost trade-off analyses. This represents a significant underestimate since basic pay is about half of total manpower costs. The AMCOS model is general enough to be used to estimate annualized manpower costs of any weapon system, given the manpower requirements of the system, by MOS and pay grade. AMCOS is a logical follow-on to earlier models such as the Hardware and Manpower (HARDMAN)[1], Man Integrated System Technology$_3$(MIST)[2], and the more recent Manpower-Personnel Integration (MANPRINT)[3] manning models, that attempt to estimate manpower mixes of different systems. These models were not intended to estimate costs.

Although the currently available AMCOS prototype has two versions--an economic cost model and a budget cost model for the enlisted force--our focus here will be on the economic cost model. Future developments of AMCOS will include comprehensive cost models of officers, civilians, and reserve component personnel.

This paper outlines the logical consistency of estimating all cost components of the prototype enlisted model, which is used to determine the total manpower costs of mechanized infantry battalions comprised of the Bradley Fighting Vehicle (BFV) or the M113 Armored Personnel Carrier. The BFV is a growing component of the Army's new equipment acquisition program. The Army had 1,000 BFVs at the end of FY1985 and is expected to increase the number of these vehicles to 2,550 by the end of FY1986[4]. It

has been projected that approximately 5,000 additional BFV's will be acquired over the next five years (FY86 through FY90)[5]. The dollar value of the BFV program is reported to be between $10.7 billion (The Army Times, December 30, 1985) and $13 billion (The Wall Street Journal, December 31, 1985). The FY87 budget proposal estimates the BFV cost at $1.2 billion[6].

This paper is organized into four Sections. The manpower mix of the M113 and BFV battalions is presented in the next Section. The cost estimating theories, empirical methodology, and the cost savings are discussed in the two subsequent sections. The last section summarizes the results and discusses potential and ongoing applications of AMCOS

MANPOWER MIX OF BFV AND M113 MECHANIZED INFANTRY BATTALIONS

Data for the manpower compositions of the M113 and the BFV battalions were obtained from the Office of the Deputy Chief of Staff for Personnel (ODCSPER). One of the most significant difference in the occupational mix is the predominance of Infantryman Miltary Occupational Specialty (MOS) 11B in the M113 and that of Fighting Vehicle Infantryman (MOS 11M) in the BFV. Even though basic pay of all soldiers is the same, the annualized comprehensive costs of the two manpower mixes can vary significantly due to differences in the costs of allowances, permanent change of station, training and, retirement. The ODCSPER data also illustrate that the total number of enlisted soldiers in an M113 is smaller (829) compared to the BFV unit (849), thereby suggesting that the cost of M113 should be lower. This need not, however, be the case. If the soldier mix in the M113 unit is in higher paygrades and/or requires more highly trained individuals, then the opposite could be true.

THEORY AND EMPIRICAL ESTIMATION

AMCOS combines several cost theories to estimate manpower costs. These theories consist of the economic theory of human capital[7], accounting theory of human resources[8], and actuarial theory of life expectations[9].

The theory of human capital states that an increase in investment in education or training tends to increase returns (or productivity) associated with that investment. The Army invests considerable amounts in soldier training. During the period of investment in training, incremental soldier costs paid to the Army exceed their incremental benefit of increased productivity or performance. After completion of the training, however, the incremental benefit exceeds the incremental cost. The Army realizes the incremental benefit during at least the first enlistment term of the soldier. Therefore, the theory of human capital suggests that the training costs incurred by the Army should not be considered as one period costs but should be amortized over the years of useful life of the training.

The theory of human resource accounting considers human resources as assets--similar to a balance sheet of a firm. The valuation of these assests is based on costs of training, the costs of recruiting, and the probabilities of continuation of employees in the organization. Methodologies used to validate this theory include such operations research techniques as linear and non-linear programming and Markov transition matrices to account for the multiple probabilities of future changes of service states by employees. The theory suggests that human assets should be depreciated as physical assets.

The actuarial theory estimates life expectations of individuals, given their age, sex, and race. It is used in the AMCOS model to estimate retirement costs. The theory states that once a soldier is vested in retirement, the present value of his retirement benefits may increase or decrease. If he continues in service after vesting, the retirement annuity payments will increase in size. The present value of the sinking fund may, however, decrease because his life expectancy after the longer service span will decrease. The net effect of an increase in payments due to increased vesting and the required decrease in sinking fund can be positive or negative. The sinking fund is generally estimated from life and annuity tables developed by actuaries.

The empirical cost estimation methodology in AMCOS varies according to the type of manpower costs incurred by the Army of which there are thirteen classes. Some of these costs are fixed or one-time costs, (such as recruitment costs and costs of basic and initial advanced individual training). As suggested by the theory of human capital, these fixed costs are annualized by amortizing them over the average term of service of a soldier in a particular MOS and paygrade. As required by the Office of Management and Budget Circular A-76[10], a discount rate of 10 percent is used for amortization of all fixed costs. Other costs, such as pay and allowances, are recurring or variable costs. These variable costs are estimated by calc lating the number of soldiers in an MOS and pay grade during 1984. As discussed below, estimation methodologies for these costs vary according to type of variable costs (such as basic allowances for quarters and subsistence). Other costs will be incurred by the Army only in the future, e.g. retirement and post-separation costs. Stochastic methods are used to project the relative proportion of soldiers who will survive in the service to achieve vesting for retirement. Statistical methods are used to forecast the final pay grades of those who will have their retirement vested. A combination of these approaches resulted in estimating a required sinking fund. Engineering variable cost elements, consisting of materials, ammunition, and other supplies used during training periods are estimated in terms of human capital theory. A final cost component is engineering fixed costs such as obsolescence or depreciation of building sites. This cost element is also added to the cost of training. Estimation methodologies for all cost elements are

summarized below.

Basic Pay

This cost element includes the costs of annual basic pay and the social security contribution (FICA) at the current (1984) tax rate. This cost, by MOS and pay grade, is estimated from the Joint Uniform Military Pay System (JUMPS) data tapes for FY1984. The results, shown in Table 1, reveal that the basic pay for the BFV battalion is higher ($9.684 million) compared to the cost of an M113 battalion ($9.467 million). Basic pay comparisons of the alternatives would suggest that the M113 is less costly than the BFV. Such a conclusion would be misleading as several other cost elements have been ignored. These addditional costs could offset this basic pay advantage.

Selective Reenlistment Bonuses

Selective reenlistment bonuses (SRBs) are paid to soldiers who reenlist for a period of three or more years. The amount of bonus paid to a soldier is a product of (i) the length of reenlistment term (in years), (ii) his/her monthly basic pay, and (iii) the value of a bonus multiplier. The values of the SRB multipliers vary from 1 to 6 -- from the least to the most critical demand for soldiers in an occupation relative to their supply[11]. The maximum SRB was $16,000 in 1984. AMCOS estimates SRBs, by MOS, by applying the official SRBs to representative reenlistment rates derived as a function of length of service. The sources of data used for the estimation included the JUMPS data and the Enlistment Master Files (EMF). Table 1 shows that the average annualized cost of SRBs was higher for a BFV unit ($316,000) compared to that for the M113 ($280,000).

Special Pays

Special pays consist of two types -- proficiency pay and hazard duty pay. Proficiency pay is paid to certain special duty soldiers (e.g. recruiters, reenlistment NCOs, and drill sergents). Hazard duty pay is restricted to either specific hazardous occupations, (e.g. explosive demolition expert MOS 55D) or specific hazardous duty assignments (e.g. duty under hostile fire, flight crew- and non-crew member duty, soldiers holding a permanent parachute assignment, experimental stress, and the handling of toxic fuel). The estimation of average cost for this component was based on the total dollar amount of special pays divided by the total number of soldiers, by MOS and paygrade. Table 1 shows that these costs for the M113 unit were $107,000. For the BFV, however, these costs were only $26,000.

Allowances

This cost element comprises (i) Basic Allowance for Subsistence (BAS),

(ii) Basic Allowance for Quarters (BAQ), and (iii) an allowance for Clothing Maintenance. The direct cash payments of these allowances were estimated from the JUMPS database, by MOS and pay grade.

Since some soldiers are not paid these allowances in cash, but are provided with lodging and boarding by the Army, the cost of providing these in-kind allowances was imputed from direct payments. The BAS-in-kind amount was obtained from the Manpower and Personnel Army (MP-A) Budget submissions[12].

The BAQ-in-kind component was imputed from the JUMPS and EMF matched file, given marital status and housing status (residing in government quarters or receiving direct cash BAQ). Table 1 shows that the average cost of these allowances was higher for the BFV ($2.924 million) compared to the M113 ($2.847 million).

Variable Housing Allowance (VHA)

This allowance is given to soldiers in specific locations where the housing costs are higher than the housing costs paid by BAQ. The BAQ is designed to cover 65% of national median housing costs, by military pay grade, disregarding location of residence[13]. The average VHA payments, by MOS and pay grade, were calculated from the JUMPS data. Table 1 shows that the average cost of these allowances was lower for the BFV, ($125,000) compared to the M113 ($147,000).

Overseas Allowances

These allowances consist of Foreign Duty Pay, Family Separation Allowance, Sea Duty Pay, Overseas Extension Pay and the Overseas Station Allowances for Cost of Living, Housing (Rent Plus Program) and Temporary Lodgings. Soldiers stationed outside of the U.S. are paid these additional allowances. An average cost per soldier receiving these payments was calculated from the JUMPS pay records by dividing total overseas payments by the number of soldiers receiving these payments by MOS and paygrade. The estmated cost of this element (shown in Table 1), was lower ($72,000 per unit) for the BFV, compared to that of the M113 ($151,000).

Medical Benefits

The Army incurs costs of various types of medical and dental benefits for enlisted soldiers, retirees, and their dependents. These costs are incurred in four major programs: (i) Civilian Health and Medical Program of the Uniformed Services (CHAMPUS); (ii) medical and dental care in Army facilities; (iii) care in nondefense facilities; and (iv) care in Veterans Administration (VA) facilities. Only the variable costs of the first three of these cost categories were estimated in AMCOS. The cost in VA facilities was excluded because it is not incurred by the Army.

CHAMPUS. CHAMPUS provides care in nondefense facilities to dependents of active duty soldiers, retired soldiers and their dependents, and dependents of deceased soldiers. The Army's total CHAMPUS obligation in FY84 was $362 million[14]. In order to allocate this amount to soldiers by MOS and pay grade, it was assumed that the utilization rates for CHAMPUS are the same as the utilization rates for medical services in the civilian economy. The latter utilization rates were obtained from the 1978 National Health Survey data reported in the Statistical Abstract of the United States[15]. CHAMPUS provided data on the costs of inpatient and outpatient care by age and use rate by dependents of Active Army, dependents of deceased/retired Army veterans, and by Army retirees. This information was used to distribute the CHAMPUS costs according to age, marital status, and the number of dependents, by MOS and paygrade.

Medical and Dental Care in Army Facilities. The required data for costs of medical and dental care in Army facilities were obtained from the Director of Operation and Maintenance, Army (OMA Budget) and the Army Office of the Surgeon General. The data from the Office of the Surgeon General were included because the OMA data did not include surgical costs. The costs of officers and their dependents were excluded to restrict the model to enlisted soldiers only.

Active Army Use of Nondefense Facilities. In 1984, the cost of the Active Army's use of nondefense facilities was $22 million. This amount was distributed between the enlisted force (93%) and officers (7%) in proportion to the reported utilization rates. The allocation by MOS and pay grade was also based on utilization rates by age, sex, years of service, and marital status of soldiers as reported in the data discussed in the preceding two sub-sections.

Table 1 (Cost Element 7) indicates that the cost of these facilities was $342,000 for a BFV battalion and $337,000 for an M113 battalion.

Accession, Basic Training, and Initial Advanced Individual Training Costs.

AMCOS combined the amortized costs of these three elements because all are incurred during the first enlistment term of a soldier. These cost elements were amortized over the first tour, because, according to the theory of human capital, the returns from these investments would be realized by the Army over at least the first terms of the soldiers.

The accession (recruitment) cost consisted of the following seven elements:

Advertising cost. These data were obtained from the U.S. Army Recruiting Command (USAREC) and were allocated only to high school graduates, by MOS and pay grade. It was assumed, that these advertising expenditures were

aimed at increasing the availability of only high quality enlistees[16]. Non-high school graduates are generally more readily available.

Cost of Recruiters. The cost of recruiters was estimated in two steps. First, an average manpower cost of a recruiter (exclusive of cost of recruiting) was estimated for the Recruitment MOS by dividing the total cost of this MOS by the number of recruiters in that MOS. Second, the incremental cost of high quality enlistments associated with a percentage increase in recruiters, was imputed from a RAND Corporation study[17]. Using that study, the incremental recruiter costs were estimated in AMCOS by increasing the estimated manpower cost of a recruiter by 0.842 percent per recruiter.

Applicants' Meals, Travel, and Lodging. The total cost of transporting the applicants to the Military Entrance Processing Stations (MEPS) and their meals and lodging during the examination process was divided by the total number of accessions by MOS and paygrades E-1/E-2. This resulted in a per soldier estimate of these costs. The required data on total cost and accessions were obtained from the MEPS.

Hometown Recruiter Assistance Program (HRAP). This program provides monetary compensation for such travel expenses as permanent change of station (PCS) and per diem expenses incurred by active Army personnel who are recruiter aides (generally in pay grade E-1 and E-2). AMCOS allocated these costs to high quality soldiers (e.g. high school graduates and those in mental categories I-IIIA).

Tour Exhibits. This cost element includes the cost of exhibits, costs of temporary duty travel, and per diem expenses for personnel on the exhibit team. Personnel costs, such as pays and allowances, were excluded from estimating these costs to avoid double counting. The required (non-personnel cost) data were obtained from the Operations and Maintenance, Army budget. The allocation of these costs to the number of accessions, by MOS and pay grade, was based on information obtained from USAREC.

Total Army Involvement in Recruitment (TAIR). The TAIR program is conducted by non-recruiter active Army personnel in the form of parades, half-time shows, and fairs. It also conducts MOS clinics, sports clinics, Army exhibits and other addresses given by prominent Army speakers. Since a major goal of this program is to increase recruitment in the Army, the cost of this program was included in accession cost. The cost elements included were travel and per diem expenses of sending the Army personnel to TAIR events, as well as transportation costs of prospective enlistees to Army installations. The required cost data were obtained from USAREC (Operations and Maintenance, Army budget) and allocated equally to total accessions by MOS, paygrade E-1/E-2, in FY1984.

Military Enlistment Processing Stations (MEPS) Cost. The MEPS conduct both

Armed Services Vocational Aptitude Battery and medical examinations of applicants for all branches of the Armed Forces. The Army's share of the total operating cost of the MEPS was assumed to be proportional to the number of tests given to Army recruits. The unit costs, estimated by the MEPS Command for medical, mental and institutional examinations were $25.37, $6.64, and $2.89, respectively[18]. AMCOS multipled these unit costs by the number of Army applicants. The resulting total costs were distributed across the number of Army accessions in 1984.

Enlistment Bonuses. Enlistment bonuses are paid to high quality recruits (high school graduates in mental catagories I-IIIA) who agree to enter hard-to-fill military occupational specialties. In 1983, there were 48 (out of 350) MOSs eligible for these bonuses[19], varying from $1,500 to $8,000 per soldier depending on initial contract period. These cost data on the total amounts paid and the number of payments made, by MOS, were provided by USAREC. These 1983 costs, by MOS, were apportioned to the number of 1984 accessions, by MOS.

Initial Training Costs

The AMCOS model spent considerable resources in estimating training costs both because of its roots in the theory of human capital and the size of the training expenditure. The Training and Doctrine Command (TRADOC) spends about 10 percent of the total $81 billion Army budget in imparting several levels of training[20]. The first levels consists of eight weeks of basic training given to all new recruits. After successful completion of their basic training, an advanced individual training (AIT) ranging from 4 to 47 weeks is given to first term soldiers in specific MOSs, for skill level one. Advanced training for skill level two and above is generally offered to non-commissioned officers (NCOs) in their second and third terms of service. AMCOS included the costs of the first two (basic and initial AIT) types of training under "accession" costs and relegated the third level of training under a separate cost item called "advanced training". The cost of basic training, included in accession cost, is amortized over the soldier's first enlistment term. This is in consistent with the theory of human capital discussed above.

In order to estimate advanced individual training (by MOS and pay grade), AMCOS developed a course cost database by merging and matching two separate data files. The first was the Army Training Requirements and Resources System (ATRRS) file[21], maintained by the U.S. Army Management Support Agency (USAMSA) for FY83. This file was used to obtain information on (i) MOS (e.g. 33S) for which a training course was designed, (ii) class (102) of instruction given, (iii) class start and end dates, (iv) class enrollment, and (v) the number of students graduating from the class. The last two records also contained a component code, so that one could distinguish between training levels (initial or advanced) and trainee

soldiers (commissioned officers or enlisted). This ATRRS database also included a Recruitment Quota System (REQUEST) file which has information on the number of training seats available for new recruits in specific occupations. The second file was the Army Training Resource Management, 159 (ATRM-159), a collection of cost analysis reports prepared by TRADOC for the Comptroller of the Army[22]. These cost data were also available from U.S. Army Management Support Agency in a computer file. These reports contain information, on (i) MOS (e.g. 33S) numbers, (ii) direct mission costs, (iii) indirect costs of base operations, and (iv) fixed and variable costs. A matching of the two files (ATRRS and ATRM-159) by MOS provided information on the cost per graduate, by MOS and paygrade.

The AMCOS project matched the ATRRS course file for FY83 with the ATRM-159 cost file for FY82. The ATRM-159 cost data were already converted into 1984 dollars. Only about half of the ATRRS courses matched with the ATRM-159 costs, perhaps because the cost reports are not updated periodically. To update the remaining costs, FY 1979 ATRM-159 costs were obtained and inflated with a price index to 1984 dollars.

It must be noted that AMCOS did not use the ATRM-159 total cost per graduate at $61,073, as the estimated training cost. This was because it contained several cost elements which were already included under other categories. For instance, the total cost contained pay and allowances of training instructors, pay and allowances of students, etc. In order to avoid such duplication, AMCOS included only the costs of (i) travel associated with the course ($127) and (ii) direct mission variable cost ($1,921 from OMA budget plus $2,605 from MPA budget), thus totalling $4,653 per graduate. To this cost, we added an opportunity cost of time spent by soldiers while they were in the training schools. The rationale for adding such a cost is that the Army was incurring a cost of their pay and allowances during this period, while the soldiers were not contributing directly or productively in their occupations. This opportunity cost was calculated in two steps. First, an annualized economic cost of a soldier in this MOS was calculated at $9,195. Second, since a soldier spent 34.8 weeks in MOS-33S out of 52 weeks, the value of proportionate lost time was $6,130. Hence, the cost of training in MOS-33S was $4,653 + $6,130 = $10,783, not $61,073 as indicated in ATRM-159. In the AMCOS model, this cost was amortized over the first enlistment term of a soldier as per human capital theory. The amortized value of the estimated training cost ($10,783) in this example amounted to $3,261.15 for MOS-33S (Electronics War Intercept Equipment System Repairer) pay grade E1/E2.

A problem with this cost element is that the available data from TRADOC and the Health Services Command covered only about 90 percent of the total training costs incurred by the Army. Future versions of AMCOS will improve upon this deficiency by obtaining data on costs of training imparted by other Army commands.

The annualized economic cost of "accession, basic, and initial advanced individual training" for M113 and BFV battalions, shown in Table 1, was $1.838 million and $1.636 million, respectively.

Advanced Training

Recall that advanced training was defined to include all types of training after the completion of training for the first duty station of a soldier. The computation of advanced training costs, and the sources of data, are similar to the cost of initial individual training. The only difference in methodology is that these advanced training costs are not amortized because most of these soldiers tend to be non-commissioned officers (NCOs) who would tend to stay with the Army longer than their reenlistment terms. Table 1 shows that the cost of this training was slightly lower for the BFV ($67,000) compared to that of M113 ($79,000) battalion. This relatively low cost is due to the small number of NCOs in these units.

Due to non-availability of required data on two types of costs, this cost element is not comprehensive. First, the NCO leadership training is provided locally at the division level. This training is undertaken as extra duty and, hence, direct resource costs are not separately available. Second, the cost of NCO leadership training provided in Europe is also not available. These gaps, however, will be filled in the future versions of AMCOS.

Rotation: Permanent Change of Station (PCS)

This cost category includes costs for Rotation (generally every three years), Operational and Organized Unit moves. It is, however, exclusive of the costs of permanent change of station moves associated with accession, training, and separation.

The required data on PCS were obtained from the Army Military Personnel Center (MILPERCEN) Current Duty Movement Designator Code (MDC) tape for FY1983[23]. This file contained each soldier's MOS, pay grade, date of last PCS move, the MDC for the latest move, and the area of current foreign service tour. The MDC also specified if the move was for accession, training, operational separation, or for an organized unit. This information was used to allocate Army expenditure in the MP-A budget to the appropriate MOSs and pay grades. Table 1 shows that the rotation PCS cost of an M113 battalion ($741,000) was almost twice the cost of a BFV battalion ($371,000) in 1984.

Retirement

These costs are difficult to estimate as they are paid in the future,

although they accrue during the active duty period of the soldier. The accrual basis of budgeting the retirement cost was adopted by the Congress in FY 1985[24]. Since the existing AMCOS model was developed for FY84, it did not use the accrual method. The economic cost of retirement was estimated by disaggregating this cost into four components: (i) non-disability retirement, (ii) severance cost, (iii) disability retirement, and (iv) death payments. The actuarial theory of retirement costs discussed above was used for estimating vesting and the sinking fund. The estimation of continuation rates, by MOS and pay grade, were based on the probabilities of continuation rates available from the theory of human resource accounting discussed above.

Non-disability Retirement. AMCOS used continuation rates of soldiers, by MOS and pay grade, to estimate the number and distribution of soldiers who will remain in the service up to the time required to achieve vesting for retirement. For those who were estimated to remain, AMCOS calculated their pay grade at the time of retirement. Actuarial, financial, and statistical methods were combined to estimate the present values of future streams of annuities paid after retirement. The annuity values were estimated for those whose probabilities of continuation rates were **until** they were vested in retirement as well as for those who were expected to continue in service **after** vesting. The sinking fund for the latter group was reduced in concert with their lower life spans after retirement due to longer service after vesting.

The retirement payment estimation methodology assumed continuation of the existing retirement system. The major components of the present system include vesting at 20 years of service, and a monthly annuity from 50 percent (for 20 years of active service) to 75 percent (for 30 or more years of service) of the average basic monthly pay over the last three years of service[25].

The source of data for continuation rates was Defense Manpower Data Center's (DMDC) Loss Edit File[26] extract and that for life expectations tables was DMDC's Office of the Actuary[27].

Severance Cost of Disablement. This is a lump sum payment made to disabled soldiers upon their separation from the Army. The amount of payment depends upon a multiplier of monthly basic pay received by a soldier prior to separation. The multiplier varies from 6 to 24, increasing with the length of military duty. AMCOS estimated sinking fund amounts required to be set aside by the Army based on data on years of service, pay grade, MOS, and probabilities of separation.

Disability Retirement. Apart from a lump-sum payment for disablement, a soldier may also be eligible for disability retirement payments. The amount of disability retirement varies according to the percentage of

disablement, subject to a minimum and a maximum amount. The maximum amount is the same as the normal retirement amount, (50 to 75 percent of the average monthly basic pay, depending on the length of service). The minimum amount is 25 percent of monthly basic pay. The information on percentage of disablement was obtained from DMDC. A sinking fund for disablement was estimated for AMCOS by projecting the percentage disablement and the associated components of future annuity payments (such as pay grade, years of service at retirement, and age at disablement).

Death Benefits. When a soldier or a veteran dies, his (her) spouse/dependents is paid $3,000 as a death benefit and $750 for cost of burial, if the actual burial is not provided by the Army. In cases where the burial is provided by the Army, AMCOS imputed this economic cost at $750 per soldier. The methodology for estimating a sinking fund based on future death payments, by MOS and pay grade, is similar to that used to estimate the sinking fund for non-disability retirement benefits. Table 1 shows that the total cost of retirement, (the sum of the preceding four types of costs) was $353,000 for the M113, compared to $359,000 for the BFV battalion.

Downtime Cost

The sum of the preceding twelve cost elements is defined as "total soldier cost" (TSC). The TSC estimation assumed that the soldier worked a standard number of hours (2,080) per year. In practice, the number of work hours could be smaller because of soldier absence due to annual or sick leave, transience, or imprisonment. During these periods of absence the Army has to assign a replacement soldier to carry out duties of the absentee. AMCOS termed such absentee (or replacement) cost as unproductive or "downtime" cost. This "downtime" cost was added to the TSC to arrive at a soldier "position cost". Table 1 shows that "downtime" cost of an M113 unit was $2.59 million, compared to $2.49 million for the BFV unit. Comparison of cost elements 1 and 14 of Table 1 shows that basic pay comprised only about one half of total soldier position cost in both M113 and BFV battalions.

MANPOWER COST SAVINGS FROM BFV

Table 2 shows the manpower cost tradeoff analysis of a battalion unit as well as per soldier cost of the BFV and the M113. It may be recalled that a BFV battalion unit required 849 enlisted soldiers compared to 829 required by an M113 battalion. Despite the higher manpower requirement, its cost is lower ($18.595 million) compared to that for an M113 battalion ($19.333 million). Therefore, a cost savings of $0.738 million per battalion unit or $1,419 per soldier is associated with the replacement of the M113 with the BFV. Any discussion of the technical efficiency of BFV in the Armor versus Infantry divisions[28] of the Army is outside the realm

of this paper.

In order to estimate the enlisted manpower cost savings, it was assumed that the future enlisted manpower size and composition of a BFV battalion will be the same as at present and that there will be no difference in manpower costs of officers in the two alternative battalions. Currently, a BFV battalion unit has 45 BFVs and 849 enlisted soldiers[29], so that there are 18 soldiers per BFV. While a BFV carries only three soldiers, there are 15 foot soldiers per BFV. Information from the BFV Cost Analyst/Program Manager suggests that the Army will have 6,882 BFV by the end of FY1990. These BFVs would be distributed over 153 battalions (6,882/45). Since the manpower cost savings per battalion unit is $0.738 million, the Army will obtain an annual savings of $113 million after all the BFVs are fielded. Further, assuming that a BFV lasts ten years, the Army can expect to save $1.13 billion with the replacement of the M113 with the BFV.

CONCLUSIONS

This paper described the Army Manpower Cost Model (AMCOS) which employs economic theory of human capital, accounting theory of human resources, and actuarial theory of life expectation to help estimate Army manpower costs of systems. Thirteen classes of costs were estimated for over 350 MOSs and 7 pay grades in AMCOS. The model was applied to estimate alternative manpower costs of the Bradley Fighting Vehicle (BFV) and the M113 Armored Personnel Carrier in mechanized infantry battalions. The empirical results revealed that manpower costs of BFV battalions were lower relative to those of M113. In particular, the BFV would save the Army over a billion dollars in manpower costs over their assumed life of ten years. The results also indicated that the often-used measure of basic pay as a proxy for soldier cost is inappropriate, as basic pay accounted for only one half of the total compensation costs incurred by the Army.

AMCOS can be usefully employed by Project Managers in the Army Materiel Command. The Project Managers can provide the MANPRINT Division with manpower requirements to which cost estimates can be furnished. AMCOS can also be used to analyze the cost effectiveness of alternative personnel policies, such as increasing reenlistments or increasing enlistments under alternative force structure scenarios.

Currently, the AMCOS prototype model is being used on a limited and test-case basis by analysts at the Missile Munition Center, Red Stone Arsenal, Army Logistics Center, and Aberdeen Proving Ground. Army contractors such as Information Spectrum, the Hay Group, and Sikorsky Aircraft are also experimenting with the prototype model. There is considerable need for accurate and comprehensive manpower cost data by Army analysts and policymakers alike.

TABLE 1

COMPARISON OF MANPOWER ECONOMIC COSTS OF M113 AND BFV BATTALIONS, 1984

(th. dollars)

COST ELEMENT	M113	BFV
1. Basic pay	9,467	9,684
2. Selective Reenlistment Bonuses	280	316
3. Special Pays	107	26
4. Allowances	2,847	2,924
5. Variable Housing Allowances	147	125
6. Overseas Allowances	151	72
7. Medical Benefits	337	342
8. Accession, Basic and Initial Advanced Individual Training	1,838	1,636
9. Advance Training	79	67
10. Rotation: Perm. Change of Stations	748	371
11. Separation	383	174
12. Retirement	353	359
Total Soldier Cost	16,743	16,103
13. Down Time Cost	2,590	2,491
14. Position Cost	19,333	18,595

TABLE 2

ENLISTED MANPOWER COST TRADEOFF:
M113 VERSUS BFV

SYSTEM	COST OF BATTALION UNIT $ MILLION	COST PER SOLDIER $
M-113	19.333	23,321
BFV	18.595	21,902
BFV Cost Savings	0.738	1,419
BFV % Savings	(3.82)	(6.08)
BFV Savings: Annual, when fully fielded	112.914	----
BFV Savings over life cycle of 10 years	1,129.14	----

REFERENCES

1. Hardman, Comparability Analysis Methodology Guide, Volume 1 through Volume V, Army Research Institute and Soldier Support Center: National Capital Region, Technical Report, 1986.

2. C. Alan Boneau, Jon S. Freda, Stanley J. Kostyla and Halim Ozkaptan, Review of Personnel Affordability Research Within the Conceptual Development of the Man-Integrated Technology (MIST) System, Army Research Institute Research Report, October 1980.

3. COL John N. Tragesser, "MANPRINT: Manpower and Personnel Integration", Army Research, Development and Acquisition Magazine, Jan-Feb 1985, P. 4-6; Robert W. Bauer, "Putting People into Armor Development," Defense Management Journal, First Quarter, 1983, p. 3-9; Tim Tice, "MANPRINT Attracts Attention From Congress," Army Times, February 3, 1986, p. 46, 63.

4. P. J. Budhan, "Army Modernization Safe for Years, But Big Cuts Lie Ahead, Thurman says," The Army Times, December 31, 1985, noted that the Army will by the end of FY86, and Tim Carrington, "Politics and Policy: Pentagon Gives In-house Critic Cold Shoulder for Questioning Tests Done on Bradley Vehicle," The Wall Street Journal, December 31, 1985, p. 28.

5. Personal Communications with Mr. Dan Marks and Ms. Jessie Foster of Army Materiel Command

6. The Washington Post, February 6, 1986.

7. Becker, Gary S., Human Capital: A Theoretical and Empirical Analysis with Special Reference to Education, New York: National Bureau of Economic Research, 1964.

8. Flamholtz, Eric G., Human Resource Accounting, (Encino, CA., Dickenson Publishing Co., 1974 and "Human Resource Accounting: State of the Art and Future Prospects," Annual Accounting Review, 1979.

9. Berterman, J., "Retirement Costs", Appendix D in Naval Manpower Costs and Cost Models: An Evaluative Study. Administrative Sciences Corporation Report R-119, Alexandria, VA., 1978; and Defense Manpower Data Center, Office of the Actuary, Valuation of the Military Retirement System, 1984, Washington, DC, 1984.

10. Office of Management and Budget, Cost Comparision Handbook-Supplement No.1 to OMB Circular A-76: Policies for Acquiring Commercial or Industrial Products and Services Needed by the Government, Washington, D.C., March 1979.

11. Hyder Lakhani, and Curtis Gilroy, "Army Reenlistment and Extension Decisions by Occupation," in Curtis L. Gilroy (Ed.) Army Manpower Economics, Westview Press, Boulder, CO., 1986, p. 225-256.

12. U.S. Department of the Army Justification of Estimates for Fiscal Year 1984, Military Personnel, Army, Submitted to Congress, February 1983; and U.S. Army Cost and Economic Analysis Center, U.S. Army OMA and MPA Cost Factors, Vols. 1 and 2, DCA-H-1, 1984.

13. Jane-yu Li and Suzanne Worth, "Evaluating the Rate Setting Methodology in the Military Variable Housing Allowance Program," paper presented at the Allied Social Science Associations meeting, New York, December 29, 1985, p. 1-20.

14. Office of Civilian Health and Medical Program of the Uniformed Services (CHAMPUS), telephone communications, 1984.

15. U.S. Department of Commerce, Bureau of the Census, Statistical Abstracts of the United States, 1984. Washington, D.C.

16. Thomas V. Daula and D. Alton Smith, "Recruiting Goals, Enlistment Supply, and Enlistments in the U.S. Army," in Curtis L. Gilroy (Ed.), op-cit., p. 101-123.

17. James N. Dertouzos, Recruiter Incentives and Enlistment Supply, RAND Corporation Report R-3065-MIL, May 1985, prepared for the Office of the Assistant Secretary of Defense, Santa Monica, CA.

18. Military Enlistment Processing Command, Correspondence, 1984.

19. U.S. Army Recruiting Command, Correspondence, 1984; and General Accounting Office, Perspectives on the Effectiveness of Service Enlisted Bonus Programs, Washington, D.C., 1983.

20. Army Finance and Accounting Center, Military Occupational Speciality Training Cost Handbook (MOS B), Fort Benjamin Harrision, Indianapolis, IN., 1983.

21. U.S. Army Management Support Agency ATRRS Course List, Computer File, Army DCS Personnel Training Requirements Office, Washington, D.C., 1984.

22. Army Training and Doctrine Command, Course Cost Analysis - ATRM 159, Computer File, TRADOC, DCRM, Fort Monroe, VA, 1984.

23. Military Personnel Center, Current Duty Movememnt Designator Code Data Tape for FY 1983, Alexandria, VA, 1984.

24. Department of Defense, Fifth Quadrennial Review of Military Compensation, Volume 1, Uniformed Services Retirement System, January 1984, Washington, D.C.

25. Op. cit. 24

26. Defense Manpower Data Center, Loss Edit File Data Extract for Army, 1984, Monterey, CA.

27. Defense Manpower Data Center, Office of the Actuary, Life Tables for Enlisted Servicemen, 1984.

28. Jim Tice, "Defense Trends: Tests Show Bradley Remarkably Resistant", The Army Times, Decemeber 30, 1985, p. 29-30, "Infantry Still Lacks Tank-Killing Weapon," The Washington Post, p.A1, A7, January 13, 1986.

29. Private communication with MAJ Jefferey Anderson, Military Personnel Center, January 1986.

THE TETRAHYMENA-DFPASES: ELUCIDATION, CHARACTERISTICS, THERAPEUTIC POTENTIAL, AND UTILITY AS NON-CORROSIVE DECONTAMINANTS

*WAYNE G. LANDIS, DR.
H. DUPONT DURST, DR.
US Army Chemical Research and Development Center,
Aberdeen Proving Ground, Maryland 21010-5423

RUSSELL E. SAVAGE, JR., DR.
Health and Effects Research Laboratory
U.S. Environmental Protection Agency
26 West St. Clair Ave., Cincinnati, Ohio 45268

BRUCE G. HARPER, DR.
US Army Dugway Proving Ground
Dugway, Utah 84022

INTRODUCTION

On 27 April 1983, an enzymatic activity from the protozoan Tetrahymena thermophila that could hydrolyze the potent acetylcholinesterase inhibitors O,O-diisopropylphosphofluoridate (DFP) and O-1,2,2-trimethylpropylmethylphosphonofluoridate (soman) was discovered on the campus of Indiana University, Bloomington [1]. Since that time, the research on the material has become national in scope and character. The purpose of this report is to review and consolidate the last three years of discovery and to evaluate the future impacts and applications of the Tetrahymena-DFPase system.

First, it is essential to introduce and define the term "DFPase." An enzyme capable of hydrolyzing the P-F bond of an organofluoromonophosphate is denoted a DFPase. Currently DFPase-activity is determined using an ion sensitive electrode to measure the fluoride produced by the hydrolysis reaction [1,2,3]. Spontaneous (non-catalyzed) hydrolysis of substrate is measured and then the material suspected of activity is added to the reaction vessel. Fluoride production is recorded at 1 minute intervals using an Orion 901 meter. Protein concentration is measured using the Bio-Rad system [4]. The Apple compatible program DFPASE2 calculates the reaction rates.

Two basic classes of DFP hydrolase enzymes, termed "Mazur-type" and "squid-type", have been partially characterized [3,5,6,7,8]. "Mazur-type DFPase" is used to designate a Mn^{2+} stimulated enzyme that hydrolyzes soman faster than DFP. Mazur-type DFPase isolated from hog kidney is dimeric and has a molecular weight of 62,000 D [9]. Escherichia coli and mammalian tissues are sources containing high concentrations of Mazur-type DFPase [5]. Squid-type DFPase is used to designate an enzyme which hydrolyzes DFP faster than soman and is either not affected, or slightly inhibited by, Mn^{2+}. The molecular weight of squid-type DFPase is 26,000 D and it is present in the optic ganglia, giant nerve axon,

hepato-pancreas, and salivary gland of cephalopods [3]. The Mazur-type enzyme from mammalian sources is not particularly stable compared to the "squid-type" DFPase. Squid-type DFPase has been bound to agarose to form a prototype bioreactor for detoxification of soman and DFP [3]. Recently the Mazur-type enzyme has also been bound and stabilized in a similar manner (Hoskin, personal communication, 1985).

Several lines of evidence indicate that many organisms may carry both classical types of DFPase-activities. White [6], using a DFP affinity column to purify DFPase from hog kidney, found that at high purification the material hydrolyzed DFP faster than soman. It was not possible to assay this material for Mn^{2+} stimulation. Hoskin [6] has repeated this work with similar results. Additional work by Hoskin [6] indicates that squid-blood contains small amounts of Mazur-type DFPase. Estimations made from a diagram comparing the log (soman/DFP) Mn^{2+} ratio and log (soman/DFP) no Mn^{2+} ratio with mixtures of purified Mazur-type (E. coli) and squid-type DFPases indicate that E. coli and hog kidney may contain 50 percent, or more, squid-type DFPase.

INITIAL STUDIES

The material used in these studies is derived from stock BIV T. thermophila grown in axenic media containing 1.0 percent w/v proteose peptone with the addition of 0.3 percent w/v yeast extract. Initially, cultures were grown in a semicontinuous flow culture apparatus containing 6-7 liters of medium continuously aerated and stirred. Tetrahymena were concentrated by algal centrifuge and packed using oil testing tubes [10]. Cells were disrupted by freeze-thawing. Initially, the DFPase activity in T. thermophila was classified a Mazur-type [1], the kind found predominantly in organisms such as E. coli and mammals. Soman hydrolysis was 10 times faster than DFP hydrolysis and was stimulated by a factor of 2.3 by Mn^{2+} (Table 1). Addition of 0.01% w/v ethylenediaminetetraacetic acid (EDTA), a powerful chelating agent, halted the hydrolysis of the substrate. Exposure of the material derived from the Tetrahymena to 65°C for 30 min destroyed 90% of the DFPase activity.

Table 1. Comparison of DFPase activity from typical sources. All rates are from extracts prior to purification.

	umoles g extract^{-1} hr^{-1}					
	DFP		Soman		Soman/DFP Ratio	
	No Mn^{2+}	Mn^{2+}	No Mn^{2+}	Mn^{2+}	No Mn^{2+}	Mn^{2+}
Tetrahymena thermophila	46	41	477	1097	10.4	26.7
Squid (6)						
Ganglion	183	143	32	35	0.2	0.2
Hepatopancreas	347	343	138	152	0.4	0.4
Rat (6)						
Kidney	10	30	172	314	17.2	10.5
Brain	2	3	18	52	9.0	17.3
Liver	23	27	311	467	13.5	17.3
E. coli	24	180	1116	1836	46.5	10.2

Tetrahymena thermophila has an excellent yield of activity, 2.5 times the rate of hydrolysis for soman compared to rat liver. The ability of EDTA to halt the enzymatic activity indicated that a divalent cation(s) is necessary for the reaction. Interestingly, the Mn^{2+} did not increase or may have slightly inhibited DFP hydrolysis, a squid-type characteristic, while soman hydrolysis was stimulated, a Mazur-type trait.

Next, the effects of pH, ionic strength and temperature on the DFPase activity from Tetrahymena were determined. Reaction rate of the homogenate was examined at 0 and 500 mM NaCl. No significant difference in reaction rate was observed. The activity versus pH curve (Figure 1) illustrates 3 general regions of activity, pH 4-6, pH 6-7.5 and above pH 7.5. At pH 10 activity greater than spontaneous hydrolysis and greater

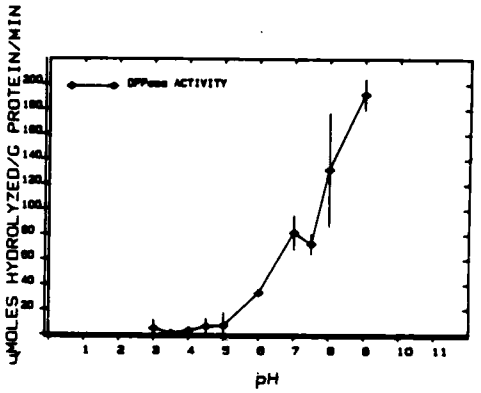

Figure 1.
DFPase Activity vs. pH. Three regions of activity are apparent, pH 4 to 6, pH 6 to 7.5, and greater than pH 8. at pHs less than 3 and greater than 9, the fluoride electrode method is inaccurate. Activity greater than spontaneous or with heat treated enzyme (70° C for 1 hr) can be measured at pH 10.

than heat treated (70°C for 1 h) homogenate was observed. As with pH, the temperature range of the DFPase activity is quite broad (Figure 2). Activity is present over a range of 20-55°C. A 3-fold increase in reaction rate occurs from 20-40°C. Again a plateau of activity occurs from 35-50°C. Activity at 55°C is still greater than at 20°C.

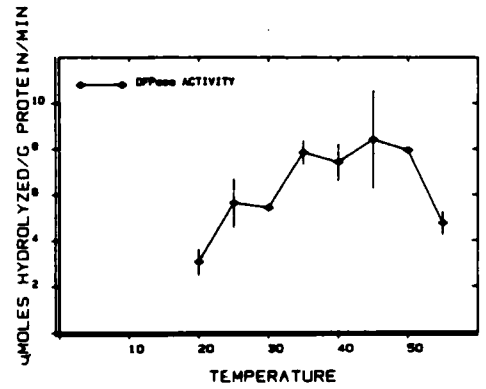

Figure 2.
DFPase Activity vs. Temperature. An approximate 4-fold increase in activity occurs at 35-50°C compared to 20°C. Again, a plateau is observed with no statistically significant change in activity from 35 to 50°C. Activity at 55°C is greater than 20°C.

Kinetics of DFP hydrolyzing activity at pH 7.2 and 25°C, 30°C and 40°C were examined at concentrations of 0.6 x 10^{-3} M. The activities are plotted in Figure 3 and the K_m and V_{max} at each temperature are listed in Table 2. The K_m decreased with an increase in temperature as the V_{max} increased 5-fold.

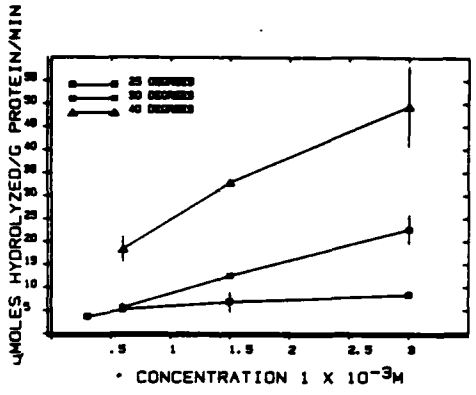

Figure 3.
Concentration, Temperature and DFPase Activity. At 25°C the activity of the DFPase was only slightly altered by a 5-fold change in concentration. At higher temperatures, the increase in concentration is followed by an increase in activity.

Table 2. Temperature and Enzymatic Kinetics of DFP-hydrolysis.

Temperature °C	V_{max} umoles DFP hydrolyzed g protein min	K_m Molar Concentration
25	8.96	4.63 x 10^{-4}
30	28.30	2.51 x 10^{-3}
40	43.70	1.17 x 10^{-3}

Initial attempts at purification of the DFPase were by using a molecular sizing column composed of Sephacryl S-200. The supernatant of the disrupted cells centrifuged at 100,000G was placed on the column. Activity of the 5 mL fractions was assayed 3 h after collection using DFP as the substrate for screening. The partial purification of activity (Table 3) varied from 4.9- to 16.4-fold increase in DFP hydrolysis. Maximum activity was found in the fraction corresponding to 75,400 daltons. The partially refined material also demonstrated enhanced stability at 0°C. Interestingly, the rate of soman hydrolysis increased on 2-3 fold. This differential enhancement of DFP hydrolysis is also apparent in the reduction of the Soman/DFP ratio. This skewing of the ratios upon purification was the first indication that another enzyme may be at least partially responsible for the hydrolysis of soman.

Table 3. Initial Purification of DFPase Activity.

	u mol substrate hydrolyzed g protein^{-1} min^{-1}					
	DFP		Soman		Soman/DFP Ratio	
	No Mn^{2+}	Mn^{2+}	No Mn^{2+}	Mn^{2+}	No Mn^{2+}	Mn^{2+}
Homogenate	11.1	9.8	113.6	261.2	10.2	11.6
Sephacryl fraction	104	116	383	550	3.7	4.7
Increase in Activity	9.4	11.8	3.4	2.1		

Further purification of the DFP-hydrolyzing peak was performed using a Sepharose-DEAE ion exchange column. A 0-500 mM NaCl gradient was used to elute the enzymatic activity. DFP was used as the substrate. A 1,000-fold purification of DFP hydrolyzing activity was accomplished (Table 4).

Table 4. Purification of Tetrahymena-DFPase.

	umol DFP hydrolyzed g protein^{-1} min^{-1}	Purification
Homogenate	6.0	
Sephacryl S-200 fraction	52.6	8.8
Sepharose-DEAE fraction	6596.7	1099.5

Vertical slab polyacrylamide gel electrophoresis was performed on the fractions from the Sephacryl and Sepharose columns that exhibited DFPase activity. Figure 4 diagrams the zymogram resulting from the electrophoresis. Upon Sepharose purification three major bands appeared on the gel that corresponded to bands from the samples derived from the molecular sizing column.

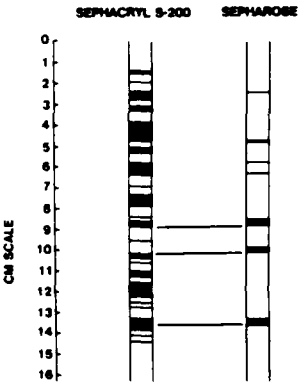

Figure 4. Polyacrylamide Cell Electrophoresis. Electrophoresis of the fraction corresponding to the peak activity of the molecular sizing column resolved at least 24 bands. Subsequent purification using the ion exchange column resulted in seven bands, the three major bands corresponding to bands of the molecular-sizing fractions.

PRODUCTION

An increase in the production of the Tetrahymena-DFPase segment of the homogenate was now mandatory in order to further characterize the material and to explore its utility. A program to produce large amounts of a material equivalent to the best purification resulting from the molecular sizing column was initiated at Dugway Proving Grounds, Utah. Scale-up of production used 200 L fermentation batches. T. thermophila reached concentrations of 7 x 10^5 viable cells/mL, a dry cell weight of 1.3 g/L. Cells were collected using a chemical centrifuge, sonicated, centrifuged, and the soluble proteins were precipitated with 60 percent $(NH_4)SO_4$. Desalting and further purification were performed using a Sephadex G-100 column. The resulting material was lyophilized for storage. A 16-fold increase in activity compared to the homogenate was accomplished with an activity greater than 45 umoles DFP hydrolyzed g of $protein^{-1}$ min^{-1}. Initial observation indicated that 1.5 g of functionally pure DFPase could be collected from a 200 L batch. The material produced was equivalent, except for the greater specific activity, to the crude Tetrahymena-homogenate. Production of stable lyophilized material that can be stored indefinitely at 5°C has become routine. Elimination of the supply problem facilitated the rapid pace of research delineated next.

DISCOVERY OF MULTIPLE DFPases

Several lines of evidence previously pointed to the existence of more than 1 DFPase existing within the cell. As previously discussed, purification of T. thermophila "DFPase" using DFP as the initial substrate for screening demonstrated that as the DFP hydrolyzing activity increased 10-fold, the soman hydrolyzing activity increased only 2-3 fold [4]. A suggestion was originally put forward that a mixture of two enzymes of close molecular weight were present within the homogenate of T. thermophila [1,11]. Additionally, while DFP hydrolyzing activity of the homogenate was not increased by Mn^{2+}, a squid-type characteristic, the soman hydrolyzing activity was doubled, a Mazur-type characteristic. An additional indication that the activity of the homogenate may be due to several enzymes is the broad range of pH and temperatures that demonstrate activity. Plateaus of activity are noted between pH 6-9 and at temperatures of 35-50°C [12]. Additionally, a shoulder often appeared on the activity versus fraction plot of the molecular sizing purification as is present in run 91185 and to a lesser extent in run 6685 (Figure 5).

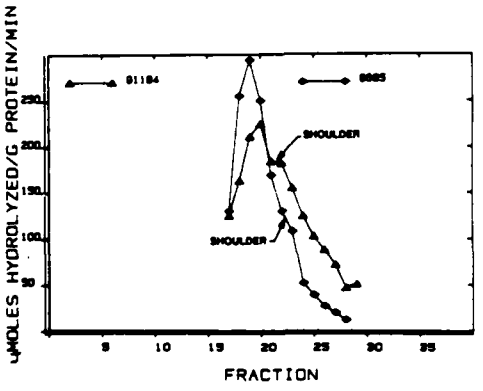

Figure 5.
Initial Purification of DFPase Activity. Initial purifications using the molecular-sizing columns and the large fracture routinely resolved a shoulder of DFPase-activity. Graphs are examples of purification efforts with two different columns. Material in 91184 is derived from the entire Tetrahymena-homogenate while the purification 6685 used the partially purified material from the large fermentations.

Upon reducing the fraction volume from 5 to 1.03 mL to increase the resolution of the molecular sizing purification, 3 major peaks of activity immediately became apparent (fractions 15-12, 21-24, and 24-27) and appeared reproducible (Figure 6a). These major regions of activity were subsequently assayed approximately 1 week later to examine the stability of the activity at 5°C (Figure 6b). The first peak had disappeared and the activity of the third was greatly reduced. The middle peak seems to be unaffected by the storage. In several of these purifications a small peak at approximately fractions 9-13 was noted. The assays using soman were also interesting (Figure 7a). Peaks corresponding to the fractions demonstrating peak DFP hydrolyzing activity were again present. A minor peak at fraction 9-13 again appeared. Of special interest was that the rate of soman hydrolysis was approximately the same as the rate of DFP hydrolysis. When 1 mM Mn^{2+} was added to the assay mixture, the pattern drastically changed (Figure 7b). The activity present in fraction 9-13 is stimulated 17-30 fold and exhibits the most rapid amount of soman hydrolysis. The peak observed in the fractions 15-20 also demonstrates significant stimulation. The fractions corresponding to the other two DFPase activities (fractions 21-24 & 24-27) showed slight increases in soman hydrolysis. Also noted for the first time is an increase in soman hydrolysis in fractions 41-42 of preparation S8185M. The presence of this peak was confirmed in subsequent purification runs. Figure 8 graphs the amount of stimulation due to 1 mM Mn^{2+}.

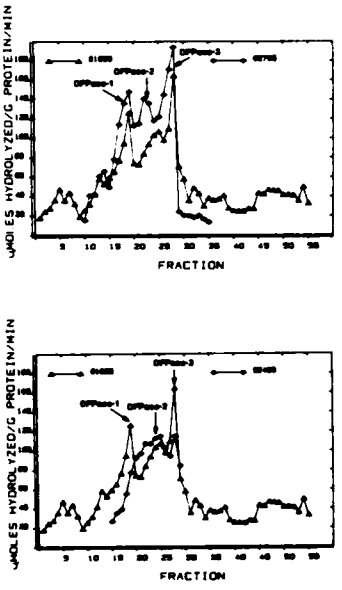

Figure 6.
Identification of DFPase. Screening of the small fractions from the molecular-sizing column with DFP revealed three major peaks of DFPase activity (6a). Storage at 5°C resulted in the degradation of DFPase-1 and DFPase-3 (6b).

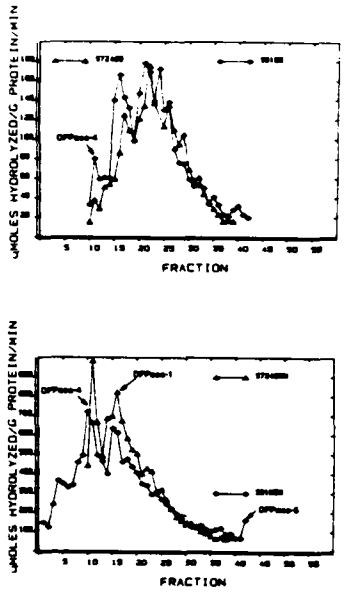

Figure 7.
Identification of DFPase. Using soman as the substrate illustrates that the rate of soman hydrolysis is approximately equal to DFP hydrolysis (7a). Addition of 1 mM Mn^{2+} drastically increases the rate of soman hydrolysis (7b).

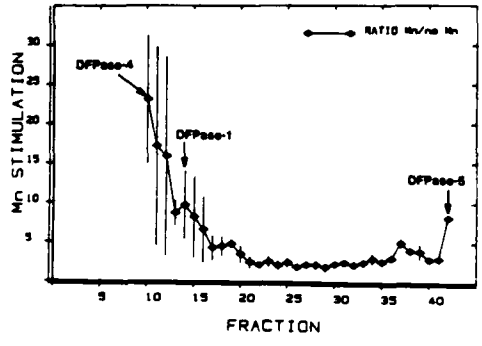

Figure 8.
Stimulation of Soman Hydrolysis by Mn^{2+}. Graph plots the ratio of soman hydrolysis with 1 mM Mn^{2+} to soman hydrolysis without Mn^{2+}. DFPase-1, -4, and -5 are stimulated the greatest. Graph is comprised of means and standard deviations from the results of two separate runs of the molecular-sizing column.

Approximate molecular weights were assigned to the five DFPases after calibration of the column (Table 5). Each DFPase is assigned

a number in the order of its confirmation, so that the 1st DFPase discovered is assigned the name DFPase-1; the second, DFPase-2; and so on. Table 6 lists the typical rates of DFP and soman hydrolysis of the enzymes and the rate of soman hydrolysis with Mn^{2+}. The DFP/soman hydrolysis ratio and stimulation due to Mn^{2+} is presented in Table 7.

Table 5. Approximate Molecular Weights of 5 DFPases from T. thermophila.

Enzyme Designation	Approximate Molecular Weight	Fraction
DFPase-1	80,000	15-20
DFPase-2	75,000	21-24
DFPase-3	72,000	24-27
DFPase-4	96,000	9-13
DFPase-5	67,000	42-44

The weights were determined graphically using the peaks observed in the assays from the Sephacryl molecular sizing columns. The molecular weight standards were run under conditions identical to the DFPase separations.

Table 6. Representative Rates of DFP and Soman Hydrolysis.

Activity in umoles hydrolyzed g $protein^{-1}$ min^{-1}

Enzyme	DFP	Soman	Mn^{2+} Stimulation
DFPase-1	148	165	721
DFPase-2	141	177	476
DFPase-3	194	137	298
DFPase-4	41	79	849
DFPase-5	59	20	162

Rates are the maximum observed in each peak.

Table 7. Classification and Comparison of the Tetrahymena-DFPase.

Enzyme	Molecular Weight	Soman/DFP Ratio†	Mn^{2+} Stimulation Soman Hydrolysis*
DFPase-1	80,000	1.12	2.5-4.0
DFPase-2	75,000	1.26	2.0
DFPase-3	72,000	0.71	1.7-2.5
DFPase-4	96,000	1.95	17-30
DFPase-5	67,000	0.34	8
Mazur-type [1] (Hog Kidney) DFPase	62,000	6.54	2
Squid-type [1]	26,000	0.25	1

†Calculated from maximum rates observed in each peak.
*Observed range over several sets of experiments.

Five entities have been elucidated that exhibit DFPase activity as defined by the ability to hydrolyze organofluorophosphates. They differ in molecular weight, soman/DFP ratio, and in the stimulation of soman hydrolysis by Mn^{2+}. None of the enzymes fit easily into the classification of Mazur-type or squid-type DFPases. For example, although soman hydrolysis is stimulated by Mn^{2+} in DFPase-5, it has a soman/DFP ratio of less than 1 (Table 7). DFPase-4 does have a soman/DFP ratio of greater than 1, is greatly stimulated by Mn^{2+}, but is larger than the Mazur-type enzyme. It is likely that DFPase-4 is responsible for the Mazur-type characteristics previously observed for the crude Tetrahymena-homogenate [4]. DFPase-1, DFPase-2, and DFPase-3 are close in molecular weight, have a soman/DFP ratio of approximately 1, and show some stimulation of soman hydrolysis by Mn^{2+}. Perhaps those enzymes are closely related, formed by the combinations of small (32,000 D) and large (40,000 D) subunits. An interesting difference among enzymes of this group is the decrease in activity of DFPase-1, and to a lesser extent DFPase-3, when stored at 5°C. DFPase-2 seems to neither gain nor lose activity. If DFPase-2 and DFPase-3 were simply degradative artifacts of DFPase-1 then an increase in the activity of both would be expected instead of the observed result.

NATURAL ROLE OF TETRAHYMENA-DFPases

Enzymes with DFPase-activity are widely distributed phylogenetically. Sources are known from bacteria, protozoa, inverterbrates and vertebrates [1,11]. Recently the suggestion was made that the DFPases are involved in the metabolism of phosphoro- and phosphonolipids [1,11]. Naturally synthesized organophosphonates are widespread [12]. The first described natural product with a C-P bond, 2-aminoethylphosphonic acid (AEP), was originally discovered in Tetrahymena strain Wk14 [13]. Dietary aminophosphonic acids are readily incorporated into the lipids of mammals [14]. Phosphonates are found free in the cell, incorporated into glycerophosphonolipids and sphingophosphonolipids, and phosphonoproteins have been reported from the sea anemone, Metridium dianthus, and T. pyriformis [15,16]. The linkage of AEP to the phosphonoproteins has not been determined although it appears to be covalently bound [12,17]. Enzymes must also be present for

the synthesis of the C-P bond and catabolic pathways capable of breaking the C-P bond are known to exist [18,19]. Perhaps the DFPases of Tetrahymena and other organisms are parts of the metabolic system for handling the varied organophosphonates incorporated into the cellular matrix.

The relationship of the DFPases to other organophosphate hydrolyzing enzymes is not clear. Zech and Wigand [20] isolated two organophosphate hydrolyzing enzymes from E. coli; one a DFPase, the other a paraoxonase. The DFPase hydrolyzed only DFP and the paraoxonase hydrolyzed only paraoxon. Both enzymes have low K_m values. No detectable hydrolysis of paraoxon occurs in the Tetrahymena-DFPase system (Durst, Seiders and Landis, unpublished results) although a related compound, 4-nitrophenyl ethyl(phenyl)phosphinate, is hydrolyzed (Durst, Landis and Tauber, in preparation). Great care should be taken when examining the substrate specificity of either DFPase or paraoxonase since both can often be found in the same organism. Cross reactivity of substrates among the two enzymes has not been demonstrated. It is certainly possible that the proteins are derived from common ancestral gene families with modifications for the hydrolysis of specific organophosphates.

UTILITY

The great recent interest in enzymes is primarily due to their specificity, catalytic nature, ability to operate at near neutral pHs, and biological compatibility. Because of the research conducted on the Tetrahymena-system, several factors must be added to those discussed above. Partially purified material is in production at an affordable cost for continued research. The DFPase activity has been demonstrated against organofluorophosphates and organofluorophosphonates. Multiple enzymes provide a range of conditions for activity and substrate specificities. Recently, it has been demonstrated that the enzymatic activity can be immobilized on a glass substrate. The immobilization further increased the stability of the activity, even at room temperature. Additionally, it has been demonstrated that the Tetrahymena-system is compatible with the cationic surfactant cetyltrimethylammonium chloride (CTAC) (Table 8) [21].

Table 8. DFP Hydrolysis by Tetrahymena-homogenate in Combination with the Surfactant CTAC

Conditions	RATE umoles DFP Hydrolyzed g protein^{-1} min^{-1}	$Hour^{-1}$
pH 7.2 Hoskin-Buffer No surfactant	16.2	970
pH 8.0 Hoskin-Buffer No surfactant	19.3	1156
pH 7.2 Hoskin-Buffer 10^{-3}M CTAC	10.6	638
pH 8.0 Hoskin-Buffer 10^{-3}M CTAC	13.2	790

Although enzymes have particular advantages, the inherent problems of working with biological systems still exist. The enzymes will be expensive in the purest and most active forms (on the order of pharmaceuticals). Therefore, it would be important to re-use the enzymes, a possibility if they are bound to a substrate in a bioreactor or detector system. Enzymes have very high molecular weights; one kilogram of DFPase-1 is only 1/80 of a mole of the enzyme. A material of lower molecular weight, with even a lower activity per mole, could provide a more useful decontaminant on a per unit weight basis. Proteins also are subject to degradation by strong oxidants, active sites can be shut down by groups that sequester protons, and competitive inhibitors often exist.

In many instances organic catalysts such as those prepared by Moss [22] may be useful alternatives to enzymes. In fact, the most important long term impact of the current studies on DFPases may be the design of an organic catalyst that circumvents the drawbacks listed above.

Noncorrosive surface decontamination is a potential use of enzymatic systems. The expense of the enzymes, however, limits their use to surfaces that cannot withstand extremes of pH and/or reactive compounds. Potential materials for enzyme decontamination include the plexiglass of aircraft canopies, composites, and electronics. Since these materials are increasingly used, especially in aircraft such as the proposed LHX, the need for noncorrosive decontamination is manifest. Due to the expense of the enzyme and disposable nature of the operation, an organic catalyst created to mimic the active site of the DFPases may prove the most workable system. Such an organic catalyst should prove practical for large-scale surface decontamination.

Two other uses of enzymes do hold potential for short-term application. Taking advantage of the ability to bind DFPase to substrates in concert with enzymes such as paraoxonase [23] and the broad spectrum of glutothione-S-transferases, construction of a bioreactor for decontamination of water supplies or contaminated effluent is possible (Figure 9). Such a system has been demonstrated on a small scale [3]. Solid state detectors using the fluoride release of the hydrolysis reaction are certainly feasible. Only relatively small amounts of pure enzyme are necessary. In a one step reaction the molecule in question could be detected and from the reaction rate the concentration determined. The advantages of a multiple enzyme system such as the Tetrahymena-DFPases, is that several ranges of K_m concentration and reaction rate are available to the bioreactor or detector designer. Perhaps enzymes with high K_ms could be bound into the early elements of the bioreactor with enzymes that work better at lower concentrations placed further downstream. Surfactants such as CTAC could also be injected into the reactor to aid in the breakdown of partially insoluble organics.

THERAPEUTIC POTENTIAL

The usefulness of DFPase in treating organofluorophosphate intoxication must be taken in light of the fact that mammals already contain a Mazur-type DFPase [25]. Also, injection of large amounts of proteins will cause an immunization against the therapeutic material unless the antigenic sites are masked. However, enzymes do have the potential in several applications. Polyethylene glycol (PEG) bound to enzymes eliminates their antigenic properties while maintaining their activity [26-33]. Recently, binding of PEG to Tetrahymena-DFPase has been accomplished by Dr. Milton Harris of the University of Alabama, Huntsville (Dr. Harris, personal communication). PEG treated DFPases should prove very useful in the decontamination of wounds of exposed casualties before

surgery. Addition of PEG-DFPase to the blood serum may also increase the rate of detoxification of the nerve agent in vivo.

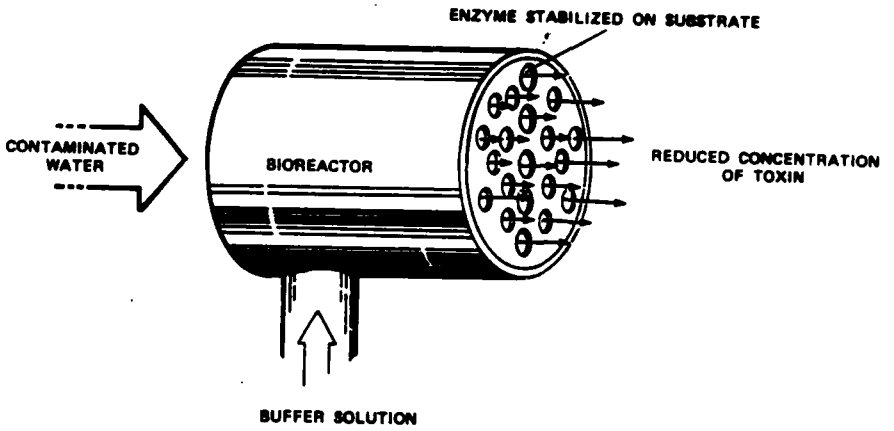

Figure 9. Bioreactors for the Decontamination of Effluents. The enzymes are stabilized on the supports within the water jacketed reactor. Buffer solution is added to maintain the physiochemical state within the operating range of the enzymes.

SUMMARY

• Multiple DFPases have been discovered in the protozoan Tetrahymena thermophila. These enzymes demonstrate an ability to operate over a broad range of physiochemical conditions. None conform well to the classical squid-type or Mazur-type classifications.

• Production of the material is underway in quantities to support an expanded research effort. Additional research should increase the yield of the fermentations.

• Tetrahymena-DFPase operates in surfactant solutions, is stable, can be bound to substrates, and PEG-DFPase can be formed.

• DFPases potentially have utility as specialized surface decontaminants, ingredients of bioreactors and detectors, as therapeutic materials. In applications where the enzymes have proven too costly or inefficient, synthetic organic catalysts based on the active site of the enzymes can be an economical alternative.

ACKNOWLEDGEMENTS

We are deeply indebted to our many co-workers who made the rapid pace of research possible. Our heartfelt appreciation goes to N.M. Chester, D.M. Haley, M.V. Haley, D.W. Johnson, R.M. Tauber and B.B. Vogel (Toxicology Division); J. Albizo and L. Cooper (Applied Chemistry Division, Chemical Research and Development Center); and L.P. Midgley (U.S. Army Proving Ground, Dugway). I (WGL) would also like to thank the

laboratory groups of Dr. John R. Preer, Jr., of Indiana University, Bloomington, and Dr. Francis C.G. Hoskin, Illinois Institute of Technology, Chicago, for their contined support and encouragement. Last, but perhaps most important, Margaret Durst typed the manuscript from a set of cryptic marks.

REFERENCES

1. Landis, W. G., Savage, R. E., Jr. and Hoskin, F. C. G. 1985. J. Protozool. 32:517-519.

2. Hoskin, F.C.G., Prusch, R.D. 1983. Comp. Biochem. Physiol. 75C:17-20.

3. Hoskin, F.C.G. and Rouch, A.H. 1982. Science 215:1255-1257.

4. Brandford, M. 1976. Anal. BioChem. 72:248-254.

5. Hoskin, F.C.G. and Steinman, K.E. 1985. In Proceedings of International Conference on Environmental Hazards of Agrochemicals in Developing Countries. (A. H. El Sebae, ed.), University of Alexandria, Egypt, Vol.1:434-447.

6. Hoskin, F.C.G., Kirkish, M.A. and Steinmann, K.E. 1984. Fundam. Appl. Toxicol. 4:S165-S172.

7. Hoskin, F.C.G., Long, R.J. 1972. J. Neurchem. 20:1317-1327.

8. Mazur, A. 1946. J. Biol. Chem. 164: 271-289.

9. Storkebaum, W., Witzel, H. 1975. ForschBer. Landes N Rhein-Westf. 2523:1-23.

10. Sonneborn, T.M. 1970. Methods Cell Physiol. 4:241-339.

11. Landis, W. G., Haley, M. V. and Johnson, D. W. 1986. J. Protozool. :in press.

12. Hilderbrand, R. L. and Henderson, T. O. 1983. In The Role of Phosphonates in Living Systems, (Hilderbrand, R. L., Ed) CRC press, Boca Raton, Florida, USA, pages 5-30.

13. Rosenburg, H. 1964. Nature 203:299-300.

14. Kittredge, J. S. and Roberts, E. 1969. Science 164:37-42.

15. Rouser, G., Kritchevsky, G., Heller, D. and Lieber, E. 1963. J. Am. Oil. Chem. Soc. 40:425-454.

16. Simon, G. and Rouser, G. 1967. Lipids 2:55-59.

17. Quin, L. D., and Shelburne, F. A. 1969. J. Marine Research. 27:73-84.

18. Cook, A.M., Daughton, C. G. and Alexander, M. 1978. J. Bacteriol. 92:623-627.

19. Pattison, F.L.M. 1959. Toxic Aliphatic Fluorine Compounds. Elsevier Publishing Co., New York.

20. Zech, R. and Wigand, K.D. 1975. Experientia 31:157-158.

21. Seiders, R.P. and Durst, H.D. 1985. Enzyme and Surfactant Compatibility. Abstract in MRCD Symposium on Enzymatic Decontamination, March 26-28.

22. Moss, R. A.; Alwis, K. W.; Bizzigotti, G. O. J. Amer. Chem. Soc., 1983, 105, 681-682. b) Moss, R. A.; Alwis, K. W.; Shin, J-S. J. Amer. Chem. Soc., 1984, 106, 2651-2655. c) Moss, R. A.; Kim, K. Y.; Swarup, S. J. Amer. Chem. Soc., 1986, 108, in press.

23. Talbot, H. W., Johnson, L., Barik, S. and Williams, D. 1982. Biotechnol. Letters 4:209-214.

24. Mounter, L.A. 1963. In Handbuch der Experimentallen Pharmakolgie: Cholinesterases and Anticholinesterase Agents (ed. Koelle, G.B.) 486-504, (Springer-Verlag, Berlin, 1963).

25. LeBlanc, G.A. and Cochrane, B.J. 1985. Comp. Biochem. Physiol. 82C:37-42.

26. Veronese, F. M., Boccu, E., Schiavon, O., Velo, G. P., Conforti, A., Franco, L., and Milanino, R. 1983. J. Pharm. Pharmacol. 35:757-758.

27. Beauchamp, C. O., Gonias, S. L., Manapace, D. P., and Pizzo, S. V. 1983. Anal. Biochem. 131:25-33.

28. Savoca, K. V., Abuchowski, A., van Es, T., Davis, F. F. and Palczuk, N. C. 1979. Biochim. Biophys. Acta 578:47-53.

29. Wieder, K. J., Palczuk, N. C., van Es, T., and Davis, F. F. 1979. J. Biol. Chem. 254:12579-12587.

30. Ashihara, Y., Kono, T., Yamazaki, S., and Inada, Y. 1978. Biochem. Biophys. Res. Commun. 83:385-391.

31. Koide, A. and Kobayashi, S. 1983. Ibid. 111:659-667.

32. Park, Y. K., Abuchowski, A., Davis, S., and Davis, F. 1981. Anticancer Res. 1:373-376.

33. Bendich, A., Kafkewitz, D., Abuchowski, A., and Davis, F. F. 1982. Clin. Exp. Immunol. 48:273-278.

34. Bendich, A., Kafkewitz, D., Abuchowski, A., and Davis, F. F. 1983. Immunol. Commun. 12:273-284.

CONTROLLING IMPULSE NOISE HAZARDS: PROGRAMMATIC MODEL FOR DEVELOPING VALIDATED EXPOSURE STANDARDS (U)

*BRUCE C. LEIBRECHT, LTC, MS
JAMES H. PATTERSON, JR., DR.
U. S. ARMY AEROMEDICAL RESEARCH LABORATORY
FORT RUCKER, AL 36362-5000

Among the health hazards posed by Army weapon systems, one of the most serious and pervasive is the threat of hearing loss from blast overpressure. Current Army weapons development efforts aimed at countering Warsaw Pact threat capabilities include improved artillery cannons, antitank weapons, and mortars. New artillery cannons and propellant charges are being developed to meet doctrinal requirements for enhanced delivery range, rapid rates of fire, and reduced weight for air mobility. Improved antitank weapons with high energy propellants may be fired from reflective enclosures such as bunkers, covered foxholes, and urban structures. Mortar technology is being advanced to achieve greater delivery ranges and rapid rates of fire. In each of these families of weapons, dangerously high levels of blast overpressure are a byproduct of advancing weapons technology.

High levels of impulse noise, which will be commonplace on the modern battlefield and on training ranges, seriously threaten the hearing of soldiers operating blast-producing weapons. Hearing loss, even temporary, can degrade critical soldier performance, endanger effective command, control and communications, and disrupt critical combat tasks such as detecting the enemy during patrol missions. Thus, hearing loss can jeopardize the soldier's capability to accomplish the combat mission.

Accurate hearing protective criteria are essential to a balanced resolution of the competing requirements to increase combat capabilities through improved weapons and to preserve combat effectiveness through conserving the soldier's hearing. In general, three different types of criteria are used to limit exposure to hazardous entities -- damage risk criteria, medical exposure limits, and materiel design standards.

Damage risk criteria are comprehensive statements of the relationships between critical parameters of hazardous entities (e.g., impulse noise) and the probability of injury of various degrees. They are characterized by their statements about the probability of specified injury resulting from specified exposure conditions in set proportions of the at-risk population. Ideally, damage risk criteria

should serve as the bases for developing medical exposure limits and materiel design standards. Thus they form the foundation for working documents used to protect crewmembers' health and insure system effectiveness. Currently, there is no true damage risk criterion for impulse noise.

Medical exposure limits are thresholds which, when exceeded, call for the use of protective measures to limit the proportion or extent of injury in the at-risk population. They should be derived from damage risk criteria by adopting acceptable rates of occurrence for the various degrees of injury and finding the associated exposure conditions. This requires value judgments as to what constitutes acceptable proportions and degrees of injury. The Army's current medical exposure limit for impulse noise is TB MED 501 (1), which incorporates the Army's materiel design standard by reference.

Materiel design standards provide specific limits for hazardous entities for use by materiel designers and manufacturers. These limits constitute specifications which must not be exceeded if the materiel is to be acceptable to the procuring activity. In general, they should not allow equipment to produce the hazardous entities in excess of the medical exposure limits. They normally will be a conservative simplification of the medical exposure limits and may include a tolerance factor for design and manufacturing uncertainty. The Army's materiel design standard for impulse noise is MIL-STD-1474B(MI) (2).

MIL-STD-1474 is today the noise standard for the design of Army weapons and for the determination of auditory hazards from impulse noise. However, it is based on a totally inadequate biomedical data base and on a number of assumptions which have yet to be validated. This standard has its origins in the proposed "damage risk criterion" (3) published by the National Research Council's Committee on Hearing, Bioacoustics and Biomechanics (CHABA) in 1968. In spite of its title, the CHABA proposed criterion is, at best, a medical exposure limit. This criterion is based primarily on data from small arms noise. The authors of the CHABA document recognized that the database available at that time was limited. Accordingly, they wrote, "While these [limit] curves do no great violence to the published data on either TTS [temporary threshold shift] or PTS [permanent threshold shift] from impulse noise ... they admittedly represent only a first attempt at a reasonable DRC for exposures to impulse noise. Parameters that are ignored in the present criterion may eventually be shown to be important." The CHABA criterion also proposes a rule for trading allowable number of impulses for intensity in an exposure. This rule represents the "educated guess" of Coles et al. (4). The criterion does not specify procedures to account for the effects of hearing

protection. Finally, it is assumed that limiting TTS will limit permanent hearing loss. This has not been empirically documented.

MIL-STD-1474 was derived by raising the CHABA criterion by 29 dB in an attempt to account for the protection afforded by hearing protective devices (5). The 29 dB factor came from a single study (6) using earplugs and was arbitrarily assumed to apply to all single hearing protectors, whether earplugs or earmuffs, regardless of the actual efficacy of the protector. In addition, it was assumed that the use of earplugs and earmuffs together would increase protection by 6.5 dB. These hearing protection factors have never been validated.

The fundamental need for a revised, validated impulse noise DRC has been recognized since 1976, when potential noise hazards were identified for the Army's new M198 howitzer. The questions raised by this system highlighted the inadequacy of the existing standard for resolving issues of impulse noise hazards. In particular, there was no way to predict whether available hearing protection would be adequate for the M198, because of the lack of a valid DRC. In the ensuing years, similar issues arose for a host of other weapon systems, underscoring the need for new standards applicable to the full range of diverse blast producing weapons.

In early 1977 a multifaceted impulse noise research program was established to develop, in part, a comprehensive foundation for a validated DRC. To provide a blueprint for this program, a model was created to guide the systematic development of a thorough scientific database. Unable to locate a relevant model in the life sciences literature, a novel planning approach was adopted to link the ultimate goal to specific research requirements. In order to achieve the ultimate goal of a validated DRC, rules for predicting injury from both protected and unprotected exposures must first be available. In turn, prediction rules cannot be developed until there exists a database relating quantifiable exposure parameters to patterns of auditory injury. Finally, development of the database requires a host of research tools including instrumentation, facilities, and methods.

This process resulted in a model (Figure 1) incorporating five categories of research activities: development of research tools, establishment of a comprehensive database, development of injury prediction rules, DRC derivation, and DRC validation. This model identifies the building blocks necessary and sufficient to achieve the ultimate goal of realistic, effective standards applicable to a broad spectrum of weapons. The elements within the model are not strictly sequential. Some can proceed in parallel, especially during tool development and database establishment. In general, elements

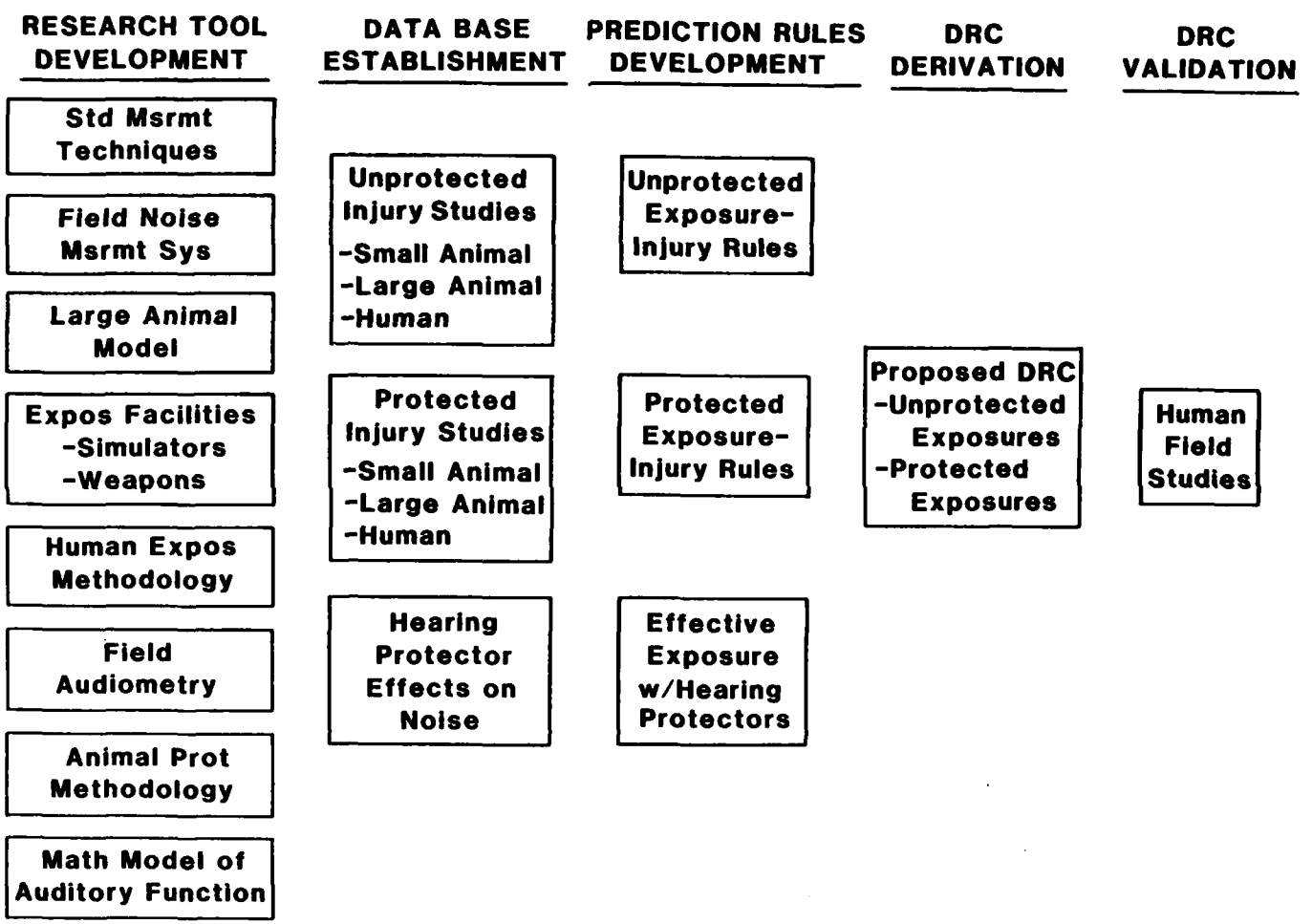

FIGURE 1. Schematic representation of programmatic model for developing valid impulse noise damage risk criterion.

regarding unprotected ears will precede those relating to protected ears.

The cornerstone of the efforts to develop a valid DRC is the comprehensive database tailored to the specific program objectives. The available data definitively relating impulse noise to auditory injury were extremely limited at the outset. This provided a rare opportunity to systematically design the structure of the necessary and sufficient database to support development of a realistic DRC. A logical analysis identified a number of fundamental issues requiring resolution in order to answer practical questions related to safe operation of weapons. These issues are: (a) Which physical noise parameters are critical determinants of injury? (b) By what rule should number of impulses be traded for intensity? (c) What is the effect of temporal spacing of impulses? (d) How do mixtures of different impulses relate to injury? (e) What is the relationship between physical noise parameters and probability of injury? (f) How do hearing protectors influence injury? (g) What is the relationship between temporary and permanent hearing loss?

From these issues were derived a number of research variables requiring empirical data: peak pressure, distribution of energy across frequency, impulse duration, rise time, impulse complexity, angle of incidence, number of impulses, temporal spacing of impulses, combinations of different impulses, and hearing protection. In devising an actual research plan, it was decided to address the various research variables in unprotected and protected ears in separate phases. Each phase includes systematic investigation of the effects of impulse noise on hearing in small animals, large animals, and humans using a mixture of laboratory and field experiments. These experiments focus on temporary and permanent threshold shifts as indicators of hearing impairment and on histological measures of cochlear damage. A separate effort was designed to quantify the attenuating effects of hearing protectors on impulse noise, to provide a basis for scaling between protected and unprotected exposures.

Of the research tools needed to establish the biomedical database, a few already were available. These included small animal models (cat, chinchilla, guinea pig), behavioral and electrophysiological audiometry methods, limited laboratory and field exposure facilities, and cochlear histological evaluation methods. To complete the complement of research tools, the following major items were required: (a) impulse noise measurement techniques standardized across different evaluation agencies; (b) an impulse noise measurement system capable of being used in the field; (c) at least one large animal model of auditory injury; (d) a variety of exposure facilities, including actual weapons and weapons noise simulators; (e) methodology

for exposing human volunteers to hazardous impulse noises; (f) a field audiometry system suitable for monitoring several volunteers at a time; (g) methodology for testing hearing protectors in animals; and (h) a mathematical model of auditory system function applicable to animals and humans.

As the biomedical database matures, systematic sets of data quantitatively relating specific exposure parameters to degrees and probabilities of injury will become available. Using these sets of data, development of injury prediction rules can begin with the derivation of functions similar to dose-response curves. These functions permit the identification of those exposure variables which are critical determinants of injury. These critical exposure variables will be incorporated in a comprehensive formulation of the exposure-injury relationships. This formulation may take the form of a multivariable mathematical model or a set of equations with rules for application. Alternatively, it may take the form of a cochlear model incorporating mechanisms of both temporary and permanent injury. Comprehensive exposure-injury formulations will be developed for both unprotected and protected ears.

The database will include sets of data relating characteristics of hearing protectors to the critical exposure variables. From these relationships will be derived a set of equations which will predict effective exposure when hearing protectors are used. This will permit estimates of noise hazards to take into account hearing protectors with different characteristics. The prediction rules resulting from these efforts will provide a realistic basis for using measured physical parameters of impulse noise to predict varying degrees of injury with different levels of hearing protection.

In developing the proposed DRC, the prediction rules developed above for unprotected exposures, protected exposures, and hearing protector effects will be integrated. The heart of the DRC will be the provisions for assessing hazards of unprotected exposures. Procedures will be specified for determining effective exposures when hearing protectors are worn. These effective exposures then will be evaluated using the provisions for assessing unprotected exposures. As currently envisioned, the proposed DRC will be applicable to all families of blast-producing weapons and all operational conditions.

The final stage of the model is validation of the proposed DRC. This stage is necessary to determine if the DRC ultimately works in practice. Human exposure methodology will be used to study troops operating actual weapons under realistic operational conditions. A representative selection of different weapons will be required, along with a variety of hearing protectors. Based on the results of the

validation studies, adjustments to the proposed DRC will be made, as appropriate.

The conclusion of the validation stage will complete the research activities necessary to establish an empirically based impulse noise DRC. Once validated, the proposed DRC will be ready to hand off to the appropriate policy setting agency for finalization, approval, and publication.

Since the establishment of the program, substantial progress has been made in implementing the model. Many of the tools missing at the outset are in place or under development now. The various US Army organizations involved in impulse noise measurement have established common methodology (7). A NATO study group is nearing completion of a guideline to help insure comparability of noise data. A computer-based, mobile, high-speed data acquisition system has been designed and constructed to measure impulse noise in the field. Laboratory exposure facilities now available include high intensity speakers, a compressed air shock tube, and spark gap generator. Safe techniques have been developed to use bare explosive charges for freefield and reverberant exposures. Specialized methodology for safely exposing human volunteers to actual weapons noise or bare explosive charges has been used successfully (8,9). A mobile audiometric test facility has been designed and constructed (10); this provides the capability to obtain simultaneous audiograms on four individuals in the field. Foam earplugs have been designed and fabricated for the chinchilla's ear.

In parallel with efforts to develop research tools, a number of small animal and human studies represent the beginning of the database development. Chinchilla studies using unprotected exposures have evaluated the role of peak pressure (11) and number of impulses (12) in producing hearing loss and cochlear damage. Additional chinchilla studies assessing the effects of temporal spacing of impulses, distribution of energy across frequency, and combinations of different intensities are underway, again with unprotected exposures. Protected exposure studies using human volunteers have been conducted with the M198 howitzer (8) and the VIPER antitank weapon (9). While these studies were designed to determine the adequacy of available hearing protectors, their results contribute useful information to the database. Finally, human volunteers served in an extensive field and laboratory evaluation of the effects of various hearing protectors on different types of simulated weapons noise. These results will contribute to the database on the influence of hearing protectors on critical parameters of impulse noise.

Despite the significant progress already achieved, much remains to be done in completing the research outlined in the model. The

large-scale, parametric projects required to establish the systematic, comprehensive database demand long-term research commitments. Until a complete database is available, a valid impulse noise DRC cannot be established.

Once established and validated, the new impulse noise DRC will need to be translated into working documents which are useful to combat developers, materiel developers, test and evaluation agencies, health hazard assessment organizations, hearing conservation personnel, and medical policy proponents. This follow-on phase will consist primarily of revising or updating existing documents, including the medical exposure limit, the materiel design standard, test and evaluation procedures, health hazard assessment procedures, and guidelines for combat developers. Armed with these powerful new tools, Army developers will be able to design and produce new blast-producing weapons which are, at the same time, safer and more effective.

REFERENCES

1. Department of the Army. 1980. Hearing conservation. Washington, DC: Department of the Army. TB MED 501.

2. Department of Defense. 1979. Noise limits for Army materiel. Washington, DC: Department of Defense. MIL-STD-1474B(MI).

3. Ward, W. D. (ED.) 1968. Proposed damage risk criterion for impulse noise (gunfire). National Academy of Sciences - National Research Council, Committee on Hearing, Bioacoustics and Biomechanics. Washington, DC.

4. Coles, R. R., Garinther, G. R., Hodge, D. C., and Rice, C. G. 1968. "Hazardous exposure to impulse noise." The Journal of the Acoustical Society of America. 43:336-346.

5. Garinther, G. R., Hodge, D. C., Chaikin, G., and Rosenberg, D. M. 1975. Design standards for noise: A review of the background and bases of MIL-STD-1474(MI). Aberdeen Proving Ground, MD: US Army Human Engineering Laboratory. Technical Memorandum 12-75.

6. Garinther, G. R. and Hodge, D. C. 1971. Small rocket noise: Hazards to hearing, (Advanced LAW Program). Aberdeen Proving Ground, MD: US Army Human Engineering Laboratory. Technical Memorandum 7-71.

7. Patterson, J. H., Jr., Coulter, G. A., Kalb, J., Garinther, G., Mozo, B., Gion, E., Teel, G., and Walton, W. S. 1980. Standardization of muzzle blast overpressure measurements. Aberdeen Proving Ground, MD: Ballistic Research Laboratory. Special Publication ARBL-SP-00014.

8. Patterson, J. H., Jr., Mozo, B. T., Marrow, R. H., McConnell, R. W., Jr., Lomba Gautier, I., Curd, D. L., Phillips, Y. Y., and Henderson, R. 1985. Direct determination of the adequacy of hearing protective devices for use with the M198, 155mm towed howitzer. Fort Rucker, AL: US Army Aeromedical Research Laboratory. USAARL Report No. 85-14.

9. Patterson, J. H., Jr. 1982. "Direct determination of the adequacy of hearing protection for use with the VIPER antitank weapon and the M198 howitzer." In: Technical Proceedings of the Blast Overpressure Workshop: The Technical Cooperation Program, Sub-Group W, Technical Panel W-2, 25-26 May 1982. Dover, NJ: US Army Armament Research and Development Command. p. 412-431.

10. Mozo, B. T., Patterson, J. H., Jr., Marrow, R., Nelson, W. R., Lomba Gautier, I. M., and Curd, D. L. 1984. Development of a microprocessor based audiometer for threshold shift studies. Fort Rucker, AL: US Army Aeromedical Research Laboratory. USAARL Report No. 84-7.

11. Patterson, J. H., Jr., Lomba Gautier, I. M., Curd, D. L., Hamernik, R. P., Salvi, R. J., Hargett, C. E., Jr., and Turrentine, G. 1986. The role of peak pressure in determining the auditory hazard of impulse noise. Fort Rucker, AL: US Army Aeromedical Research Laboratory. (In press.)

12. Patterson, J. H., Jr., Lomba Gautier, I. M., Curd, D. L., Hamernik, R. P., Salvi, R. J., Hargett, C. E., Jr., and Turrentine, G. 1985. The effect of impulse intensity and the number of impulses on hearing and cochlear pathology in the chinchilla. Fort Rucker, AL: US Army Aeromedical Research Laboratory. USAARL Report No. 85-3.

DEVELOPING TECHNOLOGIES FOR ARMY AUTONOMOUS LAND VEHICLES (U)

*ROBERT D. LEIGHTY, DR.
U.S. ARMY ENGINEER TOPOGRAPHIC LABORATORIES
FORT BELVOIR, VA 22060-5546

GERALD R. LANE, MR.
U.S. ARMY TANK AND AUTOMOTIVE COMMAND
WARREN, MI 48397-5000

INTRODUCTION

The battlefield, as described in AirLand Battle 2000, will be characterized by considerable movement, large areas of operations in a variety of environments, and the potential use of increasingly sophisticated and lethal weapons throughout the area of conflict. Opposing forces will rarely be engaged in the classical sense and clear differentiation between rear and forward areas will not be possible. To operate effectively under these conditions the Army must bring new technologies to the battlefield. In 1981 the Army commissioned a study to suggest applications of artificial intelligence (AI) and robotics technologies in Army combat and combat support functions [1]. One hundred applications were suggested and these were divided into ten categories. The technologies were indicated to be immature for a large number of the potential applications, but the number of key technology elements associated with AI and robotics is relatively small. Thus development of future Army systems that integrate AI and robotic capabilities to more effectively move, shoot, and communicate on the battlefield may depend on the maturity of relatively few key technology elements. Autonomous land vehicles represent one subclass of these systems which has been a subject of increasing Army interest [2]. The potential value of such systems for unmanned weapons platforms, reconnaissance, resupply, etc., has been recognized at all levels [3,4]. This has created a dilemma; the user community has initially expressed a need for these systems, while the laboratory community has indicated a present lack of technological maturity.

This paper describes research, development, and demonstration of robotic land vehicle technologies and a recent R&D partnership between the Defense Advanced Research Projects Agency (DARPA) and the U.S. Army

Tank and Automotive Command (TACOM). The partnership is significant because it addresses both horns of the dilemma. The DARPA program focuses on developing the key technologies for autonomous vehicle navigation and provides a critical mass of dollars and talent to meet these objectives, while the Army program integrates DARPA and other technologies to provide demonstrations of value to the user community.

DARPA STRATEGIC COMPUTING PROGRAM

The DARPA Strategic Computing Program (SCP) was a new initiative in October 1983 [5]. It was designed to seize an opportunity to leverage recent advances in AI, computer science, and microelectronics and create a new generation of "machine intelligent technology." The program focuses on three military applications of machine intelligence technology: (1) the Autonomous Land Vehicle, (2) the Pilot's Associate, and (3) the Battle Management Advisors. Each application has yearly demonstrations of prototype systems of increasing complexity and the requirements of each demonstrator have been structured to "pull" new capabilities from the technology base, rather than "push" available capabilities at the user. The SCP has a large built-in technology base research program addressing areas of advanced computing technologies such as image understanding, expert systems, voice recognition, natural language understanding, and microelectronics. These technology efforts are appropriately linked to the demonstrators. The expected expenditures of the SCP is $600 million over the five year period 1984-1988.

THE AUTONOMOUS LAND VEHICLE PROGRAM

The ALV focuses on development of a broadly applicable autonomous navigation technology base, and not vehicle development per se. The primary requirement of the ALV testbed is to provide a platform with flexibility to integrate and demonstrate the SCP technologies. Objectives of the ALV yearly demonstrations are:

1985 - Road Following Demonstration: Vehicle traverses a 2 km preset route on a paved road at speeds up to 10 km/hr. Forward motion only and no obstacle avoidance required.

1986 - Obstacle Avoidance Demonstration: Vehicle traverses 5 km road course at speeds up to 20 km/hr; must recognize and maneuver to avoid fixed objects that are small with respect to road width.

1987 - Cross-country Route Planning Demonstration: Vehicle plans and executes a 5 km traverse of open desert terrain at speeds up to 5 km/hr. Demonstrates soil and ground cover typing.

1988 - Road Network Route Planning and Obstacle Avoidance Demonstration:

Vehicle plans and executes a 20 km point-to-point traverse through a road network at speeds up to 20 km/hr using landmarks as navigation aids. Demonstration includes map updating and off-road maneuvering to avoid obstacles.

1989 - Cross-country Traverse with Landmark Recognition Demonstration: Vehicle plans and executes a 20 km traverse through desert terrain with obstacles at speeds up to 10 km/hr. Demonstration includes replanning when confronted with impassable obstacles.

1990 - Mixed road and Open Terrain Demonstration: Vehicle plans and executes a 20 km traverse in wooded terrain with isolated obstacles and a 50 km traverse on paved and unpaved roads at speeds up to 50 km/hr. Route planning includes multiple goals.

Martin Marietta Denver Aerospace, Denver, CO, won competitive competition as ALV integrating contractor in August 1984 and has responsibilities for all project research and development except vision algorithm development. In this regard, University of Maryland directly supports the ALV project and the Technology-based Vision contractors will provide vision algorithm support for the future. Martin Marietta is supported by two additional contractors; Hughes AI Research Laboratory provides planning software support and the Environmental Research Institute of Michigan (ERIM) is developing and supports the laser ranging imaging system. The U.S. Army Engineer Topographic Laboratories will produce the digital terrain data base for the Martin Marietta test area.

AUTONOMOUS LAND VEHICLE TECHNOLOGIES

FUNCTIONAL REQUIREMENTS FOR AUTONOMOUS LAND VEHICLES

Autonomous mobility in a dynamic unconstrained environment requires that a system sense its environment, model critical features from the sensed data, reason about the model to determine a mobility path, and control the vehicle along the path. Functional subsystems could be:

SENSORS: The sensors subsystem must have the capability to sense critical environmental features having impact on mobility.

PERCEPTION: The perception subsystem must be able to process sensor data to create a perceptive model of the environment.

REASONING: The reasoning subsystem must be capable of reasoning about the perceptive model and information from the knowledge base to determine appropriate mobility strategies.

CONTROL: The control subsystem must execute stable control to travel

along the selected path.

KNOWLEDGE BASE: The vehicle system must have access to knowledge about the environment, the capabilities of the vehicle, the mission requirements, and characteristics of the environmental features.

VEHICLE: The vehicle system must have a stable platform capable of carrying necessary sensors, computers, electronics, and communications equipment at required speeds for on-road and cross-country travel.

HUMAN INTERFACE: The vehicle system must interface with a human operator to accept mission goals, report on system status, and assist in problem solving.

A general scenario for operation of the ALV platform integrates these functional requirements. The mission begins when a human operator specifies mission objectives and constraints to the vehicle system via a man/machine communications interface. The reasoning subsystem interprets mission goals and constraints and decomposes them into subgoals. From information in the knowledge base and the subgoals, the reasoning subsystem prepares a global plan of its route and actions. Upon completion of the global planning, the reasoning subsystem provides goals to the preception subsystem for decomposition into tasks to be accomplished by the sensors subsystem. Scene data acquired by the sensors subsystem along the proposed route is passed to and processed by the perceptual subsystem to produce a high-level symbolic model of the environmental features along the route. If no obstacles are detected, the reasoning system updates its position along the route and issues commands to the control subsystem to move along the route. If obstacles are detected, the reasoning subsystem initiates local data acquisition and planning to effect circumnavigation around the obstacle. If local planning produces no acceptable circumnavigation path, the global planning process is reinitiated from the current location. And if no acceptable route is found, the vehicle requests assistance from the operator.

DARPA TECHNOLOGY-BASE VISION FOR THE ALV

The Technology-base Vision efforts of the SCP are focused on issues that are impediments to real-time image understanding in outdoor environments. The research addresses the perceptual subsystem in above discussion and has issues that include development of: robust and general models for objects and terrain features; general representation schema for computer vision primitives and knowledge; the ability to generate 3D scene descriptions; spatial reasoning capabilities; massive computational speedups at all levels of the computer vision problem; sound theoretical foundations for vision process models; techniques for dealing with the dynamic aspects of rapidly changing environments;and

integrated vision systems that can perform complex tasks in real time. The Technology-base Vision efforts address these issues with a substantial set of contractors which include: Carnegie-Mellon University (CMU); SRI International (SRI); Advanced Decision Systems (ADS); Stanford University (SU); General Electric Corporation (GE); Hughes AI Research Laboratory (Hughes); University of Massachusetts (UMass); University of Southern California (USC); Honeywell Corporation (Honeywell); University of Rochester (UofR); Columbia University (CU); and Massachusetts Institute of Technology (MIT). A brief description of the research responsibilities of these organizations follows.

New-Generation Vision System Development (CMU): A new-generation vision system is to be developed for dynamic image understanding environments for ALV applications. A system framework will be built to accommodate integration of component research tasks outlined below.

Common Vision Representation Schema (SRI): Different representation schema needed for various parts of the computer vision process and the construction of a spatial directory to provide a uniform means of handling differentiation models will be developed.

Visual Modeling (SRI, ADS with SU, and GE): This involves discovery of general models to represent objects and natural terrain for predicting and matching against real world observations. Also included is the application of reasoning techniques to improve geometric model construction and object identification.

Obstacle Avoidance (Hughes): Discriminatory techniques are investigated for distinguishing and evaluating obstacles in the path of a vehicle and the integration of those techniques with a planner to avoid obstacles along a planned path.

Dynamic Image Interpretation (UMass): This effort focuses on discovery of knowledge about dynamic environments and development of improved image recognition techniques that accommodate distortions arising from movement within the environment.

Target Motion Detection (USC): Motion analysis technology is studied to detect moving objects within the ALV field of view.

Object Recognition and Tracking (Honeywell): This effort involves discovery of improved object recognition techniques and higher-level knowledge to permit tracking of objects from scene to scene.

Real Time Issues (UofR, UMass, MIT, CU): Development of a parallel programming environment, common parallel processing algorithms, specialized parallel processing techniques for depth mapping, and

integrated advanced architecture for parallel processing at all levels of the computer vision process are the thrusts of these efforts.

ALV SUBSYSTEMS

The May 1985 road following demonstration was accomplished by Martin Marietta with vision algorithm assistance from the University of Maryland. This was a significant accomplishment since the contract was awarded in late August 1984 and an initial demonstration, had the vehicle autonomously traveling along 1 km of road at 5 km/hr. Later in the year the vehicle traveled 2 km at a speed of 10 km/hr and required processing at 1.75 sec/frame to segment roads with commercially available computer hardware. The ALV subsystems in place at the end of 1985, when the vehicle attained 5 km at 10 km/hr, will be briefly outlined.

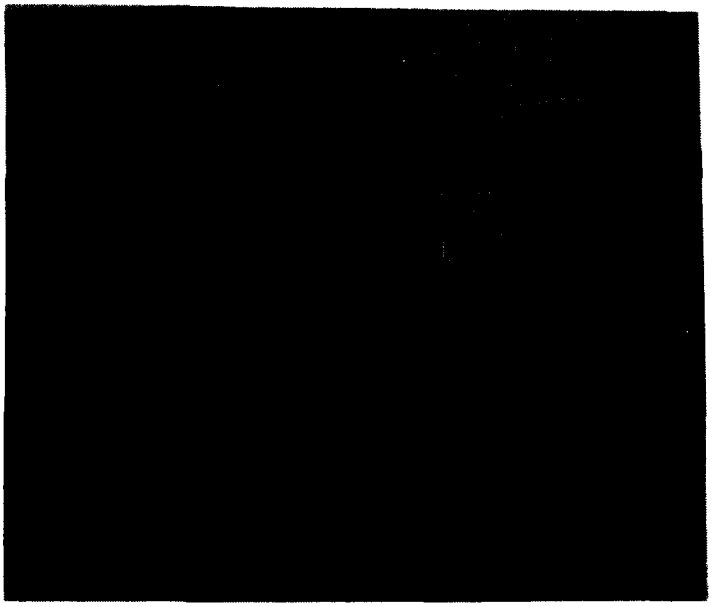

Sensors: The ALV sensor subsystem employs a RCA color video CCD TV camera and an ERIM laser range scanner. The video camera acquires 30 frames per second and delivers red, blue, and green intensity images in analog form to a VICOM image processor that digitizes the three color bands into 512x484 pixels with 8 bits/pixel. The perception subsystem controls a pan/tilt drive for this sensor. The laser range scanner is an amplitute modulated light source that is scanned over the area in front of the vehicle. Phase shift of reflected light from the scene features is measured with respect to an internal reference to determine range. The range data is processed on the VICOM in the form of a 64x256 digital array with 8 bit accuracy and requires 1 to 2 seconds to acquire and store as a range image.

Perception: The perception subsystem accepts sensor images and routes them to the appropriate processor. It has four major components: (1) a video processing component that extracts road edges and activates pan controls by cues from the reasoning subsystem, (2) a range data processing component that produces a set of 3-D points (in the sensor coordinate system) representing road edges, (3) a transformation component to correct

video or range points to 3-D vehicle coordinates, and (4) an executive that switches between components, based on a measure of plausibility of the processed edge points, to transmit a set of 3-D road edge coordinates as the scene model.

Reasoning: The reasoning subsystem receives a plan script from a human test conductor and coordinates all ALV operations. It requests scene models from the perception subsystem and converts them into smooth trajectories that are passed to the pilot to drive the vehicle. It also provides the perception subsystem with cues about upcoming events or conditions along its path and is responsible for maintaining a knowledge base that contains a map and other descriptive data about the test track. The reasoning subsystem has three major components: (1) a goal seeker that directs and coordinates the activity of the reasoning subsystem from a decomposed plan script, controls information interchange with the perception subsystem, and monitors execution of the current activity until its completion when the next plan script activity is issued; (2) a navigator that receives a scene model and a goal position, queries the knowledge base about the road location, and computes a trajectory which is sent to the pilot; and (3) a knowledge base that maintains a map of the test area.

Pilot: The pilot subsystem converts the intervals of a trajectory into steering commands for the vehicle. It calculates steer right, steer left, and speed commands by first determining error values for speed, lateral position, and heading by comparing the current vehicle heading and speed provided by the land navigation system with the desired speed and heading specified by the current trajectory internal.

Knowledge Base: The knowledge base consists of a digital representation of the road net.

Vehicle: The vehicle subsystem has an undercarriage that is an eight-wheel hydrostatically driven unit capable of traversing rough terrain at speeds up to 29 km/hr and 72 km/hr on improved surfaces. Steering is accomplished by reducing or reversing power to one of the wheel sets. A 2-inch air tight fiberglass shell is large enough to house on-board computers, sensors, associated electronics, electric power, and air conditioning for interior environmental control.

Human Interface: The human test conductor directly inputs the plan script for the road following test. A deadman switch serves as a safety device for halting unexpected or out of control trajectories.

Hardware Architecture: The primary computer architectures include an Intel multiprocessor system which supports the reasoning subsystem and pilot, and a VICOM image processor which supports the perception

subsystem. The multichannel controller provides an interface to the VICOM image processor and the laser scanner. In addition to the Intel multiprocessor and VICOM, the ALV's architecture includes a video tape recorder, a time-code generator, a Bendix land navigation system, left and right odometers, vehicle control and status sensors, and an ERIM laser scanner with an associated processor.

FUTURE ALV SUBSYSTEM DEVELOPMENTS

As indicated above, the development of the ALV capabilities is driven by the yearly demonstration objectives. As the demonstration requirements stress the performance capabilities of the methods and equipments, new approaches are necessary to continue the system evolution. In many cases the methods and equipments already employed are at or very near the state of the art and progress will require implementation directly from basic research in the technology base. Thus prediction of ALV subsystem developments is risky and subject to change. Nevertheless, it is instructional to indicate the major near-range subsystem plans, given the present state of the ALV system and the technology base program that supports it.

Sensors: A multispectral laser scanner, presently under development at ERIM, will replace the monospectral laser scanner now being employed. This scanner will use a YAG laser to develop six discrete wavelength beams which are detected as a range image and six reflected intensity images having 256x256 pixels.

Perception: The primary near-range enhancements to the perception subsystem involve generalization of road following algorithms to allow faster travel along roadways with an increased range of variability. Avoidance of road obstacles requires their recognition and segmentation from sensor data. Offroad travel requires multispectral processing and segmentation to be modeled and transmitted to the reasoning subsystem.

Reasoning: The reasoning subsystem must evolve considerably in the near-range to attain the demonstration goals. It must interpret a wide range of road, obstacle, and terrain object models; monitor the status of the vehicle; reason about its present and future location; and adjust speed and direction as necessary.

Knowledge-base: For 1986 models of roads and obstacles in the data base will be expanded. In 1987 a terrain data base will be added for apriori environmental information and terrain object models will be introduced. A "blackboard" memory structure will be used for maintaining cognizance of temporal activities and knowledge.

Vehicle: The vehicle chassis will not change through 1990, how-

ever the computers, electronics, and environmental accessories (e.g., power supplies and air conditionings) necessary for the demonstrations must be incorporated in the vehicle enclosure.

Human Interface: A user-friendly command module will be coupled to the vehicle with a communications interface.

Advanced Computers: At 10 km/hr the onboard VICOM processor is almost compute bound. There is not enough processing power to analyze both video and range data simultaneously, therefore the perception subsystem must choose the set of sensory data to process. Parallel processors are required for 1986 and beyond. To this end a 16-node BBN Butterfly parallel processor will be utilized for the reasoning subsystem and portions of the perception subsystem in 1986. Two onboard VICOM processors will be used for perceptual processing until mid-1986 and then these will be replaced by a CMU WARP computer, which is an advanced multistage programmable systolic array. Once an integrated hardware and software environment is developed, the WARP-Butterfly combination will provide powerful parallel support for perception and reasoning. Both computer systems can be upgraded as additional capacity as required.

Thus it is seen that the DARPA ALV program focuses significant efforts on key technology issues to meet the demonstration objectives leading to a new generation of intelligent machines. The following discussion will indicate how the Army plans to capture and use technology spinoffs to advance the state of the art of robotic vehicle systems capable of performing military missions.

ARMY ROBOTIC VEHICLE PROGRAM

The Army robotic vehicle program focuses on demonstration of state of the art robotic vehicle capabilities applied to combat missions of value to the Army user community. The program is structured to progressively demonstrate increasing degrees of autonomous capabilities in military missions as the technologies evolve. This program naturally complements the DARPA ALV program which is structured to demonstrate increasing capabilities of technologies associated with autonomous vehicles beginning with autonomous demonstrations of limited military value and increasing in military value as the technologies evolve. In the cooperative DARPA and Army programs the ALV provides the transfer of technology advances that enhance the Army program's degree of vehicle autonomy, while the Army provides military focus for the ALV. The Army robotic vehicle program is also a mechanism to transfer other DOD sponsored vehicle technologies and provides a test bed for evaluation of industrial Independent Research and Development (IR&D) in related efforts. Though the Army program is long-term it can provide short-term spinoffs with direct military applications.

The ultimate goal of the Army program is to demonstrate increased force effectiveness and/or improved soldiers battlefield survivability. Techniques such as remote management and multiple vehicle control will be primary tools used in the program.

ROBOTIC VEHICLE SYSTEM

Armor and Infantry type missions will be initially demonstrated with a system consisting of several robot vehicles and a Robotic Command Center (RCC). The vehicles and RCC will be coupled through communication subsystems under evaluation. Standard RF, microwave, and fiber optics links will be initially integrated.

The robot vehicles will have two sensor subsystems: The driving sensor subsystem and the mission sensor subsystem. The former will operate in two modes: (1) teleoperated extension of the operators eyes and ears through stereo and peripheral vision and stereo microphones and (2) supervisory and machine vision allowing operator management of vehicle actions while onboard image processors interpret images from the stereo cameras and laser scanners. The mission sensor subsystem incorporating thermal imaging, daylight video and laser rangefinders, shall be mounted on the mission modules. A telescoping mast will be employed providing 360° independent rotation.

Robotic vehicle machine vision processors will track those of the ALV, beginning with a VICOM image processor and advancing to WARP and Butterfly processors as the technologies and need evolves. Manual override of vision control provides added mobility in obstacle avoidance situations which may initially overburden the image processing system.

The vehicle payload will be modularized according to mission and permit mounting of modules such as weapon packages or manipulators for logistics material handling.

The RCC will be an adapted manned close combat vehicle and house all the robotic vehicle displays and operator controls. Displays will provide stereo vision, terrain data base, and peripheral and rear camera views for driving.

DEMONSTRATION PLAN

1986 - The first Army demonstrations will occur in August and September at the ALV test site. A route reconnaissance mission will be performed by two robotic vehicles under separate supervised control from robotic control stations. The supervised control will use both state of the art teleoperation and autonomous road following. The robotic vehicles under evaluation are built under IR&D programs by FMC Corporation

ADVANCED GROUND VEHICLE TECHNOLOGY (AGVT) TESTBEDS

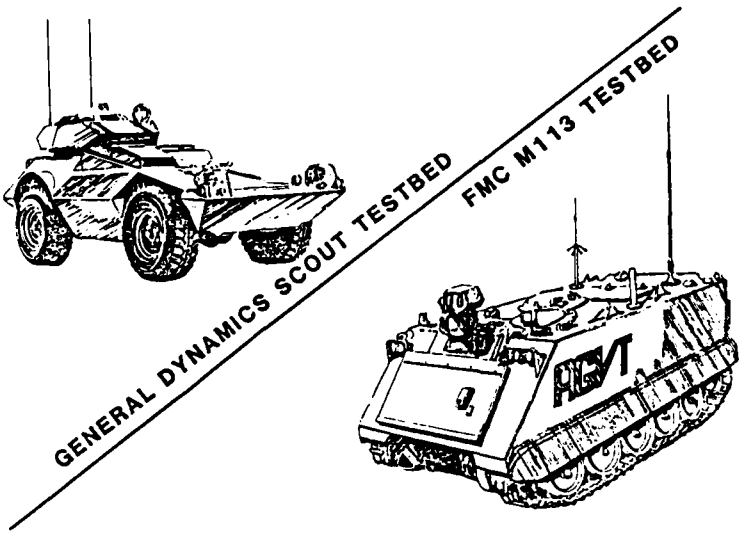

and General Dynamics. The FMC vehicle is a tracked M113 and the General Dynamics vehicle is a 4 x 4 wheeled Commando Scout (Chassis is built by Cadillac Gage). These systems will integrate ALV software and perform military/combat type missions using both teleoperated and autonomous control. The teleoperation mode will be used in cross-country terrain and more difficult maneuvers now requiring man in the control loop. The autonomous road following algorithms are a product of the November 1985 ALV demonstration. Soldier/machine issues will be evaluated during the missions. Follow-on Army demonstrations are planned to show decreasing driver workloads leading to the ability of a driver to manage multiple vehicles simultaneously.

1988 - A newly developed Army owned and operated robot vehicle system will be used to evaluate the performance of a more agressive route reconnaissance mission using ALV software demonstrated in 1986 and 1987. Route reconnaissance will be performed autonomously on the road at speeds up to 20 km/hr with obstacle avoidance and cross-country traverse at 5 km/hr. In addition to the ALV software integration, Computer Aided Remote Driving (CARD), which is a new robotic mobility technique, will be added to allow a driver to predrive a path via his display. Using a light pen and a light sensitive stereo display of the driver's sensor, the driver will designate a path for the vehicle to follow. CARD, presently being developed for the Army by JPL, is coupled to vehicle control with an onboard land navigation subsystem and optical tracking. Preliminary demonstrations of multiple robot control through teleoperation and fiber optics links will be evaluated.

1989-1990 - Improved multi-vehicle management at speeds up to 10 km/hr will be demonstrated. A platoon of vehicles will engage in both offensive and defensive missions to evaluate the potential increase in force effectiveness resulting from multiple vehicle control. One

driver and one commander/mission specialist will maneuver and operate the vehicles. Initial site selection will be road networks and smooth terrain. Speeds will be limited to 10 km/hr. These demonstrations will result primarily from the 1987 and 1988 ALV software demonstrations in cross-country route planning and obstacle avoidance.

1991+ - Armored Family of Vehicles (AFV) robotic variants will execute missions singularly, in packs, or in concert with manned vehicles. As the ALV software provides higher vehicle speeds, more realistic combat missions can be demonstrated with increasing autonomy. Vehicles mounting weapon packages or other mission modules operating in concert with manned systems will demonstrate performance of military missions. The use of robotic vehicles in the AFV family is the major objective of the Army program. AFV will use the robotic vehicle demonstrations to build follow-on requirements for singular robotic vehicles performing high risk or tasks for a platoon of robots in offensive type missions.

ARMY ROBOTIC VEHICLE REQUIREMENTS

The Army user community is very interested in the application of robotics to solve field problems and through a number of TRADOC Centers and Schools have identified potential robotic concepts. Concept requirements were formulated by a TRADOC General Officer Steering Committee (GOSC) for AI and Robotics managed by the U.S. Army Soldier Support Center (USASSC). USASSC released a broad requirements document for robotic vehicles which summarizes all submissions to the GOSC by the Schools and Centers. On 15 May 85, USASSC released a "Summary of TRADOC Requirements for Generic Robotic Vehicle Systems" which realizes the evolutionary process required to field robotic vehicles, i.e., teleoperation available now, while also being the first step in the evolution of autonomous systems.

Two leading TRADOC Schools that drove each end of the USASSC requirements were the U.S. Army Infantry School (USAIS) and the U.S. Army Armor School (USAARMS). USAIS requirements are for a teleoperated mobile platform that can mount a mission system to defeat enemy armor. An Infantry man with a control box will guide the Robotic Anti-Armor Systems (RAS) to a firing position and then locate, aim, fire, and guide the missile. Ultimately USAIS would like to product improve the RAS to provide autonomous mobility and automatic target detection and servicing.

USAARMS's Operational and Organizational (O&O) Plan for the Family of Robotic Combat Vehicles looks at using a common chassis with various mission module combinations. In normal mode of operation the robotic vehicles will receive mission guidance from a RCC in a manned close combat vehicle operating in concert with the robotic vehicles. This O&O desires autonomous operation, however, for near term applications

would field systems directed by semi-autonomous control requiring only periodic manual inputs to execute a mission. User requirements have been integrated into the AFV Umbrella O&O Plan. Robot variant vehicles in the AFV are defined as (1) Tactical Reconnaissance, (2) NBC Reconnaissance, (3) Mine Detection, (4) Mine Breaching, (5) Anti-Armor, (6) Directed Energy Weapon, (7) Air Defense, (8) Rearm, (9) Refuel, (10) Smoke Dispensing, (11) Decoy, (12) Recovery, (13) Counter Obstacle, and (14) Obstacle Implacement.

ARMY TECHNOLOGY CHALLENGES

There are several key technology challenges that must be solved before the Army plans to field autonomous land vehicles. For discussion, a robotic vehicle system can be divided into seven major subsystems: (1) sensors, (2) intelligence, (3) controls, (4) platform, (5) mission module, (6) soldier/machine interface, and (7) communications. Significant developmental work is required in all areas before the Army can field a robotic vehicle providing capabilities beyond simple teleoperation. Current technology limitations, work in process and development yet required are summarized for each area below:

Sensors: Sensor technology specifically for robotic vehicles is being developed in the DARPA ALV program. A laser scanner provides range and intensity data of a scene that is processed and interpreted with color video data as basic sources of vehicle mobility information. Scanning and processing rates are current limiting factors, but improved processors will be integrated in 1986. Development of the ALV multispectral laser scanner should provide improved information needed for all terrain mobility.

Machine Intelligence Subsystem: Perception, reasoning, and knowledge bases for autonomous vehicles is being pursued in the DARPA ALV program and provides a significant focus for development of machine intelligence subsystems. Other related issues are being pursued in DOD. An Army program at TACOM is evaluating several architectures for combat vehicles and will lead to a common architecture for future combat systems. The Naval Ocean Systems Command has developed a blackboard knowledge base architecture that is being evaluated in their robot vehicle test bed. Ultimately a common architecture is required to be versatile enough to accept various mission modules without requiring restructuring.

Controls Subsystem: This subsystem includes servos for robotic vehicle actuation, i.e., steering, braking, acceleration, etc. Most controls used in robots today are commercially available. These may require militarization to ensure ruggedness and reliability for operation in dirty environments.

Platform: Initial robotic vehicles will be adaptations of current manned chassis, but in the future several classes of chassis will be used for AFV robotic vehicle variants. These chassis will be optimized for robotic applications with lower silhouette, reduced internal volume, less armor protection, electric drive, fuel cells, etc. The changes are primarily driven by the elimination of on-board vehicle operation. To date minimal work has been accomplished in this area.

Mission Modules: These are the "end effectors" for the robotic vehicle systems. They can be configured as a tactical reconnaissance sensor, a weapons platform mounting either a cannon or a missile, a robotic arm, etc. Work in this area is just beginning. The Armament Research and Development Center (ARDC) is investigating a robotic weapon station mounting a large caliber cannon and has developed several fire control concepts suitable for integration on a robotic vehicle test bed. Mission module development will be focused on the AFV robotic variants. The Army must focus on high payoff missions resulting in hands-on experience with available robotic technologies and spinoffs from the ALV program.

Soldier/Machine Interface (SMI): The SMI issues for robotic vehicles are as critical as those for manned vehicles and they are just beginning to surface. Operator sensors and displays must provide a presence through electronic transfer of information from the vehicle to the operator. Issues such as display size, color, control handles, telepresence, voice control, etc., need to be evaluated by human factors experts in the field. The command and control station will be packaged in a combat vehicle, this leads to an entirely new set of technological challenges required to miniaturize the control and displays for installation in an already confined crew compartment of a combat vehicle.

Communications: This is the weak link in a supervised robotic vehicle system. Little technology development is devoted to communications required to operate robots on the battlefield. Non-line of sight, jam proof, and secure communication are key challenges. Communication techniques employing repeaters, low frequency, packeted and preprocessed information must be developed and evaluated in field scenarios. Requirements to communicate with multiple robotic vehicles in a noisy and hostile battlefield environment could impede their fielding unless serious technology development is undertaken.

SUMMARY

Two associated research and development programs which together have the potential of great impact on Army vehicles of the future have been described. The DARPA ALV program focuses significant efforts on key technology issues leading to a new generation of intelligent machines

and the Army robotic vehicle program focuses on demonstrating the state of the art robotic vehicle capabilities applied to combat missions of value to the Army user community. The Army has identified a need for robot variants in the AFV. Through user experience with maturing robotic vehicle technology, it is anticipated that follow-on requirements documents will be generated for engineering development of Army autonomous land vehicles. Timing for critical technology, such as the DARPA ALV software and hardware, will pace fielding of an Army AFV, however a progressive development program could be commenced to initially field a robotic vehicle that is remotely controlled with preplanned product improvements leading to an autonomous vehicle.

REFERENCES

1. Brown, D. R., et.al., "R&D Plan for Army Applications of AI/Robotics," SRI International, ETL-0296, May 1982 (AD-A118297).
2. Leighty, R. D., "The Army's Activities in Artificial Intelligence/ Robotics," SPIE, Vol 360, pp. 39-49, Aug 1982 (AD-A130128).
3. -------, "Report of the Army Science Board Ad Hoc Subgroup for Artificial Intelligence/Robotics," Sep 1982 (AD-A122414).
4. -------, "Application of Robotics and Artificial Intelligence to Reduce Risk and Improve Effectiveness - A Study for the U.S. Army," Manufacturing Studies Board, National Academy of Sciences, Oct 1983 (AD-B079746).
5. -------, "Strategic Computing - New-Generation Computing Technology: A Strategic Plan for its Development and Application to Critical Problems in Defense," Defense Advanced Research Projects Agency, 28 Oct 1983.
6. -------, "Autonomous Land Vehicle - Annual Report August 1984 to August 1985," Martin Marietta Denver Aerospace, ETL-0413, in preparation.

LENGSFIELD

APPLICATION OF THEORETICALLY COMPUTED VIBRATIONAL SPECTRA TO THE REMOTE SENSING OF CHEMICAL AGENTS AND THE STUDY OF ENERGETIC COMPOUNDS

BYRON H. LENGSFIELD, III, DR.
US ARMY BALLISTIC RESEARCH LABORATORY
ABERDEEN PROVING GROUND, MD 21005-5066

I. INTRODUCTION

During the past few years, much of the work in theoretical chemistry has been focused on means to rapidly characterize potential energy surfaces with derivative methods (1-11). One differentiates the energy functional of a SCF (self-consistent-field) or correlated wavefunction with respect to nuclear displacements. From the first and second derivative of the energy, stationary points on the potential energy surface can then be rapidly located. From the stable structures one, of course, obtains bond lenths and bond angles. From the second derivative of the energy one can extract the harmonic vibrational frequencies. The vibrational frequencies are not only used to synthesize vibrational spectra but also to build the vibrational partition function needed to compute heats of formation. So a great deal of useful information about the equilibrium properties of large molecules can be obtained in a timely manner with these derivative techniques.

If one wishes to investigate a chemical reaction, a theoretical method capable of describing bond formation and bond cleavage is needed. One then employs a correlated wavefunction, multi-configuration self-consistent-field (MCSCF), multi-reference configuration interaction (MRCI), coupled-cluster, multi-reference coupled-cluster, or one of several perturbation theories (MBPT or MPPT), to describe the quantum mechanical system. Derivative methods, based on these more sophisticated techniques, are then used to locate the transition state on the reaction path, from which an estimate of the reaction rate can be computed. More accurate theories of chemical reactions, such as variational transition state theory, require that larger portions of the reaction path be characterized and these new derivative techniques can efficiently provide this information as well. In addition, correlated wavefunctions have also been needed to obtain qualitatively correct equilibrium structures and vibrational frequencies for open-shell systems having important resonance

structures. As these structures are prevalent in many nitro-compounds, as well as combustion intermediates, of interest to BRL, we have pursued derivative techniques based on these more sophisticated wavefunctions.

Derivative methods have also proved to be very useful in the calculation of molecular properties and, ultimately, spectral quantities for large molecules. The dipole moment and static polarizability of a molecule can be obtained by differentiating the energy with respect to an applied electric field in the limit of zero field strength. As noted earlier, the harmonic vibrational frequencies are obtained from the second derivative of the energy with respect to nuclear displacements. In order to synthesize the spectrum, one needs the intensity of the various transitions. In the double harmonic approximation employed in this study, the dipole moment function or polarizability is approximated by a Taylor series expansion. Only the zeroth and first order terms are retained. The calculation of the intensity of a vibrational transition requires the derivative of the dipole moment, for IR spectra, or the polarizability, for Raman spectra, with respect to nuclear displacements. All of these quantities are readily attainable within a unified theoretical framework and we have developed a series of codes at BRL to exploit the formal similarities between energy derivatives and property derivatives in the computation of molecular spectra, molecular properties, and to characterize potential energy surfaces (11).

In a unique application of these derivative methods, we have developed a practical means of obtaining non-adiabatic coupling matrix elements for large molecules (12-14). These quantities are needed in the study of reactions and spectra where the splitting between electronic or vibronic states are small enough that the Born-Oppenheimer appoximation breaks down (15-17). This problem most often arises when one investigates the spectra of a molecule where a state is split by a Jahn-Teller or a Renner-Teller interaction, or in the study of charge-transfer reactions. The latter example has important applications in the design of high energy lasers.

In Section II of this paper, the results of several model calculations of IR spectra will be compared to experimental quantities. Section III outlines current research efforts to theoretically compute Raman spectra, work to incorporate spectral perturbations due to a non-gaseous environment (spectra taken in solution, in a solid matrix, or in realistic atmospheric conditions) and concludes.

II. APPLICATIONS

In this section the results of several theoretical studies of infrared spectra will be discussed. These studies are aimed at characterizing the level of theory needed to yield reliable IR spectra for

the class of compounds of interest to the Army. This includes a series of phosphorus and sulfur compounds which are representative of the chemical agents currently under investigation at CRDC. The effect of variations both in the basis set and in the level of correlation employed in the theoretical method will be discussed. The SCF and MCSCF dipole derivatives, needed to compute the IR intensity, were obtained analytically. The CI intensities were obtained by calculating a finite-difference derivative of the CI gradient (the analytic first derivative of the CI energy with respect to nuclear displacements) with respect to an applied electric field in the zero field limit.

Since many of the compounds of interest to BRL possess important resonance structures (nitro-compounds, combustion intermediates, boron-compounds), much of our recent effort have been devoted to developing energy and property derivatives at the MCSCF and multi-reference CI levels. The importance of these types of methods in the theoretical computation of vibrational spectra has been demonstrated in a recent study of the formyloxyl radical, HCO_2 (18). We have recently devised and implemented an efficient method for computing IR spectra at the MCSCF level (19). The results of the first application of this method to the IR spectra of formaldehyde will also be discussed and compared to SCF and CI results.

Tables 1-6 summarize some of our recent theoretical studies of sulfur and phosphorus compounds. Tables 1 and 2 contain the results of a series of SCF calculations for a model phosphine oxide (dihydrofluoro-phosphine oxide) with a number of Gaussian basis sets. We require a basis set which is large enough to adequately characterize the dipole moment function as the frequencies converge much more rapidly than the IR intensities. We find that a DZP+ basis is required for semi-quantitative results. The rapid convergence of the theoretical frequencies can again be seen in Table 3. The relatively small 3-21g+ basis yields good frequencies for difluoromethyl-phosphine oxide. Vibrational frequencies which are 5-10% to high are typical of the SCF level of theory.

In addition to yielding IR spectra, these calculations also provide a number of additional parameters which are very useful in interpreting experimental spectra. The geometrical parameters provided by these calculations are useful in the interpretation of microwave spectra. The dipole derivative information is used to obtain higher order constants from highly resolved vibrational spectra. The sign of the dipole derivatives are very difficult to uniquely determine experimentally.

Table 1. Basis Set Effects on the SCF IR Frequencies for FH_2PO. Frequencies in cm^{-1}

	Basis Sets		
	3-21g+[a]	DZP+[b]	DZP++[c]
mode			
1	449.	434.	437.
2	913.	900.	893.
3	1010.	946.	943.
4	1032.	1010.	1007.
5	1254.	1218.	1201.
6	1301.	1290.	1275.
7	1482.	1438.	1440.
8	2740.	2662.	2663.
9	2768.	2671.	2668.

a. 3-21g basis with the addition of a d-function on phosphorus.
b. DZP basis on lighter atoms and McLean-Chandler (20) basis on phosphorus.
c. Same basis as in b but two d-functions were placed on phosphorus.

Table 2. Basis Set Effects on the SCF IR Intensities for FH_2PO. Intensities in km/mole.

	Basis Sets		
	3-21g+	DZP+	DZP++
mode			
1	42.	42.	40.
2	145.	121.	107.
3	108.	190.	173.
4	.2	.7	.6
5	134.	78.	50.
6	17.	28.	25.
7	319.	306.	262.
8	164.	97.	78.
9	86.	57.	43.

Table 3. Frequencies for Difluoromethyl-Phosphine Oxide

mode	SCF frequency cm^{-1}	Experiment[a,b] frequency cm^{-1}
1	393.	407.
2	408.	415.
3	452.	468.
4	752.	755.
5	900.	857.
6	910.	881.
7	966.	925.
8	1012.	943.
9	1366.	1312.
10	1416.	1335.
11	1461.	1415.
12	1462.	1510.

a. Reference 2.
b. Only the 400-1600 cm^{-1} range is reported.

Tables 4-6 summarize our recent theoretical study of SO_2. Aside from CRDC's interest in sulfur compunds, SO_2 is of particular interest for two reasons. First, it is iso-electronic to ozone and therefore will have some diradical character which will require a multi-configuration description. Second, there have been a number of recent questions raised in the literature concerning the nature of and the proper treatment of the d-orbital participation in the bonding (22). The diradical of character of SO_2 was confirmed by examining the natural orbital occupation numbers in a single reference, singles and doubles CI calculation. Our natural orbital analysis also produced an important pi-correlating orbital with a large amount of d-character, suggestive of some hypervalent character in the bonding.

Table 4. Comparision of Theoretical and Experimental Frequencies for SO_2 in cm^{-1}

	SCF1[a]	SCF2[b]	CI[a]	Experiment[c]
mode				
1	586.	605.	533.	518.
2	1344.	1382.	1229.	1151.
3	1527.	1594.	1412.	1362.

a. DZP basis.
b. DZP basis on oxygen, DZ+2P ba..is on sulfur.
c. Reference 23.

Table 5. Comparision of Theoretical and Experimental Intensities for SO_2 in km/mole

	SCF1	SCF2	CI	Experiment
mode				
1	58.	63.	43.	25.3
2	60.	68.	37.	20.6
3	333.	348.	222.	192.0

Table 6. Comparision of Theoretical and Experimental Geometry for SO_2

	SCF1	SCF2	CI	Experiment
Bond Length (Angstroms)	1.43	1.40	1.45	1.43
Bond Angle (Degrees)	117.9	119.5	118.1	119.5

We find that the CI results are in excellent agreement with the experimental spectra. There is also a large variation in the SCF and CI results, much more so than in the formaldehyde calculations discussed in the next paragraph. The use of the two d-functions sugguested by Schaefer produces the correct trend in the bond length. The SCF bond lenght should be smaller than the experimental value as the dominant effect of including correlation in the theoretical treatment is to include anti-bonding terms

in the wavefunction. The CI results then lengthen the bonds and decrease the vibrational frequencies relative to the SCF results.

These results emphasize the need to go beyond the SCF level of theory to obtain reliable vibrational spectra in systems possessing important resonance structures. In the case of SO_2, the importance of a multi-configuration description can be predicted apriori due to the similarity in the bonding of SO_2 and ozone. The correct trend obtained in the SCF bond length with the addition of the second d-function on sulfur is indicative of the signifigant d-orbital participation in the bonding.

In Tables 7 and 8 the results of our formaldehyde study are presented. These results represent the first example of a theoretical IR spectra computed from a general MCSCF wavefunction. The MCSCF wavefunctions were obtained by generating single and double, or only double excitations from the Hartree-Fock reference into a restricted set of virtual orbitals. The doubles-MCSCF (DMC) calculation employed six virtual orbitals and gave rise to a wavefunction containing 667 configuration state functions (CSFs). The CI wavefunction was generated by performing all single and double excitations from the Hartree-Fock reference. The CI wavefunction consisted of about 25,000 CSFs.

Table 7. Comparision of Theoretical and Experimental Frequencies for Formaldehyde in cm^{-1}

mode	SCF	DMC 6/6	SDMC 6/6	CI	Experiment[a]
1	1335.	1221.	1221.	1272.	1167.
2	1367.	1292.	1291.	1305.	1249.
3	1656.	1560.	1559.	1596.	1500.
4	2006.	1850.	1849.	1868.	1746.
5	3148.	2943.	2940.	3074.	2783.
6	3226.	3006.	3001.	3173.	2843.

a. Reference 24.

Table 8. Comparision of Theoretical and Experimental Intensities for Formaldehyde in km/mole

mode	SCF	DMC 6/6	SDMC 6/6	CI	Experiment
1	1.7	2.06	1.9	3.9	3.5
2	19.	13.	13.	15.	20.
3	14.	5.8	5.6	7.6	11.
4	157.	106.	108.	93.	74.
5	72.	75.	78.	66.	75.
6	112.	125.	128.	106.	87.

As noted earlier, the dominant effect of the CI wavefunction is the incorporation of anti-bonding terms in the theoretical model. The MCSCF wavefunctions employed in this study only include these anti-bonding terms and they tend to over-estimate this effect. However, the MCSCF results are seen to be superior to the SCF results. If one increases the the number of virtual orbitals employed in the MCSCF the results will rapidly approach the CI results, while requiring signifigantly less computational effort (19).

The singles and doubles MCSCF (SDMC) was included in this study to investigate the importance of single excitations on the IR intensity. When the dipole moment is computed as an expectation value of a CI wavefunction the inclusion of single excitations in known to be needed to obtain reliable results. This is expected as the dipole moment is a one-electron operator. It has been found, however, that when the CI dipole moment is computed as the derivative of the energy with respect to an applied field, the Lagrangian contribution to the dipole moment incorporates the effects of the single excitations (25). The variational conditions, which define the MCSCF wavefuncion, force this Lagrangian contribution to the dipole to be zero. It is, therefore, of some considerable interest to determine if the variational condition negates the need to include singles in the MCSCF wavefunction. We find that it does. We see that there is no signifigant difference between the singles and doubles MCSCF results and the doubles MCSCF results. This is important as the doubles calculation has a larger radius of quadratic convergence, and is therefore a much more practical calculation, than the singles and doubles calculation.

IV. CONCLUDING REMARKS

Effective means have been to developed to compute IR spectra for SCF and correlated wavefunctions. These methods are capable of yielding semi-quantitative results. The large basis SCF frequencies are 5-10% to high

relative to the observed fundamentals. The results obtained from correlated wavefunctions generally halve this figure. The remaining discrepancy is due to the omission of anharmonic terms in the theoretical treatment. Methods have been developed at the University of California at Berkeley and at Cambridge University to include anharmonic terms at the SCF level but only model calculations have been completed at this time.

The intensity information provided by these calculations is of a more qualitative nature. This quantity is dependent on the structure of the dipole moment function and is much more variable from one molecule to another than the discrepancies in the frequencies. The computed intensities can be improved by incorporating more diffuse basis functions in the calculation, but additional work is needed to determine the optimum number of such functions and their exponents. We are currently investigating the most efficient way to include diffuse functions in our calculations. So few results have been obtained with correlated wavefunctions that no conclusions can be drawn regarding the ability of the more sophisticated theoretical models to quantify the intensity results. We plan to continue work in this area by generating more spectra from correlated wavefunctions and to investigate the effect of including higher order terms in our theoretical treatment. We will first focus on the effect of including higher order terms in the expansion of the dipole moment.

We are currently working on methods to treat Raman spectra at the same level of theory that can be applied to the study of IR spectra. SCF Raman intensities for large molecules, using derivatives of the static polarizability, have been reported by Amos (26). Our efforts are directed at computing Raman intensities with SCF and correlated wavefunctions employing the frequecy-dependent polarizability derivative in our calculations.

Many of the reactions we are interested in understanding take place in solution or in a solid matrix. In some studies it is important to include these effects in our calculations. Stevens (27) has been pursuing these goals in the framework of a "reaction field". This involves the construction of molecular psuedo-potentials to describe nearest-neighbor interactions and a multipole expansion to describe the influence of more distant molecules on the molecule or reaction site of interest. We are interested in incorporating these field effects into our derivative package both for the study of the reactions of energetic materials and for the computation of vibrational spectra. We expect to spend a signifigant portion of effort over the next year or so pursuing these goals.

REFERENCES

1. M. Dupuis and H.F. King, Int. J. Quantum Chem., Vol. 11, p. 613, 1977.

2. P. Saxe, Y. Yamaguchi, and H.F. Schaefer, III, J. Chem. Phys., Vol. 77, p. 5647, 1982.

3. H.B. Schlegel, J. Chem. Phys., Vol. 77, p. 3676, 1977.

4. J.A. Pople, R. Krishnan, H.B. Schlegel, and J.S. Binkley, Int. J. Quantum Chem. Symp., Vol. 13, p. 25, 1979.

5. R. Krishnan, H.B. Schlegel, and J.A. Pople, J. Chem. Phys., Vol. 72, p. 4654, 1980.

6. B.R. Brooks, W.D. Laidig, P. Saxe, J.D. Goddard, Y. Yamaguchi, and H.F. Schaefer, III, J. Chem. Phys., Vol. 72, p. 4652, 1980.

7. Y. Osamura, Y. Yamaguchi, and H.F. Schaefer, III, J. Chem. Phys., Vol. 75, p. 2919, 1981.

8. Y. Osamura, Y. Yamaguchi, and H.F. Schaefer, III, J. Chem. Phys., Vol. 77, p. 383, 1983.

9. R.N. Camp, H.F. King, J.W. McIver, Jr., and D. Mullally, J. Chem. Phys., Vol. 79, p. 1089, 1983.

10. M. Page, P. Saxe, G.F. Adams, and B.H. Lengsfield, III, J. Chem. Phys., Vol. 81, p. 434, 1984.

11. B.H. Lengsfield, III, in "Proceedings of the NATO Workshop on Geometrical Derivatives of Potential Energy Surfaces and Molecular Properties", August, 1985, Sonderborg, Denmark.

12. B.H. Lengsfield, III, P. Saxe, and D.R.Yarkony, J. Chem. Phys. Vol. 81, p. 4549, 1984.

13. P. Saxe, B.H. Lengsfield, III, and D.R.Yarkony, Chem. Phys. Lett., Vol. 113, p. 159, 1985.

14. B.H. Lengsfield, III and D.R. Yarkony, J. Chem. Phys., Vol. 84, p. 348, 1986.

15. (a) M. Descouter-Lecomte, J.C. Leclerc, and J.C. Lorquet, Chem. Phys., Vol. 9, p. 147, 1975; (b) J. Chem. Phys., Vol. 66, p. 4006, 1977; (c) C. Galloy and J.C. Lorquet, J. Chem. Phys., Vol. 67, p. 4672, 1977.

16. G. Hirsch, P.J. Bruna, R.J. Buenker, and S.D. Peyerimhoff, Chem. Phys., Vol. 45, p. 335, 1980.

17. R.J. Buenker, G. Hirsh, S.D. Peyerimhoff, P.J. Bruna, J. Romelt, M. Bettendoff, and C. Petrongalo, "Current Aspects of Quantum Chemistry", 1981 (Elsevier, Amsterdam, 1982).

18. A.D. McLean, B.H. Lengsfield, III, J. Pacansky, and Y. Ellinger, J. Chem. Phys., Vol. 83, p. 3567, 1985.

19. M. Colvin, H.F. Schaefer, III, S. Havriliak, and B.H. Lengsfield, III, Chem. Phys. Lett., submitted.

20. A.D. McLean and G.S. Chandler, J. Chem. Phys., Vol. 72, p. 5639, 1980.

21. L. Hoffland, CRDC, private communication.

22. E. Magnuson and H.F. Schaefer, III, J. Chem. Phys., Vol. 83, p. 5721, 1985.

23. S. Kim and J. King, J. Chem. Phys., Vol. 80, p. 969, 1984.

24. T. Nakanaga, S. Kondo, and S. Saeki, J. Chem. Phys., Vol. 76, p. 3860, 1982.

25. R. Krishnan, Bell Laboratories, private communication.

26. R.D. Amos, Chem. Phys. Lett., submitted.

27. W. Stevens, National Bureau of Standards, private communication.

A POTENTIAL NERVE AGENT DECONTAMINANT FROM MAMMALIAN LIVER (U)

*JAMES S. LITTLE, MAJ, PhD, CLARENCE A. BROOMFIELD, PhD,
MARY K. FOX-TALBOT, SGT, LISA J. BOUCHER, SGT
U.S. ARMY MEDICAL RESEARCH INSTITUTE OF CHEMICAL DEFENSE
ABERDEEN PROVING GROUND, MARYLAND 21010-5425

The highly toxic nature of organophosphorus compounds has resulted in their development as insecticides and chemical warfare agents. By irreversibly inhibiting acetylcholinesterase, an enzyme critical to the normal functioning of the nervous system, organophosphorus compounds produce a variety of toxic effects (1). Acetylcholinesterase normally hydrolyzes the neurotransmitter acetylcholine at the synaptic junction, thus terminating neuronal transmission (1). The inhibition of acetylcholinesterase leads to a rapid and large accumulation of acetylcholine at the synaptic junction, resulting in uncontrolled neuronal stimulation and subsequent blockade of neuronal function (1). The net result of such a blockade is manifested in signs such as bradycardia, pulmonary constriction, increased bronchial secretions, muscle paralysis, seizures, and eventually death from respiratory failure (2,3,4).

On the integrated battlefield, it is necessary to protect our troops against the debilitating effects of organophosphorus cholinesterase inhibitors. In addition, it is also necessary to effectively decontaminate personnel, equipment, and terrain. Currently available methods of decontamination involve the use of a strong alkaline solution to neutralize the toxic properties of these agents (5). This solution is effective, but because of its chemical characteristics, it is not the most desirable decontaminant for personnel or sensitive equipment. Therefore, a more suitable method of agent decontamination is urgently needed.

We describe here the partial characterization of an enzyme in mammalian liver which catalyzes the hydrolysis of the insecticide diisopropylphosphorofluoridate (DFP) and also of the chemical warfare G agents isopropylmethylphosphonofluoridate (sarin), ethyl-N-dimethyl phosphoramidocyanidate (tabun) and pinacolyl methylphosphonofluroridate (soman). Soman contains two chiral centers and therefore exists as four stereoisomers (6,7). Two of these isomers are extremely toxic and bind with high affinity to and inhibit acetylcholinesterase, whereas the other

two isomers are poor inhibitors and are considered essentially non-toxic (6,8). Previously reported organophosphorus hydrolases preferentially hydrolyze the non-toxic soman isomers (7,9-11). The enzyme reported here not only hydrolyzes all three G agents at a rate significantly greater than do previously reported enzymes, but also is the first example of an enzyme that hydrolyzes the extremely toxic isomers of soman at the same rate as the non-toxic isomers (9,11,12).

These unique properties make this enzyme an excellent candidate to be purified, partially sequenced, and its gene cloned to produce sufficient quantities of enzyme for practical military application. This enzyme may find use in a barrier cream to protect personnel against organophosphorus agents, or in a solution for decontaminating sensitive surfaces and equipment. It is also possible that the enzyme may be modified by microencapsulation or attachment to polymers for administration as a prophylactic measure against organophosphorus poisons. Theoretically, this enzyme should be more practical as a decontaminant or protective agent than other biologically-derived compounds that react stoichiometrically with organophosphorus compounds, e.g., antibodies, because one molecule of enzyme can destroy many organophosphorus molecules.

MATERIALS AND METHODS

Chemicals: Soman, sarin, and tabun were originally obtained from the Chemical Research and Development Center, Aberdeen Proving Ground, Maryland and subsequently analyzed and supplied to us by the Analytical Chemistry Branch of this Institute. DFP was obtained from ICN Pharmaceutical, Plainview, NY. Horseradish peroxidase and bovine akaline phosphatase, Type XX-T, were obtained from Worthington, Freehold, NJ. All other chemicals were analytical grade.

Animals: Male rats (200-250g) of the Sprague-Dawley stock [Crl: CD(SD)BR] and male mice (28-32 g) of the ICR stock [Crl:CD-1(ICR)BR] were obtained from Charles River (Kingston, NY) and maintained on Purina lab chow and tap water ad libitum. All animals were maintained on a 12 hour day-night cycle (light cycle from 0600 - 1800 hours). Rats were fasted for 18 hours before they were used in experiments. Fasting was utilized to increase the yield of hepatic subcellular fractions (13). Animal use was in accordance with AR 70-18.

Preparation of the Soluble Cell Fraction: Rat livers were removed, placed in beakers on ice, rinsed with ice-cold 0.25 M sucrose, minced with scissors, and then homogenized 12 strokes in 3 volumes of ice-cold 0.25 M sucrose. Homogenization was done at 400 rpm, using a mechanically driven teflon pestle in a glass homogenizer (Arthur H. Thomas, Inc., Philadelphia, PA). After diluting the homogenate to 5% (W/V) with 0.25 M

sucrose, nuclei and mitochondria were removed by successive centrifugation at 1,000 x g for 10 minutes and 10,000 x g for 10 minutes in a Sorvall RC-5B refrigerated centrifuge (DuPont Co., Wilmington, DE). The post-mitochondrial supernatant was then centrifuged at 205,000 x g for 30 minutes in a Beckman SW41 rotor operated in a Beckman Model L8-80 ultracentrifuge (Beckman Instruments, Inc., Palo Alto, CA) to produce a supernatant which we refer to as the soluble fraction.

Determination of Hydrolysis Rates of Organophosphorus Commpounds: The rate of hydrolysis of each substrate was measured using an automated Radiometer pH Stat system (Radiometer America, Cleveland, OH), by continuously titrating the acid generated by hydrolysis with a previously standardized 0.01 N KOH solution. Titrations were carried out at pH 7.4 and 25°C in unbuffered isotonic saline containing the substrate and metal ion concentrations indicated in the legends to the tables and figures. For all assays, 3.0 ml of a substrate solution in saline was introduced into the titration cell, and the rate of spontaneous hydrolysis was determined. For enzyme assays, 25 to 100 ul of soluble fraction containing 1 to 2 mg of protein was then introduced into the substrate solution to obtain the total hydrolysis rate. The enzymatic hydrolysis rate was then calculated by subtracting the spontaneous rate from the total rate.

Gel Filtration by High Pressure Liquid Chromatography (HPLC): To 1.0 ml of the soluble fraction was added 200 units of bovine intestinal alkaline phosphatase and 10 units of horseradish peroxidase to act as marker enzymes in the elution process. The mixture was filtered through a Millex-GV, 0.22 um filter unit (Millipore Corp., Bedford, MA) and 50 ul of the filtrate were injected onto a type G 2000 SW TSK-GEL column (Toyo-Soda, Japan) and eluted at a flow rate of 1.0 ml per minute with 0.01 M NaCl adjusted to pH 7.0. One ml aliquots were collected and each aliquot after the "hold-up" volume (10.75 minutes) was assayed for alkaline phosphatase and horseradish peroxidase activity as well as for hydrolyzing activity against sarin, soman, and tabun.

Measurement of Enzyme Activity in HPLC Gel Column Fractions:

a. Organophosphorus-Hydrolyzing Activity: To 1.0 ml of 10 mM sarin, soman, or tabun was added 1.0 ml of a 2 mM $MgCl_2$ solution and 200 ul of methyl red (1 mg per ml in H_2O). Fifty ul of this "substrate" solution was pipetted into each of 24 wells of a standard microtiter plate, each well containing 50 ul of the fraction to be tested. After 2, 10, and 30 minutes, the plate was read spectrophotometrically in a Titertek Multiscan MCC (Flow Laboratory Inc., McLean, VA) with a 510 nanometer filter. Absorbances were plotted versus fraction number to determine the elution volume of the enzyme.

b. Alkaline Phosphatase Activity: Alkaline phosphatase activity was determined spectrophotometrically as described above, except that 37 mg/ml of 4-nitrophenylphosphate in 1.0 M tris(hydroxymethyl) aminomethane (TRIS)-chloride buffer pH 8.0 was employed as the substrate and a 405 nanometer filter was used in the Titertek.

c. Horseradish Peroxidase Activity: Horseradish peroxidase activity was determined in a manner similar to that described above, except that a fresh solution of 3,3' diaminobenzidene, 50 ug/ml in 0.1 M acetate buffer pH 5.0 containing 0.1 ul of 30% hydrogen peroxide per ml was used as the substrate. Appearance of color was determined by visual observation and the horseradish peroxidase elution position verified in a separate experiment by UV detection at 280 nanometers.

Separation of Soman Stereoisomers: The stereoisomers of soman were separated by gas chromatography by a modification of the method of Benschop (10). The carbowax-20 capillary column was omitted and the samples were separated on a chirasil-val capillary column (25 m x 0.22 mm) (Chrompack, Inc., Bridgeport, NJ) and detected with an electron capture nitrogen/phosphorus detector. All other conditions of column temperature and flow rates were as described by Benschop (10).

Bioassay for Determining if the Liver Enzyme Hydrolyzes the Toxic Soman Isomers: Six mls of 5 mM soman in saline was introduced into the titration cell of the automated Radiometer pH Stat system (see above under Determination of Hydrolysis Rates). To this was added an aliquot of the soluble fraction containing the organophosphorus hydrolyzing enzyme. The initial rate of hydrolysis was determined and the time required to hydrolyze 50% of the soman was calculated. At that time an aliquot of the 50% hydrolyzed soman was removed, tested for extent of hydrolysis by gas chromatography, and diluted with saline to 5.8 ug/ml. A 5 mM soman control which had been stored on ice was also diluted to 5.8 ug/ml with saline. Twenty mice (28-32 g) were then injected into the tail vein with 0.28-0.32 ml (58 ug/kg) of either the hydrolyzed or unhydrolyzed soman. The number of surviving mice was determined 24 hours later.

Protein Assay: Protein was assayed by the method of Lowry et al. (14) using bovine serum albumin as a standard.

RESULTS

Cellular Distribution: When liver was homogenized and separated by ultracentrifugation into a particulate and soluble fraction, 85% of the soman hydrolytic activity was observed in the soluble fraction (Table 1).

Table 1. Cellular Distribution of the Liver Organophosphorus Hydrolyzing Enzyme

Two percent liver homogenates (W/V) in 0.25 M sucrose were sedimented at 205,000 x g for 30 minutes. Supernatants were decanted and saved. Pellets were washed once by suspension and recentrifugation in 0.25 M sucrose containing 20 mM TRIS-Cl pH 7.5 to remove absorbed soluble proteins (15) and subsequently suspended in 0.25 M sucrose. Washed pellets and soluble fractions were assayed as described in "Materials and Methods" with 1 mM soman and 1 mM $MgCl_2$. Recoveries were 100% ± 9. Values are mean ± S.E. (n=6).

Fraction	Percent of Original Homogenate Activity
Particulate	15 ± 1
Soluble	85 ± 3

Substrate Specificity and Kinetic Properties: The activity of the liver enzyme was determined using several organophosphorus compounds as substrates (Table II). All three common G agents (sarin [GB], soman [GD], and tabun [GA]) were hydrolyzed, with sarin being hydrolyzed at the greatest rate. As shown in Table II, hydrolysis rates were sarin > soman > tabun > DFP. The Michaelis-Menten substrate affinity constant (Km) and maximum velocity (Vmax) of the enzyme with different substrates is alsc shown in Table II. The Km, which is inversely proportional to the affinity of the enzyme for the substrate, is in the millimolar range for all three G agents and DFP. The maximum hydrolytic rate of the enzyme (Vmax) ranged from 2694 nanomoles of substrate hydrolyzed/minute/milligram of protein with sarin to 54 with DFP.

Table II. Substrate Specificity and Kinetic Properties of the Liver Organophosphorus Hydrolyzing Enzyme

The soluble fractions of six liver homogenates were prepared, combined, and assayed as described in "Materials and Methods." Five different substrate concentrations were assayed for each substrate and the Km and Vmax were determined by fitting velocity vs substrate concentration to a hyperbolic function using regression analysis (16). Results for each substrate, which usually did not differ by more than 10% for Km or 20% for Vmax, are those combined from at least two different kinetic experiments.

Substrate	Km (mM)	Vmax (nMoles/min/mg protein)
Sarin (GB)	1.9	2694
Soman (GD)	1.1	718
Tabun (GA)	8.9	586
DFP	3.7	54

Metal Ion Requirements: Since metal ions are known to stimulate the activity of other organophosphorus hydrolyzing enzymes (17) we studied the effect of Mn^{++}, Mg^{++}, and Co^{++} on the activity of the liver enzyme (Figure 1). All three ions stimulated the activity of the enzyme when sarin or soman was employed as a substrate, with Mg^{++} stimulating the most. When tabun was employed as a substrate, these metal ions had no effect on enzyme activity.

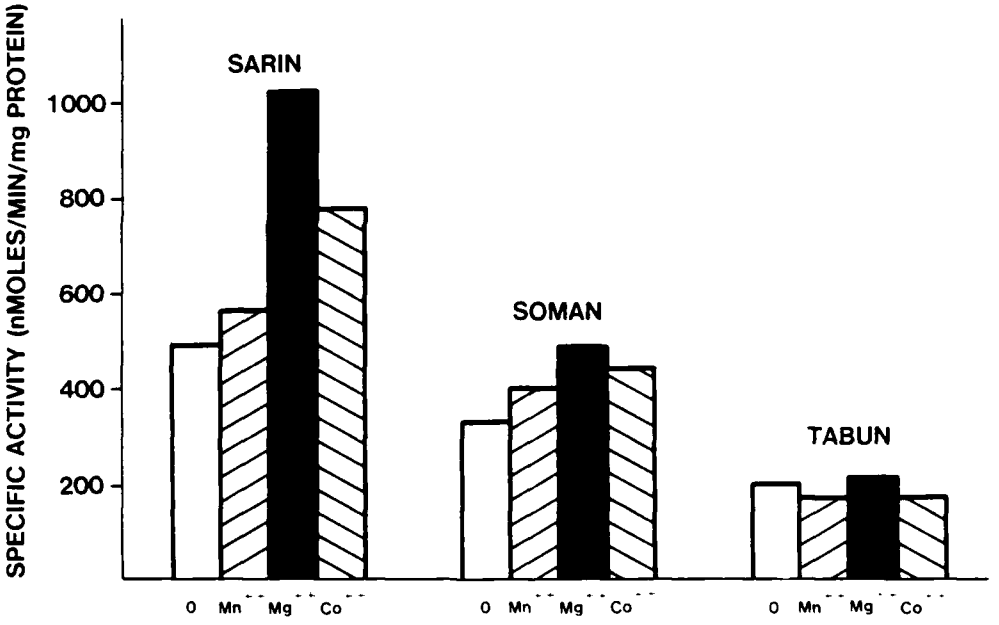

Figure 1. The Effect of Metal Ions on Enzyme Activity. Homogenates from six livers were pooled and the soluble fraction prepared as described in "Materials and Methods." This soluble fraction was assayed for enzymatic activity with 5 mM of the indicated substrate and in the presence or absence of 1 mM of the indicated metal ion. Results are shown from one representative experiment.

Effect of Various Concentrations of Mg^{++} on Enzyme Activity: Since Mg^{++} ions were shown to stimulate the activity of the enzyme to a greater extent than did Mn^{++} or Co^{++} ions when sarin or soman was employed as substrate, the effect of various concentrations of Mg^{++} on enzyme activity was determined (Figure 2). All concentrations of Mg^{++} tested were shown to stimulate enzyme activity with the greatest degree of stimulation occurring above 0.5 mM. As a result of this experiment subsequent experiments were conducted in the presence of 1 mM Mg^{++}. At Mg^{++} levels higher than 5 mM, significant non-enzymatic hydrolysis was observed.

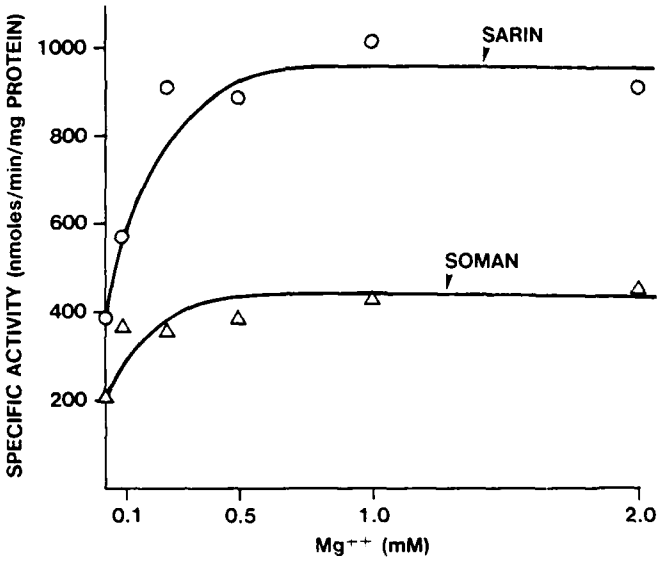

Figure 2. The Effect of Mg^{++} Ions on the Hydrolysis of Sarin and Soman by the Liver Enzyme. Homogenates from six livers were pooled and the soluble fraction prepared as described in "Materials and Methods." The activity of this fraction was determined with 1 mM sarin or soman as the substrate in the presence or absence of the indicated Mg^{++} ion concentrations. Results are shown from one representative experiment.

Molecular Weight: Elution profiles from high pressure liquid chromatography (HPLC) columns indicate that a single enzyme is responsible for the hydrolysis of sarin, soman, and tabun since the hydrolytic activity eluted from the column in a single peak (Figure 3). These results also indicate that the molecular weight of the enzyme is approximately 40 kilodaltons since the enzyme activity co-eluted with that

AD-A173 639 PROCEEDINGS OF THE ARMY SCIENCE CONFERENCE (1986) HELD 4/4
AT WEST POINT NEW..(U) DEPUTY CHIEF OF STAFF FOR
RESEARCH DEVELOPMENT AND ACQUISITIO.. 20 JUN 86

UNCLASSIFIED F/G 5/2 NL

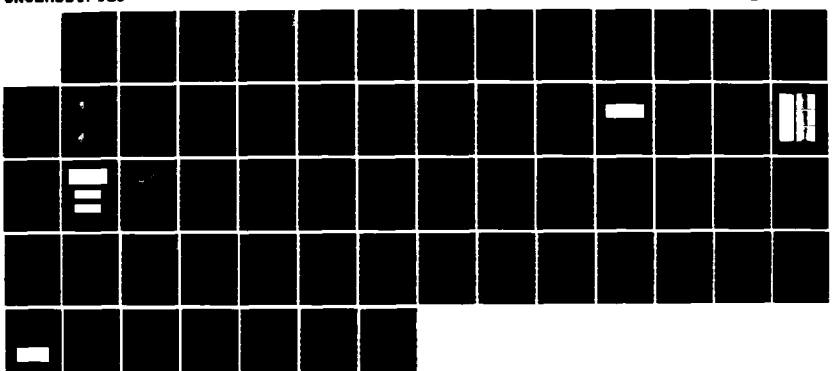

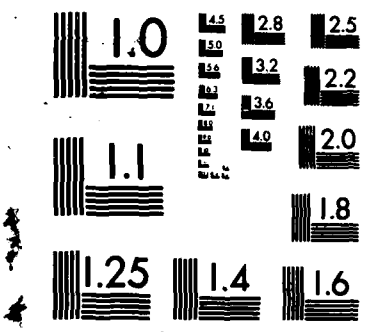

MICROCOPY RESOLUTION TEST CHART
NATIONAL BUREAU OF STANDARDS-1963-A

of horseradish peroxidase, which has a molecular weight of 39.8 kilodaltons (Figure 3).

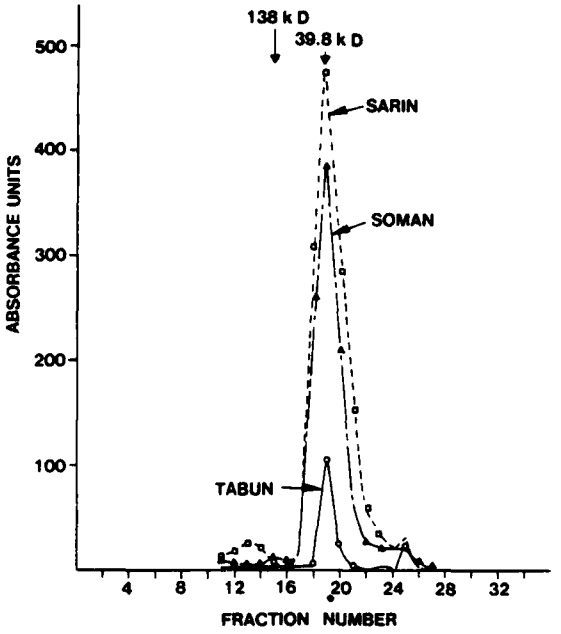

Figure 3. Molecular Weight Determination of the Liver Enzyme. This figure shows elution patterns of the organophosphorus hydrolyzing enyme from a 7.5 x 30 mm G 2000 SW type TSK gel HPLC column. The column was run and the enzymatic activity determined as described in "Materials and Methods." Molecular weight marker enzymes of 138 kilodaltons (alkaline phosphatase) and 39.8 kilodaltons (horseradish peroxidase) eluted at the indicated positions. Substrates are sarin (□), soman (Δ), and tabun (○). Results are shown from one representative experiment.

Stereospecificity of the enzyme. Due to the presence of a center of asymmetry in both the pinacolyl moiety and the phosphorus atom, four stereoisomers of soman exist (For further details please see "Discussion"). When soman was hydrolyzed by the liver enzyme for various lengths of time as indicated in the legend of Figure 4, all four stereoisomers of soman were hydrolyzed at the same initial rate. The time required for 50 percent hydrolysis was identical for each of the four stereoisomers.

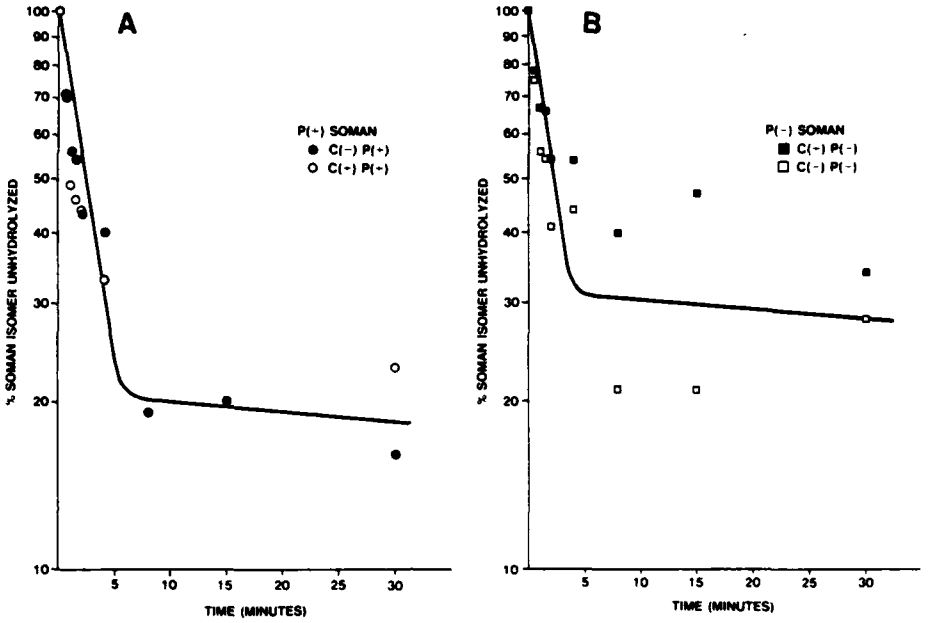

Figure 4. Hydrolysis of the Four Soman Stereoisomers by the Rat Liver Enzyme. Stereoisomers were separated as described in "Materials and Methods." All data are expressed as the percent of a DFP internal standard and have been normalized for direct comparison. All points are the average of two determinations.

(a) Hydrolysis of the P(+) soman isomers
●=C(−)P(+), O=C(+)P(+)

(b) Hydrolysis of the P(−) soman isomers
■=C(+)P(−), □=C(−)P(−)

The C(+)P(−) soman isomers at 8 and 15 minutes have large values because the area attributable to the C(+)P(+) soman peak was not resolved at these time points and is probably included in the area for the C(+)P(−) soman peak (which is the adjacent peak).

Effect of Hydrolysis on In Vivo Toxicity. To verify that the liver organophosphorus hydrolyzing enzyme hydrolyzes the toxic isomer of soman, mice were injected intravenously with either 58 ug/kg of native soman or 58 ug/kg of native soman that had been hydrolyzed to the 50% point with the liver enzyme as described in "Materials and Methods." Eight of 10

mice receiving the 58 ug/kg native soman died, while none of 10 mice receiving the partially hydrolyzed soman died.

Enzyme Stability. On the basis of a preliminary experiment, it appears as though this enzyme is stable for at least 80 days at -90°C and is completely inactivated when boiled for 5 minutes.

DISCUSSION

We have described an enzyme in the soluble fraction of mammalian liver that catalytically hydrolyzes the three G agents--sarin, soman, and tabun--as well as DFP. This enzyme hydrolyzes the G agents at rates significantly greater than those previously reported for organophosphorus degrading enzymes (12,18-21). In addition, the soluble enzyme reported here is stimulated most efficiently by Mg^{++} ions (Figure 1), whereas previously reported organophosphorus hydrolases have been reported to be stimulated most efficiently by Mn^{++} ions (12,19). This enzyme is localized almost exclusively in the soluble fraction of the liver (Table I), a characteristic that should prove useful in the purification of this enzyme since the use of detergents, which are often necessary to solubilize membrane-bound enzymes, will not be required. While it is possible that several different enzymes in the soluble fraction of the liver may be responsible for the observed hydrolytic activity against the organophosphorus compounds, this seems unlikely since the hydrolytic activity eluted from gel columns by HPLC in a single peak (Figure 3). This observation suggests that one enzyme is responsible for the observed hydrolytic activity. Since the enzyme is found almost exclusively in the soluble fraction of the liver and has eluted as a single peak from HPLC gel columns, a partial purification has already been obtained.

Another important observation regarding the enzyme reported here is that it appears to hydrolyze all four stereoisomers of soman at the same initial rate. Due to the presence of two centers of asymmetry in the pinacolyl moiety and the phosphorus atom, four stereoisomers (see below) of soman can be distinguished.

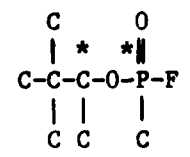

1. C(-) P(-)
2. C(-) P(+)
3. C(+) P(-)
4. C(+) P(+)

These isomers are assigned C(-)P(-), C(-)P(+), C(+)P(-), and C(+)P(+). The C stands for the pinacolyl moiety and the P for the phosphorus atom. The (-) and (+) signs refer to the relative orientation in space about the respective center of asymmetry. As shown previously, the isomers of soman vary widely in their cholinesterase inhibition rate (6,8) and in their rate of detoxification (7,9,12). It has been shown that the P(-) isomers have a high anticholinesterase activity and are therefore the most toxic whereas the P(+) isomers are relatively non-toxic (6). Others have shown that the less toxic P(+) isomers appear to be preferentially degraded by similar enzymes from other sources (7,9,10). It is noteworthy that the liver enzyme which we have described hydrolyzes each isomer at the same rate (Figure 4). The gas chromatographic evidence which suggests that this enzyme hydrolyzes the toxic isomers of soman (Figure 4) was confirmed by a bioassay. When soman was partially hydrolyzed (50%), its in vivo toxicity in mice was reduced. Mice were given a dose of native soman intravenously, which was predicted from preliminary toxicity studies to kill 80-90% of the mice. When mice were given this dose 80% of them died in 24 hours. However, when given the same dose which was hydrolyzed to the 50% point, none of the mice died. This result is consistent with our gas chromatographic data, which shows that the liver organophosphorus hydrolyzing enzyme hydrolyzes all four of the soman isomers.

In summary, the enzyme described here has several desirable characteristics: 1) it is localized in the soluble fraction, 2) it appears to be a single enzyme, and 3) it hydrolyzes all three common G agents to include the toxic soman isomers at a significant rate. These properties suggest that this enzyme may have potential for use as a chemical threat agent decontaminant. It is also theoretically possible that appropriate modifications, such as microencapsulation or attachment to polymers, would permit its use as a prophylactic or therapeutic measure against organophosphorus toxicity.

Acknowledgements

The authors thank Dr. David E. Lenz and Mr. Brian MacIver for separating the soman stereoisomers and Ms. Helen Wells and Ms. Patricia Rutherford for typing the manuscript.

References

1. Taylor, P. 1980. Anticholinesterase agents. In: Gilman, A.G., Goodman, L.S. and A. Gilman (eds.). The Pharmacological Basis of Therapeutics. 6th Ed. Macmillan, New York. 100-119.
2. Holmstedt, B. Pharmacology of organophosphorus cholinesterase inhibitors. 1959. Pharmacological Reviews 11:567-688.

3. Namba, T., Nolte, C.T., Jackson, J. and D. Grob. 1971. Poisoning due to organophosphate insecticides. Acute and chronic manifestations. Am. J. Med. 50:475-492.
4. DeCandole, C.A., Douglas, W.W., Evans, C.L., Holmes, R., Spencer, K.E.V., Torrance, R.W. and K.M. Wilson. 1953. The failure of respiration in death by anticholinesterase poisoning. Brit. J. Pharmacol. 8:466-475.
5. Seiders, R.P. 1986. Catalysis: The future for decontamination. Army Research, Development and Acquisition Magazine. January-February p. 14-15.
6. Benschop, H.P. 1975. The absolute configuration of chiral organophosphorus anticholinesterases. Pestic. Biochem. Physiol. 5:348-349.
7. Benschop, H.P., Berends, F. and L.P.A. deJong. 1981. GLC-analysis and pharmacokinetics of the four stereoisomers of soman. Fund. Appl. Tox. 1:177-182.
8. Keijer, J.H. and G.Z. Wolring. 1969. Stereospecific aging of phosphonylated cholinesterases. Biochem. Biophys. Acta. 185:465-468.
9. Nordgren, I., Lundgren, G., Puu, G, and B. Holmstedt. 1984. Stereoselectivity of enzymes involved in toxicity and detoxification of soman. Arch Toxicol. 55:70-75.
10. Benschop, H.P., Konings, C.A.G. and L.P.A. DeJong. 1981. Gas chromatographic separation and identification of the four stereoisomers of 1,2,2,-trimethylpropyl methylphosphonofluoridate (soman). Stereospecificity of in vitro "detoxification" reactions. J. Amer. Chem. Soc. 103:4260-4262.
11. Hoskin, F.C.G., and A.H. Roush. 1982. Hydrolysis of nerve gas by squid-type diisopropylphosphorofluoridate hydrolyzing enzyme on agarose resin. Science 215:1255-1257.
12. Mounter, L.A., 1963. Metabolism of organophosphorus anticholinesterase agents. In: Handbuch der Experimentallen Pharmakologie Cholinesterases and Anticholinesterases Agents. Koelle, G.B. (ed). Springer-Verlag, Berlin, Gottingen, Heidelburg Vol. 15:486-504.
13. Dallner, G., Siekevitz, P., and G.E. Palade. 1966. Biogenesis of endoplasmic reticulum membranes. I. Structural and chemical differentiation in developing rat hepatocyte. J. Cell Biol. 30:73-95.
14. Lowry, O.H., Rosebrough, N.J. Farr, A.L., R.J. Randall. 1951. Protein measurement with the Folin phenol reagent. J. Biol. Chem. 193:265-275.
15. Dallner, G., Siekevitz, P., and G.E. Palade. 1966. Biogenesis of endoplasmic reticulum membranes. II. Synthesis of constitutive microsomal enzymes in developing rat hepatocyte. J. Cell Bio. 30:97-117.
16. Statistical manual for the Prophet System. 1980. NIH Publication #80-2169. p 6.40-6.42

17. Mounter, L.A. 1955. The complex nature of dialkylfluorophosphatases of hog and rat liver and kidney. J. Biol. Chem. 215:705-711.
18. Hoskin F.C.G. 1971. Diisopropylphosphorofluoridate and tabun. Enzymatic hydrolysis and nerve function. Science 172:1243-1245.
19. Hoskin, F.C.G., Kirkish, M.A., and K.E. Steinmann. 1984. Two enzymes for the detoxication of organophosphorus compounds - sources, similarities, and significance. Fund. Appl. Tox. 4:S165-S172.
20. Adie, P.A., Hoskin, F.C.G., and G.S. Trick. 1956. Kinetics of the enzymatic hydrolysis of sarin. Can. J. Biochem. Physiol. 34:80-82.
21. Augustinsson, K.B., and G. Heimburger. 1954. Enzymatic hydrolysis of organophosphorus compounds. Acta Chem. Scand. 8:1533-1541.

This paper contains proprietary data that is releasable to representatives of NATO and/or ABCA countries.

COMPUTER ASSISTED POSTMORTEM IDENTIFICATION (U)

*LEWIS LORTON, COL, DC
WILLIAM H. LANGLEY
US ARMY INSTITUTE OF DENTAL RESEARCH
WASHINGTON, D.C. 20307-5300

INTRODUCTION

The identification of military casualties is a possible issue in any military operation. This responsibility has always been recognized by the United States Government and preparations for this eventuality include the wearing of dogtags, name labels in clothing, and maintenance of dental records and x-rays. The recovering and handling procedures have been exhaustively detailed in military and civilian publications but the enormous logistic and logic problems attendant to the actual identification process have received only scattered attention.

Although dog tags and clothing name labels often serve to establish "believed-to-be" identifications, the final confirmation of the identity is based on the presence of physical factors singular to a given person.

A military population is relatively homogeneous in all the descriptors such as age, sex, weight. and height which can more easily stratify any civilian group of similar size. The highly destructive possibilities of modern life ,such as high speed transportation and modern weapons, serve to reduce the usable identification factors to those which can resist high temperature, flames, impact, and atmospheric effects. Dental records and x-rays have long been considered to be a primary method of postmortem identification.

Dental records do not have standard formats or content. The heavy reliance on image interpretation (x-ray films) limits access to the information in the records to trained personnel. Skilled observers must compare records and x-rays from ante and postmortem cases. Properly done comparisons require some finite length of time. When many postmortem

remains must be matched with an equally large number of antemortem records, or when a single postmortem record must be compared with a very large at-risk population, the requirement for physical space and skilled observers becomes a rate-limiting factor. Wolcott at al (1) in one of the few reports of an identification process that analyzed the nature of the problems, described a mass disaster where records overwhelm physical facilities and tax the mental capacity of investigators. An the difficult process of maintaining, handling and sorting through large numbers of records is an unexepected burden in a large disaster. Only those people who have actually been involved with mass casualty identification problems are aware of the requirements for record management space and the full debilitating effect of the stress and long hours on the logical faculties of the personnel.

Thus the problems of the identification process can be seen to pivot around the issue of record keeping and record handling. Identification records must be accurate and are usually voluminous. Antemortem and postmortem records must be compared to discover the correct identity matches.

A previous study (2) done on a limited data base (under 100 subjects) indicated that dental restorations were probably suitable for selection of most probable identity matches from a larger data base.

The initial objectives of this project were:

1) to determine the selectivity of simply coded dental characteristics in the identification of postmortem remains in large 'at-risk' populations where both the antemortem and postmortem records may be fragmentary.

2) to analyze the intellectual process of identification and evaluate whether parts of this process could be performed by a computer with no loss in the sensitivity of the process.

This paper describes the results obtained in the pursuit of these objectives. An end product of this work has been a specialized data base management structure for a postmortem identification system and a large body of experience on how best to use it. The system design and implementation has been discussed previously (3).

The methodology and management system derived from this research effort has been used successfully in the postmortem identifications at a recent major disaster (US Army, 101st Airborne, Gander,Newfoundland,Dec 1985) and in the on-going identification of skeletal remains (Central Identification Lab, HI). It is also is being considered for implementation as part of a military-wide electronic medical dental record system to function in concert with a central storage site for dental panoramic films.

Experimental Approach

The first direct goal was to develop a comparison algorithm and a suitable set of codes that would allow the efficient matching of antemortem records and postmortem records. This algorithm would be incorporated into a special purpose computer program which would support the construction of antemortem and post mortem data bases and the comparison of records.

It was essential that the codes be readily usable by the health care personnel responsible for the encoding without extensive training and that the coding process should be efficient and rapid so that a database could be assembled without a deleterious effect on the normal productivity of military dental clinics.

A second direct goal was to test the automated decision making system using a data base gathered from dental records of a typical military population. The objective of the process was not to identify the questioned remains but to optimize the work of the forensic investigators by directing their attention to the most likely matches first. A measure of the selectivity of the system will be how often the correct match is designated as most likely by the decision process.

Experimental Methods

a) Selection of Codes, Comparison Algorithms, and Decision Matrix

Codes -

The goal of the comparison process is to compare an unknown record to each record in the data base, to assign a proba-

bility of correct match to each record in the data base and then provide the investigator with a listing of the data base records ordered by probability. Since decisions can be made only on available information, the choice of codes, and thus the information incorporated, is of ultimate importance. From an operational standpoint, the codes should be easily learned and applied. It was decided to limit the codes to those used in standard dental charting which described whether the tooth was present, unerupted, extracted, unrestored (no dental fillings), or if restored, which surfaces were restored. Conscious decisions were made not to include the type of materials used (gold, silver, composite etc.) since the logic chain for the decision process become extremely complex and inclusion of these codes did not promise any increased selectivity. In fact, simulations using material types demonstrated that inclusion of modifying codes in the decision process degraded the process while only contributing to the complexity of the decision trail and the comparison times.

Other requirements for the codes were that they be exhaustive, exclusive, and objective. By exhaustive it is meant that all possible responses be included; exclusive, no domain of any response overlapped another; to be objective, a response was independent of observer.

Comparison Algorithms -

The result of a decision process can be either categorical, ordinal, or interval. For example the result of an identification process may be that record 124 is a match with antemortem identity Joseph Jones. This is a categorical result in that J. Jones is placed in the 'match' category, and all of the other records are placed in the 'not match' bin. For accuracy in categorical decisions the decision criteria must be extremely clear-cut, that is exhaustive, exclusive, and objective. It is difficult to conceive of an automated process attaining this level of 'intelligence' in the field of identifications. Since the amount and quality of data available for decision making cannot be predicted for any particular comparison problem, it is impossible to complete a decision path that will be appropriate for every situation. The decision of match or no-match should be retained for a human. investigator. The weakness in a deci-

sion system with a categorical outcome is the lack of information about the relative 'scores' of the other members of the data base.

An ordinal decision process applied to an identification problem would evaluate all possible records and assign a rank to each record based on the responses to the decision criteria. There is no quantitative threshold for declaring a match or mismatch. The record with the best score, no matter how poor, is ranked first, and so forth.

Other decision systems which result in scores of some sort, such as academic tests, are theoretically interval systems. The value of each unit of the scale is known and measurable e.g. a score of 100 would be twice as good as a score of 50. Inherent in this sort of scoring is that the test instrument is accurate, equitable, and the scores given for each criteria are correct. In other words a approaching 'perfection' as a decision system.

It is possible to force ordinal data into a categorical result. A relevant example is available in scientific hypothesis testing when results that have a probability of 0.06 are declared non-significant, while results that have reached the magic threshold of .05 probability are declared 'statistically significant.'

The best matches for any search should be displayed for the investigator rather than only those records which pass some arbitrary threshold of suitability.. For this, and other reasons which will become apparent to the reader, the system described in this paper can be considered as having an ordinal measuring scale.

Decision Matrix -

Since records may vary greatly in content because of the circumstances of the original examination it is important to fix the number of decisions made on each record. This will keep the correct record with a few significant, matching characteristics from being listed after records with multitudes of trivial matches.

Only 32 decisions are accepted for each dental record, one for each tooth. There is a natural progression in the states that any single tooth can take and thus it is simple to create a decision matrix for each tooth.

0 - missing data
1 - unerupted
2 - unrestored
3 - restored (any combination of 5 surfaces)
4 - crown
5 - tooth in place but its state unknown
6 - missing and healed

For any tooth, if the later (postmortem) record is the same as the earlier (antemortem) record, the relationship is recorded as a match; if the postmortem record is lower in the hierarchy than the antemortem then that is a mismatch; if the postmortem is higher in the hierarchy than the antemortem, that is a possible match (the antemortem state can have naturally progressed into the postmortem state).

Thus, for each comparison of antemortem to postmortem record, there is a possibility of 32 points divided amongst scores for matches, mismatches, and possibles.

When a comparison is made between a single antemortem record and a database of postmortem records (or vice versa), the comparisons are made on a case by case basis. The data base is then reordered so that the records with the maximum number of matches and minimum number of mismatches are first.

Within each subset of records with the same number of matches the records are ordered with minimum number of mismatches first. A representative list is shown below.

record #	matches	mismatches	possible
4573	31	0	1
3321	30	0	2
2667	29	0	3
4553	29	1	2
6232	29	2	1

b) Experimental Methods

A trial of the data gathering methods and the comparison/selection algorithms was carried out at a US Army post. Data were gathered by the investigators who acted as the clinic examination officer for the period of the trial.

Simple, visual, dental examinations were performed on 578 soldiers who were seen at troop dental clinics. The data recorded included the Soldier's Serial Number (only to ensure the elimination of duplicate records), age, sex, and a description of the restorative status of each of their teeth according to the method described in previous sections. After the records were checked to eliminate duplicates the SSAN, was deleted and a coded record number was substituted. These examinations were then entered into 'known' record files of the Computer Assisted Postmortem Identification System (CAPMI) in the Data General MV8000 computer at Letterman Army Institute of Research.

The resulting data file was then copied onto the 'unknown' file; thus there were two identical files, one designated as the 'known' data and the other as the *'unknowns.'*

In order to test the ability of the system to match identities correctly where fragmentary records or remains are the only source of data, other 'unknown' files were constructed with only certain groups of teeth included for use in the comparison/selection process:

all 32 teeth	only teeth 1-8 included
only teeth 1-16 included	only teeth 6-11 included
only teeth 17-32 included	only teeth 24-32 included

The identification reports from the comparison procedures were first treated by a succession of custom application programs. The report for each procedure listed all the records in the data base ranked by most number of matches. For each unknown, the rank placement of the correct identity match in the report was recorded. For each comparison run, a data file resulted which contained the identification number of the unknown, the rank of the correct match in the list

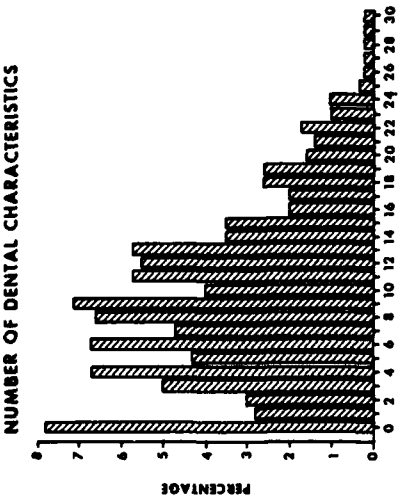

Figure 1

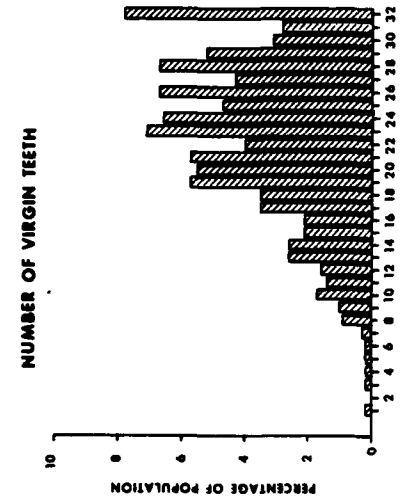

Figure 2

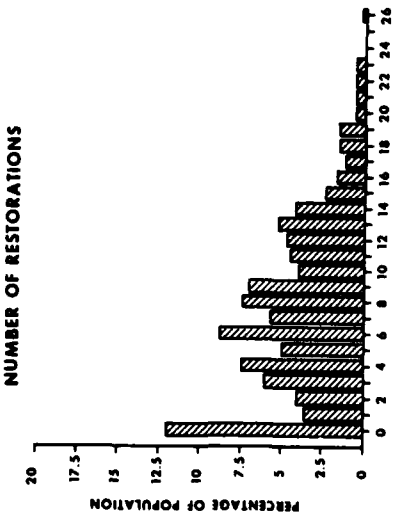

Figure 3

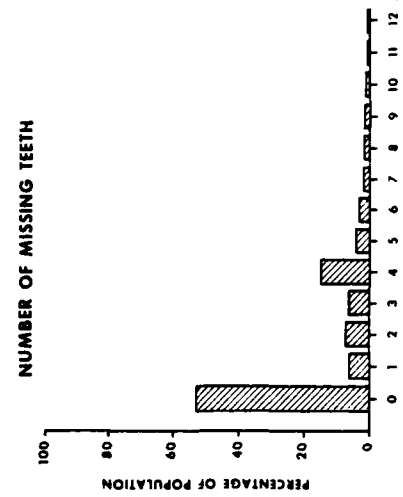

Figure 4

TABLE 1

Characteristic per subject

n (subjects) = 578

	mean	sd	max/min	median	mode
unrestored teeth/subject	22.5	6.3	32/1	23	32
restored teeth/subject	7.6	5.4	26/0	7	0
missing teeth/subject	1.9	2.5	12/0	0	0

TABLE 2

Position on 'Best-Matches' List

Number of Dental Characteristics	Correct Match Occured In (out of 578)*			
	1st	first 2	first 3	first 10
1 or more	91%	97%	98%	99.5%
2	92%	97%	98%	99.6%
3	92%	97%	98%	99.6%
5	95%	99%	99.3%	99.8%
7 or more	96%	99.6%	99.7%	100%

*assuming at least 10% error rate in recording dental characteristics in data base

and the number of dental characteristics in the unknown record. (Any restored or missing tooth was counted as a single characteristic, thus any record could have a maximum of 32 characteristics).

Simple summary statistics were gathered on the various files using the BMDP package, (UCLA, 1982).

RESULTS-

The distribution of dental characteristics in this population is described in Figure 1. The distribution of unrestored, restored, and missing teeth was determined and the frequency distribution are shown in Figures 2, 3, and 4. Since the distributions are decidedly not normal the traditional means and standard deviations are not completely descriptive of the data but are included with the complete summary data in Table 1 and 2.

A total of 578 records were used in the initial comparison runs. The results of the various comparison runs are summarized in table 2. The results of the comparison runs with the fragmentary remains paralleled the results of the complete mouth. The more teeth and the more dental characteristics the greater the selectivity of the process. The overall selectivity of the anterior segments (teeth 6 - 11, 22 - 27) was lower due to the lower average number of characteristics. In the individual cases where dental restorations were present in these teeth, the records were easily selected from the data base because of the relative infrequency of restorations in most cases. The selectivity of the the maxillary (upper) and the mandibular (lower) teeth was similar.

DISCUSSION

As stated above this system was developed on the hypothesis that simple dental characteristics provide enough information to select a small subset of most probable match identifications from a data set of fair size- in this case about 600 records. This subset of records would optimize the search effort for the investigators by deferring the least likely records from immediate consideration. The results as summarized in figures 1 to 5 and tables 1 and 2 certainly indicate that the variety of possible combinations

is great enough to insure singularity for an individual if that individual possesses even a relatively small number of dental characteristics. (A characteristic being defined as any missing or restored teeth.)

If only cases with one or more dental characteristics are considered then, in all comparison/selection runs the specificity is vastly improved. If all 32 teeth are used and only cases with one or more dental characteristics are considered then 97% are in the first or second places on the list and 99.4 % are in the first 10 records.

As figure 1 indicates, the average person in this group had seven dental characteristics. Approximately 92% of the population has 1 or more dental characteristics while about 82% have 4 or more. Even in the worst case situation, where the unknown has no missing or restored teeth, 92% of the population will be deferred from consideration.

The more dental characteristics present in any dentition or dentition segment, the better the ability of the system to report the correct identity higher in the best-matches list.

These conclusions from the initial work were tested when this system was used in the identification process at a major military disaster (Newfoundland crash). Although the details of the operation are not yet released, it can be said that the system functioned exactly as designed and as it did in the tests.

The postmortem data base consisted of over 250 dental records gathered by the examination section of the identification team. In the traditional method of handling these records, as each antemortem record was obtained, an investigator would go through the files of postmortem remains searching for the correct match. Usually lists were kept of odd or significant characteristics to aid in recovering the unusual record, but for the majority of identifications, the manual search was used. That consisted of opening each record envelope, taking out the postmortem x-ray films and mounting them on the viewer, and comparing them to the antemortem record. A team of two people usually performed each search. One member would do the initial evaluation, the other would do the drudge labor of removing envelopes, sorting out the films, replacing and refiling the records.

One complete pass through a set of records of this size would take an experienced team over one hour.

The automated system, now known as CAPMI (Computer Assisted Postmortem Identification), functioned to search either the antemortem or postmortem records. Typically, an antemortem record would be entered into the system for a search, the search completed, and the best matches list returned in under four minutes. For about 65% of the current antemortem records the correct identity match was at the top of the best matches list. In another 10% of the cases the correct match was second or third on the list. It quickly became apparent that, if the correct match was not in the top three positions on the generated best matches list, other computer techniques would be more efficient in producing the correct match.

These techniques, termed 'prospecting', were applied in two stages. In the first stage, the record was changed so that only the restored or missing teeth were used in the search, ignoring the unrestored teeth. If a good match did not result, then successive records were submitted which searched for only separate sections of the mouth. These two procedures worked successfully on three/quarters of the records not successfully identified with the original search. Approximately 92 to 95% of the records could be successfully matched using the automated system. The remainder of the records were never matched using a computer search.

Inspection of that portion of the remainder of the records which had been matched by other means (fingerprints and/or personal effects) produced significant findings. In none of the cases did charting or recording errors cause the computer system to miss an identification match. The inability of the system to place the correct match on the best matches list was, in these cases, due to lack of data. rather than misuse or misconstruance of the data available.

It became apparent that the most successful use of the system came after experience with the system. It was also apparent that, in addition saving time for the investigators indefatigable computer could indicate conclusions that a human could not easily reach.

This can be much more easily illustrated by citing two instances where the structured decision paths of a computer program was more effective than the multidimensional perception of a human observer.

Example A Twenty three records belonging to service members believed to have perished in an airplane crash were entered into the system. One individual had no information on his dental record except that all four third molars (wisdom teeth) had been removed. The dental investigators were not able to establish an identity for one of the thirteen remains. When the postmortem records were sorted against the database using the CAPMI system, the unmatched postmortem remains was paired with the previously cited individual with the incomplete dental record. The system logic indicated that only one of the twenty three persons believed to be on the plane had an antemortem dental status that could have evolved into a state that matched this remains. This identity match was made independently by other means and confirmed the system choice.

The repetitive back-chaining logic, necessary for this matching is a trivial process for an automated system yet overwhelms the logical capacity of human investigators.

In the second example, an antemortem dental record was reconstructed from anterior-posterior (A-P) skull films and entered into the system. When this record was compared to the data base, the most likely match chosen seemed incorrect. Although the coded information from the antemortem reconstructed record and the postmortem record matched almost perfectly, the postmortem dental films and the antemortem skull films seemed initially to be dissimilar.

The high degree of matching, and the lack of any other close matches in the data base, encouraged further attention and ,after study, the investigators accumulated an overwhelming number of points of similarity. Because of the unusual perspectives of the skull films, the dental structures were not easily recognized as those appearing in the postmortem dental films. The human investigators were not able to reduce what they observed in both the skull films and the postmortem dental films to a common language. Without the assurance by the computer program that this was

the most appropriate match, proper effort may not have been put into this particular match to allow the identity match to be confirmed.

In the first instance the computer system was able to apply a rather simple logical decision chain several hundred times, maintain interim results and then process these results to produce a final result. Because these decision involved the reversal of normal human decision process, each of the human investigators was quickly confused.

In the second instance, the problems the humans had in recognizing the match between the AP skull and the postmortem dental films were due to the inability to make correlations between two dissimilar-similar complex visual representations. When each of these films was described with the set of codes allowed by the decision system, the comparison process was isolated from the vast over-abundance of information available in the films and the matching pair was clearly indicated.

CONCLUSIONS

The laboratory and operational testing of a computer assisted postmortem identification (CAPMI) system has indicated that a computer program which evaluates the data base and provides the most probable matches based on comparison of dental characteristics is a valuable adjunct to the forensic effort. In an actual identification problem, the system reduced the search time for the match to an unknown record from hours to minutes. Beyond the logistic aid, the use of the computer system clarifies certain decisions by forcing the forensic investigators to reduce their perceptions to a certain limited set of codes. This is, in a primitive sense, a true use of 'artificial intelligence'.

Currently, enhancements are being made to the system to allow input from optical mark read forms. This will greatly speed the data input process, the most tedious part of the actual identification problem. The modules of the program which allow for search and sorting by a variety of physical characteristics (other than dental) have been activated and are available for use in the event of another problem. A major test of the data gathering system involving all the personnel at a major US Army post will be concluding in June. This test is evaluating the optical mark

read forms, examiner compliance, administrative procedures, and the effect on routine productivity at dental clinics. This computer assisted identification system is being considered for implementation as part of a electronic dental record system.

References

1. Wolcott JH, Hanson CA, Menzies R, Ballo J, Donohue E, Hooa N. Administrative organization and function during the identification process for mass disasters- Canary Islands crash. Aviat Space Environ Med 1980;51:1030-1033.

2. Cohen M, Schroeder DC, Cecil JC. Computer-assisted forensic identification of military personnel. Milit Med 1983;148:153-156.

3. Lorton, L and W H Langley. Decision-making concepts in forensic identification. J For Sci 1985;31:125-131.

THE ANALYSIS OF SHAPED CHARGE JET FLASH RADIOGRAPHS USING IMAGE PROCESSING TECHNIQUES

*DONALD E. LOVELACE, MR.
S. RICHARD F. SIMS, MR.
U.S. ARMY MISSILE COMMAND
RESEARCH, DEVELOPMENT, AND ENGINEERING CENTER
REDSTONE ARSENAL, ALABAMA 35898-5247

I. Introduction:

In the development and testing of anti-armor warheads, flash x-rays of the shaped charge jet during its formation and penetration are typically used in the performance analysis of specific designs. The parameters usually measured are jet tip velocity and breakup time. With the advent of modern armor and unusual shaped charge delivery modes, other jet penetrator characteristics such as mass distribution and velocity gradient have become important in evaluating performance. In order to determine these characteristics, laborious manual measurements of multi-exposure flash x-rays are required. This paper describes the use of image processing technology to reduce manual involvement and to automate analysis.

II. Shaped Charge Jets

The shaped charge jet consists of a high velocity stretching stream of solid metal (not liquid) projected from a properly detonated explosive shaped charge, figure 1. The shaped charge is detonated in such a way that

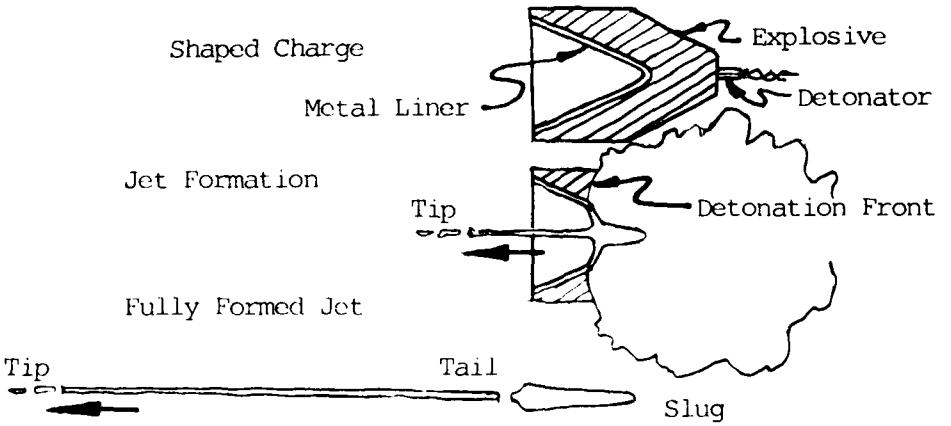

Figure 1 Shaped Charge Jet Formation

the metal lined cavity collapses on its axis at pressures so high that part of the metal liner flows out of the collapsed slug as a jet. Velocities of the jet tip can be as high as 10,000 meters per second and velocities of the tail as low as 1,000 meters per second.

Predicting the ability of a shaped charge jet to penetrate steel armor is relatively simple using a few easily measured characteristics. Jet tip velocity and jet length at breakup can readily be measured from multiple exposure flash radiographs. A typical radiograph of this type is shown at figure 2.

Figure 2. Multiple exposure flash radiograph with images of a jet at three times.

As armor has become more advanced, it has become important to know more about jet penetrators than their length and tip velocity. Measurements of the distribution of mass and velocity from tip to tail are useful in evaluating the jet effectiveness against modern armor. The knowledge of where, along a jet's length, the most energy is concentrated or at what point the velocity drops below a particular level, is very useful.

III. Manual Methods of Jet Characterization

A. Direct Measurement

The only technique for measuring velocities directly from a timed multi-exposure flash radiograph, is to trace a unique feature in a jet's image from one time to another and measure the distance that it has moved. Using this method it is easy to measure the velocity of the jet tip or any other visible feature. In a radiograph of an unbroken jet, however, there are very few obviously unique features along its length. Some other method is needed for determining how far a jet particle moves from one time to another.

B. The Mass Element Method

The method of summing mass increments for jet velocity determination is an alternate to the direct method and provides more information about jet characteristics. This technique requires the measurement of the jet diameter at many points along its length. These data points are then used to calculate the volumes of the resulting conical and cylindrical segments. A segment or mass element can be located in a succeeding jet image by summing mass, beginning at the tip and moving back to the mass increment of interest. The velocity can be determined at virtually any point along the jet. This method is illustrated in figure 3.

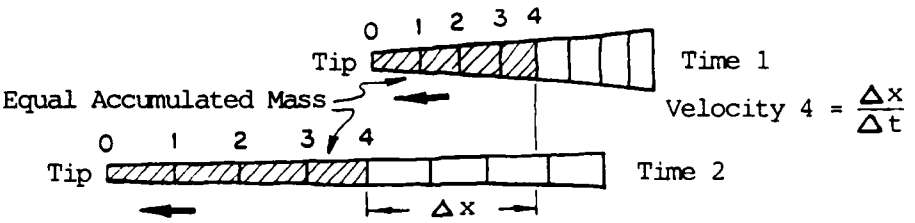

Figure 3. Mass Increment Method

C. Jet Diameter Measurement

In using the mass increment method for determining jet velocity, the calculated mass increment position and subsequent velocity are very sensitive to the accuracy of jet diameter measurement. Because jet mass is calculated incrementally starting at the tip, any error introduced accumulates and has a large effect on velocity. Jet diameter measurement needs, therefore, to be as accurate as possible.

Manual techniques for measuring diameter from jet radiographs are tediously time consuming and subject to large errors. Most of the error results from the fact that the jet image edge is unavoidably "fuzzy". The x-ray source is not a point, as one might expect, but instead has a significant diameter. As shown in figure 4, the diameter of the source, about 5 millimeters, blurrs the edge of the jet image in the film plane. The judgment required in determining the actual jet edges and the tedium of the process make manual measurement of jet diameter inherently inaccurate.

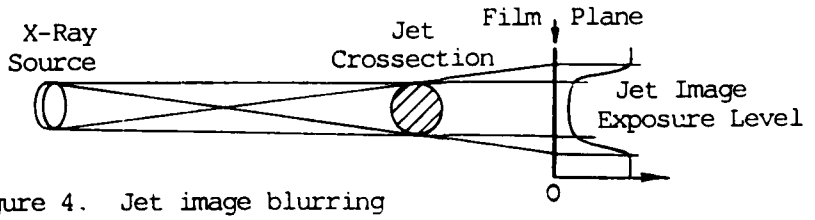

Figure 4. Jet image blurring

IV. Shaped Charge Jet Analysis

A. Automated Analysis Procedure

The procedure for analyzing jet radiographs is derived from image processing techniques previously developed and used in tactical target pattern recognition for missile seeker processing. Detecting blurred or fuzzy edges on low contrast images, although difficult to do manually, is relatively easy to do using these modern techniques. Jet diameters can be automatically measured and recorded from one end to the other of a jet image. The steps of the procedure are as follows:

- Digitize video images of the jet x-ray.
- Expand the gray scale to sharpen edges.
- Determine the image edge.
- Record diameter by counting pixels in an image slice.
- Analyze jet using diameter data and plot results.

B. Image Generation from Radiographs

A jet radiograph is recorded by digitizing each of a set of overlapping snapshot images, figure 5, taken with a high resolution CCD TV camera. The x-ray negative is mounted on a light table so that the camera can scan from end to end of the jet. The digitization produces approximately 522 samples per line of video. Each line of video is perpendicular to the jet image.

After digitization is completed, each image is displayed for cropping and defining its interface with adjacent images interactively.

C. Image Processing

1. Histogram Gray Scale Expansion is the interactive procedure by which the image gray scale is stretched to improve contrast. There are 256 possible values of gray from black (0) to white (255). In a low contrast image only a narrow range of gray values will be used, figure 6a. Expansion of this narrow range brings the background gray value closer to black and the jet gray value closer to white, figure 6b. This process increases the gray scale slope at the edge of the jet making the binary segmentation step more precise and the threshold easier to find, figure 7.

2. Binary Segmentation defines the edge of the jet image. A gray level is selected above which all gray levels will be set to white and below which all gray levels will be set to black. This gray level called the binary threshold, is selected interactively. It can be raised and lowered while watching its effect on the image until an optimum is selected, figure 8.

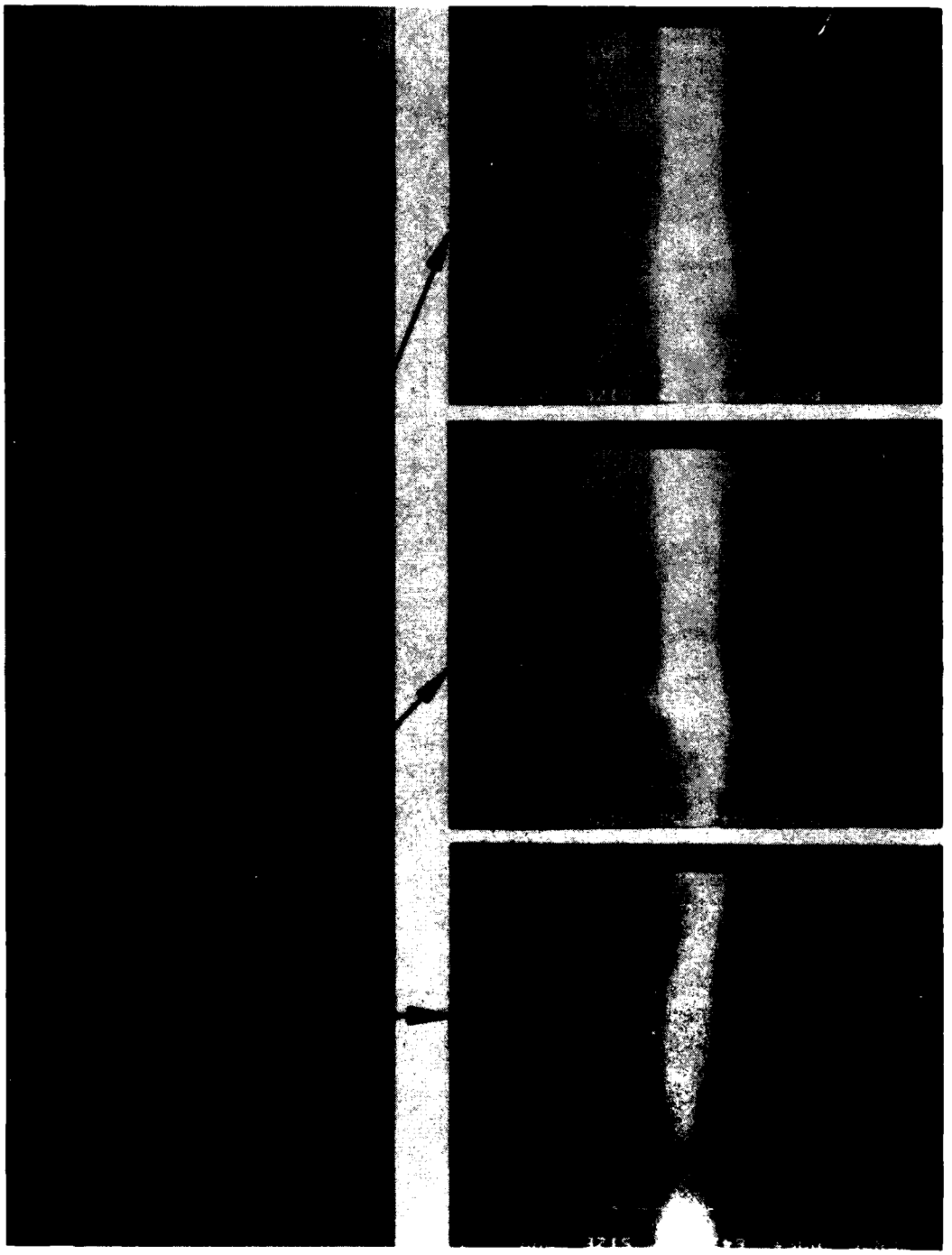

Figure 5. Jet radiograph digitized in overlapping snapshot image frames.

3. Connected Component Generation and Object Selection. The diameter measurement of the jet is made in this stage of the process. If the jet is broken, fragments are selected for measurement. Pixels are counted automatically across the diameter of the jet image in pixel width slices. The number of pixels in a slice and the position of the slice along the jet are recorded. This information forms the data base from which all characteristics of the jet can be calculated.

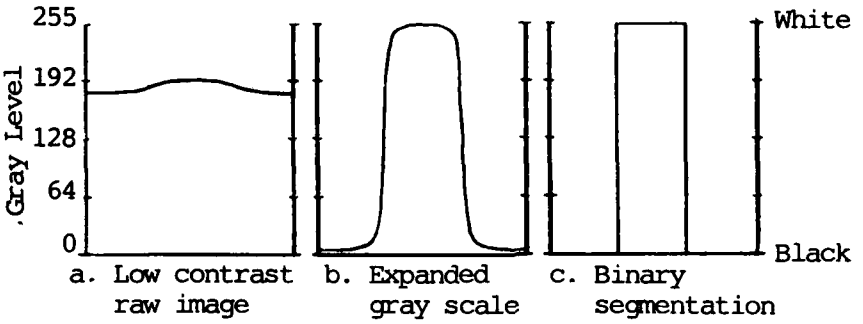

Figure 6. Image Processing

D. Jet Analysis

1. Jet Diameter. Diameters can be plotted directly from the data base. Diameter versus distance from jet tip, for radiographs of a jet at two times are shown in figure 10.

2. Jet Mass. Making the assumption that the jet cross section is circular at each pixel slice, the mass of each slice can be calculated. It is most convenient to plot accumulated mass versus distance from jet tip, figure 11.

3. Mass Increment Position. The position of discreet mass increments can be determined in successive flash x-rays using an adaptation of the Mass Increment Method described earlier. In this case, the pixel width slices of jet mass already calculated are summed to form a mass increment. Center of mass for the increment is calculated and recorded as its position. Mass increment positions can be plotted for each of the jet images in a multi-exposure flash radiograph, figure 12.

4. Velocity Gradient. The difference in relative position of a jet mass element between timed x-ray exposures of the jet constitutes a velocity for that mass element. Velocities can be plotted versus distance from jet tip or versus accumulated mass as shown in figure 13.

Figure 7. Digitized raw images before cropping.

Figure 8. Combined images after histogram gray scale expansion.

Figure 9. Image edge defined by binary segmentation.

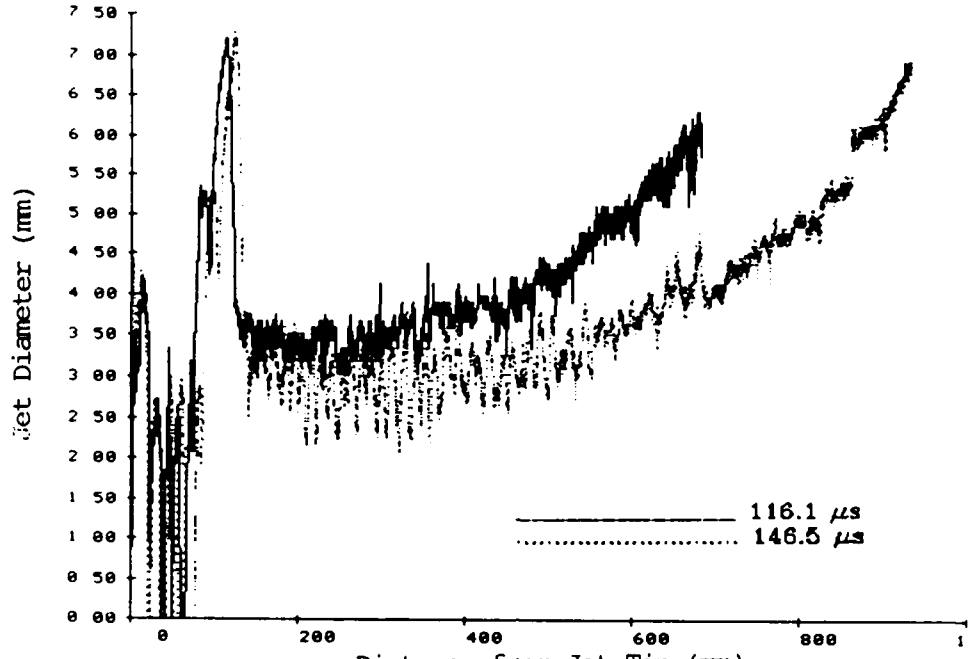

Figure 10. Jet diameter at two times.

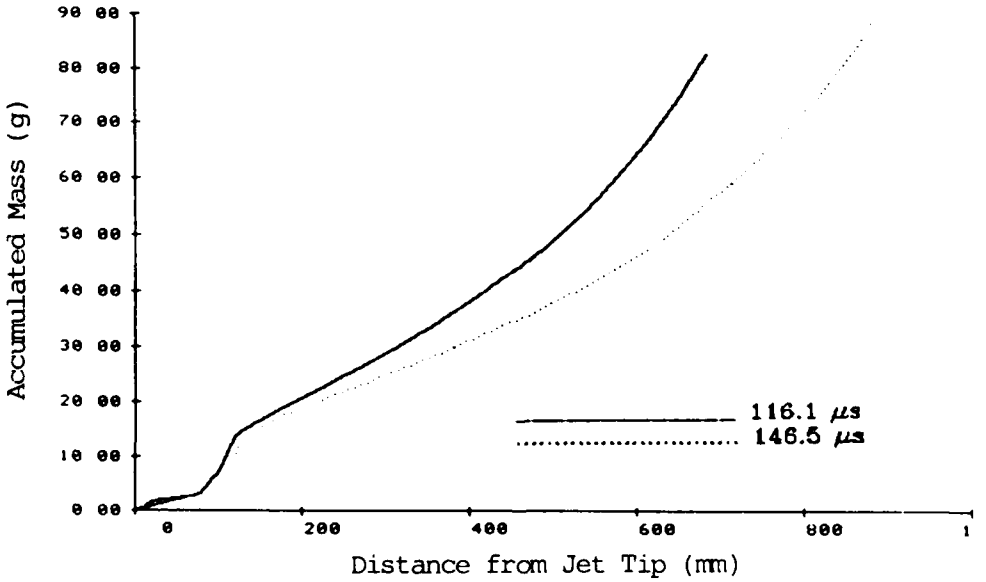

Figure 11. Jet mass distribution at two times.

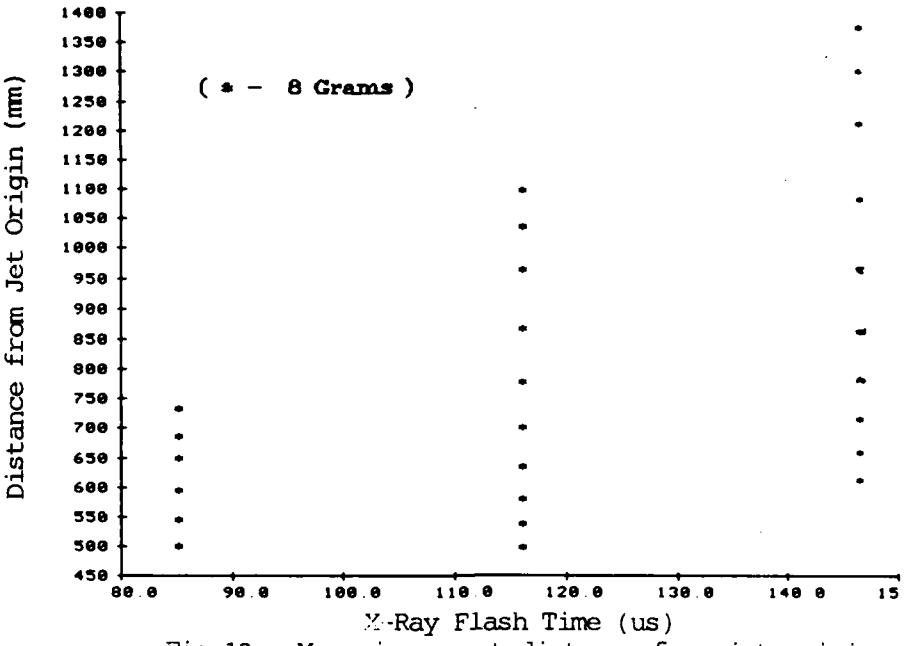

Fig 12. Mass increment distance from jet origin

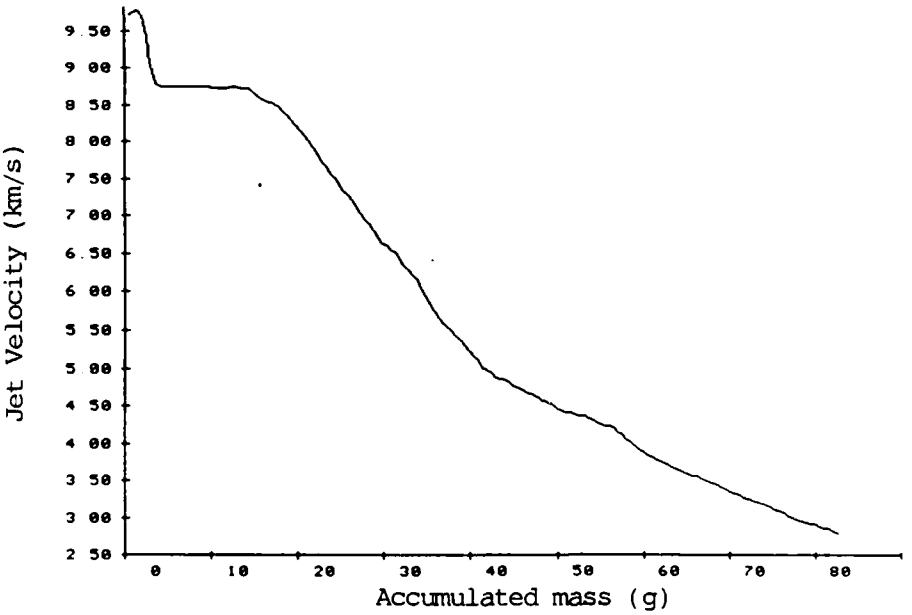

Fig 13. Jet velocity versus accumulated mass.

E. Process Limitations. Several assumptions are made in the current processes that can introduce errors:

1. The counting of pixels across the jet diameter does not allow for concavities which are sometimes present in highly distorted or fragmented jets. This limitation is relatively inconsequential because detailed analysis of bad jets is not often needed.

2. Jet cross sections are assumed to be round at every point along the jet length. For most high performance shaped charges, this is not a significant limitation. Efficient charge performance depends on near absolute symmetry. For highly fragmented or distorted jets, however, error would be large.

3. A constant magnification scale factor is currently used for processing the entire jet length. The magnification factor is constant only as long as the jet trajectory remains in a plane relative to the film cassette. Magnification error caused by a laterally displaced jet can be corrected by measurement of this distance and adjusting the magnification factor appropriately.

4. The selection of jet fragments currently requires the user to select segments that do not overlap laterally. Occasionally overlapping particles that are not part of the penetrator must be masked.

5. There is currently no way to calibrate the jet diameter measurement process. In order to estimate accuracy, a copper rod of known diameter was repeatedly measured from flash x-rays using the automated procedures. The range of error was found to be minus four percent to plus five percent. Future work will include an attempt to position small, cylindrical rods close to the jet in x-ray images to automatically calibrate the diameter measurement.

V. Conclusions

The automated measurement and analysis of shaped charge jet radiographs using image processing techniques allows the determination of mass and velocity distributions in jet penetrators with accuracy previously unattainable.

Analysts evaluating the performance capability of anti-armor warheads against modern armor now have a tool which provides better information than previously possible.

Warhead designers better able to use design prediction hydrocodes to improve shaped charge efficiency by correlating more of the tested jet characteristics with prediction.

Reference:

Sims, R., "The Analysis of Shaped Charge and Explosively Formed Penetrator (EFP) Warhead Jet Flash X-Rays Using Image Processing Techniques, "U.S. Army Missile Command Technical Report RE-85-21, July 1985.

A SMALL SYNTHETIC PEPTIDE BOUND VIA ITS HYDROPHOBIC FOOT TO MENINGOCOCCAL OUTER MEMBRANE PROTEINS BECOMES A HIGHLY IMMUNOGENIC VACCINE(U)

*GEORGE H. LOWELL, LTC, MC, LYNETTE F. SMITH, M.S.,
ROBERT C. SEID, PH.D., WENDELL D. ZOLLINGER, PH.D.
WALTER REED ARMY INSTITUTE OF RESEARCH
WASHINGTON D. C. 20307-5100

THE PROBLEM

The first step in constructing a vaccine to protect against a biologic or chemical hazardous agent is to identify the responsible organism or compound. The second step is to isolate or identify the portion of the agent that, if attacked by the right specific antibodies, will neutralize the entire agent. Most frequently, this portion is located on the outer surface of the agent so that the antibodies can have free access to attach to it. The third step is to immunize animals with that portion (now referred to as an ANTIGEN) to demonstrate that it will induce the desired antibodies. The fourth step is to prepare the antigenic portion for delivery as a vaccine for humans which is both immunogenic (i.e. generates the right antibodies) and safe.

Advances in biotechnology including use of monoclonal antibodies and genetic cloning have enabled the identification of important portions of surface proteins of several pathogenic agents of military importance. These protein portions are PEPTIDES. These peptides are composed of a series of amino acids whose ordered sequence is directly coded by genetic DNA. Such peptides have great vaccine potential since large quantities of peptides can be produced with a high degree of purity either synthetically (by coupling the correct amino acids in sequence) or by cloning the correct genetic information into producer bacteria. Thus, the techniques are now available to proceed efficiently and systematically through the first two steps cited above.

Peptide vaccines have an additional unique advantage. It is perhaps surprising to note that when immunized with a protein, the antibodies induced are predominantly directed against a limited peptide portion of the whole protein and there are many areas of the protein to which no antibodies are made even though they may be readily accessable on the protein's surface (1). The antigens that do elicit antibodies are called

immunodominant and those which do not are called immunorecessive. Nevertheless, when immunized with immunorecessive antigens in the absence of the immunodominant antigens an excellent immune response can be generated in which antibodies are directed against the recessive "poor" antigen and can bind (or neutralize) that recessive antigen even when it is present as a part of the native protein (2). Frequently, immunorecessive antigens are common (also called "conserved") portions of the protein that cross-react among many strains of a family of organisms or compounds. Since peptides can be constructed to be identical to any antigen, recessive or dominant, it is evident that peptide vaccines can be made which can recognize cross-reacting conserved antigens which may not be elicited by immunization with whole proteins due to their immunorecessivity. This is essential in attempting to protect against a family of organisms or agents which have many strains that can cause disease but share recessive common antigens.

Making protein antigens induce antibodies (i.e. immunogenic) in animals, as required for step 3, has previously been well studied and is a relatively straightforward task. Making small peptides immunogenic, however, is more difficult since small peptides are not immunogenic when given in a vaccine alone. This difficulty has been overcome in animal studies by coupling the peptides to carrier proteins and administering the vaccine complex with adjuvants. Thus, the necessary methods for investigating immunogenicity in animals and proceeding through step 3 are also available. The most effective adjuvants used without problems in animals (such as Freund's adjuvant) however, are toxic, pyrogenic or otherwise currently unsuitable for human use. Similarly, the large carrier proteins commonly coupled to peptides for use in animals such as Keyhole Limpet Hemocyanin (KLH) or Bovine Serum Albumin (BSA) are inappropriate components of vaccines for humans since they may induce undesirable allergies to the protein (e.g. to cow proteins) or are simply too toxic.

The major problem impeding the development of small peptide vaccines for human use, therefore, is the lack of a suitable carrier and adjuvant that can safely, efficiently and effectively be complexed to the peptide for use in humans. One carrier protein that has been given to people is tetanus toxoid. There are two significant problems with using tetanus toxoid as a carrier for peptides: 1) Tetanus toxoid can be coupled to peptides only by a chemical reaction which results in a covalent bond. This reaction, however, is inefficient and, due to steric hinderances and a paucity of active sites on the toxoid, relatively few peptide molecules actually complex per molecule of toxoid. This, in turn, necessitates immunization with excessive amounts of tetanus protein in order to deliver enough peptide to be immunogenic. 2) Recent experiments have confirmed that prior immunization with a carrier protein alone results in

suppression of the anti-peptide antibody responses when subsequently immunized with that carrier complexed to the peptide (3). This phenomenon, known as "epitope suppression," is particularly troublesome for a carrier protein such as tetanus toxoid which is universally repeatedly given at various ages to the entire population to protect against tetanus (4). The development of tetanus toxoid as a protein carrier for new peptide vaccines to protect us against militarily important organisms and agents is therefore highly problematic.

THE SOLUTION

The purpose of this study is to demonstrate that by adding a hydrophobic foot to a small synthetic peptide it can then be complexed simply and efficiently to meningococcal outer membrane proteins to become a highly immunogenic vaccine in the absence of any added adjuvants. This system has been developed with an emphasis on using procedures and components which are non-toxic and safe for human use and are readily applicable to large scale commercial vaccine production. Thus, this suggests a practical solution to the problem of the fourth step (described above) in the construction of vaccines that may be used in humans to protect against biologic or chemical hazardous agents of military importance.

MATERIALS, METHODS AND EXPERIMENTAL RATIONALE

The three components of this vaccine system viz. the peptides, the hydrophobic feet (and associated spacer molecules) and the outer membrane proteins are described in order:

The two peptides used i this study are identical to two different conserved antigenic portions (epitopes) of the variable surface glycoprotein of Trypanosoma brucei. These trypanosomes cause Sleeping Sickness among millions in Africa and would result in high morbidity among troops deployed in endemic areas (5). Trypanosomiasis was chosen as the model system for this study since trypanosomes typically change their variable surface glycoprotein coat during the course of infection and thereby escape the immune response of antibodies that are induced by the the surface protein (6). Since these antibodies are directed against the variable non-cross-reacting antigenic portions (epitopes) of the protein, the new variant which mutates from the original strain is not neutralized and multiplies until antibodies are develop against it whereupon the process is repeated over and over. These variable antigens, then, are immunodominant whereas the cross-reacting common antigens (the conserved epitopes) are immunorecessive. Since the amino

acid sequence of the conserved regions of these proteins has been described (7), one is virtually obligated to attempt to make a peptide vaccine from these conserved regions. It is not yet known exactly which conserved region (if any) is accessible on the outer surface of the organism to allow antibody binding and neutralization of the trypanosome and therefore the two peptides chosen for this study may not afford protection. The selection of the best peptide for protection is currently under active investigation by other researchers using hybridoma technology. Nevertheless, initial studies have indicated that antibodies to the peptides chosen will bind to the whole trypanosome and that further binding, neutralization and protection studies using live trypanosomes are warranted. The mission and purpose of this study, however, is independant of those studies since the system we have developed is emminantly applicable to virtually any peptide.

The two peptides used represent two types of peptides considered important for generating an immune response. The first, PEPTIDE G, is a pentadecapeptide (15 amino acids) with the following amino acid sequence:

Tyr-Gly-Gly-Gly-Cys-Thr-Gln-Ile-Thr-Glu-Pro-Thr-Ala-Cys-Asn

This peptide is hydrophilic, negatively charged and constrained by an internal disulphide loop which joins the two Cysteines (underlined in the sequence) in a cyclic loop. In the native proteins, cysteines also form disulphide loops and this constraint on the structure of a peptide may be important in keeping the peptide in the same configuration that it has in the native protein. It has been suggested that such cyclic loops are important for peptide immunogenicity (8).

Some investigators, however, maintain that it is important for the peptide to be free and unconstrained by internal loops in order to allow the peptide to acquire a multitude of configurations (2)(9). The second peptide used, therefore, PEPTIDE M, is an undecapeptide (11 amino acids), uncharged, less hydrophilic and has the following sequence:

Tyr-Gly-Val-Pro-Val-Ala-Gln-Thr-Gln-Thr-Gly

The initial Tyrosine of PEPTIDE G and the initial Tyrosine-Glycine of PEPTIDE M were added to the native peptide sequence in order to serve as radioactive markers and spacers between the peptide and the hydrophobic foot. In addition, PEPTIDE M was tested with and without the amino acid Cysteine added to the left side of the peptide. This cysteine addition resulted in dimerization of PEPTIDE M so that two peptide molecules (and their hydrophobic feet, when present) were joined. The peptides were synthesized by solid phase Merrifield synthesis technology and purified according to our specifications by Peninsula Labs, Belmont, CA.

Two types of hydrophobic "feet" were used: Either 1) LAURIC ACID, a 12 carbon fatty acid or 2) a PENTAPEPTIDE (5 hydrophobic amino acids) with the sequence Phe-Leu-Leu-Ala-Val. The foot was added (by Peninsula Labs) to the left side (the amino terminus) of the peptide. The LAURIC ACID foot was added by an EDAC reaction after the peptide was synthesized whereas the PENTAPEPTIDE foot was synthesized sequentially as a continuous part of the peptide antigen.

Meningococcal Outer Membrane Proteins were chosen to be carrier proteins for three reasons. 1) They can be extracted and isolated in great quantities from cultures of meningococci, 2) We and others have safely and effectively given them to many people as part of meningococcal vaccines (10)(11), and 3) We have found that these proteins are are B-cell mitogens and polyclonal activators for human as well as murine lymphocytes (12). We hypothesized, therefore, that these proteins may have special "carrier + adjuvant" activity by targeting the peptides they carry to B-lymphocytes thereby enhancing antigen presentation to T-lymphocytes. Since B-lymphocytes both produce antibody and present and process antigen for T-lymphpocytes, a protein that activates B-cells, it was reasoned, would be a superior carrier.

The hydrophobic feet were covalently added to the peptides in order to solve the problem of how to complex the peptides to the meningococcal Outer Membrane Proteins in a simple and efficient manner. These membrane proteins are exceedingly hydrophobic. They are not soluble in water; they may be solubilized either by detergent or by complexing them to a substance which, like polysaccharides, has a hydrophilic portion that can interact with water. On the meningococcus, they are naturally hydrophobically complexed to membrane lipids including lipopolysaccharide (LPS). We have previously hydrophobically complexed these types of proteins to meningococcal polysaccharides by ethanol co-precipitation to make meningococcal vaccines (10). Those complexes were possible only when a small lipid was present on the polysaccharides. Since small peptides would not precipitate in ethanol even with the hydrophobic foo attached, a new method had to be devised to effect protein-foot-peptide binding.

A simple solution was found to this problem: the proteins and peptides (with their added feet) were solublized in detergent (1% Empigen BB in a saline buffer), placed into a dialysis bag with a molecular weight cutoff of 1000 daltons so that the proteins and the peptides would remain inside the bag while the detergent dialyzed away over 7-10 days. This gradual removal of the detergent allowed the hydrophobic parts of the peptide to insert into the membrane proteins leaving the hydrophilic trypanosomal peptide ends freely accessable external to the proteins to

be recognized by the immune system. Equal amounts by weight of protein and peptide were combined in this process. Since the molecular weight of the proteins are ca. 40,000 daltons, and that of the peptides was 1300 to 1800 daltons, at least 12 to 20 molecules of peptide (allowing for some loss of the peptide through the dialysis bag) complexed with each protein molecule. Furthermore, the membrane proteins themselves are not single molecules but are actually membrane vesicles which have been partially fragmented during preparation. It is estimated that ca. 50-100 protein molecules are associated in each fragment so that the immune system actually is presented with many peptide molecules associated with a multifaceted protein carrier.

Outer membrane complex vesicles were extracted from whole bacteria by suspending the cells in an aqueous buffer, heating at 56° C for 30 min, and then mixing vigorously for 3 minutes in a blender. These outer membrane vesicles (which are naturally approximately equal in size to whole viruses) were isolated by differential centrifugation and washed twice in water or buffer. The outer membrane proteins were separated from the other outer membrane constituents by dissolving the membrane complex in buffer containing the zwitterionic detergent Empigen BB and precipitating the proteins with ammonium sulfate in the presence of the detergent. The precipitated proteins were collected by centrifugation and redissolved in the detergent solution. The ammonium sulfate precipitation was repeated twice and the final solution then dialyzed against the detergent solution to remove residual ammonium sulfate. The resulting solution which contained less than 1% lipopolysaccharide, capsular polysaccharide, and nucleic acid was stored at -20° C.

In this study, we have begun to call the Outer Membrane Proteins "PROTEOSOMES" since, like liposomes, they are hydrophobic, membranous and vesicular in nature although the vesicles are partially disrupted in the Empigen preparation. Unlike liposomes which have also been used as peptide vehicles, "proteosomes" are composed of immunogenic proteins and can therefore serve as "carrier proteins" to provide stimulation of T-cells for an anamnestic IgG immune response according to classical immunologic theory.

Normal adult BALB/C mice were used for most of this study. Some experiments, as noted, used C3H/HeJ mice which are non responsive to the mitogenic and adjuvant effects of bacterial lipopolysaccharide (LPS). These mice were used to confirm the effects of the membrane proteins since the protein preparations contained <1% LPS. We note that although LPS is pyrogenic and toxic to humans, meningococcal protein vaccines containing 10-fold more LPS have already been safely given to people without untoward side effects. It is precisely because of the safety of these protein preparations that they were chosen as carriers for the

peptide vaccines. Mice were immunized ip with 40 ug of peptide and boosted with the same amount 3 and 7 weeks later. No adjuvants were given except as noted. When ALUM was used, it was a preparation of aluminum potassium sulphate or aluminum hydroxide which has been safely used in humans with the tetanus toxoid and other vaccines. Murine sera were tested in an enzyme-linked immunosorbant assay (ELISA) which has been previously widely described. The detecting antigen in the ELISA was either PEPTIDE G or PEPTIDE M alone or linked to BSA (as a carrier to more efficiently help the peptide stick to the test plate). Control tests were run using a heterologous trypanosome peptide (alone or hooked to BSA) or BSA alone as the detecting antigen in order to insure that the results reported reflected specific anti-PEPTIDE G (or anti-PEPTIDE M) antibodies and not non-specific sticking of antibodies to the test plate.

RESULTS

The ability of outer membrane protein (OMP) PROTEOSOMES to confer immunogenicity upon PEPTIDE G when a LAURIC ACID foot is attached to the peptide is clearly demonstrated in TABLE 1. The CONTROL groups, which consisted of 4-8 mice per group, had no detectable IgG or IgM antibodies directed against PEPTIDE G. Thus, immunizing with PEPTIDE G alone (group 1), PEPTIDE G with its LAURIC ACID foot attached (group 2) or PEPTIDE G with Outer Membrane Protein PROTEOSOMES (group 3) was not able to elicit any antibody response. Similarly, PEPTIDE G given with either Freund's adjuvant, ALUM, muramyl dipeptide (MDP) or steroyl-MDP (group 4 -- each of these adjuvant control groups consisted of 4-5 mice per group) was also totally ineffective as was immunizing with PEPTIDE G with its LAURIC ACID foot attached in the presence of ALUM (group 5). MDP was used as an adjuvant control because it has been widely reported that MDP is the major active ingredient in Freund's adjuvant and, although it is pyrogenic, may (via one of its derivatives) have human vaccine potential. As, noted, however, it is inefective with peptides alone as is Freund's adjuvant.

In marked contrast, PEPTIDE G with its LAURIC ACID foot complexed to Outer Membrane Protein PROTEOSOMES (group 7) was a highly immunogenic vaccine eliciting specific anti-PEPTIDE G IgG serum antibody titers over 1:200,000 (i.e. these sera, even when diluted 204,800-fold, contained specific antibody that was significantly above control sera diluted only 50-fold). The addition of ALUM to this preparation (group 8) did not significantly enhance this immune response. These high antibody responses were predominantly of the IgG class as would be expected using a protein carrier like Outer Membrane Protein PROTEOSOMES. Similarly, the anamnestic response seen after the booster immunization is indicative of good T-cell help and recognition of the peptide antigen. Indeed,

TABLE 1: Anti-PEPTIDE G antibody titers in sera of BALB/C mice after 1, 2 & 3 immunizations with PEPTIDE G and LAURIC ACID (a hydrophobic fatty acid foot) plus meningococcal outer membrane protein PROTEOSOMES given with & without ALUM.

VACCINE GROUPS (see * below)	ANTIBODY CLASS	ANTI-PEPTIDE G RECIPROCAL SERUM TITERS AFTER IMMUNIZATION # 1 (primary)	# 2 (boost)	# 3 (boost)
1 - 5: CONTROLS: (see ** below)	IgG	<50	<50	<50
	IgM	<50	<50	<50
6. PEPTIDE G + LAURIC ACID ft + OMP PROTEOSOMES:	IgG	400	204,800	204,800
	IgM	<50	800	1,600
7. PEPTIDE G + LAURIC ACID ft + OMP PROTEOSOMES + ALUM:	IgG	800	102,400	204,800
	IgM	50	200	400
8. PEPTIDE G + KLH: (Keyhole Limpet Hemocyanin)	IgG	1,600	25,600	51,200
	IgM	400	1,600	3,200

* Sera obtained from groups of 5-8 mice 2-3 weeks after each immunization were tested in an ELISA for anti-PEPTIDE G IgG & IgM. Titers shown are the highest serum dilutions with ELISA values >0.1 & >twice pre-vaccine sera diluted 1:50.

** CONTROL groups: PEPTIDE G given 1) alone, 2) + LAURIC ACID, 3) + OMP PROTEOSOMES, 4) + ADJUVANT [Freund's Adjuvant, ALUM or muramyl dipeptide (MDP)] or 5) + LAURIC ACID + ADJUVANT.

PEPTIDE G covalently linked to Keyhole Limpet Hemocyanin (KLH) did not have a stronger booster effect than the LAURIC ACID ft-PROTEOSOME vaccine and provided no advantage overall.

The effect of replacing the LAURIC ACID hydrophobic foot with the hydrophobic PENTAPEPTIDE Phe-Leu-Leu-Ala-Val is shown in TABLE 2. In addition to the control groups mentioned in TABLE 1, PEPTIDE G with the Phe-Leu-Leu-Ala-Val foot either with or without added ALUM was totally negative as a vaccine (groups 9 & 10). Once again, however, PEPTIDE G complexed via this Phe-Leu-Leu-Ala-Val foot to Outer Membrane Protein PROTEOSOMES resulted in a high titered specific antibody response that was predominantly IgG and was anamnestically enhanced by booster immunizations (group 11). In this instance, ALUM enhanced the primary antibody response and the response after one boost. However, ALUM did not result in more antibody after 2 boosts compared to this vaccine without ALUM (group 12).

The strength of this immune response is emphasized by the fact that 5 months post-immunization the anti PEPTIDE G IgG antibody titers in these mice were still 1:100,000 to 1:200,000.

The ability of the PROTEOSOME vaccines to induce anti-peptide IgG antibodies even in C3H/HeJ mice which are resistant to the adjuvant effects of lipopolysaccharide is shown in TABLE 3. PEPTIDE G bound to Outer Membrane Protein PROTEOSOMES via its LAURIC ACID foot (group 16) generated titers of 1:51,200 after three immunizations. Indeed, the PROTEOSOME-pentapeptide foot vaccine (group 17) displayed the highest titers seen (1:409,600) thereby effectively ruling out any contribution of the <1% contaminating LPS in the Outer Membrane Protein preparations toward the vaccines's immunogenicity. C3H/HeJ and BALB/C mice also responded similarly following immunization with the negative controls (groups 13-15) and the KLH-PEPTIDE G vaccine (group 18).

The specificity of the anti-PEPTIDE G antibodies detected in the ELISA was confirmed in a series of inhibition experiments in which all the antibody detected was inhibited by pre-incubating the sera for one hour with the homologous antigen (PEPTIDE G). This caused the specific anti-PEPTIDE M antibodies present in the sera to bind to the free inhibiting antigen so that it was not available to bind to the PEPTIDE G antigen fixed to the test ELISA plate. In contrast, no inhibition was detected by pre-incubating with a heterologous trypanosome peptide even when 1600 ug/ml of the heterologous peptide was used. The 50% inhibition mark was obtained with a pre-incubation concentration of only 5 ug/ml of pure PEPTIDE G while PEPTIDE G linked to BSA inhibited 50% with as little as 3 ug/ml.

The results obtained using the second peptide, PEPTIDE M, are shown

TABLE 2: 'Anti-PEPTIDE G antibody titers in sera of BALB/C mice after 1, 2 & 3 immunizations with PEPTIDE G plus Phe-Leu-Leu-Ala-Val (a hydrophobic pentapeptide foot) plus Outer Membrane Protein PROTEOSOMES with & without ALUM

VACCINE GROUPS (see * below)	ANTIBODY CLASS	ANTI-PEPTIDE G RECIPROCAL SERUM TITERS AFTER IMMUNIZATION # 1 (primary)	# 2 (boost)	# 3 (boost)
9 & 10 : CONTROLS: (see ** below)	IgG	<50	<50	<50
	IgM	<50	<50	<50
11. PEPTIDE G + Phe-Leu-Leu-Ala-Val + OMP PROTEOSOMES:				
	IgG	400	12,800	102,400
	IgM	100	1,600	6,400
12. PEPTIDE G + Phe-Leu-Leu-Ala-Val + OMP PROTEOSOMES + ALUM:				
	IgG	6,400	204,800	102,400
	IgM	800	6,400	6,400

* Sera obtained from groups of 5-8 mice 2-4 weeks after each immunization were tested in an ELISA for anti-PEPTIDE G IgG & IgM. Titers shown represent serum dilutions with ELISA o.d. values >0.1 & >twice that of pre-vaccine sera diluted 1:50.

** CONTROL groups: In addition to the CONTROL groups cited in TABLE 1, mice were also immunized with PEPTIDE G + Phe-Leu-Leu-Ala-Val without adjuvant (Vaccine Group 9) and PEPTIDE G + Phe-Leu-Leu-Ala-Val + ALUM (Vaccine Group 10).

TABLE 3: Anti-PEPTIDE G IgG antibodies in sera of C3H/HeJ LPS-hyporesponsive mice after 1, 2 & 3 immunizations with PEPTIDE G plus Outer Membrane Protein PROTEOSOMES plus either LAURIC ACID (the hydrophobic fatty acid foot) or Phe-Leu-Leu-Ala-Val (the hydrophobic pentapeptide foot).

VACCINE GROUPS (see * below)	ANTI-PEPTIDE G RECIPROCAL SERUM TITERS OF IgG ANTIBODIES AFTER IMMUNIZATION # 1 (primary)	# 2 (boost)	# 3 (boost)
13 - 15: CONTROLS: (see ** below)	<50	<50	<50
16. PEPTIDE G + LAURIC ACID + OMP PROTEOSOMES:	200	6,400	51,200
17. PEPTIDE G + Phe-Leu-Leu-Ala-Val + OMP PROTEOSOMES:	100	102,400	409,600
18. PEPTIDE G + KLH (Keyhole Limpet Hemocyanin):	6,400	51,200	102,400

* Sera obtained from groups of 6 mice 2-4 weeks after each immunization were tested in an ELISA for anti-PEPTIDE G IgG. Titers shown represent the highest serum dilution with ELISA values >0.1 & >twice that of pre-vaccine sera diluted 1:50.

** CONTROL groups: 13) PEPTIDE G alone, 14) PEPTIDE G + LAURIC ACID & 15) PEPTIDE G + Phe-Leu-Leu-Ala-Val

in TABLE 4. As noted in the MATERIALS AND METHODS section, each of the variables of PEPTIDE M was used with and without a Cysteine added to its amino terminal (the left side of the peptide) resulting in dimerization of the peptide. The rationale for adding the Cysteine to the left side of PEPTIDE M between the trypanosome epitope (antigenic portion) and the LAURIC ACID hydrophobic foot was three-fold: 1) Insertion into the Outer Membrane Protein PROTEOSOMES may be more efficient or stronger since the dimerized peptide with the Cysteine has two feet with which to bind to the PROTEOSOMES; 2) Interaction of the peptide with immune recognition lymphocytes may be more effective if following dimerization by the Cysteine, the two hydrophobic feet bind to each other and then complex with the PROTEOSOMES. This may result in twice as many peptides bound to the protein since the two hydrophobic feet when joined may occupy a single PROTEOSOME binding site which otherwise would bind only one peptide; 3) The dimerized peptide epitopes may interact with each other to form a more stable configuration for easier recognition by lymphocytes. These possibilities did not exist with PEPTIDE G since it contained two Cysteines within its trypanosome epitope and was allowed to form an internal loop so that dimerization or polymerization could not occur.

Whatever the reason, it is clear from TABLE 4 that the Cysteine added to PEPTIDE M was of critical importance. Specific anti-PEPTIDE M IgG antibody titers in mice immunized with PEPTIDE M with its LAURIC ACID foot and bound to Outer Membrane Protein PROTEOSOMES were 1:400, 1:102,400 and 1:409,600 after 1, 2 and 3 immunizations respectively (group 26). In contrast, the PEPTIDE M-LAURIC ACID ft-PROTEOSOME vaccine without the Cysteine never elicited titers >1:200 (group 24). Once again, the role of the PROTEOSOMES is emphasized as the PEPTIDE M-LAURIC ACID foot vaccines were virtually ineffective without the PROTEOSOMES even when the Cysteine was present (groups 23 & 25). Similarly, PEPTIDE M given with Freund's complete adjuvant did not induce any detectable antibodies whether or not the Cysteine was present (CONTROL groups 19 - 22). Titers induced by PEPTIDE M with Cysteine covalently linked at its amino terminus to KLH were 1:6400 and 1:102,400 after two and three immunizations respectively (group 27).

CONCLUSIONS AND SIGNIFICANCE

The data presented in this paper clearly demonstrate that:

1) Small synthetic peptides (with at least 11-15 amino acids) can become highly immunogenic vaccines by adding a hydrophobic foot to their amino terminus and then hydrophobically complexing it to Outer Membrane Protein PROTEOSOMES.

2) The peptides may be either cyclized in an internal disulphide

TABLE 4: Anti-PEPTIDE M IgG antibodies in sera of BALB/C mice after 1, 2 & 3 immunizations with PEPTIDE M plus LAURIC ACID (the hydrophobic fatty acid foot) and Outer Membrane Protein PROTEOSOMES with & without Cysteine.

VACCINE GROUPS (see * below)	RECIPROCAL SERUM TITERS OF ANTI-PEPTIDE M IgG ANTIBODIES AFTER IMMUNIZATION # 1 (primary)	# 2 (boost)	# 3 (boost)
19 - 22: CONTROLS: (see ** below)	<50	<50	<50
23. PEPTIDE M + LAURIC ACID:	<50	50	50
24. PEPTIDE M + LAURIC ACID + OMP PROTEOSOMES:	<50	200	100
25. PEPTIDE M + Cysteine + LAURIC ACID:	<50	<50	100
26. PEPTIDE M + Cysteine + LAURIC ACID + OMP PROTEOSOMES:	400	102,400	409,600
27. PEPTIDE M + KLH:	50	6,400	102,400

* Sera obtained from groups of 6 mice 2-4 weeks after each immunization were tested in an ELISA for anti-PEPTIDE M IgG. Titers shown represent the highest serum dilution with ELISA values >0.1 & >twice that of pre-vaccine sera diluted 1:50.

** CONTROL groups: 19) PEPTIDE M alone, 20) PEPTIDE M + Cys, 21) PEPTIDE M Freund's & 22) PEPTIDE M + Cysteine + Freund's.

loop formed by including two Cysteines in its sequence or it may be non-cyclic if it is dimerized by placing a single Cysteine at its amino terminus. This Cysteine may allow "two-foot" binding and insertion of the dimerized foot into the PROTEOSOMES and "two-headed" presentation of the dimerized peptide antigen to the antigen recognition leukocytes.

3) The hydrophobic "foot" can consist of either the fatty acid, LAURIC ACID or the PENTAPEPTIDE Phe-Leu-Leu-Ala-Val.

4) The PROTEOSOMES can consist of Outer Membrane Proteins extracted from meningococci using methods we have previously described for the preparation of the meningococcal vaccines for human use.

5) The specific anti-peptide antibodies generated by this system are particularly desirable since they are of the IgG class, anamnestically reach exceedingly high titers and can be long-lasting.

6) Although no other adjuvants are necessary in order to attain peak antibody levels, ALUM can enhance the primary or early secondary immune response when more rapid generation of antibodies are required.

The advantages of this immunopotentiating system compared to using conventional proteins or peptides covalently-linked to carrier proteins and adjuvants are:

1) At least 3 - 5 fold more peptide molecules can bind hydrophobically to PROTEOSOMES than can be linked covalently to tetanus toxoid thus avoiding excessive administration of carrier protein.

2) Since 18 distinct serotypes of meningococcal outer membrane proteins have been identified (many of which are rarely found in nature), the problem of epitope suppression of the induction of anti-peptide antibodies which occurs subsequent to primary immunization with tetanus toxoid alone can be avoided.

3) Hydrophobic complexing occurs via a simple one-step dialysis procedure after mixing the components in a detergent buffer.

4) When the PENTAPEPTIDE foot Phe-Leu-Leu-Ala-Val is used, it can be synthesized as a part of the solid phase synthesis of the desired peptide epitope without additional covalent linking procedures.

5) Synthesis of pure peptides, addition of the hydrophobic foot and extracting the PROTEOSOMES and complexing them to the peptides can all be readily accomplished using current technology and standard good laboratory procedures for the production of large scale lots of vaccine.

6) Freund's adjuvant, muramyl dipeptide, lipopolysaccharide and other experimental or potentially toxic or pyrogenic adjuvants or vehicles are not necessary since the major components of this immunopotentiating system have already been used safely and effectively in thousands of people.

7) Conserved, common peptides which cross-react among many strains of organisms or compounds can be selected for inclusion in peptide vaccines whether or not antibodies are induced against those peptide antigens when they are presented as a part of the native protein. i.e.

immunorecessive antigens can be made into highly immunogenic vaccines when isolated from the immunodominant antigens of the native protein.

We suggest that this method for making peptides immunogenic may have wide applicability in develping vaccines against a variety of pathogenic microorganisms, toxins or hazardous chemical agents of particular interest to the military since hydrophobic feet and cysteines can be readily attached to many potentially useful epitopes or compounds. We propose that multi-disease vaccines should be distinctly feasible since several peptide-foot-PROTEOSOME mixtures may be either given together or simultaneously complexed. The sole criterion for inclusion in this type of vaccine should be that antibodies directed against the antigen are effective since virtually any antigen should be able to become a part of a highly immunogenic PROTEOSOME vaccine.

BIBLIOGRAPHY

1. D. C. Benjamin. J. A. Berzofsky, I. J. East, F. R. N. Gurd, C. Hannum, S. L. Leach, E. Margoliash, J. G. Michael, E. M. Prager, M. Reichlin, E. E. Sercarz, S. J. Smith-Gill, P. E. Todd and A. C. Wilson. Annu. Rev. Immunol. 2:67 (1984).

2. N. Green, H. Alexander, A. Olson, S. Alexander, T. M. Shinnick, J. G. Sutcliffe and R. A. Lerner. Cell 28:477 (1982).

3. L. A. Herzenberg, T. Tokuhisa and L. A. Herzenberg. Ann. Rev. Immunol. 1:609 (1983).

4. M. Schutze, C. Leclerc, M. jolivet, F. Audibert and L. Chedid. J. Immunol. 135:2319 (1985).

5. P. de Raadt and J. R. Seed. In: Parasitic Protozoa, Vol. 1 (ed. J. P. Kreier) p. 175 (Academic, New York, 1977).

6. P. J. Bridgen, G. A. M. Cross and J. Bridgen. Nature 263:613 (1976).

7. A. C. Rice-Ficht, K. K. Chen and J. E. Donelson. Nature 294:53 (1981).

8. R. Arnon, E. Maron, M. Sela and C. Anfinsen. Proc. Nat. Acad. Sci. 68:1450 (1971)

9. J. A. Berzofsky. Science 229:932 (1985).

10. W. D. Zollinger, J. Boslego, E. E. Moran, B. Brandt, H. Collins, R. Mandrell, P. Altieri and S. Berman. In: Bacterial Vaccines Symposium, (ed. J. B. Robbins et al.) p. 186 (NIH, 1984).

11. C. E. Frasch. WHO Bull. (1985)

12. G. H. Lowell, L. F. Smith and W. D. Zollinger. ICAAC 21:691 (1981)

AUTOMATED SCREENING OF RECONNAISSANCE IMAGERY (U)

GEORGE E. LUKES
U.S. ARMY ENGINEER TOPOGRAPHIC LABORATORIES
FORT BELVOIR, VIRGINIA 22060-5546

SIGNIFICANCE OF AUTOMATED SCREENING

Automated analysis of remotely sensed imagery represents an elusive goal that has been pursued by many for two decades. The motivation for extensive research activity in both the military and civil sectors is obvious. Since World War II, there has been tremendous progress in the development of diverse image acquisition systems now flown on a variety of airborne and spaceborne platforms. The civil National High Altitude (aerial photography) Program and the National (radar) Mapping Program managed by the U.S. Geological Survey and the NASA Lunar Mapping, Landsat, Shuttle Imaging Radar and Large Format Camera Programs provide good illustrations of the diversity and capabilities of modern mapping and reconnaissance systems. Simply stated, considerable technological success in fielding image acquisition systems has led to an abundance of image data which far surpasses existing or planned image exploitation capabilities in both the civil and military sectors.

This problem has grown dramatically with the successful development of electronic imaging systems with capabilities to transmit image data in real-time to ground receiving stations. Unclassified meteorological and earth resources satellite systems, for example, operate in the visible, near-infrared, thermal-infrared and microwave regions of the spectrum, often as multichannel, multispectral imaging systems. Such systems create new opportunities for near-real-time image exploitation. These systems have also increased the volume of acquired imagery dramatically; moreover, the perishability of much of this data introduces serious time constraints which add another dimension to the image exploitation dilemma.

In almost all significant problem domains, human image interpretation techniques currently represent the state-of-the-art for extracting useful information from image data. Given the growing abundance of image data, however, few have advocated significant expansion of existing manual image

interpretation staffs. On the other hand, the emergence of the digital computer led to significant investments in earth resources, mapping and military reconnaissance research programs in pursuit of automated image interpretation capabilities. After twenty years of research activity, the results of these efforts can be characterized as occasionally demonstrating partial success in limited problem domains under restricted conditions. It is the premise of this paper that automated image interpretation research has been driven by ambitious objectives that have consistently underestimated the difficulty of the problem; further most efforts have emphasized the extension of fragile methods to large volumes of diverse image data that is both highly variable and complex. Clearly, new approaches are required.

An alternative strategy is to pursue opportunities to enhance the productivity of human image interpretation specialists. One approach, the development of computer-assisted interpretation techniques to aid the image analyst directly, represents a significant objective of the research and development program at USAETL in support of the Field Army and the Defense Mapping Agency (8). A second approach is to pursue the development of automated techniques with limited goals to reduce or prioritize the volume of imagery presented to the human analyst. This process is termed automated screening.

Ideally, an automated image screening process tailored to a specific application would detect and rank all significant components in a set of imagery for subsequent analysis by a domain specialist. The value of the concept is that far less capable performance can be of considerable benefit. An automated screening process that would reliably eliminate some significant fraction of the image inventory from further analysis would have immediate and profound operational impact. This is a non-trivial objective, but one that is far less demanding than the goal to fully automate the image interpretation process which has dominated past efforts.

The sections that follow introduce two well-known approaches to the automated screening problem, image-to-image comparison and statistical pattern recognition, and suggest inherent limitations in each technique as applied to reconnaissance imagery. Opportunities to simplify the problem based on exploitation of digital terrain and intelligence data will then be introduced. Ongoing research to explore these opportunities emphasizing the concept of map-to-image correspondence and explicit representation of map, terrain, sensor and mission knowledge will be presented. General trends relevant to this problem will be reviewed and selected management issues will be highlighted.

TYPICAL APPROACHES TO IMAGE SCREENING

Research in automated screening has been dominated by approaches grounded in image processing and statistical pattern recognition based on techniques that have been successfully applied to other, less demanding tasks. Both share the characteristic and limitation of operating on two-dimensional image data without considering the inherent three-dimensional geometry of the scene and the imaging geometry of the sensor.

Image-to-Image Comparison

The well-known image processing approach to automated image screening is change detection based on direct comparison of a new image with a previously acquired reference image. The assumption is that precise registration of two digital images, picture element (pixel) for picture element, will permit the simple substraction of one image from the other to create a new image where only the changes are evident.

Considerable effort has been directed towards the development of effective image registration techniques (2,3). Although computationally intensive, these techniques are well-suited for implementation on special-purpose hardware or parallel processors. Good performance has been demonstrated as long as the inherent two-dimensional image assumptions are not stressed; this is the case if both images are obtained by the same sensor from the same approximate position and orientation such as Landsat multispectral imagery, or in the special case of flat terrain. In general, military reconnaissance and mapping applications are far more demanding where the analysis of diverse imagery acquired by many different sensors operating from a variety of platforms with a wide range of viewpoints is the norm.

Under such conditions, obtaining precise correspondence between two dissimilar digital images is difficult at best. Modest errors in geometric registration generate many "false alarms" which degrade performance and lead to requirements for considerable post-processing. Even in ideal cases, the approach is highly vulnerable to temporal variability. Natural changes in scene illumination, soil moisture, snow cover or natural vegetation state are detected which are often irrelevant to specific interpretation tasks.

Statistical Pattern Recognition

Application of statistical pattern recognition techniques to image data is also well-known (4,14) and extensively investigated. A problem-specific feature extraction process is required to represent each picture element in an image by a set of measurements, often multispectral or

intensity/texture measures, as a multi-dimensional feature vector. In some mathematical fashion, the multi-dimensional feature space is partitioned to uniquely represent the set of classes to be identified. Any unknown feature vector can be assigned to the class corresponding to its position in feature space.

Statistical pattern recognition approaches have proven to be very useful in applied tasks where a stable, well-behaved feature space can be established and effectively partitioned. Considerable success has been demonstrated in some highly constrained two-dimensional industrial inspection problems and several products are commercially available. Automated analysis of reconnaissance and mapping imagery, however, has met with little success with the notable exception of automated cloud screening (7), a relatively simple problem.

The difficulties stem from the complexity and variability of both the terrain and objects operating on the terrain. Sources of temporal variability noted previously with regard to image-to-image comparison also degrade the performance of pattern recognition algorithms. Shadows, differential illumination and a variety of other diurnal, seasonal and aperiodic phenomenon all contribute to terrain variability. Identification of three-dimensional targets on the terrain is complicated by differential scale, variable aspect and rotation introduced by the wide range imaging conditions that characterize two-dimensional reconnaissance imagery. Finally, targets are embedded, often partially obscured, within the terrain background. In the past, system designers have often treated target detection as a "signal-to-noise" problem where the terrain background has been modeled simply as undifferentiated "clutter."

APPROACHES TO SIMPLIFY THE PROBLEM

When the techniques of image-to-image comparison and statistical pattern recognition were initially investigated for automated screening of digital imagery, they appeared to be sophisticated processes. In retrospect, they can now be characterized as simple approaches to a complex set of problems. Additional sources of information are needed to constrain and simplify these tasks. Fortunately, a number of new opportunities can be considered based on the availability of digital map data, the exploitation of analytical sensor models and the concept of map-to-image correspondence (8,9).

Map-to-Image Correspondence

Analytical techniques developed to support the generation of digital map data from stereoscopic imagery can be exploited to automatically project previously compiled digital map data into reconnaissance imagery.

Photogrammetrists refer to this operation as projection; computer vision researchers have adopted the term map-to-image correspondence. Prerequisites for map-to-image correspondence include an analytical sensor model for the imaging system, routine recovery of image acquisition parameters and the availability of three-dimensional digital map data.

In conventional mapping practice, use of sensor models and recovery of the image acquisition parameters are routine prerequisites to stereo mapping compilation or precise point positioning. Additionally, these procedures provide a rigorous basis for automatic prediction of precise image coordinates corresponding to terrestrial objects described by three-dimensional ground coordinates as a basis for map-guided scene analysis.

Sensor Model

Mathematical models have been developed for mapping and reconnaissance sensors which analytically characterize the image forming geometry of each system. Essentially, the simple mathematical model of the idealized "pinhole" camera has been generalized and extended to a variety of operational frame and dynamic imaging devices. Non-perspective imaging geometries, particularly the range imaging geometry of synthetic aperture radar, have also been successfully modeled (12,13).

Recovery of Acquisition Parameters

For a given image or set of images, recovery of image acquisition parameters which characterize the position and attitude of the sensor during the imaging event is a standard photogrammetric or radargrammetric operation. These procedures are described as block adjustment or triangulation when performed on multiple images and as the resection of a single image.

The development of improved capabilities for monitoring the position and attitude of acquisition platforms including inertial navigation technology and the Global Positioning Satellite system provide new opportunities to derive initial estimates of image acquisition parameters automatically.

Digital Map Data

Generation, management and exploitation of digital map data is the major focus of mapping research and development in the world leading to the production and use of digital elevation models (DEM) and digital planimetric or feature data. Digital elevation data is inherently three-dimensional as required for map-to-image correspondence. Existing planimetric data has been largely derived from two-dimensional manuscripts; however,

three-dimensional planimetry can be generated by interpolating elevation values from the corresponding DEM. In the future, direct data capture of three-dimensional planimetry from stereoscopic aerial photography using analytical plotters (8) will become increasingly common providing increased photo interpreter productivity and improved metric accuracy.

Map-Guided Scene Analysis

In the near-term, the most valuable use of map-to-image correspondence may lie in the elimination of areas from manual image exploitation based terrain characteristics and military doctrine. Interactive digital image exploitation in particular, supports and requires careful management of image exploitation assignments to maximize interpreter throughput. In the long run, several more challenging tasks can be considered based on direct utilization of digital map data to support automated image analysis.

A digital map encodes an explicit model of the shape and composition of the terrain that enables map-guided analysis of the general landscape. In the context of mapping and terrain analysis, this suggests the potential for automated screening to detect changes in terrain patterns, such as those introduced by road building, land clearing or military operations, given knowledge of the previous conditions. Similarly, automated target recognition can be pursued given an explicit characterization of the terrain background rather than some generalized description of background "clutter."

In the context of automated target recognition, digital map and collateral intelligence data can be used to specify where to look for individual objects or classes of objects. Automatically searching for vehicles on or adjacent to roads, bridging operations on or adjacent to rivers, or monitoring activity at motor pools and depots, represent challenging, but constrained, localized scene analysis tasks.

Geometric constraints can be exploited in other ways to support automated analysis of three-dimensional objects. Scale, aspect, relief displacement or layover, illumination and shadows can all be predicted for terrestrial objects given knowledge of the sensor, acquisition parameters and terrain. In some instances, such as road-bound vehicles or docked boats, rotation uncertainty can be reduced to one or two orientations. Such mensuration tools represent some of the analytical processes necessary to adequately interpret the two-dimensional data recorded in images of three-dimensional objects.

AN EXPERIMENTAL RESEARCH PROGRAM

Concepts of map-guided scene analysis for automated screening of diverse mapping and reconnaissance imagery based on map-to-image correspondence are being explored by the author in an in-house research study at the USAETL Research Institute. The study focuses on a European testsite situated west of the city of Freiburg and east of the Rhine River in southwestern West Germany. The area is characterized by diverse land use and is the object of several ongoing remote sensing research programs. A diverse set of digital map and image data has been assembled.

Digital Map Data

Selected digital map overlays were extracted from the German 1:50,000 map sheets which serve as the NATO standard topographic maps for the area. These planimetric files were transformed from two-dimensional to three-dimensional coordinate data representations based planimetric augmentation using a corresponding digital elevation model. A plot of the digital data compiled in the transportation map including roads, railroads, canals and powerlines is shown in Figure 1.

Image Data

A time sequence of aerial photography obtained with conventional frame cameras has been assembled representing several film types and a range of photo scales. Space photography of the testsite was initially acquired from the Space Shuttle using the European Space Agency (ESA) Metric Camera (Freiburg was obscured by cloud cover) and later with the NASA Large Format Camera (cloud-free stereo coverage was obtained). A scanning microdensitometer at USAETL is used to convert film duplication imagery into digital data.

Synthetic aperture radar (SAR) imagery has been obtained over the Freiburg testsite during several international experiments. In July 1981, the ESA SAR 580 Campaign made an extensive set of digital SAR acquisitions. This study uses a digital X-band imagery acquired with a nominal ground resolution of 3 meters as an example of airborne SAR imagery (see Figure 2). In October 1984, the site was imaged from space during the Shuttle Imaging Radar Experiment (SIR-B). Two digital images acquired during this mission at a nominal ground resolution of 25 meters provide experimental spaceborne SAR imagery. Recently, additional SAR imagery of the testsite has been acquired by the Intera Corporation using the airborne STAR-1 X-band system.

Figure 1. Freiburg Testsite Transportation Data. Linear features representing the transportation network as compiled from 1:50,000 topographic maps including autobahn, national roads, secondary roads, railroads, canals and powerlines.

Figure 2. SAR Image with Transportation Overlay. Map-to-image correspondence was used to project transportation network onto SAR 580 radar image.

Geometric Constraints

For the digitized photography, photogrammetric procedures (8) are used to recover the acquisition parameters and map-to-image correspondence is based on the corresponding projective (collinearity) equations. Experimental radargrammetric software was modified to recover acquisition parameters of the digital SAR images by space resection (9) and the radar range equations were adapted to support SAR map-to-image correspondence. In both cases, the same general procedures are applicable whether the imagery was acquired from aircraft or spacecraft.

Explicit Knowledge Representation

The organization and maintenance of a heterogeneous knowledge base to support exploitations of a diverse set of digital map and image data via map-to-image correspondence requires flexible extensible data structures. The concept of knowledge representation using frames is well documented in the artificial intelligence literature and has been used extensively in computer vision research. For this study, a family of frame-based systems based on the FRL system developed at MIT have been designed to capture shallow, but critical, representation of knowledge concerning the digital map, terrain phenomenon, sensor and mission parameters.

Useful knowledge describing a digital map includes relevant specifications and rules used to compile the map, descriptions of the source materials and some measure of metric accuracy. In particular, it is essential to encode the terrain patterns that can be present within a mapped feature due to cartographic generalization. The German forest, for example, depicted as a homogeneous unit on a map is typically partitioned into intensively managed compartments; these compartments are linked by a network of forest roads which may or may not be encoded in the map.

For automated screening, knowledge of terrain phenomenon focuses on the phenological criteria that influence the state of a terrain pattern as a function of time. Obvious examples include state of crops in agricultural fields, canopy condition of deciduous forests and the surface state of standing water bodies.

For each sensor to be utilized, essential knowledge includes instrument calibration and performance data as well as explicit references to the appropriate processes, implemented in computer code, that model the image formation process, image illumination phenomenon and radiometric response criteria.

Mission knowledge can include descriptions of the platform, sensor suite and flight plan or mission trajectory. At a minimum, explicit

representation of acquisition parameters of position, orientation and time is required for each image to be processed.

Current Status

This paper describes research in progress. The digital map and image data set described above have been installed on the Image Understanding Testbed at USAETL in conjunction with the frame-based knowledge representation system. Processed for map-to-image correspondence based on rigorous photogrammetric and radargrammetric principles have been implemented. A generate-and-test strategy has been formulated to drive a series of automated screening experiments. The approach relies on prediction of plausible signals for given map features expected to be present in a new image in the absence of significant change. Current efforts center on the implementation of a control strategy embedded within a tailored frame system and development of the specific domain knowledge bases.

CURRENT TRENDS

Issues raised in automated screening research based on map-guided scene analysis are related to a number of current trends and ongoing activities. A dramatic increase in the volume of reconnaissance imagery was cited earlier; concurrently, the Defense Mapping Agency is producing and distributing increased quantities of digital map data in the form of standard Digital Terrain Elevation Data and Digital Feature Analysis Data products for major landmasses. Specific Army initiatives in digital mapping include the development and fielding of the Digital Topographic Support System (DTSS) and the current technical base program for the Terrain Analyst Work Station (TAWS).

Related research activity is being conducted under several Defense Advanced Research Projects Agency (DARPA) programs. Significant applications of map-to-image correspondence are being explored under the Image Understanding Program with continuing efforts at Carnegie-Mellon University (10) and SRI International (5). Potential cartographic applications of image understanding techniques leading to improved interactive and partially automated systems represent a major area of interest in digital mapping research today (11).

A new DARPA program entitled Advanced Digital Radar Image Exploitation System (ADRIES) is directed to the development and demonstration of an advanced technology base for exploitation of multi-resolution SAR imagery (1). The program emphasizes largely autonomous exploitation capabilities with extensive use of collateral and contextual information to assist image analysis. Maintenance of a digital spatial model of

specific geographic areas of interest and map-to-image correspondence are essential components of the program. The ADRIES program, formulated and conducted with close Army support, will lead to the development of a naional SAR research testbed facility at USAETL.

The DARPA Strategic Computing Program, a major national commitment to developing advanced computational capabilities, is leading to the development of novel computer architectures and processing capabilities that enable serious consideration of computationally intensive tasks such as automated screening of reconnaissance imagery. In addition, the Autonomous Land Vehicle demonstration, described elsewhere in these proceedings (6), presents challenging tasks for use of digital map data to support real-time computer vision processes as well as mission planning.

CLOSING REMARKS

The mapping and reconnaissance communities have entered an age that is data rich. In the pursuit of techniques to process abundant image data into useful information, it is important to recognize that the only common frame of reference for these dissimilar data sources is a three-dimensional model of the world with additional capabilities to record temporal change. In the past, topographers emphasized metric processing of imagery to produce accurate maps and to direct weapons systems; in other image exploitation applications, positional accuracies have been less critical -- the nearest kilometer grid cell was often close enough. Today, technical advances make it possible to extend metric fidelity to a broad range of imaging systems which will create significant opportunities for computer-assisted and automated image exploitation. The implications of this observation are clear. Optimized multisensor fusion will require analytically modeled and calibrated imaging sensors. Image acquisition parameters must be recovered routinely and made available to support image exploitation. The concept of the three-dimensional digital map must be generalized to include current situation data, analogous to the existing grease pencil overlays, to realize the potential of our mapping and reconnaissance systems to create and maintain a working model of a geographic area of interest that is current, flexible and responsive.

REFERENCES:

1. Anonymous (1985) "Advanced Digital Radar Image Exploitation System (ADRIES) Program Plan," Advanced Information & Decision Systems, Mountain View, California.

2. Anuta, P.E. (1980) "Spatial Registration of Multispectral and Multitemporal Digital Imagery Using FFT Techniques," IEEE Trans. Geosci. Electron., Vol. GE-8, No. 4, pp. 353-368.

3. Barnea, D.I. and H.F. Silverman (1982) "A Class of Algorithms for Fast Digital Image Registration," IEEE Trans. Comput., Vol. C-21, pp. 179-186.

4. Duda, R.O. and P.E. Hart (1973) Pattern Classification and Scene Analysis, John Wiley & Sons, New York.

5. Fischler, M.A. and A.J. Hanson (1983) "Image Understanding Research and Its Application to Cartography and Computer-Based Analysis of Aerial Imagery," SRI International, Menlo Park, California.

6. Leighty, R.D. and G.R. Lane (1986) "Developing Technologies for Army Autonomous Land Vehicles," 1986 Army Science Conference, West Point, New York.

7. Lukes, G.E. (1977) "Rapid Screening of Aerial Photography by OPS Analysis," Proc. SPIE, Data Extraction from Film, Vol. 117, pp. 89-97.

8. Lukes, G.E. (1981) "Computer-Assisted Photo Interpretation Research at the United States Army Engineer Topographic Laboratories (USAETL)," Proc. SPIE, Techniques and Applications of Image Understanding III, Vol. 281, pp. 85-94.

9. Lukes, G.E. and J.H. Raggam (1986) "Implementation of Map-to-Image Correspondence for Synthetic Aperture Radar Image Analysis," 52nd Annual Meeting, American Society of Photogrammetry and Remote Sensing, Washington, D.C.

10. McKeown, D.M. (1984) "Knowledge-Based Aerial Photo Interpretation," Photogrammetria, Vol. 39, pp. 91-123.

11. McKeown, D.M. and G.E. Lukes (1984) "Digital Mapping and Image Understanding," XVth International Congress of Photogrammetry and Remote Sensing, Rio de Janeiro, Brazil.

12. Norvelle, F.R. (1972) "AS-11-A Radar Program," Photogrammetric Engineering, Vol. 38, pp. 77-82.

13. Slama, C.C. (Ch. Ed.) (1980) Manual of Photogrammetry, American Society of Photogrammetry, Falls Church, Virginia.

14. Tou, J.T. and R.C. Gonzalez (1974) Pattern Recognition Principles, Addison-Wesley, Reading, Massachusetts.

END

12-86

DTIC